7-1-2011

Feedback regulated star formation in cool core clusters of galaxies

Grant Tremblay

Feedback Regulated Star Formation in Cool Core Clusters of Galaxies

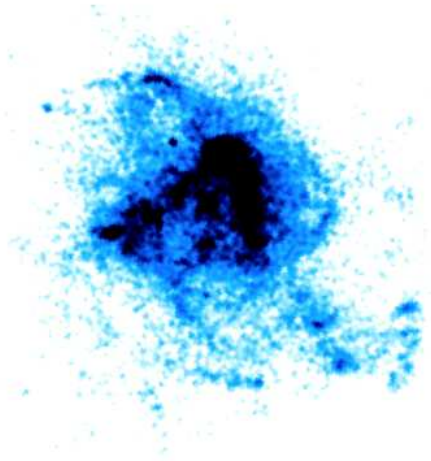

Grant Russell Tremblay

A dissertation submitted to the
Rochester Institute of Technology
in partial fulfillment of the requirements for the degree of
Doctor of Philosophy *in* Astrophysics.

Approved by the dissertation committee on 26 July 2011
Dr. Christopher P. O'Dea Dr. Stefi A. Baum
Dr. Harvey E. Rhody Dr. Joel H. Kastner Dr. Andrew Robinson

July, 2011

For my Mother and Father,
who prove that the brightest stars will always lead you home.

ABSTRACT

The classical "cooling flow" model historically associated with "cool core" clusters of galaxies fails in the absence of an external, non-gravitational heating mechanism needed to offset catastrophic radiative losses of the X-ray bright intracluster medium (ICM). Numerous proposed solutions exist, including feedback from active galactic nuclei (AGN), which may elegantly calibrate fundamental relationships such as the coupled co-evolution of black holes and the stellar component of their host galaxies. AGN feedback cannot completely offset cooling at all times, however, as the brightest cluster galaxies (BCGs) in cool core clusters harbor extensive warm ($\sim 10^4$ K) and cold ($10 < T < 10^4$ K) gas reservoirs whose physical properties are regulated by ongoing star formation and an unknown, non-stellar heating mechanism.

We present a doctoral thesis broadly related to these issues, particularly as they pertain to cooling flows, the triggering of AGN activity, and the associated energetic feedback that may play a critical role in heating the ambient environment on tens to hundreds of kiloparsec scales. We begin with a summary of the relevant background material, and in Chapter 2 we present a multiwavelength study of effervescent AGN heating in the cool core cluster Abell 2597. Previously unpublished *Chandra* X-ray data show the central regions of the hot intracluster medium (ICM) to be highly anisotropic on the scale of the BCG, permeated by a network of kpc-scale X-ray cavities, the largest of which is cospatial in projection with extended 330 MHz radio emission. We present spectral maps of projected, modeled gas properties fit to the X-ray data. The X-ray temperature map reveals two discrete, "hard-edged" structures, including a ~ 15 kpc "cold filament" and an arc of hot gas which in projection borders the inner edge of the large X-ray cavity. We interpret the latter in the context of the effervescent AGN heating model, in which cavity enthalpy is thermalized as the ambient keV gas rushes to refill the wake of the buoyant bubble. The hot arc revealed in the temperature map may be one of the first instances in which ICM/ISM heating by AGN feedback is directly observed. The ~ 15 kpc soft excess filament, part of which is cospatial with extended 1.3 GHz radio emission, may be associated with dredge-up of low entropy gas by the propagating radio source. Results from our study of the hot X-ray gas are framed in the context of inferred young stellar component ages associated with the central emission line nebula in the BCG. We find that inferred ages of the young stellar component are both younger and older than the inferred ages of the X-ray cavities, suggesting that low levels of star formation have managed to persist amid the AGN feedback-driven excavation of the X-ray cavity network.

In Chapter 3 we present *Hubble Space Telescope* far-ultraviolet imaging of seven BCGs in cool core clusters selected on the basis of elevated star formation rates. We find that even at low levels,

star formation provides a dominant contribution to the ionizing photon reservoir required to power the observed luminosities of the emission line nebula. Weak, compact radio sources are observed in each of these seven BCGs. The combination of higher SFR and lower radio power is consistent with a scenario wherein a low state of AGN feedback allows for increased residual condensation from the ambient X-ray atmosphere, accounting for the elevated star formation rates.

In Chapter 4 we present a comparison study of episodic star formation and AGN activity in the giant radio galaxy 3C 236, which is not associated with a cluster. We find that an episodic AGN/starburst connection can be fostered by a non-steady transport of gas to the nucleus. These results are then compared with Abell 2597, enabling a better understanding of the roles that may be played by cooling flows vs. mergers and hot vs. cold accretion modes in depositing the gaseous reservoirs that fuel both star formation and AGN activity.

In Chapter 5 we broaden the context of the thesis with a search for high redshift Fanaroff-Riley class I radio galaxies, which may act as observable "beacons" for assembling protoclusters. Probing the epoch of cluster assembly will be critical to a better understanding of the evolution of the cool core phenomenon and the history of cluster entropy regulation in general. The relative inability of X-ray cluster selection techniques to extend to these redshifts necessitates alternative detection methods, one of which we describe in this thesis.

Finally, in Chapter 6 we discuss the main conclusions of this thesis, which can be summarized as follows: (1) AGN feedback is real, and likely plays a dominant role in regulating the pathway of entropy loss from hot ambient medium to cold gas to star formation; (2) AGN feedback does not establish an impassable "entropy floor" below which gas cannot cool; and (3) star formation plays an important role in determining the temperature and ionization of the warm ($\sim 10^4$ K) and cold ($10 < T < 10^4$ K) gas phases in brightest cluster galaxies.

CONTENTS

ACKNOWLEDGEMENTS

Without actually knowing what it meant, I've told people that I wanted to be an astrophysicist since I was in seventh grade. Those who enable childhood dreams are very special people indeed. For this reason, I begin by thanking my awesome, astonishingly brilliant mentors Chris O'Dea and Stefi Baum, without whom none of this would have been possible. They're simply human beings of the highest order, effortlessly generous and kind — and, by the way, awesome friends to have a beer (or two) with. Their unwavering support has enabled me to spend my life doing what I love, and for that I will always be grateful. I know that we will be life-long collaborators and, more importantly, friends. On that note, I officially suggest that our next face-to-face science meeting be held in Munich next year — during Oktoberfest, perhaps?

I am lucky to have been part of the Astrophysics Ph.D. program's inaugural class at RIT. I know that it will grow and flourish, as it is run by the most phenomenal people that any department could ask for. I am especially grateful to Andy Robinson, our incredible program director, and the mentors like Joel Kastner and David Axon who have helped shape who I am as a scientist. I thank my Ph.D. committee for their guidance, advice, and patience (the latter is especially true, given the comically late hour in which this thesis was finished). Thanks are also due to the wonderful Staff at the Center for Imaging Science and the Department of Physics, particularly Sue Chan, our Academic Coordinator.

I would never have gotten anywhere in science had it not been for my friend, collaborator, and former undergraduate advisor Alice Quillen, who has supported me for eight years. Thanks entirely to her, I spent two incredible years at the Space Telescope Science Institute, where I learned from the best: Marco Chiaberge, Bill Sparks, and Duccio Macchetto, to whom I am endlessly grateful. I met amazing friends in Baltimore: David Radburn-Smith, Megan Sosey, Jen Mack, Benne Holwerda, Nor Pirzkal, Rolly Bedin, Will Clarkson, Katrina Exter, Scott Noble, Somayeh Shams, Parviz Ghavamian, Elena Sabii, Francesca Annibali (among many, many others). They might recall that, over beers, many of them frequently promised me faculty jobs one day. I'll be reminding them in a few years time. I also wish to thank Diane Bowen, my extraordinary seventh grade science teacher, who inspired me to pursue a career in astronomy.

My scientific life has been enriched by discussions with a long list of great collaborators. Besides, of course, Chris, Stefi, Marco, Bill, and Alice, I wish to thank Tracy Clarke, Alessandro

Capetti, Alastair Edge, Andy Fabian, Anton Koekemoer, Brian McNamara, Rupal Mittal, Raymond Oonk, Helen Russell, Craig Sarazin, Arno Schoenmakers, Mark Voit, and Mike Wise. I'll consider myself successful if I can achieve even a tenth of the scientific insight that these wonderful people have, particularly Chris and Stefi. "Star stuff contemplating star stuff", indeed.

Because I am surrounded by amazing friends, my years in Rochester have been some of the happiest of my life. Dave Principe, Fabio Antonini, Christine Trombley, Colin Kingsley, Rudy Montez, Rosa Mitsumasu, Marcelo Ponce, Dan Dicken, Rachel Curran, Germano Sacco — I'll miss you like crazy, but I know that I'll see you again soon. Thank you Maša for making what should have been the most stressful year of my life my favorite year of all.

One of my favorite quotes is from Carl Sagan, who said that "*we are the custodians of life's meaning*." Astronomers may look upwards for meaning, but I never needed to look further than my Family. This includes my Aunts, Uncles, and Cousins, who have loved and supported me all my life. It includes my Grandmother, one of the most extraordinary and selfless people I've ever known, and my Grandfather, Mémère, and Pépère, who I miss dearly. It also includes Andrew, who will always be my best friend and my brother. I love you all more than you can imagine.

Finally, everything I am and ever will be was a gift from my Mother and Father, who I love more than anything on or above the Earth. I dedicate everything to them.

– Grant
April 22, 2011

DECLARATION

I, GRANT RUSSELL TREMBLAY ("the Author"), declare that no part part of this thesis is substantially the same as any that has been submitted for a degree or diploma at the Rochester Institute of Technology or any other University. I further declare that this work is my own. Those who have contributed scientific and other collaborative insights are fully credited in this thesis, and all prior work upon which this thesis builds is cited appropriately throughout the text. This thesis was successfully defended in Rochester, NY, USA on April 27, 2011.

For illustrative and discussion-oriented purposes, I have reproduced various figures appearing in **Chapter 1** from the work of other authors. These figures are always fully credited in the associated caption.

Modified portions of this thesis have previously been published by the Author in peer-reviewed articles appearing in *The Astrophysical Journal* (ApJ). Details on these papers are provided below.

- **Chapter 2.** The majority of the work presented in this chapter will be submitted as part of a paper in preparation by Tremblay and collaborators, entitled *Persistent Star Formation amid Effervescent AGN Feedback in Abell 2597*. Co-authors on this work include C. O'Dea & S. Baum (the Thesis advisers), T. Clarke, J. Bregman, A. Edge, A. Fabian, B. McNamara, R. Mittal, R. Oonk, A. Quillen, H. Russell, J. Sanders, C. Sarazin, M. Voit, R. Wilman, and M. Wise. The work is expected to be submitted shortly after the certification date of this thesis. All work presented in this chapter was undertaken by Tremblay, the paper's primary author. The invaluable input from co-authors on this work is (a) fully credited and (b) limited to collaborative scientific insight: that is, all text, figures, and the bulk of the scientific analysis appearing in this chapter are solely the work of the Author.

- **Chapter 3.** A slightly modified version of this chapter has been published by O'Dea *et al.* (2010) unter the title *Hubble Space Telescope Far-ultraviolet Observations of Brightest Cluster Galaxies: The Role of Star Formation in Cooling Flows and BCG Evolution* (2010, ApJ, 719, 1619). Co-authors on this work include A. Quillen, C. O'Dea, G. Tremblay, B. Snios, S. Baum, K. Christiansen, J. Noel-Storr, A. Edge, M. Donahue, and M. Voit. Tremblay contributed a significant fraction of the scientific analysis, as well as large portions of the text and figures. So as to preserve the integrity of the work, we have not excised the invaluable scientific and material contributions of the other co-authors. These contributions are fully

credited.

- **Chapter 4.** A slightly modified version of this chapter has been published in ApJ by Tremblay *et al.* (2010) under the title *Episodic Star Formation Coupled to Reignition of Radio Activity in 3C 236* (2010, ApJ, 715, 172). Co-authors on the work include C. O'Dea, S. Baum, A. Koekemoer, W. Sparks, G. de Bruyn, and A. Schoenmakers. All work presented in this chapter was undertaken by Tremblay, the paper's primary author. The invaluable input from co-authors on this work is (a) fully credited and (b) limited to collaborative scientific insight: that is, all text, figures, and the bulk of the scientific analysis appearing in this chapter are solely the work of the Author. The original proposal for the data presented in this chapter was led by Dr. Christopher O'Dea, and the proposal's co-investigators appear as co-authors on the published version of the paper.

- **Chapter 5.** A slightly modified version of this chapter have been published in a paper by Chiaberge *et al.* (2010) under the title *Low-Power Radio Galaxies in the Distant Universe: A Search for FR I at 1 < z < 2 in the COSMOS Field* (2009, ApJ, 696, 1003). Co-authors on the work include G. Tremblay, A. Capetti, F. D. Macchetto, P. Tozzi, and W. Sparks. Tremblay was responsible for the bulk of the data collection, analysis, figures, and approximately 50% of the text in the paper, which was a very collaborative effort on the part of Chiaberge and Tremblay. M. Chiaberge had the initial idea for the project, and was responsible for approximately 50% of the interpretation and text appearing in the paper. To preserve the integrity of the work, we have not excised the invaluable material contributions of Chiaberge (i.e., text and figures) from the chapter. The text (which has since been modified by Tremblay) and (two) figures directly provided by Chiaberge are fully credited throughout this chapter.

Of course, none of the work presented in this thesis would be possible were it not for the unending support and unrivaled scientific insight of Dr. Christopher O'Dea and Dr. Stefi Baum, my thesis advisers. See the previous section for a special acknowledgment of their innumerable contributions to both this work and my scientific career in general.

G. R. Tremblay
Rochester, May 2011

LIST OF PUBLISHED WORKS

1. K. P. O'Dea, A. C. Quillen, C. P. O'Dea, **G. R. Tremblay**, B. T. Snios, S. A. Baum, K. P. Christiansen, J. Noel-Storr, A. C. Edge, M. Donahue, & G. M. Voit, "*HST FUV Observations of Brightest Cluster Galaxies: The Role of Star Formation in Cooling Flows and BCG Evolution*", 2010, ApJ, 719, 1619.

2. **G. R. Tremblay**, C. P. O'Dea, S. A. Baum, A. M. Koekemoer, W. B. Sparks, G. de Bruyn, & A. P. Schoenmakers, "*Episodic Star Formation Coupled to Reignition of Radio Activity in 3C 236*", 2010, ApJ, 715, 172.

3. F. Massaro, D. E. Harris, **G. R. Tremblay**, D. J. Axon, S. A. Baum, A. Capetti, M. Chiaberge, R. Gilli, G. Giovannini, P. Grandi, F. D. Macchetto, C. P. O'Dea, G. Risaliti, & W. B. Sparks , "*Chandra Observations of 3C Radio Sources with* $z < 0.3$*: Nuclei, Diffuse Emission, Jets, and Hotspots*", 2010, ApJ, 714, 589.

4. M. Chiaberge, A. Capetti, F. D. Macchetto, P. Rosati, & P. Tozzi, **G. R. Tremblay**, "*Three Candidate Clusters of Galaxies at Redshift* ~ 1.8*: The Missing Link Between Protoclusters and Local Clusters?*", 2010, ApJL, 710, 107.

5. **G. R. Tremblay**, M. Chiaberge, W. B. Sparks, S. A. Baum, M. G. Allen, D. J. Axon, A. Capetti, D. J. E. Floyd, F. D. Macchetto, G. K. Miley, J. Noel-Storr, C. P. O'Dea, E. S. Perlman, & A. C. Quillen, "*HST/ACS Emission Line Imaging of Low-redshift 3CR Radio Galaxies. I. The Data*", 2009, ApJS, 183, 278.

6. M. Chiaberge, **G. R. Tremblay**, A. Capetti, F. D. Macchetto, P. Tozzi, & W. B. Sparks, "*Low-Power Radio Galaxies in the Distant Universe: A Search for FR I at* $1 < z < 2$ *in the Cosmos Field*", 2009, ApJ, 696, 1103.

7. D. J. E. Floyd, D. J. Axon, S. A. Baum, A. Capetti, M. Chiaberge, F. D. Macchetto, J. P. Madrid, G. K. Miley, E. S. Perlman, A. C. Quillen, W. B. Sparks, & **G. R. Tremblay**, "*Hubble Space Telescope Near-infrared Snapshot Survey of 3CR Radio Source Counterparts. II. An Atlas and Inventory of the Host Galaxies, Mergers, and Companions*", 2008, ApJS, 177, 148.

8. **G. R. Tremblay**, M. Chiaberge, C. J. Donzelli, A. C. Quillen, A. Capetti, W. B. Sparks, & F. D. Macchetto, "*Isophotal Structure and Dust Distribution in Radio-loud Elliptical Galaxies*", 2007, ApJ, 666, 109.

9. **G. R. Tremblay**, A. C. Quillen, D. J. E. Floyd, J. Noel-Storr, S. A. Baum, D. J. Axon, C. P. O'Dea, M. Chiaberge, F. D. Macchetto, W. B. Sparks, G. K. Miley, A. Capetti, J. P. Madrid, & E. S. Perlman, "*The Warped Nuclear Disk of Radio Galaxy 3C 449*", 2006, ApJ, 643, 101.

The papers currently in preparation have been excluded from this list. Conference proceedings have also been excluded.

LIST OF FIGURES

LIST OF TABLES

1

INTRODUCTION

The Heating *of* Rapidly Cooling Cluster Cores

And whether or not it is clear to you,
no doubt the Universe is unfolding as it should.
DESIDERATA, 1927

The hierarchical assembly of luminous structure in the Universe begins with the first stars at the epoch of reionization and ends with massive clusters of galaxies after a Hubble time. Observations of the latter suggest that the process is inefficient with respect to the formation of stars and galaxies, as these comprise only ten percent of the baryonic mass fraction in a galaxy cluster. The majority of baryons do not participate in the growth of structural complexity, and are instead heated at early epochs by adiabatic compression and accretion shocks to tens of millions of kelvin, roughly the virial temperature of the cold dark matter halos into which they collapse. The result is a quasi-hydrostatic bath of X-ray bright, optically thin plasma occupying hundreds of cubic megaparsecs. The processes regulating the entropy of this intracluster medium are poorly understood, but surely fundamental to our understanding of galaxy evolution as a whole. This doctoral thesis presents new observational insights into these issues, for which we now provide a contextual summary.

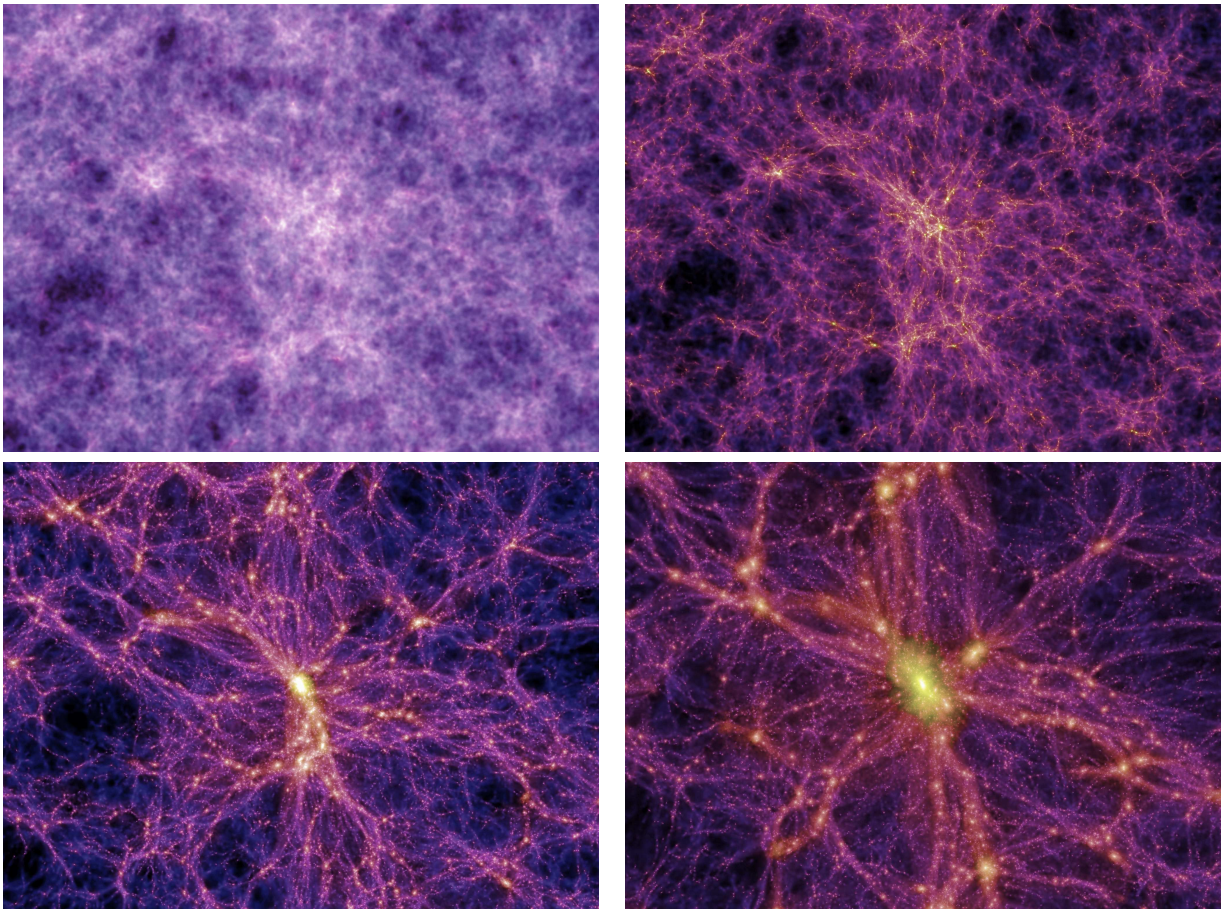

Figure 1.1: Both dark matter halo and baryonic structure grows hierarchically in the ΛCDM cosmological paradigm. This visualization, from the 10^{10} particle *Millennium* simulation of Springel *et al.* (2005), shows the spatial density of dark matter halos at various epochs in the simulation. In the top left panel, the Universe is 0.2 Gyr old, while the bottom right panel shows the distribution of dark matter as it might exist now. The massive halo at the core of the filamentary web would be host to a rich cluster of galaxies. Each visualization is approximately 70 Mpc h^{-1} across and projects a slice through the density field 15 Mpc h^{-1} thick.

1.1 An Overview of the Science in this Thesis

For a subset of galaxy clusters[1] with sharply peaked X-ray surface brightness profiles, the intracluster medium (ICM, e.g., Sarazin 1986) can cool via bremsstrahlung processes from $> 10^7$ K to $\ll 10^4$ K on timescales much shorter than a $\sim$Gyr within a radius of $\sim$100 kpc[2]. Simple models predict that runaway entropy loss by gas within this radius accompanies subsonic, nearly isobaric compression by the ambient hot reservoir, driving a long-lived classical "cooling flow" onto the central brightest cluster galaxy (hereafter BCG, e.g., Lea *et al.* 1973; Cowie & Binney 1977; Fabian & Nulsen 1977; see cooling flow reviews by Fabian 1994; Peterson & Fabian 2006). Such a phenomenon might constitute an observable low-redshift analog to cooling processes thought to drive the formation and evolution of massive galaxies at early epochs (e.g., Silk 1977; Rees & Ostriker 1977). Amongst the largest galaxies in the Universe, BCGs in rapidly cooling cluster cores ("cool cores", hereafter CC[3]) therefore represent critical tests for hierarchical structure formation models.

Two decades of progress have demonstrated that the cooling flow model historically associated with CC clusters fails in the absence of an additional, non-gravitational heating mechanism. Uninhibited, catastrophic condensation should drive massive cold gas repositories ($\sim 10^{12}$ $M_\odot$, e.g., Fabian 1994; O'Dea & Baum 1997) and extreme star formation rates in the BCG ($10^2 - 10^3$ $M_\odot$ yr^{-1}, e.g., Peres *et al.* 1998), but results from searches for these mass sinks were often orders of magnitude below predictions (e.g., Allen, 1969; De Young & Roberts, 1974; Peterson, 1978; Haynes *et al.*, 1978; Baan *et al.*, 1978; Shostak *et al.*, 1980; O'Dea & Baum, 1987a; McNamara & O'Connell, 1989; O'Dea *et al.*, 1994b; O'Dea & Baum, 1997; O'Dea *et al.*, 1998; Allen, 1995; Mittaz *et al.*, 2001; Edge & Frayer, 2003). Moreover, the absence or strong under-production of expected coolant lines in high resolution X-ray spectroscopy of large CC cluster samples effectively proves that no more than 10% of the supposedly cooling gas actually cools below $\lesssim 1$ keV (e.g., Fig. 1.3 and Tamura *et al.* 2001; Peterson *et al.* 2001, 2003; Xu *et al.* 2002; Sakelliou *et al.* 2002; Sanders *et al.* 2008).

[1]This section (1.1) provides a focused and brief summary of the background material that is directly relevant to this thesis. So as not to distract the reader with too much secondary or contextual detail, some prior knowledge of galaxy clusters is assumed. A longer, more general review of this material can be found in Section 1.2.

[2]One parsec (pc) is approximately 3.26 light years (ly) or $\sim 3.09 \times 10^{18}$ cm.

[3]The defining characteristic of a "cool core" cluster is somewhat inconsistent throughout the literature. CC clusters have been classified as such given (1) an observed central temperature drop (e.g., Sanderson *et al.* 2006; Burns *et al.* 2008), (2) a short *inferred* central cooling time $t_{\rm cool}$ (shorter than the age of the cluster, i.e., $t_{\rm cool} \lesssim 1/H_0$ or sometimes $t_{\rm cool} < 10$ Gyr, e.g., Bauer *et al.* 2005; Donahue *et al.* 2007), or (3) a high classical mass deposition rate (e.g., Chen *et al.* 2007). For a recent discussion of the issue, see Hudson *et al.* (2010). This thesis exclusively focuses on clusters whose CC status is unambiguous, regardless of the specific criterion used (meaning they satisfy all three). See section 1.2.3 for a more detailed discussion of cool core clusters and their historical association with the cooling flow model.

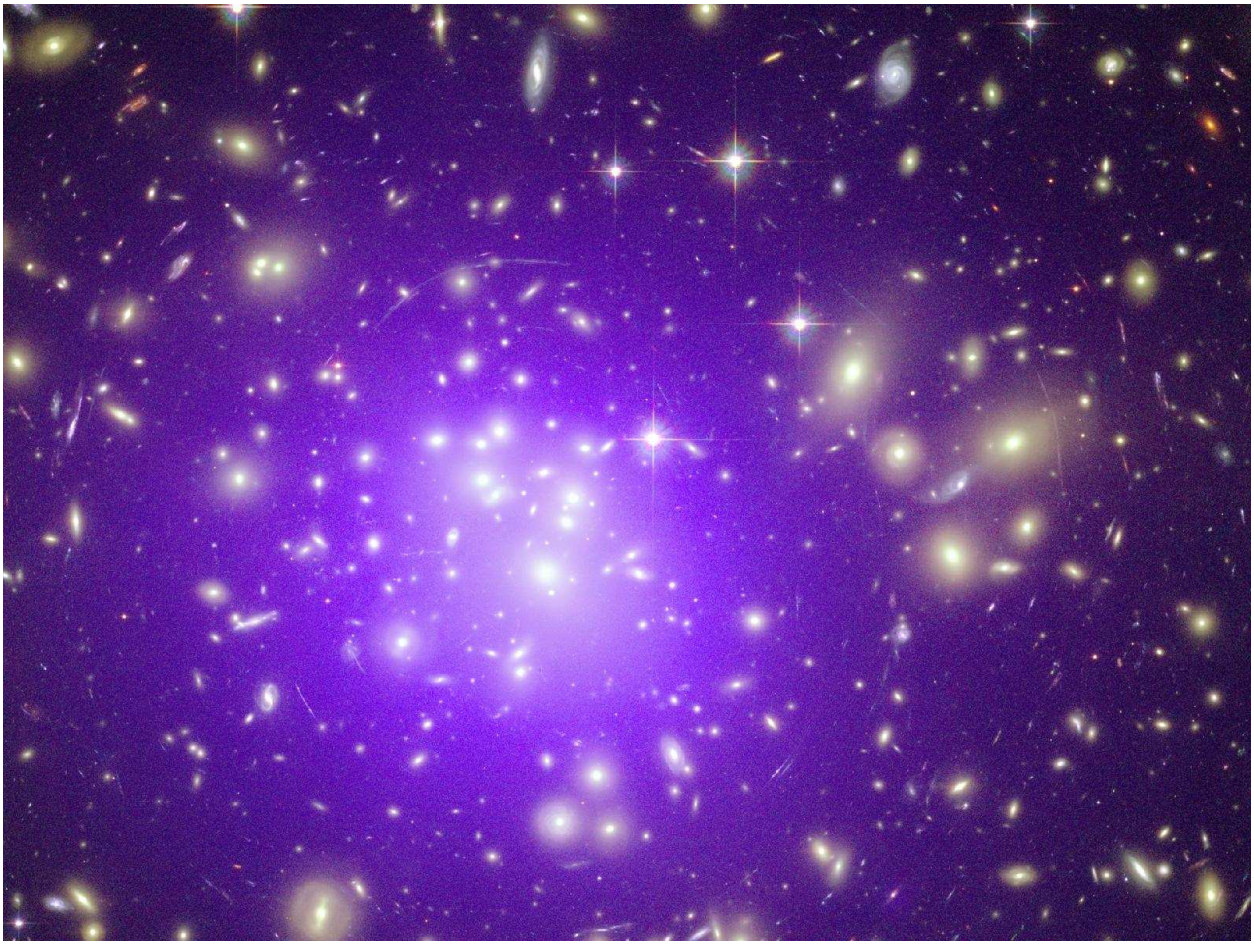

Figure 1.2: *Hubble Space Telescope* (optical) and *Chandra X-ray Observatory* (X-ray, in purple) composite image of the galaxy cluster Abell 1689 ($z = 0.18$, corresponding to a luminosity distance of order 2.8 billion light years). The hot ($10^7 - 10^8$ K or $1 - 10$ keV), X-ray luminous intracluster gas (in purple) comprises $\sim 80 - 90\%$ of the cluster's *baryonic* mass fraction. The entire cluster resides within a dark matter halo comprising 90% of the *total* mass fraction. Clusters of galaxies are the largest virialized structures in the Universe, containing masses exceeding $10^{15}\ M_\odot$ within radii that can reach several Mpc. The faint arcs in the image arise from the gravitational lensing effect, wherein the massive cluster warps spacetime and alters the apparent trajectory of photons passing through it. The field of view of the image is $\sim 3.2'$, corresponding to a projected angular size of order ~ 0.5 Mpc. (Credit: X-ray: NASA/CXC/MIT/E. H. Peng et al.; Optical: NASA/STScI).

1.1.1 Brightest Cluster Galaxies in Cool Cores

Nevertheless, there is circumstantial evidence that some residual cooling to $\lesssim 10^4$ K manages to persist at a few percent of the expected levels. Relative to BCGs in non-cool core clusters or field giant ellipticals (gEs), BCGs in cool cores are far more likely to harbor Hα-bright optical emission line nebulae with complex filamentary morphologies, blue continuum excess associated with low levels of ongoing star formation ($\lesssim 10\ M_\odot\ \mathrm{yr}^{-1}$), and compact central radio sources (e.g., the archetypal NGC 1275 / Perseus, see Fig. 1.4 and e.g., Minkowski 1957; Lynds 1970; Sabra *et al.* 2000; Conselice *et al.* 2001; Fabian 2003). The power of these phenomena appears to correlate with upper limits on X-ray derived ICM cooling rates (Hu *et al.*, 1985; O'Dea & Owen, 1987; Heckman *et al.*, 1989; McNamara *et al.*, 2004; Rafferty *et al.*, 2006; Salomé *et al.*, 2006; Quillen *et al.*, 2008; O'Dea *et al.*, 2008), and the emission line nebulae are almost always cospatial with the coolest X-ray gas (Crawford *et al.*, 1995, 2005; Fabian, 2003). In a few cases, estimates of condensation and star formation rates are in near agreement (O'Dea *et al.*, 2008). Moreover, repositories of up to $10^{10}-10^{11}\ M_\odot$ of cold[4] molecular hydrogen have been detected on 20 kpc scales through CO observations in $15-30$% of CC clusters (depending on the sample, Edge 2001; Edge & Frayer 2003; Salomé *et al.* 2006), as have extended distributions of vibrationally excited H_2 emission (Donahue *et al.*, 2000; Jaffe *et al.*, 2001; Egami *et al.*, 2006; Wilman *et al.*, 2009). Recently, *Herschel Space Observatory* observations of 11 CC BCGs (hereafter the *Herschel* OTKP sample) have confirmed the presence of substantial ($\sim 10^{10}\ M_\odot$) cold gas reservoirs via spectroscopic detection of major coolant lines (e.g., [C II]λ157 μm, [O I]λ68 μm) stemming from < 50 K gas (Edge *et al.* 2010a,b; Oonk et al. 2011, in preparation; Mittal et al. 2011, in press). These pools of cold gas appear to be correlated with the luminosity, dynamics and morphology of the Hα nebulae.

While this is strongly suggestive of an intrinsic connection between short ICM cooling times and the presence of these phenomena, debate continues as to whether these active gas reservoirs are direct condensates from a cooling flow (e.g., O'Dea *et al.* 2008, and references therein), or are instead deposited through wet mergers or gas-rich tidal stripping from nearby companions (e.g., Sparks *et al.* 1989; Holtzman *et al.* 1996, and references therein). If it were the latter case, a preferentially high gas rich merger rate in cool cores would be needed to reconcile observations that CC BCGs are more than three times as likely as non-CC BCGs to host emission line nebulae

[4]Throughout this thesis, we will use "hot" to describe $10^7 < T < 10^8$ K (X-ray bright) ICM/ISM phases, "warm" to describe $\sim 10^4 < T < 10^5$ K (optical and UV bright) components, and "cold" to describe $\sim 10 < T < 10^4$ K (N/M/FIR bright) components. By nature of the data we will present, we will not discuss the critically important $10^5 - 10^7$ K regime at great length in this thesis.

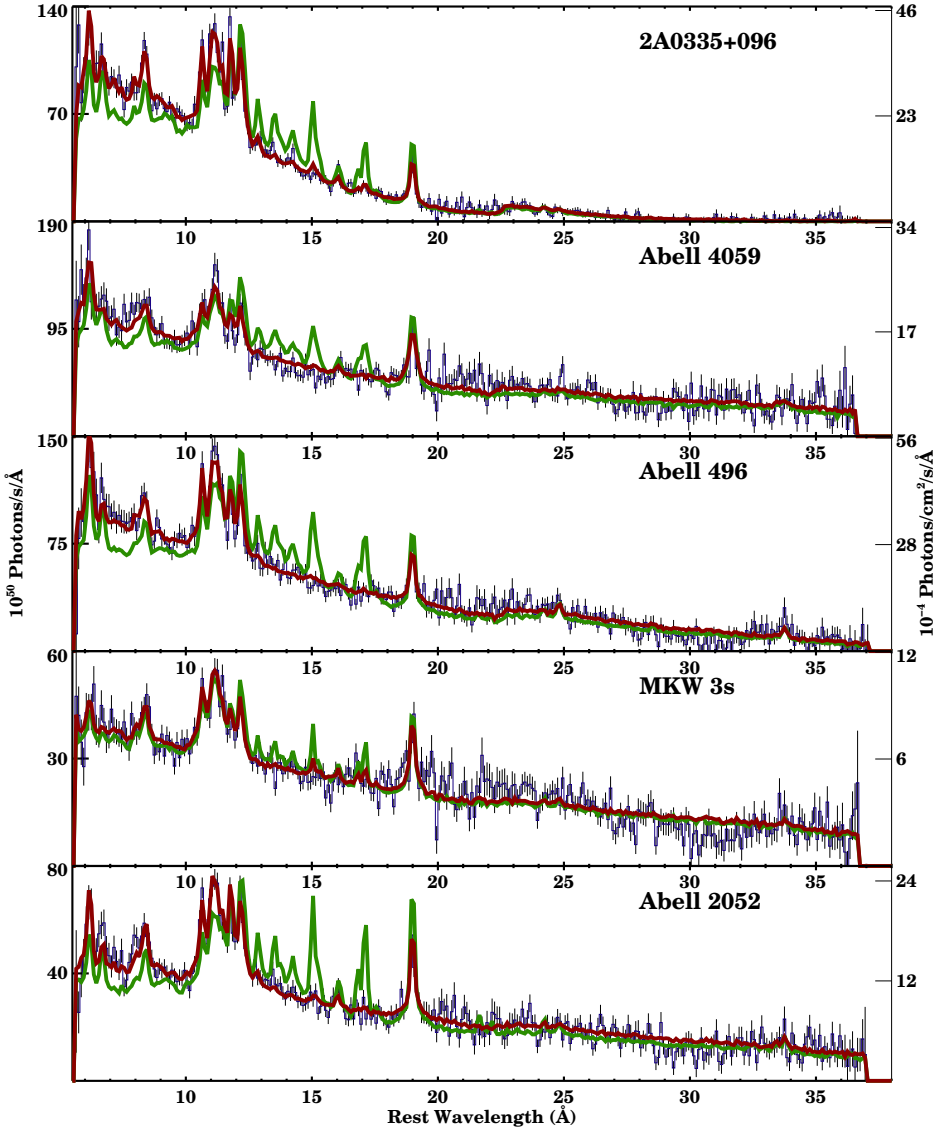

Figure 1.3: Presented here is one of the most important instances in which the classical, uninhibited cooling flow model to fails match observations. Plotted in blue is the high spectral resolution *XMM-Newton* X-ray spectroscopy of Peterson *et al.* (2003), with 1σ error bars. An empirical model is fit to the data, and plotted in red. The standard cooling flow model is plotted in green. Clearly, the uninhibited cooling flow model severely overpredicts cooling line fluxes stemming from the soft X-ray gas. This figure is reproduced from Fig. 4, panel 2 in Peterson *et al.* (2003), with permission from Dr. John Peterson.

($\sim$ 45% vs. $\sim$ 10%, respectively, Crawford *et al.* 1999; Best *et al.* 2006; Edwards *et al.* 2007) and central radio sources ($\sim$ 70% vs. $\sim$ 20%, respectively, Burns 1990), though it is not obvious why this should be the case.

On the other hand, it is now clear that the emission line nebulae are not simply the 10^4 K phase of a cooling flow. While the bulk of the "baryon budget" for these phenomena might be accounted for by condensation from the ambient hot reservoir, the cooling flow model in isolation seriously underpredicts the observed Hα luminosities by orders of magnitude in a pure radiative cooling scenario (e.g., Heckman *et al.*, 1989; Voit & Donahue, 1997). The nebulae are also characterized by low ionization forbidden line flux that greatly exceeds the flux emerging from recombination lines, requiring models to impart a great deal of heating per ionization event (Donahue & Voit, 1991; Voit & Donahue, 1997). The low levels (a few $M_\odot$ yr^{-1}) of star formation observed in half of all CC BCGs can often account for the ionizing photons required to power the observed Hα luminosity (e.g., Bildfell *et al.*, 2008; O'Dea *et al.*, 2008, 2010; McDonald *et al.*, 2010, 2011), but another heating mechanism is required to account for the inverted forbidden-to-Balmer and other diagnostic line ratios (e.g., Voit & Donahue, 1997). Collisional heating by suprathermal electrons (cosmic rays) has gained favor in recent years (Ferland *et al.* 2009; Donahue *et al.* 2011; Fabian *et al.* 2011; Mittal et al. 2011, in press).

1.1.2 Heating cluster cores with "effervescent" AGN feedback and conduction

While the cooling flow model is inconsistent with observations, there is no doubt that the ICM in CC clusters is losing energy at a rate proportional to its X-ray luminosity, which can be extreme in some cases ($\lesssim 10^{45}$ ergs sec^{-1}). A compensatory heating (or reheating) mechanism is therefore needed to balance cooling in the majority of cases, thereby accounting for the dearth of predicted warm and cold mass sinks associated with the cooling flow model. CC clusters account for $> 50\%$ of the X-ray luminous cluster population below $z < 0.4$ (e.g., McNamara & Nulsen, 2007), so they must be heated at an average rate approximately of order their X-ray luminosity (heating rates far in excess of this would push cooling times past the Hubble time, destroying the CC phase). Such a scenario might naturally arise if the heating and cooling rates were tightly coupled by a self-regulating feedback mechanism (e.g., Begelman 2001; Ruszkowski & Begelman 2002; Churazov *et al.* 2002; Reynolds *et al.* 2002; Bîrzan *et al.* 2004).

Conductive thermal interfaces that impart radiative inefficiency is a natural and energetically feasible explanation (Bertschinger & Meiksin, 1986; Bregman & David, 1988; Sparks *et al.*, 1989;

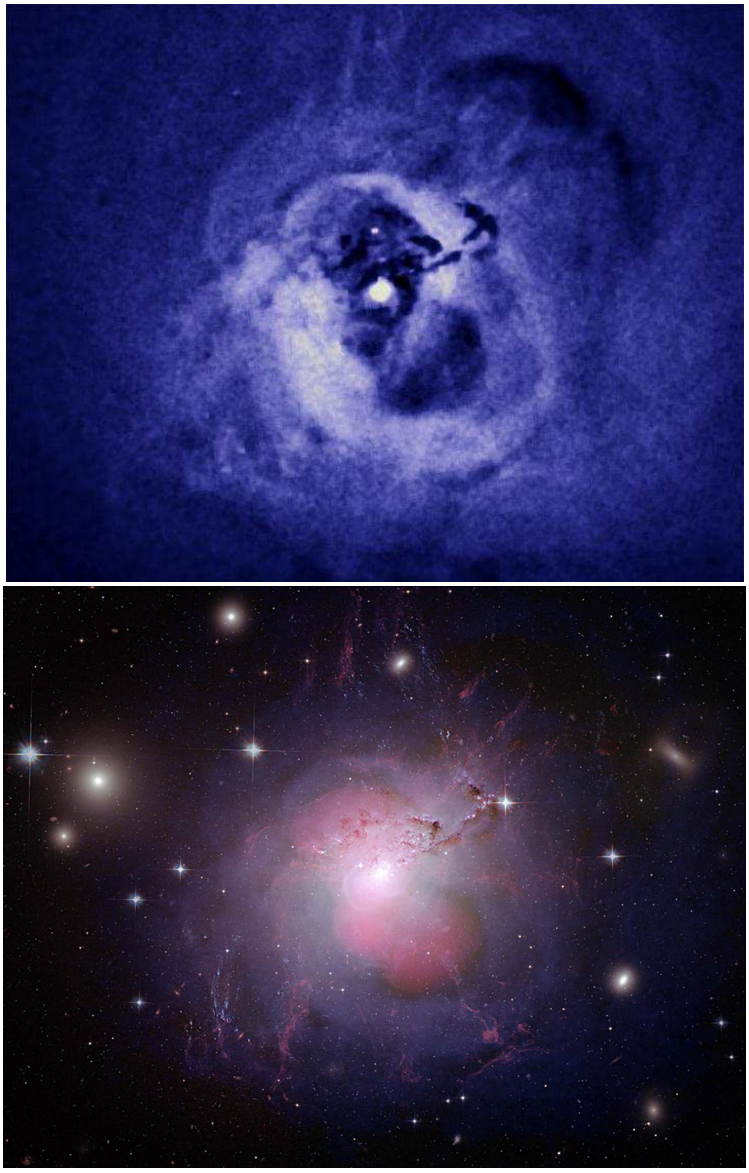

Figure 1.4: *Chandra X-ray Observatory* X-ray image (*top*) and *Hubble Space Telescope* (optical, red filaments), *Chandra X-ray Observatory* (X-ray, in blue), and Very Large Array (Radio, in pink) composite image (*bottom*) of the central brightest cluster galaxy in the massive Perseus cluster. This is a canonical example of AGN feedback associated with a radio source subsonically excavating kiloparsec-scale buoyant cavities into the surrounding hot intracluster gas. AGN feedback is currently the favored mechanism by which catastrophic radiative cooling of the intracluster gas is balanced by heating associated with the $p\,dV$ work done during cavity excavation by the radio source. This energy can exceed 10^{61} ergs, enough to balance radiative losses. Spatial distribution of this energy is one of many important problems challenging the model.

Sparks, 1992), though debate is ongoing as to whether or not conduction-balanced radiative cooling can establish stable temperature and density gradients that match observations for necessarily long timescales ($\gg 1$ Gyr), due to the strong temperature-dependence of conduction efficiency (Spitzer, 1962; Cowie & Binney, 1977; Fabian, 1994; Soker, 2003; Voit, 2005). Conversely, pure radiative cooling does not establish the observed gradients either, unless conduction efficiency is suppressed by a (possibly) unrealistic two orders of magnitude (Bregman & David, 1988; Malyshkin & Kulsrud, 2001; Narayan & Medvedev, 2001). Conduction therefore cannot be dismissed off-hand, and may play a particularly important role in the outer regions of the cool core (Sparks *et al.*, 1989; Sparks, 1992; Ruszkowski & Begelman, 2002; Brighenti & Mathews, 2003; Sparks *et al.*, 2009).

Rosner & Tucker (1989) and Baum & O'Dea (1991) were among the first to suggest that the dissipation of active galactic nucleus (AGN) power could fully replenish ICM radiative losses in regions near radio-loud BCGs. This AGN-driven feedback mechanism, in concert with conduction and heating by cosmic rays, has since become the most favored candidate model by which cool cores are heated. The radio-mode feedback model is largely motivated by observations of kiloparsec scale X-ray cavities in strong spatial anti-correlation with radio emission stemming from AGN outflows (e.g., see Fig. 1.4 and Böhringer *et al.* 1993; Fabian *et al.* 2000, 2006; Churazov *et al.* 2001; McNamara *et al.* 2000, 2001; Blanton *et al.* 2001; Nulsen *et al.* 2005; Forman *et al.* 2005, 2007; Bîrzan *et al.* 2004).

In the general radio-mode AGN feedback model, the cooling ICM collapses into the BCG, reaching the center and triggering black hole (BH) activity. The associated outflowing plasma can subsonically excavate cavities in the thermal gas, driving sound waves that eventually dissipate into heat (Fabian, 2003). These cavities are effectively lower density "bubbles" which buoyantly rise amid the ICM, entraining colder gas phases and magnetic fields (required to keep them long-lived, e.g., Robinson *et al.* 2004; Dursi & Pfrommer 2008), lowering the total mass inflow rate in the cool core and thermalizing cavity enthalpy as the ICM refills its wake (Begelman, 2001; Ruszkowski & Begelman, 2002; Churazov *et al.*, 2002; Reynolds *et al.*, 2002; Bîrzan *et al.*, 2004). Over the cluster lifetime, enthalpy dissipation associated with cavity inflation can range from $\sim 10^{55}-10^{61}$ ergs, theoretically enough to counter radiative losses in the ICM on average (e.g., Bîrzan *et al.* 2004; Rafferty *et al.* 2006), though spatial distribution of this energy is one of several important problems that challenge the model (see e.g., McNamara & Nulsen 2007, for a review). Moreover, AGN heating is almost certainly episodic at a rate coupled to the AGN duty cycle[5] (10^7-10^8 yr). Not only is this naturally expected, it is effectively *required* in order to reconcile the model with

[5]We define the "AGN duty cycle" to be the fraction of total time that the AGN is "on".

observations of (1) entropy gradients that increase monotonically with CC cluster radius (Kaiser & Binney, 2003), (2) the $\sim$ 30% of CC clusters that lack detectable X-ray cavities (Dunn & Fabian, 2006) and (3) some "ghost" X-ray cavities that are apparently devoid of cospatial radio emission (e.g., Abell 2597, McNamara *et al.* 2001). Regardless, AGN feedback is an attractive heating candidate, and recent years have seen feedback emerge as a critical component in models of galaxy evolution (e.g., Springel *et al.* 2005). The addition of feedback-driven "anti-hierarchical" quenching of star formation may elegantly regulate the possibly coupled co-evolution of black holes and the stellar component of their host galaxies (Magorrian *et al.*, 1998; Ferrarese & Merritt, 2000; Gebhardt *et al.*, 2000), in addition to truncating the bright end of the galaxy luminosity function and explaining the bimodality of galaxies in color-magnitude space (e.g., Silk & Rees, 1998; Scannapieco *et al.*, 2005; Bower *et al.*, 2006; Croton *et al.*, 2006; Sijacki *et al.*, 2007).

While only 20% of non-CC BCGs are radio loud, 70% of CC BCGs harbor active central radio sources, (Burns, 1990; Ball *et al.*, 1993; Mittal *et al.*, 2009; Sun, 2009), the power of which appears to correlate with the X-ray luminosity from within the cooling radius (e.g., Bîrzan *et al.* 2004; Mittal *et al.* 2009). Considering this, an elegant scenario emerges wherein condensation from a rapidly cooling ambient atmosphere may directly provide substantial components of the fuel reservoir for multiple episodes of AGN activity, in addition to the active central emission line nebulae and star formation residing amid pools of cold gas. In turn, energy input from the AGN regulates the pathway of entropy loss by heating the ambient gas such that the heating rate tightly regulates the cooling rate (and vice-versa) in a feedback loop.

1.1.3 Some important outstanding issues

Nevertheless, fundamental open questions remain. The detailed physics of feedback are still not understood. It is still not known whether the spectacularly mysterious emission line filament complexes are "dragged upward" by radio sources or are associated with infalling cold gas (e.g., McDonald *et al.*, 2010, 2011; Fabian *et al.*, 2011). As discussed, additional heating mechanisms such as photoionization from young stars and possibly collisional heating from energetic particles is required to regulate the observed temperature and ionization state of the warm and cold gas phases. AGN feedback is generally invoked as a mechanism by which star formation is *quenched*, and yet there is some evidence that, at least on small size scales, the propagation of a radio source through a dense molecular medium can *trigger* localized sites of star formation (e.g., van Breugel *et al.*, 2004; O'Dea *et al.*, 2004). Finally, if a substantial component of the ISM in CC BCGs has indeed condensed from a cooling flow, it is clear that AGN feedback cannot establish an impassable

"entropy floor", and completely inhibit cooling in all CC BCGs at all times. Some cooling must manage to persist, either during quiescent periods of AGN inactivity, or at constant low levels. Discriminating between the many scenarios requires a better understanding of all temperature phases of the ICM, the transport processes between these phases, and their associated mass and energy budgets. Our ability to do so is critically dependent upon multiwavelength data that sample these various discrete temperature phases.

This is a short and highly incomplete contextual summary of the issues this thesis seeks to address, at least in part. As a necessary primer for better understanding of the results we will present, the section below provides an abridged review of some of the finer historical and technical details pertaining to galaxy clusters and cool cores.

Figure 1.5: The 100 kpc-scale supercavity system in Hydra A. Wise *et al.* (2007) estimate that the radio source has returned upwards of 10^{61} erg to regions of the cluster that extend even beyond the cooling radius. Note the strong spatial anti-correlation of the radio source (in pink) with the X-ray cavities (in blue). Such correspondence is typical of cool core clusters with cavities and extended radio sources, presenting strong circumstantial evidence in support of the AGN feedback model. See Bîrzan *et al.* (2004) for a comprehensive census of the currently known X-ray cavity systems in groups and clusters of galaxies. (Credit: X-ray: NASA/CXC/U.Waterloo/C.Kirkpatrick et al.; Radio: NSF/NRAO/VLA; Optical: Canada-France-Hawaii-Telescope/DSS).

1.2 A Review of Galaxy Clusters, the Intracluster Medium, and AGN Feedback

The previous section summarized the contextual background directly relevant to this thesis, and took many opportunities to sacrifice detail for the sake of brevity. Our goal was to provide an introduction to the various issues addressed in this thesis, without distracting the reader with too much secondary or background detail. Of course, these "details" are critical to understanding of the topics at hand, so we attempt to summarize them here, at least in part. This should in no way be mistaken for a comprehensive review; rather, it is more a "brief tour" of some of the major aspects that define our current understanding of galaxy clusters, particularly with regards to the cooling and heating models that attempt to describe the observed properties of the intracluster medium. While we devote more attention to the AGN feedback model than we do alternative heating scenarios (like thermal conduction), this should not be construed as advocacy for one model over another, as that is not the point of this thesis. In each section, we will point the reader to more comprehensive reviews relevant to the subject being discussed.

1.2.1 Galaxy clusters in a cosmological context

Galaxy clusters are the largest gravitationally collapsed structures in the Universe[6], with masses of order $10^{15}\ M_{\odot}$ and volumes that span hundreds of cubic Mpc. The tens to thousands of galaxies inhabiting this volume encode a history of hierarchical structure assembly in the Universe. At the earliest epochs, small scale, large amplitude baryonic density perturbations exceeding the mean density of the rapidly expanding Universe decouple from the Hubble flow and gravitationally collapse. These sub-stellar clumps coalesce, triggering hierarchical structure growth which proceeds non-linearly by the accretion of ever larger and more complex arrangements of baryonic matter, including stars, stellar clusters, and eventually galaxies. Galaxy clusters are the final manifestation of this 13 billion year-long process, forming at late times (redshifts $z < 2$) in massive dark matter halos. Just as for the baryonic component of the Universe, dark matter structure also grows hierarchically, and the largest halos (hosting the richest galaxy clusters) are found at the intersections of large scale dark matter filaments (see, e.g., Fig. 1.1 and Springel *et al.* 2005).

[6]Throughout this thesis we adopt the concordance (ΛCDM) cosmological model, with $H_0 = 71$ km s^{-1} Mpc^{-1}, $\Omega_M = 0.27$, and $\Omega_\Lambda = 0.73$. The Hubble constant H_0 scales the relationship between recessional velocity v_r and distance D in the expansion of the Universe, such that $v_r = H_0 D$. Ω_M is the ratio of the mass density and Ω_Λ is the ratio of the energy density due to Einstein's cosmological constant to the critical density of the Universe. Parameterized in this fashion, the Universe is 13.7 Gyr old, and was 5.9 Gyr old at a redshift of $z = 1$.

Many of the important properties of galaxy clusters are expressed in terms of a cluster's "virial radius", which can be understood in the context of a simple "violent relaxation" model (e.g., Lynden-Bell, 1967). During cluster assembly, gravitational interaction between infalling baryonic clumps produces a time-variable gravitational potential that yields randomized particle velocities following a roughly Maxwellian distribution. The result is a state of "virial equilibrium", in which the total kinetic energy E_K and gravitational potential energy E_G are related by

$$2E_K + E_G = 4\pi P_\mathrm{b} r_\mathrm{b}^3, \tag{1.1}$$

where P_b is the effective pressure at r_b, the outer boundary of the relaxed system. If $P_\mathrm{b} = 0$, we recover the usual form of the virial theorem, e.g., $2E_K + E_G = 0$. The outer boundary (r_b) of a cluster is not especially well-defined in practice, and is therefore not measurable in the strictest sense. It can, however, be estimated with a spherical "top-hat" model, wherein a uniform, constant density sphere is assumed to cause the perturbation leading to cluster collapse. In this case, the virial theorem posits that a collapsed cluster's bounding radius should be of order 0.5 times the turnaround radius r_turn. If all mass in the relaxed cluster resides within $r_\mathrm{turn}/2$, then the mass density within this sphere is $6M/\pi r_\mathrm{turn}^3$, which for an Einstein-deSitter (flat, matter-dominated) cosmology is ~ 178 times the critical density of the Universe, defined as

$$\rho_\mathrm{crit} \equiv \frac{3H^2}{8\pi G}. \tag{1.2}$$

This is the density threshold above which the expansion of the Universe would stall, leading to recollapse. Here, G is Newton's gravitational constant, and H accounts for the redshift dependence of the Hubble constant H_0,

$$\frac{H}{H_0} = \sqrt{\Omega_M (1+z)^3 + 1 - \Omega_M}, \tag{1.3}$$

where Ω_M is the ratio of the mass density of the Universe to its critical density. The two quantities are equal (e.g., $\Omega_M = 1$) in an Einstein-deSitter Universe. In this case, the radius enclosing $178\rho_\mathrm{crit}$ would be the virial radius r_vir. Sometimes, alternative definitions are used, such as $r_\mathrm{vir} = r_{200}$. In this nomenclature, r_N is defined to be the radius at which the average cluster density is $N \times \rho_\mathrm{crit}$, so

$$r_{200} \equiv 200 \times \frac{3H^2}{8\pi G}. \tag{1.4}$$

The virial radius has also been approximated as the "scale radius"

$$r_{180M} = 180 \times \Omega_M(z)\,\rho_{\rm crit}. \tag{1.5}$$

If $\Omega_M \approx 1$, these alternative definitions are very close to the $r_{\rm vir} = 178\rho_{\rm crit}$ derived in the Einstein-deSitter case, so $r_{200} \approx r_{180M} \approx r_{\rm vir}$. However, $\Omega_M \approx 0.3$ in the currently favored ΛCDM cosmology, which gives $r_{\rm vir} \approx 100\rho_{\rm crit}$. Nevertheless, r_{200} and r_{180M} are still used throughout the literature, for the sake of consistency. Regardless of the definition used, typical virial radii for rich clusters are on the order of $1-3$ Mpc.

As they are the largest of all structures whose mass can be reliably estimated, galaxy clusters are among the best laboratories in which cosmological parameters and galaxy formation models can be constrained by observables. This thesis is broadly related to the latter. For a more cosmologically-oriented review of galaxy clusters, see Rosati *et al.* (2002) and Voit (2005). For a review of the critically important Sunyaev-Zeldovich effect (Sunyaev & Zeldovich, 1970, 1972) as it pertains to galaxy clusters and cosmological probes, see e.g., Carlstrom *et al.* (2002).

1.2.2 Properties of the intracluster medium

Galaxy clusters were first associated with extended, luminous X-ray sources in the late 1960s and 1970s after the launch of the Uhuru, Ariel 5, and OSO 8 X-ray satellites (Giacconi *et al.*, 1971; Gursky *et al.*, 1971; Forman *et al.*, 1972; Mitchell *et al.*, 1976; Gursky & Schwartz, 1977; Serlemitsos *et al.*, 1977). In observing the Perseus, Coma, and Virgo clusters, Mitchell *et al.* (1976) and Serlemitsos *et al.* (1977) were the first to confirm a thermal origin for the X-ray emission in detecting collisionally excited Fe-K features above 6 keV.

At the same time, our understanding of hierarchical structure formation was maturing (e.g., Silk 1968; Gunn & Gott 1972; Silk 1977; Rees & Ostriker 1977). This motivated the interpretation that the ICM itself, which is largely composed of ionized hydrogen and helium, is a relic from the gravitational collapse at early times of "proto-baryons" that do not participate in star and galaxy formation (Gunn & Gott 1972 were among the first to suggest this). We now know that $\sim 85\%$ of all baryons in galaxy clusters reside in the ICM, though not *all* of them can be primordial. A significant fraction of the ICM needs to have been processed in one or more generations of star formation in order to account for the presence of heavier elements in the ICM at abundances ~ 0.4 solar (e.g., Arnaud *et al.* 1992). This can be explained by invoking the return of higher metallicity gas from supernovae, as well as ram pressure and tidal stripping from galaxies as they fall into the

cluster.

For comprehensive reviews of the ICM, see Sarazin (1986), Mushotzky (2004), and Arnaud (2005). What follows is largely an abridged version of topics covered at length in these reviews.

Radial density and mass profiles

Models of the ICM treat it as an optically thin coronal plasma[7] in ionization equilibrium. Observed (measured) particle densities n in the ICM are of order $10^{-4} - 10^{-2}$ cm^{-3}, and increase from the outer halo inward to the cluster core. The radial density profile depends on many subtle physical processes (the most important of which we will summarize later), but will generally follow hydrostatic equilibrium to maintain pressure support. Assuming spherical symmetry, the hydrostatic gas pressure profile will rise with decreasing radius as

$$\frac{dp}{dr} = \frac{d(nkT)}{dr} = -\rho g = -n\mu m_p \frac{GM(<r)}{r^2}, \tag{1.6}$$

where k is the Boltzmann constant, T is the gas temperature, $\rho = n\mu m_p$ is the mass density, g is the local gravitational acceleration, $M(<r)$ is the mass enclosed within radius r, μm_p is the mean mass per particle, and m_p is the proton mass. The hydrostatic approximation allows for rough estimates of cluster mass profiles, e.g.,

$$M(<r) = -\frac{kTr}{G\mu m_p}\left(\frac{d\log n_e}{d\log r} + \frac{d\log T}{d\log r}\right). \tag{1.7}$$

Observations can be used to parameterize the density (and therefore temperature) profiles in the above equations. A common method is to fit an isothermal "beta" (β) model to the observed X-ray surface brightness profile, as first introduced by Cavaliere & Fusco-Femiano (1976); Branduardi-Raymont *et al.* (1981); Forman & Jones (1982). In the beta model, the X-ray surface brightness $\Sigma_{\rm X}$ at projected radius r varies as

$$\Sigma_{\rm X}(r) = \Sigma_{\rm X}(0)\left[1 + \left(\frac{r}{r_0}\right)^2\right]^{(-3\beta+1/2)}. \tag{1.8}$$

[7]The term "coronal plasma" refers to the "coronal approximation" described by e.g., Mewe (1999), wherein electron-driven collisional ionization rates are exactly balanced by recombination rates. See Sarazin (1986) and Peterson & Fabian (2006) for more details as they pertain to galaxy clusters.

Here, $\Sigma_X(0)$ is the central X-ray surface brightness and r_0 is the core radius. The model assumes that the galaxies, ambient hot gas, and underlying dark matter halo (assumed to follow a King profile) are hydrostatic and isothermal. β is defined as the ratio of galaxy-to-gas velocity dispersions (effectively the energy per unit mass in galaxies divided by that in gas) ,

$$\beta \equiv \frac{\mu m_p \sigma^2}{kT}, \tag{1.9}$$

Here, σ is the 1-D velocity dispersion of the galaxies along the line of sight. Typically, the ICM in galaxy clusters is well-fit by models with $\beta \approx 0.6$ (Sarazin, 1986). The beta model form for X-ray emissivity can be converted to electron density using

$$n_e(r) = n_e(0)\left[1+\left(\frac{r}{r_0}\right)^2\right]^{(-3\beta/2)}. \tag{1.10}$$

Temperature

At early epochs, adiabatic compression and supersonic accretion shocks are thought to heat the ICM to its observed temperature (Kaiser, 1986), which ranges from $10^7 \lesssim T \lesssim 10^8$ K ($1 \lesssim kT \lesssim 10$ keV). This is roughly the virial temperature of the underlying gravitational potential, so

$$kT \approx \frac{GMm_p}{r_{\rm vir}} \simeq \mu m_p \sigma^2 \simeq 6 \times \left(\frac{\sigma^2}{10^3 \text{ km s}^{-1}}\right) \text{ keV}. \tag{1.11}$$

Combining equations 1.11 and 1.3 and applying simple manipulations (the details for which can be found in e.g., Rosati *et al.* 2002), we can relate the ICM temperature to the virial mass of the cluster M_v (e.g., the mass contained within r_v) by

$$kT = 1.38\left(\frac{M_{\rm vir}h}{10^{15}M_\odot}\right)^{2/3}[\Omega_m \Delta_{\rm vir}(z)]^{1/3}(1+z) \text{ keV}. \tag{1.12}$$

Here, h is the dimensionless Hubble parameter[8] allowing for simple conversion between cosmologies, and $\Delta_{\rm vir}(z)$ is the average cluster density within the virial radius divided by the mean cosmic density at redshift z. If $\Delta_{\rm vir}(z)$ is constant (as it is for e.g., an Einstein-de-Sitter cosmology), then

[8]The dimensionless Hubble parameter h is related to the Hubble constant H_0 by $h = H_0/(100 \text{ km s}^{-1} \text{ Mpc}^{-1})$.

the net implication is that there is a fundamental scaling relation

$$T \propto M^{2/3}(1+z). \tag{1.13}$$

This is one of the several examples in which quantities measured from X-ray observations (like density and temperature) can be used to infer cluster mass, and therefore constrain cosmological models which make independent cluster mass predictions.

Spectrum

The dominant coolant for ionized hydrogen at $> 10^7$ K is thermal bremsstrahlung (free-free) emission driven by Coulomb interactions between electrons and ions. This powers an extremely bright X-ray continuum of luminosities $L_X \sim 10^{43} - 10^{45}$ erg sec^{-1}, with the total power radiated per unit volume V given roughly by

$$\frac{dL}{dV} \approx 10^{-27} n_e n_H T^{1/2} \text{erg sec}^{-1} \text{ cm}^{-3}, \tag{1.14}$$

where n_e and n_H are the electron and hydrogen densities in cm^{-3}, respectively. In a fully ionized gas with hydrogen and helium mass fractions of $X = 0.7$ and $Y = 0.28$ (respectively), the electron and hydrogen densities are approximately equal ($n_e \approx 1.18 n_H$). The energy loss rate by bremsstrahlung emission therefore scales with the square of the gas density (this has very important consequences, which we will discuss later). Below about 3×10^7 K, cooling by iron, oxygen, and silicon recombination lines becomes increasingly important and significantly alters the shape of the X-ray spectrum. Prominent X-ray spectral features include the Fe K and L lines at ~ 6 and ~ 1 keV, respectively. These are used in X-ray spectral fitting (which plays an important role in our Chapter 2) to ascertain elemental abundances in the ICM (which, as mentioned previously, are usually $\sim 0.3 - 0.4$ solar).

Entropy

One of the most important physical quantities dictating the structure and density of the ICM is entropy, unique in its ability to encode and preserve the thermodynamic history of the gas. Considered alone, temperature and density fail in this regard, as the temperature largely reflects the underlying gravitational potential well, and the density reflects the degree to which gas is compressed within the well. Entropy, however, only changes via gains or losses of heat energy, and

breaks the degeneracy with the underlying potential because at constant pressure, the density of the gas is determined by its specific entropy. Quantitatively, the entropy S can be defined by rewriting the expression for the adiabatic index ($K \propto p\rho^{-5/3}$) in terms of the observables kT and n_e,

$$S = kT n_e^{-2/3}. \tag{1.15}$$

One may also write

$$K \equiv \frac{kT}{\mu m_p \rho_g^{2/3}}, \tag{1.16}$$

where K is merely the proportionality term in the equation of state for an adiabatic monatomic gas, $p = K\rho_g^{5/3}$. K is also directly related to the standard thermodynamic definition of entropy per particle, namely $s = k \ln K^{3/2} + s_0$. One may convert from one definition to the other by

$$S = kT n_e^{-2/3} = 960 \text{ keV cm}^2 \left(\frac{K}{10^{34} \text{ erg cm}^2 g^{-5/3}} \right). \tag{1.17}$$

Because high entropy gas "floats" and low entropy gas "sinks" (Voit, 2005), the intracluster gas will convect until it establishes an entropy gradient that corresponds to the underlying gravitational potential. In other words, convection will attempt to establish a match between the isentropic surfaces of the ICM and the equipotential surfaces of the DM halo, and will reach convective equilibrium when $dK/dr \geq 0$ everywhere (e.g., Voit 2005, and references therein). There are many important works which focus specifically on intracluster entropy and its many consequences, see e.g., Lloyd-Davies *et al.* (2000); Voit *et al.* (2002); Piffaretti *et al.* (2005); Pratt *et al.* (2006); Donahue *et al.* (2006); Cavagnolo *et al.* (2009), and references therein.

Scaling relations

If the ICM is entirely characterized by gravitational processes and bremsstrahlung emission, and the cosmological model is scale-agnostic, then all clusters of varying masses can be assumed to be scaled versions of the same "unit phenomenon". One may then apply consequences arising from self-similarity, and construct simple scaling relations following arguments similar to those yielding equation 1.12. For example, as shown in equation 1.14, the X-ray luminosity L_X arising from pure

bremsstrahlung emissivity should scale with cluster mass and temperature as

$$L_X \propto M\rho_g T^{1/2} \propto T^2 (1+z)^{3/2} \propto M^{4/3} (1+z)^{7/2}. \tag{1.18}$$

Similarly, entropy should scale with temperature as

$$S \propto T (1+z)^{-2}, \tag{1.19}$$

and so on.

Decades of observations have shown these self-similar scaling relations to be incorrect. For example, the actual observed luminosity-temperature relation for the $3-10$ keV range is of order $L_X \propto T^3$ rather than $\propto T^2$ (Markevitch, 1998; Arnaud & Evrard, 1999), and is even steeper for < 1 keV groups of galaxies. The breaking of self-similarity in scaling relations could possibly be explained by *pre*-heating of the gas prior to virialization at early epochs, which would provide an entropy excess needed to explain this departure. Early epochs of AGN activity and metal-enriching supernovae are proposed pre-heating candidates (see Rosati *et al.* 2002; Voit 2005, and references therein, for far more detail than we present here).

Magnetic Fields and Thermal Conduction in the ICM

Faraday rotation measurements of radio galaxies embedded within clusters confirm that the ICM is permeated by magnetic fields of a few to tens of μG in strength. The strongest fields are found in cool core clusters (Clarke *et al.*, 2001), and are thought to be (1) primordial, initially weak fields amplified over time by intracluster turbulence, convection, and adiabatic compression, and / or (2) injected by radio galaxies. Even for the strongest fields, the gas pressure greatly dominates over the magnetic pressure, e.g.,

$$nkT \gg \frac{B^2}{8\pi}, \tag{1.20}$$

but one must still not underestimate the importance of magnetic fields in regulating the global physics of the ICM (see, e.g., Soker *et al.* 2001, and references therein). For example, an electron in the ICM will strongly couple to the magnetic field because its mean free path l_e is far larger than

its Larmor radius ρ_e,

$$\frac{l_e}{\rho_e} \sim 10^{14} \left(\frac{B}{1\ \mu\mathrm{G}}\right) \left(\frac{n_e}{10^{-2}\ \mathrm{cm}^{-3}}\right) \left(\frac{T}{3\ \mathrm{keV}}\right). \tag{1.21}$$

This will have significant impacts on transport coefficients like viscosity, and give rise to anisotropic heat conduction whose efficiency is almost entirely regulated by the magnetic field. The degree to which this efficiency may be suppressed (e.g., Tribble 1989) is an area of rigorous debate (to put it mildly). We will briefly touch upon this later in discussing thermal conduction as it applies to inhibiting cooling flows. We hesitate to so briefly summarize such an important area of study, but it is at least worth noting that magnetic fields have been invoked to solve problems related to (1) the perplexing longevity of buoyant X-ray cavities, which should disrupt on the order of a single sound crossing time (e.g., Dursi & Pfrommer 2008, see Section 1.2.6), as well as (2) the mysterious filamentary morphologies of emission line nebulae in CC BCGs (e.g., Fabian *et al.* 2008) and (3) the observed presence of large radio relics in the ICM (e.g., Markevitch *et al.* 2005).

1.2.3 The classical cooling flow model

If the hot ICM is optically thin to its own radiation, it will lose energy at a rate directly proportional to its X-ray luminosity. If this energy loss is not balanced by any other non-gravitational forms of heating, the gas will radiate away all of its energy on a timescale set by the gas enthalpy divided by the energy lost per unit volume. The timescale over which this should occur, t_{cool}, can be expressed in terms of the gas pressure p,

$$t_{\mathrm{cool}} = \frac{p}{[(\gamma-1)n_e n_H \Lambda(T)]}, \tag{1.22}$$

where γ is the ratio of specific heats and $\Lambda(T)$ is the cooling function, which integrates all emission processes in the plasma (dominated by bremsstrahlung in the keV gas), weighted by photon energy. See, for example, the ICM cooling functions of Sutherland & Dopita (1993); Ruszkowski & Begelman (2002).

Cool core clusters of galaxies are categorized as such because the radiative lifetime (t_{cool}) of their ICM within the "cooling radius" is shorter than the Hubble time, e.g., $t_{\mathrm{cool}} < H_0^{-1} \sim 13.7$ Gyr. The X-ray luminosity within the ~ 100 kpc-scale cooling radius r_{cool} can reach 10^{45} erg s^{-1} in the most extreme cases, for which $t_{\mathrm{cool}} \approx 3 \times 10^8$ yr (which is only 1/30th the Hubble time). The pressure at the cooling radius r_{cool}, beyond which cooling can be considered unimportant, is set

to first order by the weight of the overlying gas. Energy loss by gas within the cooling radius is accompanied by a localized drop in entropy, but it still must maintain pressure support for these outer layers. This can only happen if its density increases, which, to first order, is only possible if it compresses and flows inward. As is obvious from Equation 1.22, the cooling time is inversely proportional to the gas density. This leads to a "runaway" effect, wherein the cooling *rate* of gas within $t_{\rm cool}$ increases catastrophically. Cooling times are nonetheless much longer than free-fall times at common radii, and gas "lost" to the cooling flow is constantly replenished by the ambient hot reservoir. Thus, the cooling flow is subsonic, quasi-hydrostatic, pressure-driven, and long-lived (e.g., Lea *et al.* 1973; Cowie & Binney 1977; Fabian & Nulsen 1977; see reviews by Fabian 1994; Peterson & Fabian 2006).

As the name implies, entropy loss within the cooling radius is associated with a loss of heat, but surprisingly, this does not necessarily mean that the *temperature* of the gas should decrease inwards as a direct result of the cooling flow. Rather, the gas will cool only if its initial temperature is greater than the local virial temperature of the underlying gravitational potential. When the two temperatures are equal, gravity will "take over", and adiabatic compression associated with the release of gravitational energy will act as a thermostat for the gas, keeping it at roughly the local virial temperature, i.e.,

$$\frac{kT}{\mu m_H} \approx \frac{GM(<r)}{r}. \tag{1.23}$$

This means that, counter-intuitively, the "cooling flow" is effectively isothermal. The observed (and predicted) temperature of the gas *does* drop inwards toward the BCG, but this is less a direct consequence of the cooling flow, and is instead a reflection of the flattening gravitational potential as the BCG begins to dominate over the cluster potential at the innermost radii. Stated another way, as the temperature of gas within the cooling flow matches the local virial temperature, we observe cooler gas in the central regions because the virial temperature is lower in the BCG than it is in the ambient cluster. Note that this simple observation is actually model-agnostic, meaning observed temperature profiles are effectively unrelated to the cooling flow model, regardless of whether or not it is correct in principle. The term "cooling flow" is therefore something of a misnomer, and is better thought of as a runaway cascade of localized *entropy* loss governed by

$$\frac{ds}{dt} = \frac{-n_e n_H \Lambda(T)}{\rho T}. \tag{1.24}$$

To first order, the X-ray luminosity associated with a perpetual, single phase, isobaric cool-

ing flow can be calculated by finding the ratio of the enthalpy carried along with the flow to the gravitational potential energy dissipated within the flow, or

$$L_X \simeq \frac{\dot{M}(5kT)}{2\mu m_H} \simeq 1.3 \times 10^{44} \left(\frac{kT}{5\ \mathrm{keV}}\right) \left(\frac{\dot{M}}{100\ M_\odot\ \mathrm{yr}^{-1}}\right)\ \mathrm{erg\ s}^{-1}, \tag{1.25}$$

where $\dot{M} = dM/dt$ is the X-ray derived mass deposition rate associated with the classical cooling flow. It is important to note that this predicted luminosity is roughly 10% of the gravitational potential energy release associated with a 0.02 $M_\odot$ yr^{-1} accretion rate onto a supermassive (10^8 – 10^9 $M_\odot$) black hole. We will discuss the important implications of this later.

As mentioned previously, the cooling flow is always subsonic, though its Mach number will steadily increase inward until it reaches approximately the sound speed. Prior to this point, any growth of thermal instabilities associated with the flow are quickly "smoothed out" by buoyant motions (Balbus & Soker, 1989). The instabilities can persist for longer times as the flow becomes sonic, however, at which point Rayleigh-Taylor and shearing effects can disrupt the homogeneous flow into discrete, thermally unstable clouds which decouple from the bulk flow. These instabilities, manifest as overdensities, then "lag" behind, persist, and grow. The result is expected to be a long-lived, inhomogeneous "rain" of cold gas clouds over a large central region within the CC BCG, which should then pool and collect over a small number of dynamical times. Inhomogeneous cooling flow models such as these were historically more successful than the steady state, single-phase cooling flow models which overpredicted the central X-ray surface brightness (Nulsen, 1986). As we summarize below, however, *major* problems remain.

The "failure" of the simple cooling flow model

As discussed in section 1.1, the cooling flow model fails to match observations in three critical ways:

1. It predicts that CC BCGs should possess massive repositories of cold gas of order $\sim 10^{12}$ $M_\odot$. Sensitive searches for these cold mass sinks in the optical, IR, sub-mm, and radio returned empty-handed for many years. Since that time, some CC BCGs have been found to harbor substantial amounts ($10^9 - 10^{10}$ $M_\odot$) of cold molecular hydrogen (Edge, 2001; Edge & Frayer, 2003; Donahue *et al.*, 2000; Salomé *et al.*, 2006). However, even in those cases when they are detected, these repositories are one to three orders of magnitude smaller than predictions. Moreover, cold molecular gas has so far only been detected in 15 – 30% of CC

clusters (depending on the sample), though this could largely be due to the highly difficult nature of such observations.

2. Such extreme cooling rates and massive predicted cold gas repositories should drive similarly extreme star formation rates up to $\lesssim 10^3\ M_\odot\ \mathrm{yr}^{-1}$, two to three orders of magnitude in excess of results from three decades of observations.

3. There is *very little* high resolution X-ray spectroscopic evidence that more than $\sim 10\%$ of the hot phase gas is cooling below $T_{\rm vir}/3 \approx 1$ keV (e.g., Peterson *et al.* 2003). For example, the very prominent and *expected* Fe XVII line at 12 Å is very weak or completely absent in most CC clusters (except for A2597, the subject of the next chapter). Unlike *most* circumstances in astronomy (and life, as it turns out), this is one instance in which "absence of evidence" (i.e., the lack or severe under-production of X-ray coolant lines) *really is* "evidence of absence".

These "three nails in the coffin" gave rise to the now famous "cooling flow problem", and represented a significant challenge for models of galaxy formation and evolution (e.g., Silk 1977; Rees & Ostriker 1977). Anecdotally, after the problem's emergence, a movement began within the community to rename "cooling flow clusters" to "cool core clusters" (with the same definition that $t_{\rm cool} < H_0^{-1}$), in an attempt to disassociate the *phenomenon* from the *model*, which now suffered serious challenges[9].

There are two overriding implications of the cooling flow problem:

- The classical cooling flow model is either entirely wrong or severely overpredicts mass deposition rates by factors approaching 1000 (while remaining correct in principle), or

- Radiative losses of the ICM are replenished by a non-gravitational heating mechanism.

There are, of course, very simple scenarios in which the cooling flow model *could* be considered "wrong" (loosely speaking). Assuming the ICM to be optically thin, for example, could result in critical underestimation of the effects of transport coefficients like thermal conduction (which we will discuss later). What is not arguable, however, is that *the ICM is unequivocally cooling*, given the simple fact that we directly observe it losing energy through its thermally-driven X-ray radiation. This must, at least in part, support the second scenario wherein an external heating mechanism is at play. We review what is currently the most favored heating candidate below.

[9]Some, however, still argue that the term "cooling flow" should not be abandoned, even if only for nostalgic reasons. See, for example, Soker *et al.* 2001, who points out that the Planetary Nebula community did not change terminology despite PNe being entirely unrelated to planets. The Author remains agnostic on the "cool core" vs. "cooling flow" issue, and finds either term equally catchy.

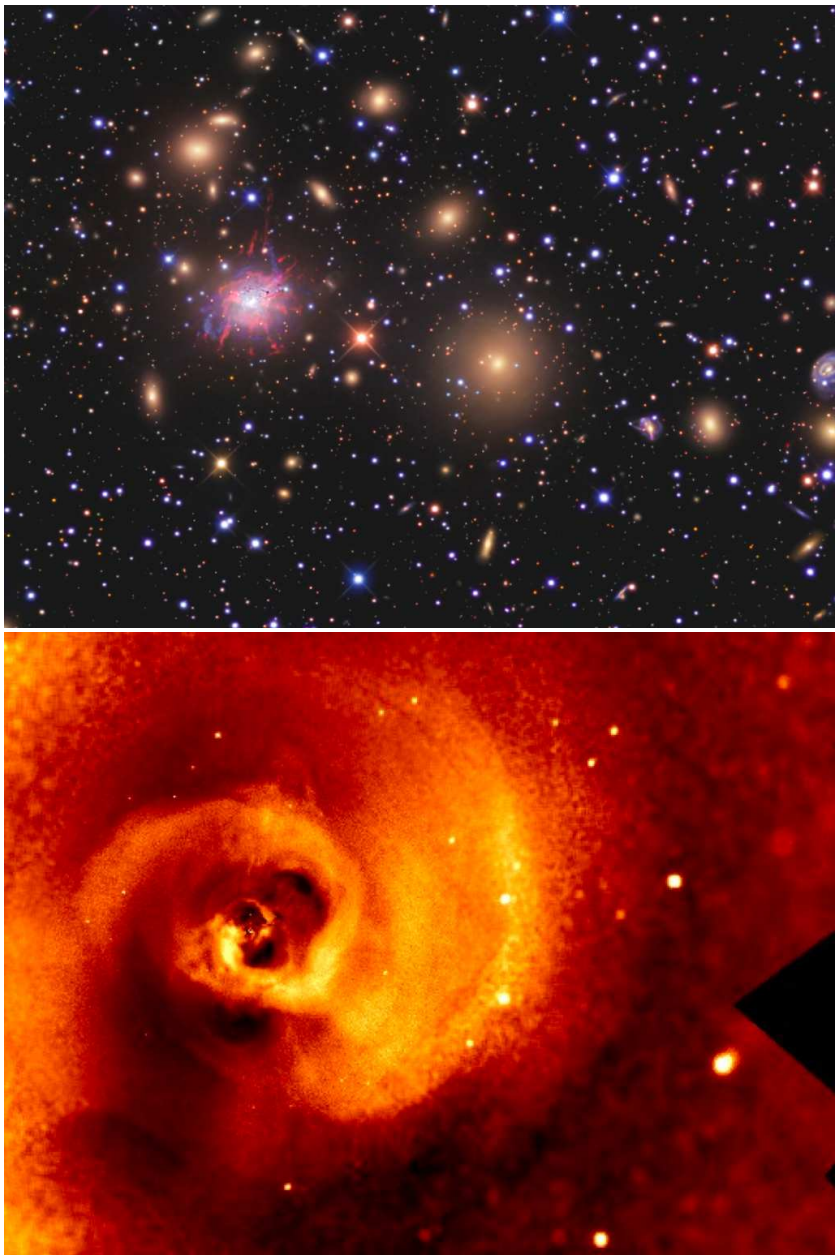

Figure 1.6: Another view of the Persesus cluster (and NGC 1275, center left) in optical (*top*) and X-ray (*bottom*). The two fields of view are identical. The top optical image is a ground-based RGB+Hα composite by R. Jay GaBany, reproduced here with his permission. The X-ray image is a 1.4 Msec *Chandra* exposure kindly provided by A. Fabian and J. Sanders, originally published in Fabian *et al.* (2011).

1.2.4 Evidence in support of AGN feedback

McNamara & Nulsen (2007) have compiled an excellent review of the current evidence in support of AGN as the heating mechanisms in cool core clusters. We refer the reader to that far more comprehensive work, and merely summarize their conclusions here.

Summary of current evidence supporting AGN feedback as the heating mechanism in CC clusters:

1. Consider the near 70% detection rates of X-ray cavity systems in cool core clusters (Dunn *et al.,* 2005), combined with the near 70% detection rates of radio emission in cool core clusters[10] (Burns, 1990). As "icing on the cake", the X-ray cavities often directly trace the projected shapes of the extended radio sources, strongly suggesting that the former are created by the latter.

2. If *not* regulated by a feedback loop, then heating rates *must* exceed cooling rates in order to ensure that no more than 10% of gas can cool from the hot phase, and thereby match observations which turn up a dearth of the predicted cold reservoirs. However, heating rates that exceed cooling rates would raise the central entropy, eventually lengthening cooling times to the Hubble time. This would destroy the CC phase. Cool core clusters account for $> 50\%$ of the X-ray luminous cluster population below $z < 0.4$, so the phase *must be long-lived*. Of course, heating rates cannot be significantly lower than cooling rates either, or else the "cooling flow problem" would not exist to begin with. *The ICM must therefore be heated at a rate approximately of order its X-ray luminosity*. A feedback loop, wherein the heating rate is directly coupled to the cooling rate, would be a simple explanation for this.

3. Two obvious heating mechanisms which could establish a feedback loop with the cooling rate are (1) supernova feedback arising from star formation associated with the cooling flow, and (2) central AGN in the BCGs that are triggered by accretion reservoirs that stem from the cooling flow. Supernova feedback has been shown for many years to suffer crippling energetics issues, and has effectively been ruled out (as the dominant heating mechanism, at least, e.g., Voit 2005).

4. Nearly 90% of energy radiated away in a cooling time must be replenished, and this must happen on timescales roughly as short as the *shortest* cooling time in order to account for the relative lack of observed mass sinks (star formation, cold gas reservoirs) in CC BCGs.

[10] It is important to note that these are not the "same 70%", although there is significant overlap. The majority of CC clusters with detected X-ray cavities also possess extended radio emission.

5. Entropy profiles in CC clusters (which are generally power laws, Piffaretti *et al.* 2005) decay inwards toward the core, where they flatten by levels consistent with the supposed amount of entropy injection by AGN (~ 10 keV cm^2, McCarthy *et al.* 2004; Voit & Donahue 2005).

6. AGN energy injection estimates based upon measurements of the "$p \times dV$" work associated with X-ray cavity excavation strongly correlates with X-ray luminosity (see Fig. 6 in Rafferty *et al.* 2006). This is *consistent with* (though not necessarily *suggestive of* [11]) the notion that the AGN heating rate is thermostatically controlled by the cooling rate, as would occur in a feedback loop.

7. If one *averages* over both CC cluster population and lifetime, there is apparently *just enough* mean heating power from AGN (1.01×10^{45} erg s^{-1}) to balance mean cooling power (6.45×10^{44} erg s^{-1}, Rafferty *et al.* 2006).

Important qualifiers and caveats to the above lines of evidence

1. Only slightly more than half of CC clusters with *observed* X-ray cavities are associated with enough energy (again, based on pV estimates) to actually offset inferred cooling rates for that specific cluster (Dunn & Fabian, 2006; McNamara & Nulsen, 2007). This argument, however, is strongly tempered given (1) extremely strong biases against X-ray cavity detection frequency due to e.g., the highly variable exposure times / count rates in X-ray images from *Chandra* archival studies; and (2) the highly episodic nature of AGN (e.g., pV-estimated AGN injection rates do not account for cavities which may have been inflated in the past and since dissipated).

2. 30% of all CC clusters do not have detectable X-ray cavities (Dunn & Fabian, 2006). This supposed evidence against AGN heating must of course be weighed with the caveats in point (1) above. To reiterate, the combination of (1) difficulties associated with detecting X-ray cavities and (2) the fact that AGN heating is almost certainly episodic ("on again, off

[11] When making mention of any "luminosity vs. luminosity" plot, one should at least bear in mind the words of Dr. Robert "Ski" Antonucci, who best paraphrased the intentions of Robert Kennicutt:

> "*Kennicutt (1990) has extended the L(CO)-L(FIR) correlation for galaxies by adding points for a burning cigar, a Jeep Cherokee, the 1988 Yellowstone National Park forest fire, and Venus. I think the lesson is you get correlations in luminosity-luminosity plots (even without any sample completeness) just because big things have more of everything. There is probably a good correlation between the number of bookstores in a city and the number of bars, even with a complete sample, but no direct correlation is necessarily implied.*" – Antonucci (1999)

Note that this should not be mistaken for criticism of the excellent (and convincing) work by Rafferty *et al.* (2006)

again") significantly diminishes (though does not completely eliminate) the power of this argument. We must await comprehensive studies of *deeper* X-ray imaging in order to make more definitive statements (to the contrary or otherwise).

3. Some CC clusters with detected X-ray cavities lack extended radio emission.

4. It is not clear if the X-ray cavity "method" is truly an accurate tracer of AGN power injection (though it's probably one of the best available means). The efficiency by which cavity enthalpy is converted to ICM heating is also somewhat uncertain (we discuss this below).

5. Energy injection from AGN heating is very "spatially discrete". In other words, only the ICM in the vicinity of (1) X-ray cavities and (2) sound waves arising from the creation of these cavities, will be *mechanically* heated by the AGN. To quote Dr. Megan Donahue (private communication), "[this is] *like saying we in principle have enough drywall to block the drafts without saying where the drywall is*".

6. Hybrid models which include both AGN feedback *and* thermal conduction (which may be more important in the outer regions of the cool core) have proven to be successful in predicting, to some degree, the observed radial temperature, density, and entropy profiles. In some cases, these hybrid models are *more* successful than models that include AGN feedback only (Ruszkowski & Begelman, 2002; Brighenti & Mathews, 2003; Voit, 2005). The net implication is that many mechanisms, in addition to feedback, may be working *in concert* to offset cooling. While this is almost certainly true to some degree, debate is ongoing as to whether or not one process clearly dominates over all others.

We return to point (7) above: If one takes an *average* over CC cluster population and lifetime, one finds that there is enough *average* heating power from AGN to offset *average* cooling power. The mean heating power quoted by Rafferty *et al.* (2006) was calculated by taking $4pV \times t_{\rm buoy}$ for the observed cavities. Here, $t_{\rm buoy}$ is the buoyant lifetime, one of three common estimates used to determine X-ray cavity ages. We discuss these below.

1.2.5 A qualitative summary of X-ray cavity inflation and age dating

Here we outline a very simple schematic for the excavation of an X-ray cavity by a radio source. Although we discuss the details of this model in a confident tone, it is important to keep in mind that this is a vastly oversimplified "cartoon", and not necessarily an accurate representation of reality.

In this simple schematic, X-ray cavity inflation is expected to be initially rapid as the nascent radio jet expands supersonically into the ambient medium. At this stage, cavities excavated by the jet are small, narrow, and younger than the local sound-crossing time, as the (possibly) shocked ISM gas is found only at the tip of the supersonic propagation front (Heinz *et al.*, 1998; Enßlin & Heinz, 2002; McNamara & Nulsen, 2007). These "infant" cavities would only be associated with minor and spatially small depressions in the X-ray surface brightness, and would be difficult to detect, particularly given a large amount of intervening X-ray gas along the line of sight. The jet decelerates to transonic speeds as its ram pressure equalizes with the ambient ISM pressure, truncating the supersonic inflation stage, typically at distances $\lesssim 1$ kpc from the radio core. The cavity continues to expand subsonically and will eventually "catch up" with the now-decelerated jet on slightly more than a sound crossing time, at which point the buoyant force takes over as the dominant mechanism regulating cavity dynamics.

The buoyant bubble rises amid the ambient pressure gradient and expands adiabatically during its ascent to maintain pressure equilibrium with the surrounding gas. It eventually becomes large enough to cause a detectable, roughly circular deficit in X-ray surface brightness. At this stage, the cavity's maximum age is set by its terminal velocity in the medium,

$$v_t \approx \sqrt{\frac{2gV}{SC}} \tag{1.26}$$

which is set by the balance of the local buoyant and drag forces. Here, V is the volume of the cavity, S is its cross-sectional area, and g is the local gravitational acceleration. The majority of X-ray cavities (including those in A2597) are cospatial with the BCG stellar isophotes, implying that they rise amid a potential dominated by the BCG. The local gravitational acceleration at radius R from the center of the host galaxy may therefore be inferred from the stellar velocity dispersion σ,

$$g \simeq \frac{2\sigma^2}{R}, \tag{1.27}$$

assuming that the galaxy is an isothermal sphere. The terminal velocity v_t of the cavity is always subsonic, as the Kepler speed $v_{\rm K} = \sqrt{gR}$ is of order the sound speed c_s in the gas

$$c_{\rm s} = \sqrt{\frac{\gamma kT}{\mu m_{\rm H}}}, \tag{1.28}$$

where $\gamma \simeq 5/3$ is the ratio of specific heats and $\mu \simeq 0.62$ is the mean molecular weight, appropriate for fully ionized gas.

Based on these simple assumptions, three estimates are generally used in age-dating X-ray cavities. The most simple of these is the sound crossing time t_{c_s},

$$t_{c_s} = \frac{R}{c_s} = R\sqrt{\frac{\mu m_{\rm H}}{\gamma kT}}, \tag{1.29}$$

which assumes a direct sonic rise of the bubble along the plane of the sky to its current projected radius R. As the initial stages of cavity inflation are thought to be supersonic, followed by subsonic buoyant rise, this admittedly simple approach may best reflect an "average" of the two stages. Alternatively, if initial inflation is a small fraction of the cavity's age, the buoyant rise time $t_{\rm buoy}$ may be used, which takes drag forces into account. Following the discussion of the terminal buoyant velocity above, $t_{\rm buoy}$ is given by

$$t_{\rm buoy} \simeq \frac{R}{v_t} \simeq R\sqrt{\frac{SC}{2gV}}. \tag{1.30}$$

Finally, cavity age is constrained by the time it takes for gas to refill the bubble's "wake", which can be roughly estimated by the time it would take a bubble of radius r to rise through its own projected diameter,

$$t_{\rm refill} = 2\sqrt{\frac{r}{g}}. \tag{1.31}$$

In Chapter 2, we undertake this exercise for the X-ray cavities in Abell 2597. For more comprehensive work focusing on the age dating of cavities, see Bîrzan *et al.* (2004); Rafferty *et al.* (2006), and McNamara & Nulsen (2007) for an updated review.

1.2.6 A note on X-ray bubble longevity and magnetic field draping

As a purely hydrodynamic X-ray bubble buoyantly rises, it induces vortical motions in the ambient fluid, its leading edge sees the rapid growth of of Rayleigh-Taylor instability modes, and shear along the bubble walls gives rise to secondary Kelvin-Helmholtz instabilities (e.g., Soker *et al.* 2002; Robinson *et al.* 2004; Dursi & Pfrommer 2008, and references therein). Together, these effects should disrupt an initially spherical, hydrodynamic X-ray bubble into a "smoke ring" on

one bubble rise time, $t_{\rm refill}$ (see Eqn. 1.31). Roughly circular, well defined X-ray cavities have been observed at clustercentric radii many times larger than their own radii, however, indicative of ages far older than one bubble rise time (if they are indeed inflated at the core, as the AGN heating model suggests).

Of course, a purely hydrodynamic description of X-ray bubbles is not adequate, as magnetic fields play an important role in the hot ICM (see the discussion in Section 1.2.2). Magnetohydrodynamic simulations of bubbles have shown that the draping of magnetic fields over the leading edge of the bubble can strongly suppress the growth of these instabilities, inhibiting bubble disruption for long timescales (Robinson *et al.*, 2004; Dursi & Pfrommer, 2008). This is now one of the most favored scenarios accounting for the apparent longevity of X-ray cavities. For a more comprehensive discussion, see Robinson *et al.* (2004); McNamara & Nulsen (2007); Dursi & Pfrommer (2008), and references therein.

1.2.7 How heating by AGN feedback might work

We again summarize some of the major points presented by McNamara & Nulsen (2007), and references therein. The energy associated with an X-ray cavity is equivalent to its enthalpy ("free energy") H, which is merely the $p \times dV$ work required to "inflate" the cavity, plus the thermal energy E within the cavity. That is,

$$H = E + pV = \frac{\gamma}{\gamma - 1} pV, \tag{1.32}$$

where V is the cavity volume, p is the pressure of the radio lobe which displaced the thermal gas, and γ is the ratio of specific heats, dependent on the (largely unknown) contents of the cavity. If the bubble is filled by relativistic particles, we may take $\gamma = 4/3$, in which case the cavity enthalpy would be $H = 4pV$. If the contents are magnetically dominated, then $\gamma = 2$ and $H = 2pV$. A bubble filled with non-relativistic particles would be an intermediate case ($\gamma = 5/3$, $H = 2.5pV$). Cavity enthalpy is therefore likely to be somewhere in the range of $2pV - 4pV$, regardless (to first order) of cavity contents.

Churazov *et al.* (2002); Reynolds *et al.* (2002); Bîrzan *et al.* (2004) propose a simple mechanism wherein the enthalpy of a buoyantly rising cavity can be entirely dissipated as the displaced intracluster gas rushes to refill its wake. This results in the conversion of ICM potential energy U

to kinetic energy by a degree given by

$$\delta U = Mg\delta R \tag{1.33}$$

where M is the mass of the ICM that is displaced by the cavity as it rises through δR, and g is the local gravitational acceleration, as before. Assuming $M = \rho V$, hydrostatic (so that $\rho g = -dp/dR$), and approximately isobaric local conditions (so the pressure gradient $\left[dp/dR\right]$ can be ignored, giving $\delta R = \delta p$), the potential energy dissipation is given by

$$\delta U = V(\rho g)\delta R = -V\frac{dp}{dR}\delta R = -V\delta p. \tag{1.34}$$

The corresponding change in cavity enthalpy is simply given by the first law of thermodynamics,

$$\delta H = T\delta S + V\delta p. \tag{1.35}$$

The cavity is assumed to be entirely adiabatic (non-radiative), so entropy S remains constant and $\delta S = 0$. We therefore see that

$$\delta H = V\delta p = -\delta U, \tag{1.36}$$

meaning the amount of kinetic energy associated with the thermal gas rushing to refill the cavity ($-\delta U$) wake is equal to the enthalpy (free energy) of the cavity. This is the general idea behind "effervescent" cavity heating models like those described by Begelman (2001); Ruszkowski & Begelman (2002). In Chapter 2, we explore energy budgets associated with this model in the context of the Abell 2597 X-ray cavities.

Long-lived sound waves and weak shocks associated with cavity inflation are also expected to heat the ICM. By injecting *potential* energy into the ICM (effectively the opposite of the cavity heating model), the waves decrease gas density and therefore lower the cooling rate (which, if you will recall, is proportional to the square of the gas density). There is very strong observational evidence in the Perseus cluster (work by Fabian and collaborators) of sound waves driven during excavation of its cavities[12]. The waves are expected to dissipate into heat over longer timescales.

[12] Anecdotally, the evidence in Perseus is so strong that it enabled a rough estimate of the frequency of the sound waves: 3C 84 may effectively be "playing" a "B-flat" into Perseus at ~ 60 octaves below "middle C". This would be one of the lowest known "musical notes" in the Universe (A. Fabian, private communication; see the press release from Fabian and collaborators).

Again, see McNamara & Nulsen (2007) for a more comprehensive review of the effervescent cavity heating model.

1.3 Brightest Cluster Galaxies in Cool Cores: Testing Cooling Flow and AGN Feedback Models

This thesis (particularly the first half) is broadly related to the AGN feedback model as it pertains to star formation in brightest cluster galaxies. It is therefore important to briefly review the observed properties of BCGs in a relatively model-agnostic manner.

1.3.1 Observed properties of BCGs

To again quote Dr. Megan Donahue, brightest cluster galaxies are the "trash heaps" of the Universe. As they reside at the bottom of cluster potential wells, they are subject to extremely high relative merger rates at early times, gas-rich tidal stripping from nearby companions, and (if the cooling flow model is at least correct in principle), the accretion of cooling intracluster gas at late times. These factors conspire, yielding masses that can exceed $\sim 10^{12}\,M_{\odot}$ and stellar halos that can extend hundreds of kpc into the cluster center, making BCGs by *far* the largest and most luminous galaxies in the Universe (e.g., Sarazin 1988).

BCGs clearly stem from more extreme formation histories than do typical giant elliptical (gE) field galaxies (e.g., those galaxies not associated with a cluster), and so their properties differ in several important ways:

- As stated above, BCGs as a class are generally much more massive and luminous than gEs by about an order of magnitude.
- Although more luminous, BCGs generally have lower central surface brightness than do gEs, and their outer stellar halos do not follow a typical $\left(R/R_e\right)^{1/4}$ de Vaucouleurs' law (as gEs do).
- Optically selected BCGs *in non-cool core* clusters are *less* likely to harbor active central emission line nebulae than are gEs, by about a factor of two (10% vs. 20%, respectively).
- Optically selected CC BCGs *in cool core clusters* are *far more* likely to harbor active central emission line nebulae than are gEs, by more than a factor of two (45% vs. 20%, respectively,

Best *et al.* 2006; Edwards *et al.* 2007). It follows that CC BCGs are more likely than non-CC BCGs to host these systems by a factor of four (45% vs. 10%, respectively).

- CC BCGs are more likely to host radio-loud AGN than are non-CC BCGs or gEs (Burns, 1990).

- Radio sources associated with CC BCGs are unusual as compared to radio-loud AGN as a whole: they are generally more compact (< 30 kpc), have steep spectral indices at low frequencies (~ -2), and are more "blob-like" in morphology (O'Dea & Baum, 1987b; Baum, 1987).

1.3.2 Origin of the Emission Line Nebulae and Star Formation in CC BCGs

The clear connection between cool core clusters and the optical emission line nebulae in BCGs has been known for decades (Hu *et al.*, 1985; Baum, 1987; Heckman *et al.*, 1989), but consensus has never been reached on the *origin* of this phenomenon. Independent of the "cooling flow problem", it is now very clear that the emission line nebulae are not exclusively the 10^4 K phase of a cooling flow, given the issues discussed at length in section 1.1 (e.g., Hα luminosities, forbidden-to-Balmer ratios, etc.). The debate has instead focused upon whether or not the gas reservoirs from which the emission line nebulae and stars form have (a) condensed from a cooling flow or (b) are deposited through mergers.

Those who reject the cooling flow model (given its inability to reproduce observations) generally favor some form of the latter argument. Their position is naturally sound, as mergers are the primary agents of structure growth in ΛCDM cosmology, and their ability to quickly deposit large gas reservoirs into their merger products make them efficient triggers of star formation and black hole growth periods (this would account for BCGs being so massive and luminous). Then again, the majority of galaxies in the central regions of clusters are generally quite gas-poor, possibly because their gas contents are easily stripped (tidally and via ram pressure) during cluster assembly. In fact, field gEs, which should have been subject to a *lower* merger rate than BCGs at early times, are *more* likely than non-CC BCGs to host emission line nebulae and star formation amid gas-rich reservoirs (by a factor of two, see above).

Alternatively, there is strong evidence that the emission line nebulae and star formation arise from gas reservoirs which have condensed from the ICM in cool cores. While only 10% of optically selected BCGs in non-CC clusters possess central emission line nebulae (Best *et al.*, 2006; Edwards *et al.*, 2007), this fraction spikes to $> 45\%$ for BCGs in cool cores (Crawford *et al.*, 1999;

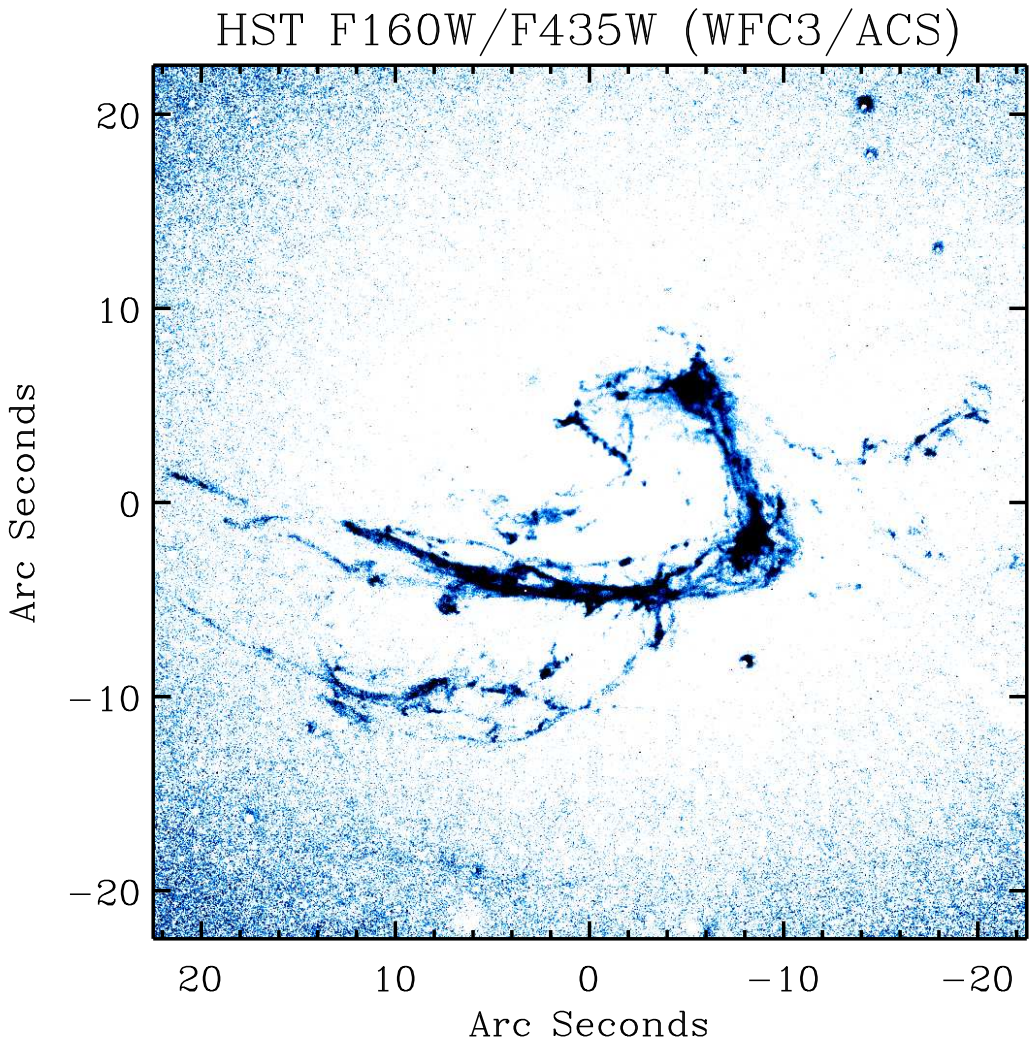

Figure 1.7: Absorption map of the dust lane in NGC 4696, the brightest cluster galaxy at the center of the Centaurus cluster of galaxies. The map was made via division of *HST* WFC3 F160W and ACS F435W broadband images. NGC 4696 has a very low FUV-derived star formation rate, and may be in the process of a merger, as evidenced by the dynamically young dust structures. At the redshift of NGC 4696, $1''$corresponds to 0.20 kpc. Figure by Grant Tremblay.

Edwards *et al.*, 2007). Of these, about half are known to exhibit ongoing star formation (detected by a variety of means; Johnstone *et al.* 1987; McNamara & O'Connell 1989; O'Dea *et al.* 2004, 2008; Quillen *et al.* 2008; O'Dea *et al.* 2010). These pieces of circumstantial evidence are strongly supportive of some intrinsic connection between clusters with short central X-ray-derived cooling times and the presence of emission line nebulae and star formation in BCGs. The strongest pieces of direct evidence are:

1. Star formation rates in CC BCGs strongly correlate with upper limits on ICM cooling rates from X-ray spectroscopy (McNamara *et al.*, 2004; Rafferty *et al.*, 2006; Salomé *et al.*, 2006; Quillen *et al.*, 2008; O'Dea *et al.*, 2008, 2010).

2. Velocity structures of the cold gas in CC BCGs are consistent with expectations for gas that has cooled from an ambient hot, static atmosphere (Jaffe *et al.*, 2005; Salomé *et al.*, 2006).

3. The power of central radio sources in CC BCGs correlates with X-ray derived cooling times (O'Dea & Baum, 1987b).

4. The Hα luminosity correlates with the radio luminosity in CC BCGs[13] (Heckman *et al.*, 1989).

Note that, of course, the above luminosity-luminosity correlations must always be considered in the context of Footnote 8 above ("big things have more of everything"). Regardless, the tight cross-correlations and high statistical significance of the results very clearly support a scenario wherein (1) at least a significant fraction of gas in the BCG condenses from the ICM, (2) coalesces within the BCG, and (3) provides the reservoir from which emission line nebulae arise, from which stars form, and from which black holes grow in a mutually connected way. It is *very difficult* to imagine a purely coincidental scenario wherein (1) short ICM cooling times and (2) the highly active nuclei of exclusively cool core BCGs are not intrinsically and directly related. If they are *not* directly related, then gas-rich tidal stripping or wet mergers would need to occur preferentially in CC BCGs in order to explain the near five-fold increase in star formation and emission line activity. It is not obvious why this would be the case, particularly given the relatively gas-poor companions of CC BCGs.

There are direct observational tests that can be used to help discriminate between these two scenarios. Gas condensing from a cooling flow and being deposited through a merger are expected

[13]Then again, this is true of radio galaxies in general (Baum *et al.*, 1988; Baum & Heckman, 1989a). As mentioned previously, "bigger is bigger", so this is not necessarily surprising or indicative of an intrinsic connection.

to have very distinct dynamical properties. Cooling gas from a static hot atmosphere should be associated with low net angular momentum, with a flow velocity that gradually increases from the systemic velocity at large radii, outside the BCG, to velocities of order a few hundred kilometers per second at smaller radii, with low levels of observed rotation. On the other hand, gas stemming from mergers should possess high net angular momentum at all stages, and therefore be associated with rotation and high velocities at distant radii. The now-onlining Atacama Large Millimeter/submillimeter Array (ALMA), with its unprecedented sensitivity and spatial resolution at sub-mm wavelengths, will be critical in discriminating between these two scenarios for nearby cool core and non-cool core clusters.

1.3.3 Star Formation and a Ghost Ionization Mechanism in the Cold Reservoirs

Despite the strong circumstantial connections discussed above, it is now clear that the emission line nebulae are not simply the 10^4 K phase of a cooling flow. While the bulk of the "baryon budget" for these phenomena might be accounted for by condensation from the ambient hot reservoir, the cooling flow model in isolation seriously underpredicts the observed Hα luminosities by $2-3$ orders of magnitude in a pure radiative cooling scenario (e.g., Heckman *et al.*, 1989; Voit & Donahue, 1997). The nebulae are also characterized by inverted forbidden-to-Balmer ratios, requiring models, independent of or in addition to cooling, which impart a great deal of heating per ionization event (Donahue & Voit, 1991; Voit & Donahue, 1997).

Star formation plays a critical but not exclusive role in regulating the physics of both the warm and cold components of the ISM in CC BCGs. Substantial young stellar components have been observed in half of all CC BCGs, and these can often account for the ionizing photons required to power the observed luminosity of the Hα nebulae and extended diffuse components of Lyα that are always observed to be cospatial with the more clumpy and filamentary FUV continuum emission from O and B stars (Johnstone *et al.*, 1987; Romanishin, 1987; McNamara & O'Connell, 1989, 1993; McNamara *et al.*, 2004; McNamara, 2004; Hu, 1992; Crawford & Fabian, 1993; Hansen *et al.*, 1995; Allen, 1995; Smith *et al.*, 1997; Cardiel *et al.*, 1998; Hutchings & Balogh, 2000; Oegerle *et al.*, 2001; Mittaz *et al.*, 2001; O'Dea *et al.*, 2004; Hicks & Mushotzky, 2005; O'Dea *et al.*, 2008; Bildfell *et al.*, 2008; Loubser *et al.*, 2009; Pipino *et al.*, 2009; O'Dea *et al.*, 2010; McDonald *et al.*, 2010, 2011; Oonk *et al.*, 2011). However, stellar photoionization almost never correctly predicts the observed forbidden-to-Balmer ratios in the gas, and some emission line filaments are devoid of any observable star formation whatsoever (e.g., many of the NGC 1275

filaments, Conselice *et al.* 2001). In addition to star formation, another mechanism is needed to calibrate the ionization state of the gas. Proposed models have included AGN photoionization (long ruled out due to lack of radial gradients in ionization state), repressurizing and fast shocks (Cowie *et al.*, 1980; Binette *et al.*, 1985; David *et al.*, 1988), thermal conduction (e.g., Sparks *et al.* 1989; Narayan & Medvedev 2001; Fabian *et al.* 2002; Voit *et al.* 2008) reconnection of magnetic fields (Soker & Sarazin, 1990), self-irradiation by gas from a cooling flow (Voit & Donahue, 1990; Donahue & Voit, 1991) and turbulent mixing layers (Begelman & Fabian, 1990), as well as heating by convective instabilities (e.g., Chandran & Rasera 2007) and, recently, cosmic rays (Ferland *et al.* 2008, 2009; Donahue *et al.* 2011; Fabian *et al.* 2011; Mittal et al. 2011, in preparation).

1.4 AGN Feedback in Context

The addition of "anti-hierarchical" quenching of star formation is clearly needed in merger-driven hierarchical galaxy formation models in order to account for the decades-old "over cooling problem", wherein star formation is effectively catastrophic, grows along with the complexity of structure, and makes predictions that are effectively *opposite* to what is observed. Namely, this "anti-hierarchical" mechanism is needed to explain

- The exponential turnover at the bright end of the galaxy luminosity function (e.g., Benson *et al.* 2003)
- The bimodality of galaxies in color-magnitude space (i.e., galaxies inhabit a "blue cloud" or a "red sequence", separated from one another by a very under-dense "green valley". Evolution from "cloud-to-sequence" is too rapid to be accounted for by passively evolving star formation rates. They must instead be actively quenched).

The need for this anti-hierarchical growth mode can be broadly contextualized as a need to explain the "cosmic downsizing" phenomenon, wherein the dominant contributors to the star formation rate density shifts from high mass galaxies to low mass galaxies with increasing cosmic time. The net implication is that more massive galaxies form at higher redshifts, and less massive galaxies form at lower redshifts — this "big-to-small" behavior is not predicted in cosmological models based upon hierarchical, "big-to-bigger" growth.

Moreover, the $M_{\rm BH}-\sigma$ relation (Magorrian *et al.*, 1998; Ferrarese & Merritt, 2000; Gebhardt *et al.*, 2000), if real, suggests that the growth of black holes and their host galaxy stellar components is not only *tightly coupled*, but also *self calibrating*. To first order, it seems that if the $M_{\rm BH}-\sigma$

relation is intrinsic, it must be fostered by mutual growth amid gas coalescing in newly formed galaxies. But in order to explain the very tight calibration, there may also be a second order effect wherein this infalling gas triggers, for example, a feedback loop.

The three most important pieces of evidence which point to AGN feedback as a promising solution are:

- the "AGN cosmic downsizing phenomenon", wherein lower luminosity AGN peak in co-moving space density at lower redshifts than do higher luminosity AGN, which peak at $z \sim 2$ (Giacconi *et al.*, 2002; Cowie *et al.*, 2003; Steffen *et al.*, 2003; Hopkins *et al.*, 2007). The fact that this observed phenomenon closely resembles the "cosmic downsizing" of star formation rate densities is probably not a coincidence.

- The onset of decline in star formation rates occurs at $z \sim 2$ (Pérez-González *et al.*, 2008), and the epoch of peak quasar activity is at $z \sim 2$ (Schmidt *et al.*, 1991; Steffen *et al.*, 2003; Hopkins *et al.*, 2007).

- The Kormendy relation implies that all bright galaxies harbor central black holes and that these black holes must grow, suggesting that all bright galaxies go through active phases (Kormendy & Richstone, 1995; Haehnelt & Rees, 1993).

The notion that just one solution – AGN feedback – may partly account for several major outstanding questions in modern astrophysics is attractive for obvious reasons, not the least of which is elegance and simplicity. Given the (literally!) universal implications of the above issues, it is clear that the study of BCGs in cool core clusters — where we may *directly* observe the effects of AGN feedback — are critical to our understanding of galaxy evolution as a whole.

Although the involved microphysics is poorly understood, AGN feedback has now become a necessary component in models of galaxy evolution. Many models now include AGN powered by continuous or discrete, merger-driven episodes of black hole growth. While there are many varieties of modern simulations, consensus is mounting that "quasar-mode feedback" at early times and "radio-mode feedback[14]" at late times yield results which match observations to a considerable degree, especially given the involved uncertainties and assumptions. In the so-called "quasar-mode", wet mergers drive rapid black hole and stellar bulge growth between $2 < z < 3$, imprinting

[14]The difference between these two terms is subtle, but important: in "quasar-mode feedback", powerful winds associated with a quasar quench star formation on global scales, accounting for the rapid "blue-to-red" evolution of galaxies. In "radio-mode feedback", radio-bright AGN outflows heat the ambient medium and suppress cooling flows by the mechanisms described in Section 1.2. This thesis focuses more on the radio-model model.

a persistent $M_{\rm BH} - \sigma$ relation that is fairly consistent with the observed relation. Eventually, the associated quasar winds quench star formation at $z \simeq 2$ (corresponding with observations), marking the onset of more quiescent "radio mode" feedback epochs needed to suppress cooling flows at late times (Springel *et al.*, 2005; Di Matteo *et al.*, 2005; Sijacki & Springel, 2006; Croton *et al.*, 2006). The most successful radio-mode models are episodic at rates corresponding to the average AGN duty cycle. For example, models by Sijacki & Springel (2006) include effervescent, feedback-driven bubble injection every 10^8 yr, and show that bubble heating successfully prevents massive galaxies from growing too large. Not including the bubble heating results in unphysically massive galaxies at late times. Critically, while radio-mode feedback successfully suppresses star formation associated with cooling flows, it also allows *low* levels of star formation to persist beyond $z < 1$, consistent with observations (see Chapters 2 and 3). The Sijacki & Springel (2006) model also closely reproduces the entropy profiles of CC clusters, including the central flattening characteristic of kinetic energy injection from AGN.

1.5 A Note on Powerful Radio Galaxies

Of course, the radio-mode AGN feedback model exists because powerful radio galaxies are commonly associated with BCGs in galaxy clusters (particularly in cool cores, Burns 1990). Because of this, and because the later parts of this thesis deal specifically with radio galaxies in general, it is important to (very) briefly review our understanding of these sources. This is especially relevant as cluster environments and ICM cooling models may play critical roles in shaping two of the major observational dichotomies associated with radio galaxies, namely the Fanaroff-Riley and high- / low- excitation divides. We discuss these below, after a short review of the orientation-dependent unification paradigm.

Unified models of radio-loud AGN

Unification schemes for radio-loud and radio-quiet[15] AGN rely on orientation-dependent obscuration to construct a singular model wherein all AGN, regardless of their many diverse properties, are intrinsically the same phenomenon viewed at different angles (e.g., Barthel 1989; Antonucci 1993;

[15]Roughly 90% of all AGN are considered "radio quiet" (Seyfert galaxies and radio-quiet quasars). For the purposes of this thesis, we focus on the remaining 10% of AGN considered "radio-loud" (radio galaxies, BL Lacs, and radio-loud quasars). For a review of the critically important radio-loud/radio-quiet dichotomy, see e.g., Capetti & Balmaverde (2010).

Urry & Padovani 1995). In the most basic, radio-loud scenario (the focus of this review), an accretion region about a central supermassive ($10^8 - 10^9\ M_\odot$) black hole is surrounded by an equatorial obscuring dusty torus. The liberation of gravitational potential energy from the accreting material as it falls inward toward the BH powers not only the characteristically intense nuclear emission associated with AGN, but also collimated bipolar outflows that are the progenitors of ~ 100 kpc (and even up to Mpc) scale radio jets (which are of course the basis for the mechanical AGN feedback model). For lines of sight nearly perpendicular to the radio jet axis, the dusty torus obscures the accretion region and the surrounding broad line region (BLR), while the more extended narrow-line region (NLR) remains visible. An observer with this line of sight would classify the object as a narrow-line radio galaxy (NLRG). Conversely, emission along a viewing angle nearly parallel to the jet axis would be dominated by relativistically boosted, non-thermal synchrotron processes in the jet, and the object would be classified either as a radio-loud flat-spectrum quasar (QSO) or a BL Lac, depending on the presence or absence (respectively) of strong emission lines. Along intermediate viewing angles, wherein both the BLR and NLR remain visible, the observer sees a steep-spectrum, radio-loud QSO or a broad-line radio galaxy (BLRG) for higher and lower intrinsic nuclear luminosities, respectively.

The model effectively implies that all type 2 AGN harbor hidden type 1 nuclei[16], and the spectropolarimetric detection of highly polarized broad emission lines – in some otherwise narrow-line radio galaxies – has lent important supporting evidence in this regard (e.g., Robinson *et al.* 1987; Cimatti *et al.* 1997; Ogle *et al.* 1997; Cohen *et al.* 1999; Zakamska *et al.* 2005). Stemming from this simple geometry-based scenario is the paradigmatic view that quasars and powerful radio galaxies intrinsically belong to the same population, viewed at different orientations. An extension of this is the view that low-power radio galaxies may be unified as the parent population of BL Lac objects, but this particular hypothesis has since given way to mounting evidence to the contrary. Indeed, while elegant in its simplicity, the orientation-dependent unification scheme has increasingly suffered from major unanswered questions – and even outright problems – as understanding of radio galaxies has evolved. Of course, this is not to say that the model is *wrong* (quite the contrary), but it clearly requires additional levels of complexity, for reasons we discuss below.

Current open problems with radio-loud unification models

Extended, 100 kpc scale radio emission associated with radio galaxies has long been classified into two morphological groups: lower power, edge-darkened Fanaroff-Riley (hereafter FR) class

[16]Broad-line AGN are typically called “type 1”, while narrow-line AGN are called “type 2”.

I objects with (often) two "plume-like" jets, and higher power, edge-brightened FR II objects characterized by bright terminal hotspots and the absence of an obvious counterjet (Fanaroff & Riley, 1974). This dichotomy in morphology and luminosity is almost certainly intrinsic (i.e., it is not a result of orientation), and the luminosity break separating the two classes appears to depend on host galaxy brightness (Owen & Ledlow, 1994; Ledlow & Owen, 1996). FR I are generally lower redshift than are FR IIs, which is not surprising given the tight redshift-luminosity correlation wherein higher power sources will preferentially be selected at higher redshifts (i.e., the Malmquist bias arising from flux-limited samples). This should therefore not be mistaken as inference that FR I are less numerous at high redshifts than FR IIs; in fact, the opposite may be true (we explore these issues in Chapter 5). Whether or not FR Is and FR IIs are intrinsically distinct objects, or if they represent stages of an evolutionary sequence, should therefore not be inferred from their redshift distributions.

The Fanaroff-Riley dichotomy is not well understood, and its better characterization has been a major pursuit of the field for decades, as it clearly stems from important jet physics. An increasingly popular view is that all initially propagating jets are launched relativistically, and FR Is stem from the disruption of those jets over sub-kpc scales, slowing to possibly trans-sonic speeds, likely through interaction with the ambient medium through which they propagate (e.g., Bicknell 1995; Laing *et al.* 2008). In this case, intrinsic differences in jet power would help to reconcile the Owen-Ledlow divide between the high radio luminosities of FR IIs and the lower luminosities of FR Is. In fact, if all jets really are intrinsically FR IIs with varying total powers (coupled, perhaps, to the accretion rate or mode), the Owen-Ledlow divide may be a self-reinforcing phenomenon: higher power, intrinsically FR II jets might better survive propagation through a dense ISM during the initial stages of its launch and therefore *retain* their FR II morphology on 100 kpc scales. On the other hand, lower power, a would-be FR II jet may become disrupted through ISM mass loading, and eventually form a lower-power jet of FR I morphology. The Owen-Ledlow divide is more of a "rough boundary" than it is a true divide, however, so some high luminosity FR I radio galaxies approach the brightness of low-power FR II radio galaxies. Problems with the above interpretation therefore arise when one observes a high power FR I in a sparse environment or a low-power FR II in a dense environment: if the former was disrupted, why wasn't the latter?

Most evidence is supportive, however, as the vast majority of FR Is are associated with cD ellipticals in clusters (see e.g. Owen *et al.*, 1996, for a review). FR IIs, particularly at low redshifts, are almost invariably associated with Mpc environments that are far lower density than those for FR Is. The contrary evidence arises mostly from the *small* population of FR IIs that are found in the centers of richer groups or clusters at redshifts higher than ~ 0.5 (Zirbel, 1997). Cosmological

evolution may certainly be at play (e.g., Sadler *et al.* 2007). While consensus has not yet been met, the clear fact that FR I reside in higher density environments is strongly supportive of the notion that it is the *environment* which gives rise to the Fanaroff-Riley dichotomy. Current quantitative models for mass entrainment in radio jets currently require an intrinsically FR II jet to be disrupted into an FR I on *sub-kpc* scales, however (e.g., Laing *et al.* 2008, and references therein). This is obviously problematic, as these scales are unrelated to cluster environment unless, for example, the ISM in the BCG is more dense because of a cooling flow (see e.g., Chapter 2, and the dynamically frustrated radio source associated with the BCG in Abell 2597).

An overriding issue prohibiting better understanding arises because the actual *formation* of the jets is not well understood, nor is the mechanism by which they remain tightly collimated over such vast distances. Jet formation models often include threading magnetic field lines, coupled to the accretion flow, through the ergosphere of the Kerr BH. A net Poynting flux is carried away by a relativistic outflow aligned with the BH spin axis, thereby extracting BH spin energy and providing an outlet for excess angular momentum from the system (e.g., Blandford & Znajek 1977; Blandford & Payne 1982; Punsly & Coroniti 1990; Meier 1999; De Villiers *et al.* 2005).

Equally important as the Fanaroff-Riley dichotomy is the discovery that the nuclear optical emission associated with radio galaxies can be characterized as having either "weak" or "strong" emission lines, and that the divide appears to depend on radio luminosity. Weak-lined, low-excitation radio galaxies (LEGs) tend to have low radio power, while strong-lined, high-excitation galaxies (HEGs) have higher radio luminosities (Hine & Longair, 1979; Laing *et al.*, 1994; Rector & Stocke, 2001). As the Fanaroff-Riley dichotomy also traces a divide in radio power, many years have been spent investigating whether the FR I/FR II and HEG/LEG dichotomies are related. Indeed, most narrow-line FR IIs and (crucially) *some* FR Is harbor hidden quasars with associated broad lines, and those sources with a hidden quasar are typically HEGs, while those sources lacking a hidden quasar are typically LEGs.

As this understanding was evolving, a confused and now largely inaccurate picture began to emerge: paper after paper began to associate FR Is, which are generally LEGs, as the parent population of BL Lacs (which are largely emission-line free). Similarly, high power FR IIs, which at the time were thought to generally associate with HEGs, became unified with flat-spectrum quasars. This view is almost certainly false, and some have argued that it achieved near-paradigm status because the community continually focused on – and even *assumed* – that the FR I/FR II and HEG/LEG dichotomies were directly related (e.g., Hardcastle et al. 2009, and references therein). Indeed, the HEG/LEG divide does not trace the Fanaroff-Riley divide with a one-to-one correspondence. There is a significant population of FR II radio galaxies with LEG-type

optical spectra, and there are sources with FR I radio morphology and high-excitation optical properties (Hine & Longair, 1979; Barthel, 1994; Laing *et al.*, 1994; Jackson & Rawlings, 1997; Chiaberge *et al.*, 2002; Hardcastle *et al.*, 2004; Whysong & Antonucci, 2004). Examples include the famous broad-lined FR I radio galaxy 3C 120, quasars with FR I morphology (e.g., Blundell & Rawlings 2001), and BL Lacs with FR II morphology (e.g., Rector & Stocke 2001), though these outliers typically reside near the FR I/FR II luminosity break. In a way, the Fanaroff-Riley and HEG/LEG dichotomies have conspired together to vastly complicate and even confuse the field of radio galaxies in the two decades since the ("official") emergence of the orientation-dependent unification scheme[17].

A unifying connection between radio galaxies and cool core clusters?

Now, there is even an emerging notion that LEGs may *completely lack* the fundamental components of the unification scheme, namely the obscuring torus and radiatively efficient accretion disk (Zirbel & Baum, 1995; Baum *et al.*, 1995; Chiaberge *et al.*, 2002; Whysong & Antonucci, 2004; Hardcastle *et al.*, 2006). Those works instead argue that the X-ray to radio SEDs of such systems can be almost entirely reconciled with emission from the base of the jet. In such a scenario, the LEG/HEG dichotomy may stem from different accretion modes, wherein HEGs arise from the accretion of a cold gas reservoir stemming from a recent merger with, or tidal stripping from, a gas-rich companion (Baldi & Capetti, 2008). Following the merger, the cold gas settles into a symmetry plane of the host galaxy and falls inward toward the nucleus at a rate dependent on the efficiency with which the gas sheds angular momentum. Eventually, the cold gas reaches the nucleus and forms the requisite structures required in the orientation-dependent unification scheme, i.e. the cold dusty torus and the geometrically thin accretion disk. On the other hand, work by (e.g.) Baum *et al.* (1992, 1995) gave rise to the now widely argued notion (e.g., Hardcastle *et al.* 2007, and references therein) that LEG are powered by the "hot-mode" accretion of hot ($\sim 10^7$ K) gas stemming from cooling flows in CC clusters. Ignoring the outlier populations (for the moment), if we (dubiously) assume that in *general*, "FR I are LEG" and "FR II are HEG", a consistent picture arises wherein CC clusters play a fundamental role in shaping the two observational dichotomies (FR I/FR II and HEG/LEG) in radio galaxies.

In this scenario, cooling from the hot phase accretes onto the central BH, triggering the AGN,

[17] In truth, implying that Urry & Padovani (1995) marked the "official" emergence of the orientation-dependent unification scheme isn't quite fair: more than two decades of important preceding work lead to the notion that orientation plays a major role in unification. See, for example, Antonucci (1984).

which in turn re-heats any cold gas that may have accumulated (both radiatively and by the mechanical mechanisms discussed above). This effectively prevents the gas from cooling on any significant scale, inhibiting coalescence of the material into the dusty torus and thin accretion disk required by the unification scheme. This picture is not complete, and the hot-mode accretion model is thus far incapable of sufficiently powering most narrow-line radio galaxies (Hardcastle *et al.*, 2007). Moreover, the argument by Chiaberge and collaborators that FR I may lack an obscuring torus operates under the assumption that emission from the base of the jet stems from a size scale *smaller* than any obscuring torus that may or may not be present. If the optical emission associated with the base of the synchrotron jet is from a region larger than the size of the torus, then its presence or absence cannot be directly inferred. It is also worth noting that settled, kpc-scale dusty disks and lanes *are* observed in FR I radio galaxy CC BCG hosts. Moreover, the FR Is are generally more dusty than FR II, and their dust distributions generally appear more "dynamically settled" (e.g., coherent disks as opposed to filamentary, wispy lanes, de Koff *et al.* 2000; Tremblay *et al.* 2007). While these kpc scale dust structures should not be confused for obscuring tori on far smaller scales, it is at least worth questioning why the former structures could form but not the latter. Clearly there is at least *some* important connection uniting the Fanaroff-Riley and HEG/LEG dichotomies with cluster environments (or lack thereof), but the strength of this connection is, as of yet, entirely unknown. This is certainly an instance where the importance of outliers (i.e., FR II LEGs, FR I HEGs and FR IIs in rich clusters) cannot be downplayed or ignored.

1.6 In this Thesis

We have so far provided a very broad contextual summary for the issues related to this doctoral thesis. Much of this is background material, of course, and only a very small fraction of the issues discussed above will be directly addressed in the forthcoming chapters. Before summarizing the pages to come, it is important to keep in mind that *in order to know an answer, we must first know the question*. This thesis will not *answer*, either fully or in part, any questions pertaining to cool cores, AGN feedback, or CC BCGs. Rather, it is our hope that the observational results we present will further our understanding, at least in a small way, of some of the major *questions* related to these issues. Below we summarize a subset of these questions, and describe how their better understanding may be brought about by the results presented in this thesis.

The questions this thesis will address

- **What role does AGN feedback play in regulating star formation and the entropy of the ICM?** What might be learned by comparing the morphology and magnitude of compact star forming regions in CC BCGs with the energy and timescale budgets associated with effervescent AGN feedback models? In **Chapter 2** we will present an in-depth, unified study considering the energy, mass, and timescale budgets of both the hot and warm/cold gas phases in the BCG of the cool core cluster Abell 2597. This canonical, well-studied source exhibits both low levels of ongoing star formation and signatures of episodic, effervescent AGN feedback. Using new *Chandra* and *HST* observations, we will provide new insights into the effervescent AGN feedback model, and the role it may play in regulating star formation and heating the ambient ICM/ISM.

- **What is the role of star formation in regulating the physics of the warm and cold ISM phases in CC BCGs?** In **Chapter 3** we will present *HST* FUV imaging for a sample of seven CC BCGs selected on the basis of an IR excess thought to be associated with elevated levels of star formation. We will show that these young stellar populations play a critical, even dominant role in providing the reservoir of ionizing photons needed to power the emission line nebulae in these systems. A comparison with radio data and results from the literature may reveal clues into the behavior of systems experiencing a low level of feedback from the AGN, which may allow for increased residual condensation from an ambient hot atmosphere, accounting for the heightened star formation rates.

- **How can we disentangle the roles played by cooling flows and mergers in depositing the gas reservoirs which fuel episodes of star formation and AGN activity?** What might we learn by comparing Abell 2597, associated with a moderately strong cooling flow, with a radio galaxy not associated with a cluster, but also exhibiting evidence of episodic star formation and AGN activity? In **Chapter 4** we will present a multiwavelength study of the giant radio galaxy 3C 236, one such source. Clearly, a cooling flow cannot be responsible for triggering star formation and AGN activity in this object. Might the differences between A2597 and 3C 236 yield new insights into hot and cold accretion mechanisms?

- **How might we find assembling protoclusters at high redshift, so as to study the cosmic evolution of (e.g.) the cool core phenomenon?** Galaxy clusters assemble at redshifts $1 < z < 2$, though to date, very few have been detected in this redshift range because of the difficulties associated with extending galaxy cluster selection methods to these depths. Understanding protoclusters at high redshift will be critical to understanding clusters in the

local Universe, particularly in terms of the cool core/non-cool core dichotomy. Studying the cosmic evolution of FR I radio galaxies, many of which are embedded in clusters, may lend new insights into these issues. In **Chapter 5** we will broaden the context of this thesis with a search for high redshift FR I radio galaxies that may act as observable "beacons" for assembling protoclusters.

Finally, in **Chapter 6**, we will revisit the questions posed above, and assess what we have learned.

Figure 1.8: Radio (pink) and X-ray (blue) composite of M87, the CC BCG in Virgo. See Harris *et al.* (2006); Forman *et al.* (2007); Sparks *et al.* (2009); Batcheldor *et al.* (2010) for some recent papers on this canonical radio galaxy (Credit: X-ray: NASA/CXC/KIPAC/N. Werner, E. Million et al; Radio: NRAO/AUI/NSF/F. Owen).

2

A Close Look

Effervescent AGN Feedback *in* Abell 2597

Ruddy Stargazers.
Never interested in anythin' closer'n the moon.
J. K. Rowling, 1997

In this chapter we present a multiwavelength study of the archetypal cool core cluster Abell 2597, accounting for the energy budget associated with the feedback-driven excavation of the central X-ray cavity network within the BCG. This study is enabled by previously unpublished *Chandra* observations that are a factor of four deeper than any that have previously been studied, allowing for more detailed spatial and spectral analysis. These new data, in concert with a rich suite of archival data including *Hubble Space Telescope* (*HST*) imaging of ongoing star formation in A2597, enable a "unified", cross-spectrum interpretation of this canonical CC cluster, particularly in the context of AGN feedback and its effects on the warm and cold gas phases in the central BCG.

2.1 The Brightest Cluster Galaxy in Abell 2597

Abell 2597 (hereafter A2597) is an Abell (Abell, 1958; Abell *et al.*, 1989) richness class 0 galaxy cluster of total X-ray luminosity $L_X = 6.45 \times 10^{44}$ ergs s^{-1} (2-10 keV, David *et al.* 1993). The X-ray surface brightness profile is sharply peaked about the centrally dominant (cD, Matthews *et al.* 1964) elliptical BCG (Fig. 2.1, in red) at redshift $z = 0.0821$ (Voit & Donahue, 1997), whose central region is host to the compact powerful radio source PKS 2322-122 (PMN J2323-1207, Wright & Otrupcek 1990; Griffith & Wright 1994). The radio source has 1.5 and 5.0 GHz flux densities of ~ 1.7 and ~ 0.3 Jy, respectively (Owen *et al.*, 1992; Ball *et al.*, 1993; McNamara *et al.*, 2001; Morris & Fabian, 2005), giving a relatively steep spectral index of $\alpha = -1.3$ (where $S_\nu \propto \nu^\alpha$). At 8.4 GHz (Sarazin *et al.* 1995, Fig. 2.1*a*, white contours) the source features two lobes extended $\sim 5''(\sim 8$ kpc) approximately NE-S. There is a significant position angle (P. A.) offset between the two lobes owing to a sharp bend in the southern lobe and a bright knot immediately south of the core. There is evidence of spatial anti-correlation with the 8.4 GHz source and the emission line nebula that is extended on approximately the same scale (Heckman *et al.*, 1989; Sarazin *et al.*, 1995; Koekemoer *et al.*, 1999; O'Dea *et al.*, 2004; Oonk *et al.*, 2011). Assuming a canonical jet spectral index of –0.7, the estimated spectral index of the northern and southern lobes is $\alpha \sim -1.5$, indicative intrinsic compactness arising from frustration by dynamical confinement (as opposed to compactness arising from simple youth). O'Dea *et al.* (1994b) suggests that PKS 2322-122 may be one of the nearest known compact steep spectrum (CSS) sources (see O'Dea *et al.* 1998, for a review). Taylor *et al.* (1999) observed the central 0.3 arcsec of the radio core with the Very Long Baseline Array (VLBA) at 1.3 and 5.0 GHz, detecting straight symmetric jets on ~ 50 pc scales that are aligned along P.A.$\sim 65^\circ$ and -110°, a significant offset from the major axis of the 8.4 GHz lobes. Extended 330 MHz and 1.3 GHz emission was observed to lie on approximately the same position angle as the VLBA jet, suggestive of a common axis, save for the 8.4 GHz source (Clarke *et al.*, 2005).

Owing to its close proximity, high X-ray emissivity, and spectacular central emission line nebula, A2597 has been the subject of three decades of cross-spectrum analysis in the literature (X-ray — Crawford *et al.* 1989; Sarazin *et al.* 1995; Sarazin & McNamara 1997; McNamara *et al.* 2001; Clarke *et al.* 2005; Morris & Fabian 2005; UV/optical — McNamara & O'Connell 1993; Voit & Donahue 1997; McNamara *et al.* 1999; Koekemoer *et al.* 1999; Oegerle *et al.* 2001; O'Dea *et al.* 2004; Jaffe *et al.* 2005; Oonk *et al.* 2011; IR — McNamara & O'Connell 1993; Voit & Donahue 1997; McNamara *et al.* 1999; Koekemoer *et al.* 1999; O'Dea *et al.* 2004; Jaffe *et al.* 2005; Donahue *et al.* 2007, 2011; sub-mm — Edge *et al.* 2010a,b; radio — O'Dea *et al.* 1994a; Sarazin *et al.*

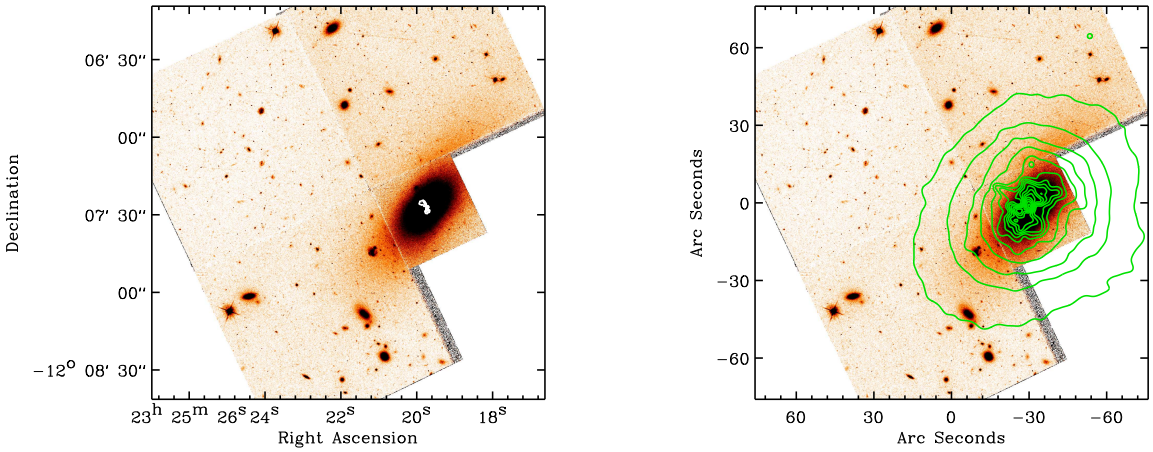

Figure 2.1: Broad-band *HST*/WFPC2 F702W (*R*-band) exposure of the central regions of the Abell 2597 galaxy cluster (in orange), with (*a*) VLA 8.4 GHz radio contours tracing radio emission from PKS 2322-122 (in white) and (*b*) *Chandra* 0.5-7 keV X-ray contours (in green) overlaid. North is up, east is left. At the redshift of the A2597 BCG ($z = 0.0821$), $1''$corresponds to ~ 1.5 kpc, such that the full field of view of the figures is $\sim 200 \times 200$ kpc. Note that the spatial anisotropy of the X-ray emission (in green contours) is largely confined to the scale of the central brightest cluster galaxy.

1995; Taylor *et al.* 1999; Pollack *et al.* 2005; Clarke *et al.* 2005).

In Section 2.2 of this chapter, we discuss the new and archival data presented as part of this analysis, as well as the steps taken to reduce the data to "science-ready" status. In Sections 2.3 and 2.4 we present a spatial and spectral analysis of the new *X-ray* observations sampling the hot $10^7 - 10^8$ K phase of the ICM. In Section 2.6 we compile the local energy budget for AGN feedback in A2597, as inferred from X-ray cavity analysis. In Section 2.7 we consider our results in the context of the central emission line nebula and the cold gas reservoir in which it resides. A discussion, in which we interpret the flagship results of this chapter in the context of multiple scenarios, is presented in Section 2.8. A summary and concluding remarks follow. In this chosen cosmology of this thesis, $1''$ corresponds to ~ 1.5 kpc/arcsec at the redshift of the Abell 2597 BCG ($z = 0.0821$). This redshift corresponds to an angular size distance $D_A \approx 315$ Mpc and a luminosity distance $D_L \approx 369$ Mpc.

Table 2.1. **Summary of Observations of Abell 2597**

Observatory (1)	Instrument (2)	Mode/Config (3)	Band/Filter/Line (4)	Exp. Time (5)	Prog. #/Obs. ID (6)	Obs. Date (7)	Program PI (8)	Reference (9)
			X-RAY OBSERVATIONS					
Chandra	ACIS-S	FAINT	X-ray (0.5 – 7 keV)	39.8 ks	922	28 July 2000	McNamara	1
···	ACIS-S	VFAINT	X-ray (0.5 – 7 keV)	52.8 ks	6934	1 May 2006	Clarke	New
···	ACIS-S	VFAINT	X-ray (0.5 – 7 keV)	60.9 ks	7329	4 May 2006	Clarke	New
			FAR ULTRAVIOLET / OPTICAL / NEAR-INFRARED OBSERVATIONS					
HST	ACS	SBC	F150LP (FUV)	8141 s	11131	21 July 2008	Jaffe	2
···	WFPC2		F410M	2200 s	6717	27 July 1996	O'Dea	3
···	WFPC2		F450W	2500 s	6228	07 May 1995	Trauger	4
···	WFPC2		F702W (*R*-band)	2100 s	6228	07 May 1995	Trauger	4
···	NICMOS	NIC2	F212N	12032 s	7457	19 Oct 1997	Donahue	5
···	NICMOS	NIC2	F160W (*H*-band)	384 s	7457	03 Dec 1997	Donahue	5
			MID- / FAR-INFRARED OBSERVATIONS					
Spitzer	IRAC	Mapping	3.6, 4.5, 5.8, 8 μm	3600 s (each)	3506	24 Nov 2005	Sparks	6
···	MIPS		24, 70, 160 μm	2160 s (each)	3506	18 Jun 2005	Sparks	6
Herschel	PACS	Photometry	70, 100, 160 μm	722 s (each)	13421871(18-20)	2009 Nov 20	Edge	7
···	SPIRE	Photometry	250, 350, 500 μm	3336 s	1342187329	2009 Nov 30	Edge	7
···	PACS	Spectroscopy	[O I] λ68.4 μm	6902 s	1342187124	2009 Nov 20	Edge	8
···	···	···	[O III] λ88.36 μm	7890 s	1342188703	2009 Dec 30	Edge	8
···	···	···	[N II] λ121.9 μm	7384 s	1342188942	2010 Jan 04	Edge	8
···	···	···	[O Ib] λ145.52 μm	7382 s	1342188704	2009 Dec 30	Edge	8
···	···	···	[C II] λ157.74 μm	6227 s	1342187125	2009 Nov 20	Edge	8
···	···	···	[Si I] λ68.47 μm	11834 s	1342210651	2010 Dec 01	Edge	New
			RADIO OBSERVATIONS					
VLA		A array	8.44 GHz	15 min		1992 Nov 30	Sarazin	9
···		A array	4.99 GHz	95 min		1996 Dec 7	Taylor	10,11
···		A array	1.3 GHz	323 min		1996 Dec 7	Taylor	10,11
···		A&B	330 MHz	5.3 hr		Jun, Aug 2003	Clarke	9

Note. — A summary of the new and archival observations used in our analysis. (1) Facility name; (2) instrument used for observation; (3) configuration of instrument / facility; (4) wavelength regime / spectral line observed or filter used; (5) exposure time; (6) facility-specific observation or program ID; (7) date of observation; (8) principal investigator (PI) of observation or program; (9) reference to publication where the data were first published. Those marked "new" have not yet been published, and appear for the first time in this paper.

References. — 1: McNamara *et al.* (2001); 2: Oonk *et al.* (2011); 3: Koekemoer *et al.* (1999); 4: Holtzman *et al.* (1996); 5: Donahue *et al.* (2000); 6: Donahue *et al.* (2007); 7: Edge *et al.* (2010b); 8: Edge *et al.* (2010a); 9: Sarazin *et al.* (1995); 10: Taylor *et al.* (1999); 11: Clarke *et al.* (2005)

2.2 Observations & Data Reduction

A summary of all new and archival observations used as part of this analysis is presented in Table 2.1. Below, we discuss those observations we use most directly in this study.

2.2.1 Chandra X-Ray Observations & Data Reduction

Three *Chandra X-ray Observatory* AXAF CCD Imaging Spectrometer (ACIS) observations of X-ray emission from Abell 2957 exist in the archive. Only one of these observations have been

published, namely the 40 ksec exposure (ObsID 922, PI: McNamara) taken in July 2000 (McNamara *et al.*, 2001). For this exposure, the BCG nucleus was centered on node 0 of the ACIS-S3 chip, and the observations were made in FAINT, full-frame, timed exposure mode at a focal plane temperature of -120° C. The data were published by McNamara *et al.* (2001) (hereafter M01) in a study of the A2597 ghost cavity (which we will discuss later). As noted in M01, ObsID 922 was badly impacted by flaring events, yielding only $\sim$ 18 ksec of data suitable for spectral analysis. In May 2006, two new observations were made (ObsIDs 6934 and 7329, PI: Clarke), in VFAINT mode, for a total of 52.8 and 60.9 ksec. These data appear in this thesis for the first time. Below, we discuss the steps taken to reduce these data (in addition to re-reducing the 922 dataset), and merge the exposures for spatial analysis.

The three observations (ObsIDs 922, 6934, and 7329) were obtained as primary and secondary data products from the *Chandra* Data Archive. The data were reduced in the CIAO environment (*Chandra* Interactive Analysis of Observations, version 4.2, Fruscione *et al.* 2006) with version 4.3.1 of the calibration database (CALDB). For each ObsID, we used the CIAO 4.2 script `chandra_repro` to automate the creation of a new `level=1` event file with the latest standard pipeline calibrations applied. In order, these steps include charge transfer inefficiency (CTI) correction, time-dependent gain adjustment, application of latest gain maps, creation of a new bad pixel file, PHA and pixel randomization, VFAINT mode background cleaning (for ObsIDs 6934 and 7329), and corrections for continuous clocking mode times of arrival. The new `level=1` event file was then converted (by the script) to a new `level=2` event file using the CIAO tool `acis_process_events` to apply standard grade, status, and good time filters. Only those events with *ASCA* grades 0, 2, 3, 4, and 6 are used in this analysis.

For spatial analysis, we combined the three observations using the CIAO 4.2 script `merge_all`, which required subtraction of the `PHAS` column due to an array size mismatch introduced by differences in the FAINT and VFAINT data modes (this has no net effect as the `PHAS` column is not used after reprocessing of the data). The merged data was cut in energy space using standard `dmcopy` techniques, rejecting all channels below 0.5 keV and those above 7 keV. This filter was chosen as the high energy particle background is reasonably flat between the 2-7 keV range, but rises dramatically between 7-10 keV. As we are interested in low surface brightness features in the X-ray spatial distribution, this filter was chosen so as to minimize background levels. Soft (0.5-1 keV), medium (1-2 keV), and hard (2-7 keV) energy cuts were also made to enable hardness analysis. The merged and energy filtered data was then spatially smoothed with the CIAO tool `csmooth` using an adaptive kernel whose width was dynamically adjusted based on the local event density. We also created versions of these images with contaminating compact sources removed (including

X-ray emission associated with other cluster members and the central weak point source associated with the AGN). The total effective exposure time of the merged data is ~ 150 ksec, a factor of ~ 3.8 deeper than any previous X-ray analysis of the source.

Merged exposures cannot be used for spectral analysis due to response matrix variations, and because the corresponding exposure maps and the exposure corrected image lack statistical errors and meaningful source flux values. Instead, the spectra must be extracted from the individual observations, then simultaneously analyzed. To prepare the individual ObsIDs for spectral analysis, each was filtered for background flaring events, which can adversely effect interpretation of spectral data. This was done using the CIAO `deflare` script with an iterative sigma clipping method to create a good time interval (GTI) filter which rejects those times associated with three sigma flares over the mean quiescent background rate. This filtering strategy retained ~ 18 ksec of flare-free data (of the original 40 ksec) for the ObsID 922. ObsIDs 6934 and 7329 were not significantly impacted by flaring events, and no more than 2 ksec for either observation were rejected. See Fig. 2.2 for an illustration of this flare rejection technique. The total net combined flare-free effective exposure time is ~ 128 ksec (though, as was mentioned previously and will be discussed later, merged data was not used for spectral analysis: the three individual flare-free exposures were analyzed simultaneously).

2.2.2 FUV/Optical/NIR Hubble Space Telescope Observations & Data Reduction

We have obtained numerous archival *Hubble Space Telescope* (*HST*) observations of A2597, and employ them either in direct analysis or cursory reference to inform discussion. Table 2.1 contains a summary of the *HST* data obtained, along with references to the papers in which they were originally published. The data we most directly use, in terms of quantitative analysis, is the 8141 sec Advanced Camera for Surveys (ACS) Solar Blind Channel (SBC) FUV observation stemming from *HST* General Observer (GO) program 11131 (PI: Jaffe). This image was taken with the F150LP filter, with an effective wavelength of 1612 Å. The pixel scale for the SBC is approximately $0\farcs034 \times 0\farcs030$/pixel. The camera field of view is $34\farcs6 \times 30\farcs8$. At the redshift of A2597, the F150LP filter includes FUV continuum but excludes Lyα from the bandpass. These data were recently published and analyzed by Oonk *et al.* (2011). See that work for more details pertaining to the observations.

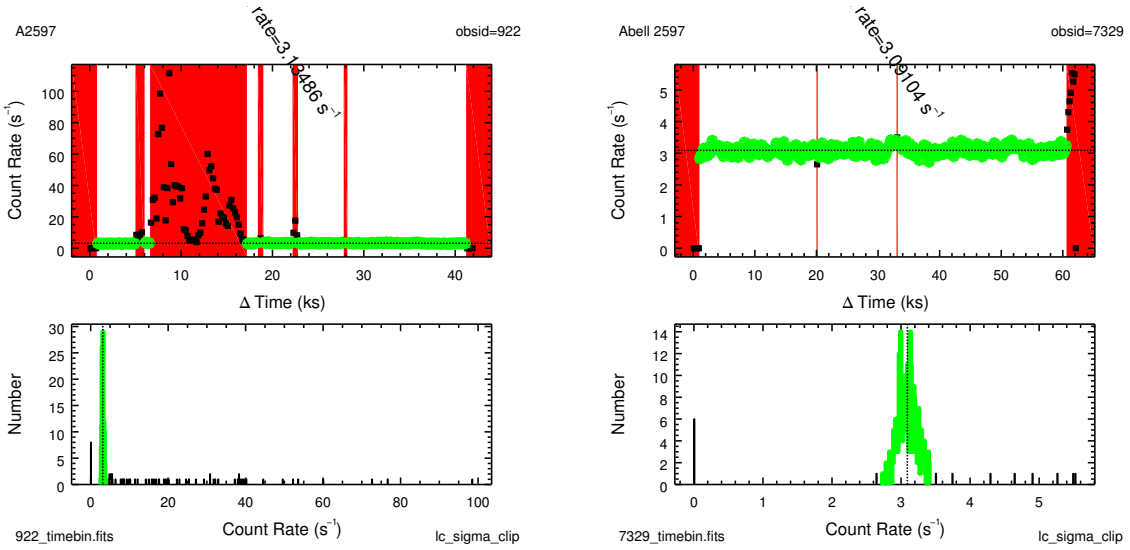

Figure 2.2: Example of our process of temporal filtering for flaring events in the *Chandra* data prior to spectral analysis. The figure at left is for ObsID 922, while the figure at right is for 7329. Note that ObsID is heavily impacted by strong flaring events, marked with red bands, which we filter with an iterative σ clipping method. The remaining "good" exposure times, in green, were 26.6, 51.9, and 58.4 ksec for ObsIDs 922, 6934, and 7329, respectively. We do not show a similar figure for ObsID 6934 as it looks very similar to 7329 (e.g., neither were badly impacted by flaring events).

2.2.3 Other archival datasets used in this analysis

The other data used in this analysis is found in Table 2.1. In all cases the paper in which the these data were originally published is referenced in column (9) of that table. See those referenced papers for information regarding the observations and data reduction for those datasets.

2.3 X-ray Spatial Analysis

Previous X-ray studies have been published for A2597 using the 40 ks (18 ksec of good time) *Chandra* observation 922. M01 was the first to report on the western and northeastern "ghost" cavities inferred from localized depressions in the X-ray surface brightness. Later work by Clarke *et al.* (2005) (hereafter C05) extended this analysis to include a detailed study between the X-ray spatial distribution and the VLA radio observations at 8.4 GHz, 1.3 GHz, and 330 MHz. In addition to confirming the presence of the M01 ghost cavities, C05 described an "X-ray tunnel" apparent in the "unsharp-mask" presented in that work. Roughly 22″ (33 kpc) in projected length and 1.5″(2.3 kpc) in projected radius, the "tunnel" appeared to connect the peak of the X-ray sur-

face brightness distribution, cospatial with the radio and BCG optical core, with the M01 western cavity. It was not apparent whether this was a truly discrete feature, or was simply part of a larger cavity encompassing both the tunnel and the M01 cavity. Extended 330 MHz radio emission was observed to be cospatial with the tunnel and also the M01 cavity (so the previously used "ghost cavity" term may no longer be appropriate). Our deeper X-ray data, the results from which we present in this section, enhance some of the lower surface brightness features only faintly visible in the 922 dataset, enabling a more detailed interpretation of the AGN outburst history.

2.3.1 General X-ray morphology

In Fig. 2.3 we present the new, deeper 0.5-7 keV data. This data consists of the original *Chandra* observation merged with the two new ~ 53 and ~ 61 ksec observations, and is a factor of four deeper (in terms of combined effective exposure time) than any that has previously been published. The X-ray image in Fig. 2.3 has been adaptively smoothed using a variable width Gaussian kernel. As a viewing aid, we overlay black contours with arbitrary levels that trace the surface brightness distribution. In the chosen color map, "purple" corresponds to regions of high surface brightness (e.g., the center), and "red" corresponds to regions of lower surface brightness (e.g., the outer regions). The field of view (FOV) of the figure is $\sim 60'' \times 60''$, corresponding to $\sim 90 \times 90$ kpc.

As noted in M01 and C05, it is immediately apparent that the X-ray surface brightness distribution is highly anisotropic, and exhibits several prominent features which we categorize and describe in this and later sections. In Fig. 2.1*b* we overlay the same 0.5-7 keV X-ray data as green contours on an *HST* WFPC2 *R*-band observation of the central 200×200 kpc of A2597. Cluster members are visible in the reddish hue. The conspicuous central BCG dominates the WFPC2 FOV and occupies much of the WFPC2 planetary camera (PC) chip (i.e., the smallest "quadrant"). From this figure it is apparent that the anisotropy of the X-ray emission is largely confined to the scale of the BCG, while the outermost regions assume a generally smoother and more elliptical shape. At all scales, the X-ray surface brightness distribution is extended along a position angle that matches the major axis of the BCG host galaxy stellar isophotes (which lie on a P.A. $\sim 45^{\circ}$). This is especially true at the innermost scales where the local gravitational potential is dominated by the BGC.

As is evident in Fig. 2.3, the innermost 20″of the 0.5-7 keV emission assumes a "butterfly"-like shape encompassing two high surface brightness knots with cores $\sim 1''$ W and $\sim 3''$ SE of the center of the figure (at α = 23 : 25 : 19.745, δ = –12 : 07 : 26.91, J2000). The knot $1''$ W is approximately cospatial with the radio core. A fraction of the X-ray emission in this knot stems

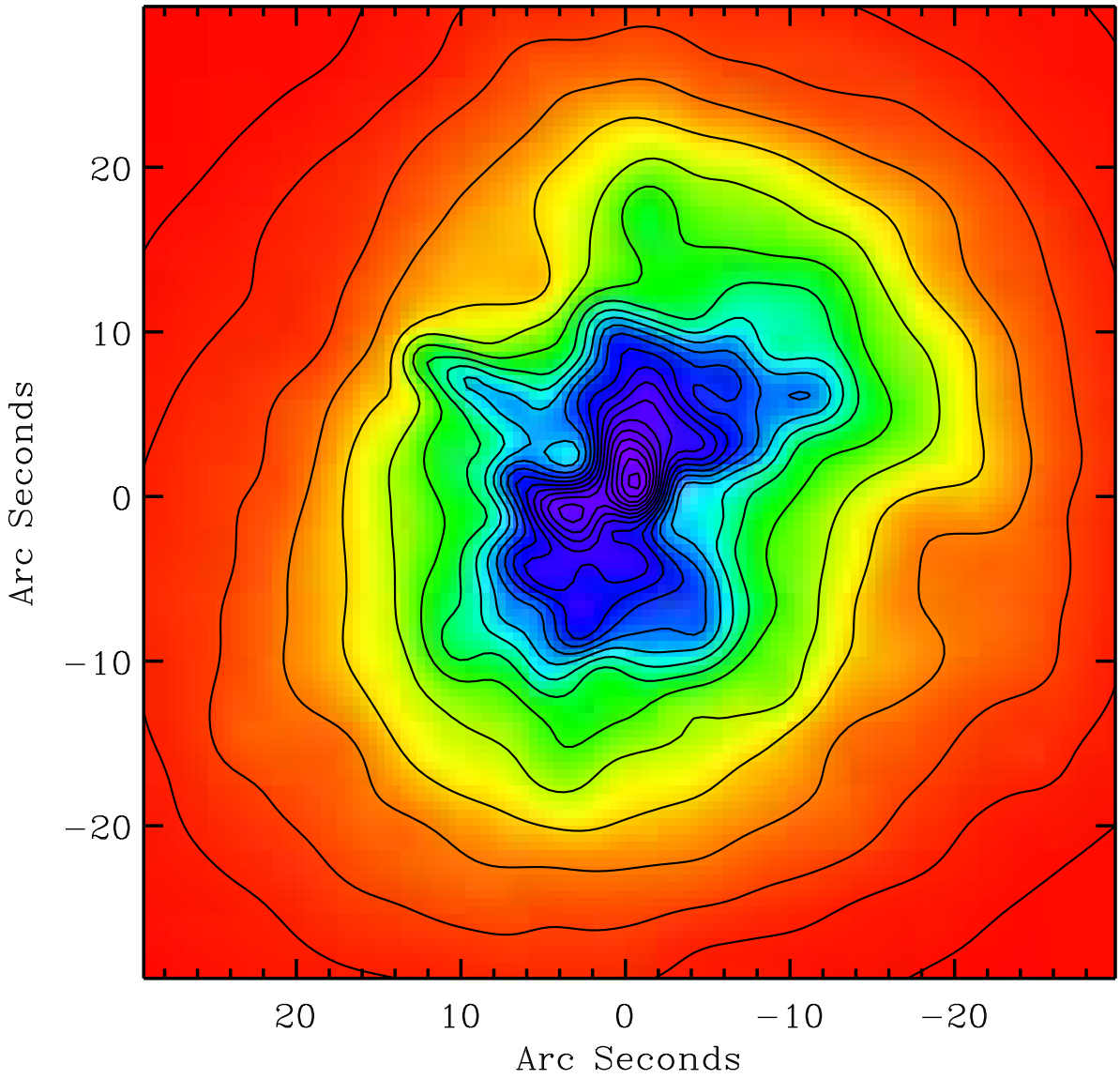

Figure 2.3: X-ray surface brightness map of three merged *Chandra* observations of Abell 2597, for which the combined effective exposure time is 150 ksec. The data have been smoothed with an adaptive Gaussian kernel. Black contours have been overlaid to better show the highly anisotropic inner surface brightness distribution. North is up, east is left. At the redshift of Abell 2597 (z = 0.082), $1''$corresponds to ~ 1.5 kpc, such that the full field of view of the figure is $\sim 90 \times 90$ kpc. Choice of the "rainbow" color map is arbitrary and meant only to aid viewing. "Purple" traces more intense emission, while "orange/red" traces less intense emission.

from the weak point source associated with the AGN. Two sharp deficits of X-ray emission $\sim 2''$ NE and $\sim 2''$ SW define the inner ridges of the "butterfly wings". As noted previously, the major axis along which the X-ray emission is extended strongly aligns with the major axis of the host galaxy stellar isophotes. One of the most prominent features visible in Fig. 2.3 is a $10''$($\sim$ 15 kpc in projection) linear filament extending along a P.A.$\approx 45^{\circ}$, effectively perpendicular to the major axis of the "butterfly" feature and aligned (in projection) with the minor axis of the BCG stellar isophotes (see Fig. 2.1*b*). The western edge of the primary M01 ghost cavity is faintly seen $\sim 18''$ W, $5''$ S of the center.

To enable more detailed investigation into the X-ray morphology we create residual "unsharp mask" images from the 0.5-7 keV *Chandra* data, and present these in Fig. 2.4. The left panel is simply the residual left from subtraction of an elliptical model from the adaptively smoothed version of the image. The "unsharp mask" shown in the right panel employs the edge-enhancement technique described by Fabian (2003), and is made by subtracting a $20''$ Gaussian smoothed image from a $5''$ Gaussian smoothed version. The residual is then divided by the sum of the two smoothed images. In the left panel, regions of X-ray surface brightness excess over the subtracted elliptical background appear in black, while deficits (cavities) appear in white. In the right panel, this color scheme is inverted (excesses are in white, deficits are in black.

In both figures, regions of X-ray excess and deficit define the features discussed above in more detail, and additionally highlight several features not readily apparent from the broadband X-ray image in Fig. 2.3. In the unsharp mask we label and roughly outline the six features we will analyze in detail in this and following sections. Throughout our analysis we will consistently refer to each of these features by a common name and number-based label. They are: (1) the "M01 western ghost cavity", (2) the "C05 X-ray tunnel", (3) the "M01 northern ghost cavity", (4) the "eastern ghost cavity", (5) the "cold filament" (we will discuss why we call it "cold" in later sections), and (6) the "filament base cavity". By comparing counts in like sized regions, we estimate the significance of each of these labeled features to be $\gtrsim 10\sigma$ deficits (in the case of cavities or the tunnel) or excesses (in the case of feature 5, the filament) over the mean. Using the short ($\sim$ 18 ksec) exposure, C05 estimated the significance of features (2) and (6) to be 18σ and 7σ deficits, respectively. Note that, for "historical" reasons (i.e., allowing for direct comparisons with past studies), we label the M01 western ghost cavity and C05 X-ray tunnel as two features (1 and 2, respectively), but we do not mean to imply that they are distinct from one another. The opposite is most likely true, as we discuss below.

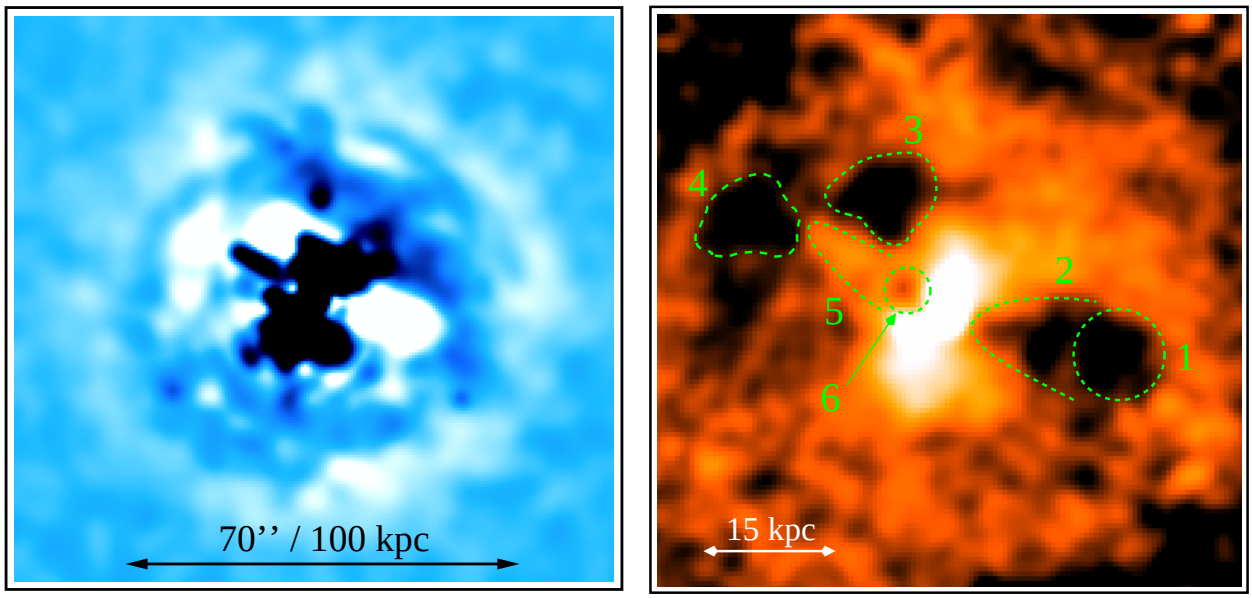

Figure 2.4: Residual and “unsharp mask” maps of the merged 150 ksec *Chandra* 0.5-7 keV observation. The panel at *left* was made via subtraction of a 20″Gaussian smoothed version of the image from the adaptively smoothed version. The unsharp mask at *right* was made by subtracting the same 20″ Gaussian smoothed version of the image from a 5″ Gaussian smoothed version. The difference was then divided by the sum of the two images to rescale. The major morphological features which will be the subject of further spatial and spectral analysis have been labeled 1-5 and outlined in green. Although we label them separately, we do not mean to imply that features 1 and 2 are necessarily discrete, rather, feature 1 is labeled separately to enable a clearer comparison with the McNamara *et al.* (2001) “ghost cavity”. Features 1 and 2 may well be one larger cavity.

2.3.2 Feature (1) and (2) — one large western cavity?

McNamara *et al.* (2001), in their study of the short original *Chandra* image of A2597, described feature (1), the “western ghost cavity”, as a discrete feature which was detached from the center-most regions of X-ray emission. The residual image published by Clarke *et al.* (2005) revealed the so-called “X-ray tunnel” which apparently “connected” (in projection, at least) the M01 cavity to the X-ray surface brightness peak cospatial with the radio core. A simple interpretation, as suggested by Clarke *et al.* (2005), is that the M01 cavity and the “tunnel” simply make up one larger X-ray cavity. As is particularly apparent in the left-most panel of Fig. 2.4, our deeper data unambiguously reveal the M01 and C05 cavities (features 1 and 2) to be one larger cavity ~ 24 kpc in projected length. This changes the interpretation of the AGN outburst history, which we will discuss in later sections. For the remainder of this chapter, we will typically refer to features (1) and (2) together as the “western large cavity”.

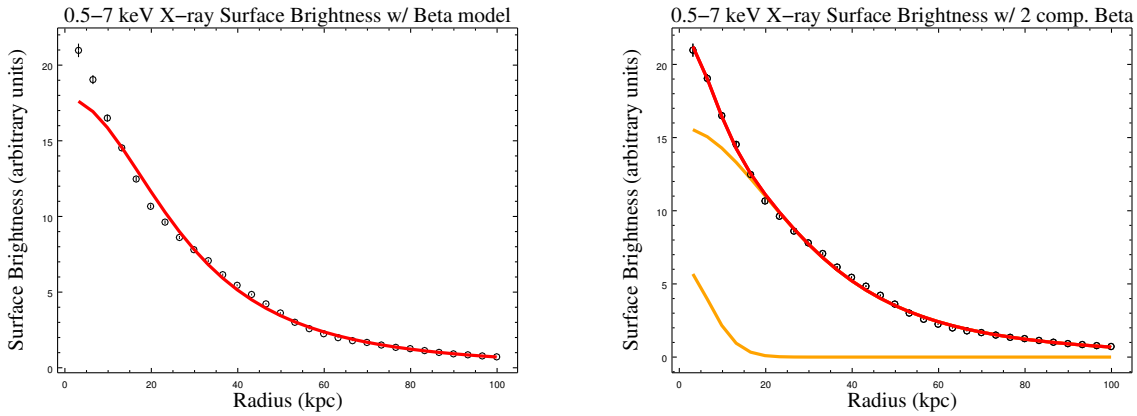

Figure 2.5: X-ray surface brightness profile extracted from a series of concentric annuli spanning from the central regions out to 100 kpc. In the figure at (*left*), a one component beta model has been fit, while in the figure at (*right*), a two-component (additive) beta model has been fit, yielding better overall correspondence to the measured profile. The additive two-component model is in red, while the two individual components to the model are shown in yellow.

2.3.3 X-ray surface brightness profile

In Fig. 2.5 we plot azimuthally summed X-ray surface brightness against projected radius, using fluxes extracted from narrow concentric annuli spanning $\sim 5-100$ kpc (see middle panel in Fig. 2.7). We fit both singular and additive two-component Lorentz 1-D "beta" models with a varying power law (`beta1d` in CIAO Sherpa) to the data, wherein the surface brightness Σ_X at projected radius r varies as

$$\Sigma_X(r) = \Sigma_X(0)\left[1+\left(\frac{r}{r_0}\right)^2\right]^{(-3\beta+1/2)}. \tag{2.1}$$

Here, $\Sigma_X(0)$ is the central X-ray surface brightness and r_0 is the core radius. The model assumes that the galaxies, ambient hot gas, and underlying dark matter halo (assumed to follow a King profile) are hydrostatic and isothermal. β is defined as the ratio of galaxy-to-gas velocity dispersions (effectively energy per unit mass in galaxies divided by that in gas),

$$\beta \equiv \frac{\mu m_p \sigma^2}{kT} \tag{2.2}$$

where μ is the mean molecular weight in amu, m_p is the mass of the proton, σ is the 1-D velocity dispersion, and T is the gas temperature. Typically, the ICM in galaxy clusters is well-fit by models

with $\beta \approx 0.6$ (Sarazin, 1986). Our data are consistent with this: if we fit a one-component beta model, shown in the left panel of Fig. 2.5, we find $\beta = 0.633$ with core radius $r_0 = 16''.4$ (or ~ 24 kpc). A far better fit is obtained with an additive two-component beta model, which we plot in the right panel in Fig. 2.5 (red line). This model consists of a $\beta = 0.686$ fit with a core radius of $r_0 = 19''.1$ (or ~ 29 kpc) and an inner steep component ($\beta = 10$) to fit the cusp (yellow lines). The small deviations between the model and data arise (in part) because the annuli from which the spectra are extracted effectively give an azimuthal average of X-ray fluxes that vary wildly as a function of position angle, owing to the highly disturbed nature of the X-ray gas. In the plots, errors bars are shown, though difficult to see because they are smaller than the data points.

2.3.4 Radio / X-ray correlations

As AGN outflows are thought to be mechanisms by which cavities are created (see Section 1), it is important to revisit the radio/X-ray correlations first discussed in M01 and C05. In Fig. 2.6 we overlay 8.4 GHz, 1.3 GHz, and 330 MHz radio contours in white, blue, and green (respectively), on the X-ray residual image from Fig. 2.4. As noted by M01 and C05, the northern and southern lobes of the 8.4 GHz source (white contours) are bounded to the west and east by deficits of X-ray emission associated with features (6) and (2), respectively. Beyond this, it is difficult to discern whether or not the 8.4 GHz lobes are interacting with the keV gas on these scales. No X-ray cavities are observed to be directly cospatial with the 8.4 GHz lobes, though this lack of evidence should not be interpreted as evidence of absence. Any cavities that may exist on these scales would be very difficult to detect given a combination of (a) the compactness of the radio source compared to the X-ray emission and (b) a great deal of intervening keV gas along the line of sight.

The 330 MHz VLA A-configuration observation (in green contours) does not resolve structures at the scale of the 8.4 GHz source, though a prominent arm of emission extends ~ 70 kpc to the west (projected) in strong spatial correlation with the C05 X-ray tunnel (feature 2 in Fig. 2.4) and the M01 western ghost cavity (feature 1 in Fig. 2.4). The symmetric 50 pc scale VLBA jets of Taylor *et al.* (1999) are approximately aligned (within $\sim 5°$) with the major axis along which the 330 MHz emission extends as well as the long axis of the C05 X-ray tunnel, though this of course involves a comparison at vastly different scales. The relationship between the bent 8.4 GHz source and the 330 MHz emission is difficult to ascertain with the available data, though we will discuss possible scenarios in later sections.

The 1.3 GHz contours in blue, also from Clarke *et al.* (2005), exhibit extensions along the same axis as the 330 MHz eastern extension, the projected VLBA jet axis, the western large cavity, as

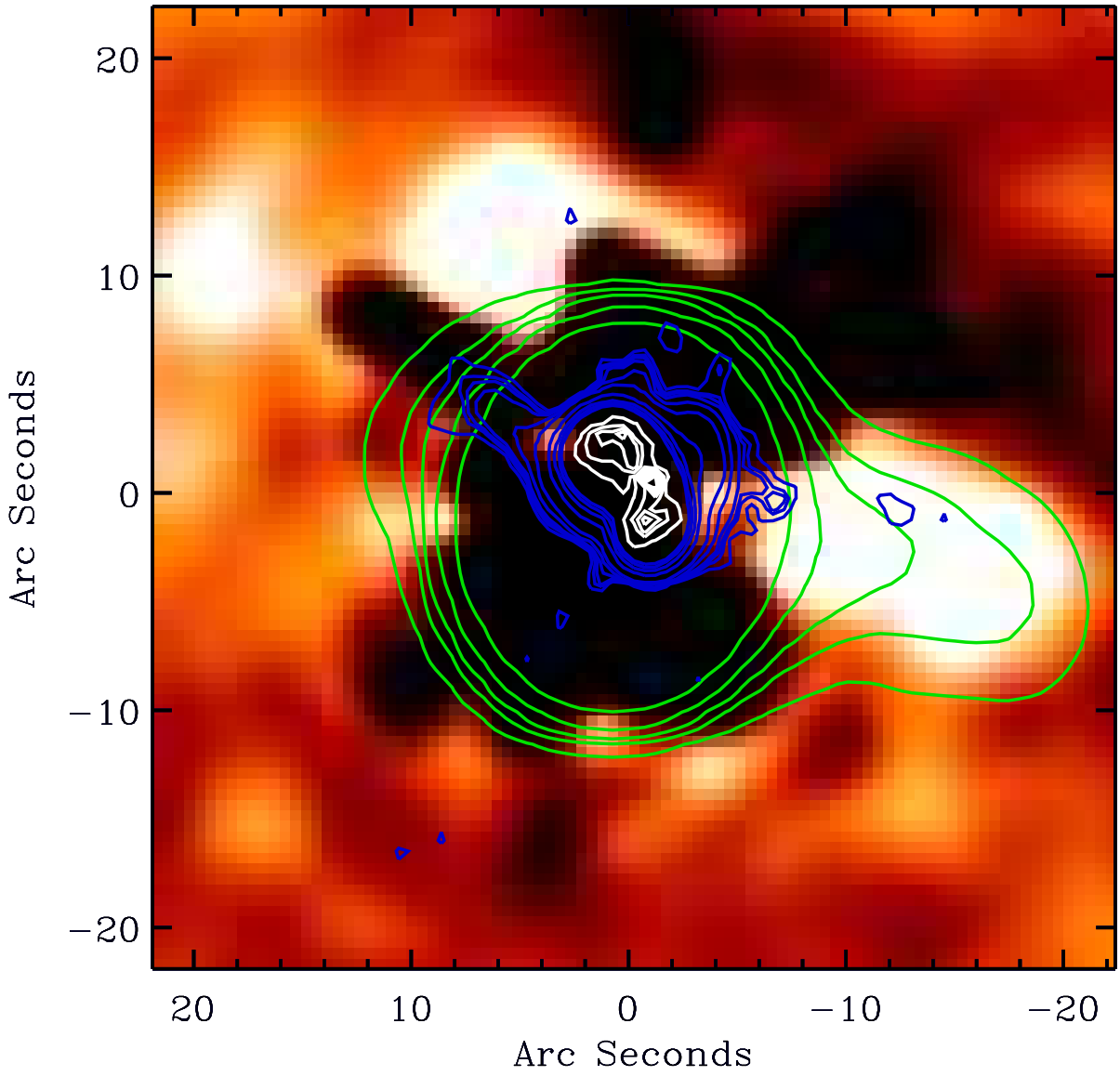

Figure 2.6: Residual image of the merged 150 ks *Chandra* 0.5-7 keV observation, made via subtraction of a 30″ Gaussian smoothed version of the image with the adaptively smoothed version shown in Fig. 2.3. 330 MHz VLA contours from have been overlaid in green, while the 1.3 GHz radio contours are plotted in blue, and the 8.4 GHz radio contours appear in white. All of the radio data is from Clarke *et al.* (2005). Note how the extended 330 MHz emission corresponds in both linear extent and projected P.A. with the apparent X-ray cavity consisting of features (1) and (2), as labeled in Fig. 2.4. Note also that the northeast extension of the 1.3 GHz emission (blue) is aligned with the "bottom" of the 15 kpc linear X-ray filament. Deficits in X-ray surface brightness as compared with the smooth elliptical distribution appear in white, while excesses appear in black.

well as ~ 8 kpc along the "bottom half" of the 15 kpc linear X-ray filament (feature 5). The NE 1.3 GHz extension, which is ~ 15 kpc from the radio core, also covers the "filament base cavity", which we highlight as feature (6) in Fig. 2.4*b*. There is also a ~ 1 kpc extension to the SW, into the "bottom opening" of the western large cavity. The projected spatial coincidence of all of these features is strong evidence for a common, "current" jet axis. While the P.A. of the 8.4 GHz source is offset from this axis, it is the exception, and may arise from dynamical frustration of the jet as it propagates amid the dense molecular medium harboring the 10 kpc emission line nebula. That the 1.3 GHz emission is extended along the bottom edge of the 15 kpc X-ray filament (feature 5 in Fig. 2.4) may be evidence for dredge-up of low-entropy keV gas amid propagation of the radio source, a possibility we will investigate in later sections. Oonk *et al.* (2010) reported reported high velocity dispersion ($\sim 200-300$ km s^{-1}) streams of H_2 and H II coincident with the southern edge of the northern 8.4 GHz radio lobe and approximately aligned with the projected VLBA jet axis, were one to extend it from pc to kpc scales (Taylor *et al.*, 1999). This could be interpreted as further evidence for kinematical interaction (e.g., mass entrainment) between the jet and the gas through which it is propagating.

Our new X-ray data do not necessarily aid in discriminating between these and other scenarios, though it is worth noting that the close projected alignment of (1) the western large cavity, (2) the 15 kpc linear X-ray filament, (3) the extended "arms" of the 1.3 GHz and 330 MHz radio emission, (4) the projected current VLBA jet axis and (5) the high velocity molecular gas stream in the Oonk *et al.* (2010) data may stem from common dynamical processes arising from propagation of the radio jet. We will investigate this possibility further in later sections.

2.4 X-ray Spectral Analysis

Our deeper (> 120 ksec of good time) *Chandra* observations enable more detailed spectral analysis than was previously possible with the original *Chandra* exposure used in M01 and C05, which was badly impacted by flaring events (as noted before, only 18 ksec of the original 40 were suitable for spectral analysis). In this section, we present an updated analysis that includes, for the first time (a) detailed spectral fitting of the total X-ray spectrum, (b) radial profile analysis using "onion-skin" spectral deprojection and, most significantly, (c) 2-D spectral/spatial maps of the projected temperature, emission measure, and pressure distributions for the central regions of the BCG. We present these results in order below.

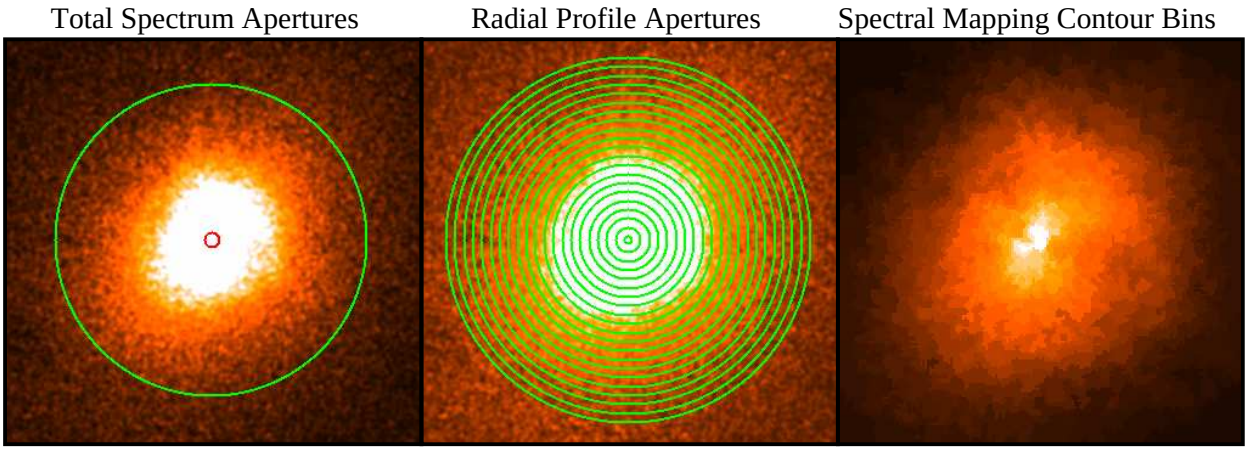

Figure 2.7: (*left*) The circular aperture from which the 0.5-7 keV X-ray spectrum was extracted. The extraction radius, in green, extends to 100 kpc. The weak central point source, outlined by the inner red circle, was removed prior to spectral extraction so as to remove any non-thermal components that would otherwise contaminate modeling of the intracluster thermal plasma; (*middle*) concentric annular regions used for extraction of spectra used in radial profile modeling; (*right*) the spatially binned image created by the `CONTBIN` algorithm of Sanders (2006). 277 individual regions were created from this technique, defined such that (a) a S/N threshold of 30 is met and (b) their length can not be more than twice their width. These bins were used to create region files which were mapped to the two individual *Chandra* exposures used in the creation of 2D spectral maps. See §2.5 for more information. The field of view of this figure is $80'' \times 80''$. East is left, north is up.

2.4.1 Total 0.5-7 keV spectrum

From each of the three GTI filtered observations, a spectrum was extracted from a single $63.3'' \sim$ 100 kpc aperture encompassing most of the source emission (see Fig. 2.7*a*). Prior to this, compact contaminant sources associated with other cluster members were removed, as was the very central region harboring the weak X-ray point source coincident with the radio core. The spectra were extracted using the CIAO 4.2 script `specextract`, and count-weighted response matrices were generated for each extraction.

Using simultaneous fitting techniques in XSPEC version 12.5 (Arnaud, 1996), we fit a variety of models to the total 0.5-7 keV spectrum extracted from the 100 kpc aperture. The most simple of these is a Mewe-Kaastra-Liedahl thermal plasma model (`MEKAL` in XSPEC) that has been absorbed to account for attenuation by the galactic hydrogen column (`WABS` $\times$ `MEKAL`). We also fit absorbed two-component `MEKAL` models (`WABS` $\times$ [`MEKAL` + `MEKAL`]) as well as the standard cooling flow model in XSPEC (`WABS` $\times$ `MKCFLOW`). In all cases, the source redshift was fixed to $z = 0.08$, and the gas temperature kT and `MEKAL` or `MKCFLOW` normalization N was allowed to

Table 2.2. **Single Aperture Fits to Total X-ray Spectrum**

XSPEC Model (1)	$N_{\rm H}$ (10^{20} cm^{-2}) (2)	$kT_{\rm low}$ (keV) (3)	$kT_{\rm high}$ (keV) (4)	Abundance (solar) (5)	MEKAL Norm. ($\times 10^{-2}$) (6)	MKCFLOW $\dot{M}$ ($M_\odot$ yr^{-1}) (7)	red. chi sq. (χ^2/dof) (8)
WABS × MEKAL	1.5 ± 0.12	···	3.42 ± 0.02	0.43 ± 0.01	1.501 ± 0.009	···	745/735 = 1.014
WABS × MEKAL	1.63 ± 0.19	···	3.39 ± 0.04	(0.4)	1.524 ± 0.008	···	754/736 = 1.025
WABS × MEKAL	(2.48)	···	3.31 ± 0.03	(0.4)	1.55 ± 0.005	···	807/737 = 1.096
WABS × [MEKAL + MEKAL]	(2.48)	2.68 ± 0.13	6.01 ± 1.05	(0.4)	1.10 ± 1.52 & 4.57 ± 2.06	···	759/735 = 1.032
WABS × MKCFLOW	(2.48)	1.88 ± 0.07	5.33 ± 0.16	(0.4)	···	497 ± 33	763/736 = 1.04
WABS × MKCFLOW	1.59 ± 0.17	1.87 ± 0.08	5.61 ± 0.17	(0.4)	···	454 ± 29	707/735 = 0.96

Note. — Examples of simultaneous spectral fitting to 0.5-7.0 keV X-ray spectra extracted from a single 100 kpc source aperture encompassing the bulk of the emission in the *Chandra* observations 6394 and 7329. Prior to extraction, a temporal filter was applied to the data to reject flaring events, and compact sources associated with other cluster members as well as the central weak point source associated with the AGN was removed. The spectra were rebinned using to a 30 count threshold. Observation 922 has been excluded from spectral analysis due to significant flaring events and high background levels. One sigma confidence intervals are shown on fit parameters. Parameters that have been frozen to a specific value prior to fitting are shown in parentheses.

vary. We alternated between fixing and freezing the galactic hydrogen foreground column $N_{\rm H}$ and the gas abundance Z. $N_{\rm H}$ was sometimes frozen to the galactic value (2.48×10^{20} cm^{-2}), and fits in which it was allowed to vary always returned best-fit values that were below this, indicative of a soft excess that may arise from the cool core. Allowing the abundance parameter Z to vary almost always found best fit values very near to 0.4 (for example, 0.397 ± 0.01 solar, in the case of the simple absorbed MEKAL). Fixing $Z = 0.4$ sometimes resulted in a marginal improvement reduced chi squared.

Results from this model fitting strategy are presented in Table 2.2. As evident in column (8) of that table, the fits are uniformly excellent in terms of reduced χ^2, indicative of the degeneracy that almost always arises from this type of X-ray spectral fitting. Regardless, excepting the MKCFLOW normalization, the best-fit values are physically reasonable and consistent with those from M01. The MKCFLOW normalization is the X-ray predicted mass deposition rate $\dot{M}$ in units of $M_\odot$ yr^{-1}. This parameter is a relic from the uninhibited cooling flow model, and has more historical significance than it does physical significance. In reality, high spectral resolution X-ray spectroscopy from *XMM-Newton* is needed to better characterize what evidence there may (or may not) be for a cooling flow. Morris & Fabian (2005) presented that data, which we will discuss in later sections. In Fig. 2.9 we present the best-fit absorbed MEKAL model we obtained (in terms of chi squared), for which $kT = 3.42 \pm 0.2$ keV, $Z = 0.43 \pm 0.01$, and $N_H = (1.5 \pm 0.12) \times 10^{20}$ cm^{-2}. These best-fit values reflect averages of phase-mixed gas within this 100 kpc aperture.

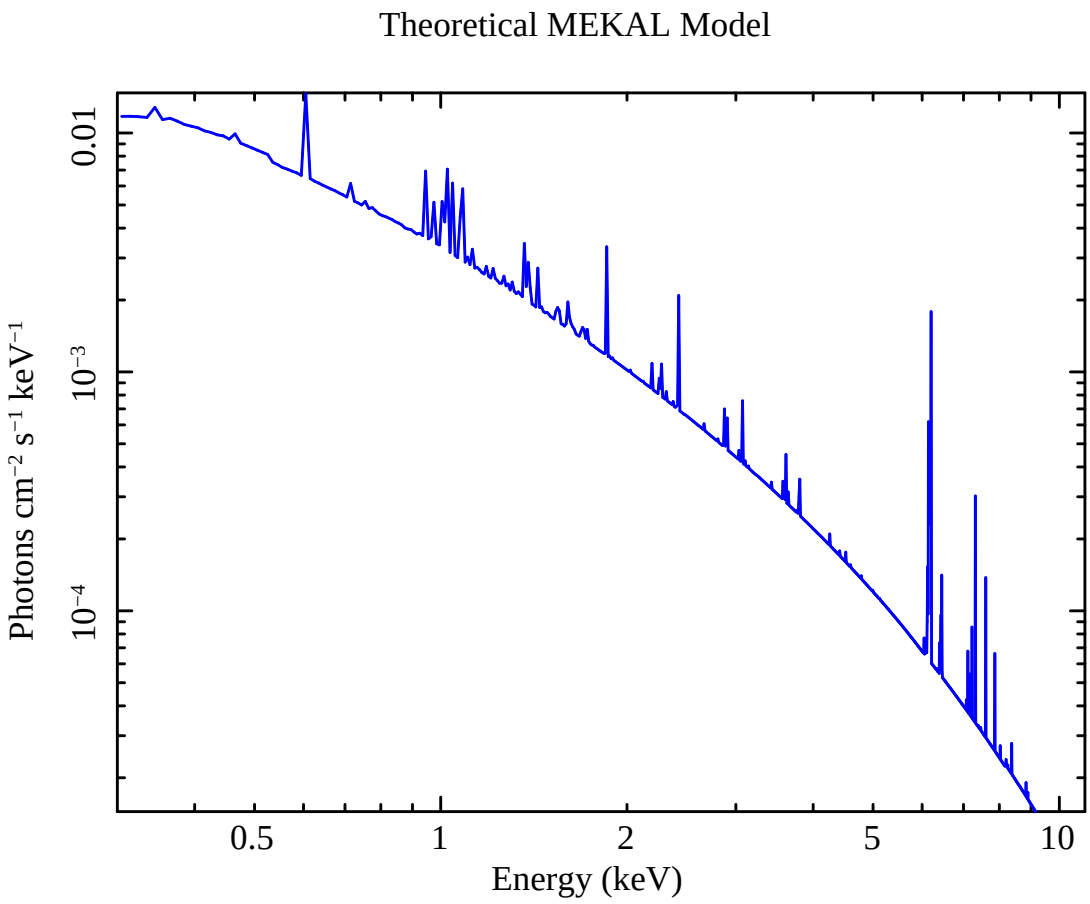

Figure 2.8: The theoretical MEKAL collisional plasma model, based upon the coronal approximation (ionization balance).

2.4.2 Radial Profiles and Spectral Deprojection

We obtain radial profiles of best-fit spectral parameters by extracting spectra from a series of 20 concentric circular annuli with a 1″.5 inner radius, 3″.6 stacking increment, and 74″ outer radius (see Fig. 2.7*b*). As before, the extracted spectra from ObsIDs 7329 and 6934 are fit simultaneously in XSPEC.

Spectral deprojection

Of course, the spectra fit from these annuli do not sample a 2D "cross section" like the extraction region implies: all fit spectral parameters represent an emission-weighted superposition of properties from the line of sight extending through a 3D distribution of thermal plasma. One may roughly

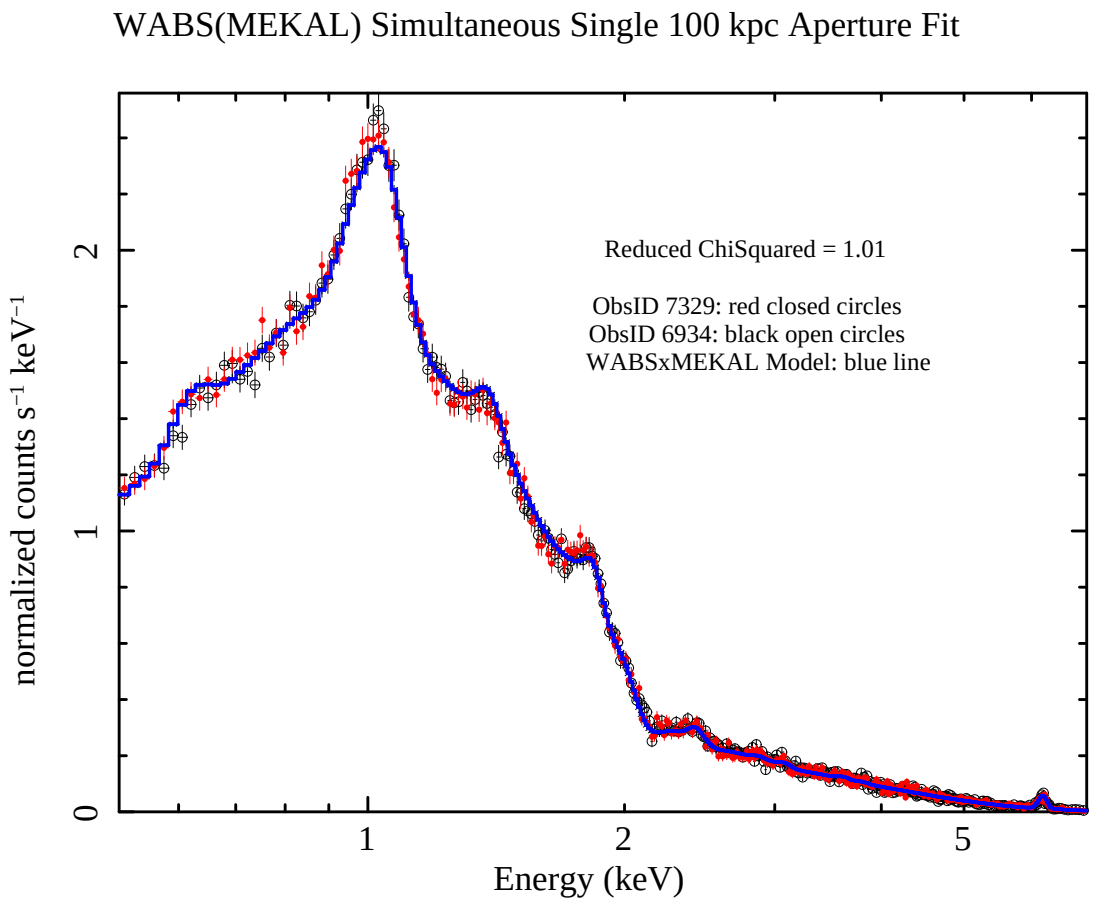

Figure 2.9: 0.5-7 keV X-ray spectrum of Abell 2597, extracted from *Chandra* observations 6394 (black open circles) and 7329 (red closed circles) from an identical 63″/100 kpc source aperture, centered on the central weak point source. The spectra have been grouped using a 30 count bin size. Background subtraction and removal of contaminating sources has been performed. Using the XSPEC package (v. 12.5), a simple absorbed thermal plasma model (blue solid line) has been fit (WABS×MEKAL). The hydrogen absorbing column ($N_{\rm H}$), temperature (kT), abundance, and normalization have been allowed to vary, while the redshift of the source has been fixed to z = 0.08. *Chandra* observation 922 has been excluded from this analysis due to significant flaring events. The best-fit $N_{\rm H}$ value is below that of the MW absorbing column, possibly due to a soft excess intrinsically associated with the source (relative to the prediction of the simple MEKAL model). See the first entry in Table 2.2 for model parameters associated with this fit.

account for these projection effects with the "onion peeling" spectral deprojection technique commonly employed in the literature (e.g., Jetha *et al.*, 2005; Russell *et al.*, 2010). Here the ICM is modeled as a series of concentric spherical shells, such that a geometric weight may be applied to the radial profiles in an attempt to account for blended contributions from inner and outer shells. Of course, assuming that the ICM is a sphere is spurious at best, and almost certainly incorrect for the highly anisotropic inner X-ray surface brightness distribution in A2597 (see Fig. 2.3). It is nonetheless a worthwhile exercise, the results from which we present below.

A script was used to iteratively extract the spectra (both source and background) from each of the 20 annuli. Weighted response matrices were generated. The background-subtracted spectrum from each annulus was then iteratively fit with an absorbed `MEKAL` model (N_H, Z, and z were frozen to the appropriate values). The CIAO *Sherpa* module `deproject` was used to enact the onion peeling technique. Often, severe unphysical radial profile oscillations can result from the radial binning process in spectral deprojection, due to the multiphase nature of the gas and its arrangement in non-spherical distributions that are azimuthally averaged under the assumption of spherical symmetry. The effect is more severe at larger radii, where the bins sample ever larger spatial cross sections of the gas. The method developed by Russell *et al.* (2008) alleviates many of these issues, however, our profiles cover only the inner 100 kpc of the cool core, so the differences were negligible as the oscillations were not severe in the first place. Furthermore, little difference was noted between the deprojected spectra and the "default" projected spectra. Nevertheless, because (a) little difference was noted and (b) the innermost regions of the X-ray emitting gas are permeated by a network of cavities and other spatial anisotropies, we choose to show and discuss only the *projected* gas profiles throughout the remainder of this analysis. The central X-ray surface brightness is so highly anisotropic that the assumption of spherical symmetry is not reasonable. Rather than arbitrarily add unquantifiable uncertainty to our data by assuming everything to be a perfect spherical shell (which it most certainly is not), we instead show the data "as is", with the caveat that all profiles shown are of *projected* gas properties.

Temperature

In Fig. 2.10*a* we show the projected temperature (kT) profile out to 100 kpc. The projected temperature drops from ~ 3.8 keV at ~ 100 kpc to ~ 2.6 keV in the central few kpc. We outline the region permeated by X-ray cavities, and note that the temperature gradient is steepest within that region. While this could be interpreted as evidence for AGN feedback heating in this region, as would be expected theoretically, the radial binning of highly anisotropic X-ray emission in this

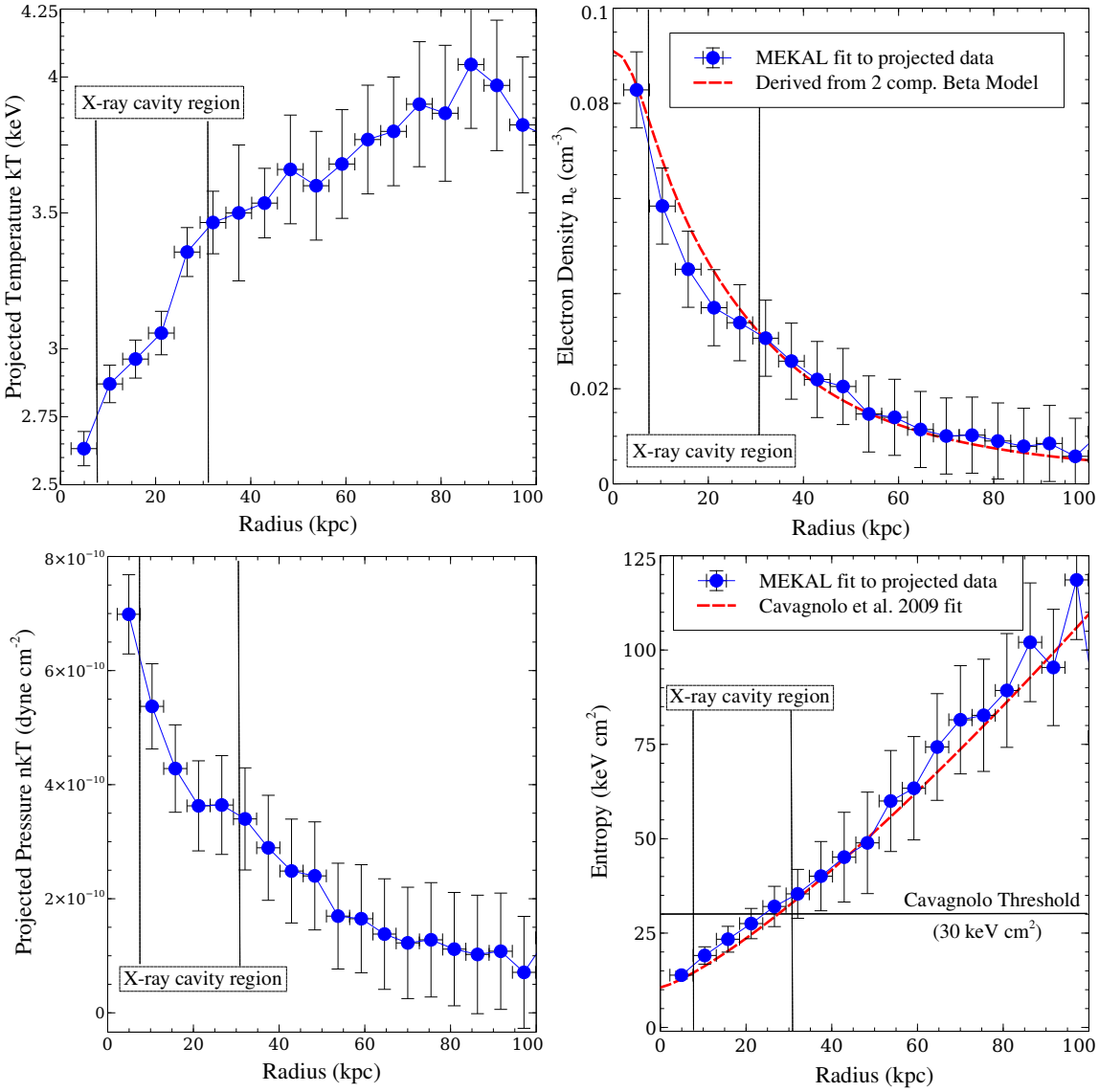

Figure 2.10: (*top left*) Projected temperature and (*top right*) projected density profiles derived from MEKAL thermal plasma models fit to radially extracted spectra from the inner 100 kpc of A2597. The temperature kT is a fit parameter from the MEKAL model. The electron density (n_e) was derived from the MEKAL normalization, while the pressure (P) and entropy (S) profiles, shown at (*bottom left*) and (*bottom right*), were calculated using $P = nkT$ (assuming $n = 2n_e$) and $S = kT\,n_e^{-2/3}$, respectively. In each profile we mark the ~ 25 kpc region permeated by the X-ray cavity network. Independent consistency checks on the electron density and entropy profiles are plotted in red. In the electron density plot, the consistency check is from the two-component additive beta model fit to the X-ray surface brightness profile. In the entropy profile, we plot the best-fit entropy profile from Cavagnolo *et al.* (2009). All of our profiles are consistent with past X-ray results (McNamara *et al.*, 2001; Morris & Fabian, 2005).

region will also significantly add to scatter in the overall gradient. It should also be noted that, although the temperature profile predictably declines from the outer regions inwards toward the core, this should not be mistaken as evidence for a cooling flow. As the name implies, entropy loss within the cooling radius is associated with a loss of heat, but this does not necessarily mean that the *temperature* of the gas should decrease inwards as a direct result of a cooling flow, if one exists at all. Rather, the gas will cool only if its initial temperature is greater than the local virial temperature of the underlying gravitational potential. When the two temperatures are equal, gravity will "take over", and adiabatic compression associated with the release of gravitational energy will act as a thermostat for the gas, keeping it at roughly the local virial temperature. In light of this, we choose not to draw any conclusions relative to cooling flows from our derived temperature profile (preferring instead to defer to high resolution *XMM-Newton* spectroscopy, which we will discuss below). It is likely that the temperature profile in Fig. 2.10*a* is merely a reflection of the flattening gravitational potential as the BCG begins to dominate over the cluster potential at the innermost radii.

Density and pressure

The MEKAL normalization $N_{\rm MEK}$ is given by

$$N_{\rm MEK} = \frac{10^{-14}}{4\pi D_a^2 (1+z)^2} \int n_{\rm H} n_e dV \tag{2.3}$$

where D_a is the angular diameter distance to the source in cm (which for the A2597 BCG is $\sim 9.716 \times 10^{26}$ cm or ~ 314.9 Mpc), z is the redshift ($z = 0.08$), and n_H, n_e are the hydrogen and electron densities, respectively, in cm^{-3}. Note that the MEKAL normalization is simply the emission measure (EM= $\int n_{\rm H} n_e dV$ in units of cm^{-3}) of the source scaled by its distance (specifically, $N_{\rm MEK} = {\rm EM} \times 10^{-14}/[4\pi D_a^2 (1+z)^2]$). For our purposes, it is sufficient to assume that $n_e = 1.18 n_{\rm H}$, appropriate for a fully ionized gas with $X = 0.7$ and $Y = 0.28$ hydrogen and helium mass fractions, respectively (e.g., Jetha *et al.* 2005). Assuming the MEKAL normalization is fit over a volume V, the electron density may therefore be obtained from the best-fit MEKAL normalization by

$$n_e = \left\{ \frac{4\pi [D_A (1+z)]^2 N_{\rm MEK}}{1.18 \times 10^{-14} V} \right\}^{\frac{1}{2}}. \tag{2.4}$$

Subsequently, the density can be used in concert with the best-fit temperature to calculate the pressure $p = nkT$ (assuming $n = 2n_e$) and entropy $S = kT n_e^{-2/3}$.

Following this method, in Fig. 2.10*b* and *c* we show the projected electron density (n_e) and pressure (nkT) profiles, respectively. Our best-fit projected electron density declines from 0.09 cm^{-3} in the innermost annulus to 0.01 cm^{-3} at 100 kpc. Our best-fit projected pressure profile declines from 7×10^{-10} dyn cm^{-2} in the innermost annulus to $\sim 1 \times 10^{-10}$ dyn cm^{-2} at 100 kpc. In the analysis by M01 of the 922 observation, density and pressure reached central values of $0.07-0.08$ cm^{-3} and 2.5×10^{-10} dyn cm^{-2}, respectively. Sarazin *et al.* (1995), using *ROSAT* data, found a value for the central X-ray pressure of 6×10^{-10} dyn cm^{-2} within a radius of 5 kpc. Our value of 7×10^{-10} dyn cm^{-2} is consistent at the same radius. We note that the derived central X-ray pressure is comparable to the estimated pressure of the $10^4 - 10^5$ K gas on 10 kpc scales ($\sim 5.5 \times 10^{-10}$ dyn cm^{-2}), implying that the two phases are in pressure equilibrium (Koekemoer *et al.*, 1999). Sarazin *et al.* (1995) estimated the pressure of the northern radio lobe to be $\sim 1.7 \times 10^{-9}$ dyn cm^{-2}, which would suggest that the radio lobe is somewhat overpressured with respect to the 10^4 K and 10^7 K ambient gas. We will discuss this in more detail in later sections.

An independent check on our radial profiles of density and pressure can be obtained from the beta model fit to the X-ray surface brightness profile, discussed in Section 2.3.3. The beta model form for X-ray emissivity can be converted to electron density using

$$n_e(r) = n_e(0)\left[1+\left(\frac{r}{r_0}\right)^2\right]^{(-3\beta/2)}. \tag{2.5}$$

Using our best-fit two component beta model, we plot (in red) the above form for electron density over our density profile in Fig. 2.10*b*. There is close agreement between the two profiles, particularly in terms of the two extrema at ~ 5 and 100 kpc. The most significant deviation between the two profiles is found in the region permeated by X-ray cavities (between $\sim 5-30$ kpc), which we also outline in the plot. X-ray emissivity scales positively with gas density, so X-ray surface brightness deficits (cavities) are associated with lower density gas (bubbles). It is therefore not surprising that the region in which the two profiles disagree the most is also the region permeated by the X-ray cavity network, which the beta model does not directly take into account (though it does indirectly, as X-ray surface brightness is lower there).

Entropy

In Fig. 2.10*d* we show the projected entropy ($kTn_e^{-2/3}$) profile, which rises from a central value of ~ 15 keV cm^2 at 5 kpc to ~ 115 keV cm^2 at 100 kpc. Entropy is one of the most important

physical quantities dictating the structure and density of the ICM, and is unique in its ability to encode and preserve the thermodynamic history of the gas (e.g., Voit 2005, and references therein). Considered alone, temperature and density fail in this regard, as the temperature largely reflects the underlying gravitational potential well, and the density reflects the degree to which gas is compressed within the well. Entropy, however, only changes via gains or losses of heat energy, and breaks the degeneracy with the underlying potential because at constant pressure, the density of the gas is determined by its specific entropy.

Our derived entropy profile is consistent in terms of values with cool core clusters in general, though lacks a significant "plateau" at small radii that sometimes characterizes these systems (e.g., Voit, 2005; Cavagnolo *et al.*, 2008, 2009). As an independent consistency check, in red we overplot the fit to the 922 dataset (from M01) made by Cavagnolo *et al.* (2009), who used a simple power law,

$$S(r) = S_0 + S_{100}\left(\frac{r}{100\ \mathrm{kpc}}\right)^{\alpha}. \tag{2.6}$$

The Cavagnolo *et al.* (2009) best fit values were $S_0 = 10.60 \pm 1.52$ keV cm^2, $S_{100} = 98.8 \pm 15.18$ keV cm^2, and $\alpha = 1.26 \pm 0.19$. We plot this best-fit in red over our data in Fig. 2.10*d*, and find that the two profiles are consistent. We note a very marginal flattening of the entropy profile from our data (in blue) in the region permeated by X-ray cavities. We do not, however, observe a significant entropy "plateau" characteristic of CC clusters in general.

Comparison of spectral results with other observations

The X-ray derived cooling time for A2597 has been presented several times in the literature using a variety of datasets. By far the best constraints on cooling of the X-ray gas come from high spectral resolution *XMM-Newton* Reflection Grating Spectrometer (RGS) observations, which are capable of resolving the critical X-ray coolant lines stemming from < 1 keV gas. Morris & Fabian (2005) presented the *XMM-Newton* data for A2597, detecting Fe VIII $15-17$ Å thermometer lines characteristic of ~ 0.3 keV gas. These line fluxes were compared to those predicted by classical cooling flow models, and the data were found to be consistent with a mass deposition rate on the order of 100 $M_{\odot}$ yr^{-1} within a radius of 130 kpc. Results from the European Photon Imaging Camera (EPIC) aboard *XMM-Newton* were also consistent with this mass deposition rate, suggesting that A2597 may be associated with a moderately strong cooling flow.

The results of Morris & Fabian (2005) were consistent with *FUSE* FUV spectroscopic observa-

tions of A2597 presented by Oegerle *et al.* (2001). That work found O VI λ1032 Å emission with an inferred luminosity of 3.6×10^{40} ergs s^{-1}. The O VI λ1032 Å resonance line is characteristic of gas at $\sim 3 \times 10^5$ K, and comparing its luminosity to a cooling flow model yielded a UV-derived mass deposition rate of $\sim 40\ M_\odot$ yr^{-1} within the *FUSE* effective radius of 40 kpc. Extrapolating outwards, this result is consistent with the *XMM-Newton* mass deposition rate of $\sim 100\ M_\odot$ yr^{-1} at 100 kpc. Note, however, that just because tracers of 10^5 K gas have been detected, it is not necessarily direct evidence of a cooling flow. A conductive thermal interface between 10^7 K gas and embedded 10^4 K gas phases would establish a temperature gradient which would naturally include at 10^5 K component. Sparks *et al.* (2009) recently detected a C IV resonance line emission filament in M87 which is also a tracer of 100,000 K gas, and interpreted the result in the context of conduction models. Oonk *et al.* (2011) enacted a similar search for C IV emission in A2597, but did not detect any.

As *Chandra* lacks the spectral resolution to resolve the critical coolant lines for < 1 keV X-ray gas, we will not comment on cooling in interpreting our results. We note, however, that our results are consistent with those from *XMM-Newton* RGS spectroscopy, as reported by Morris & Fabian (2005). For example, our profiles from $5-100$ kpc span $2.6-4$ keV, $0.08-0.01$ cm^{-3}, and $15-115$ keV cm^2 in temperature, electron density, and entropy, respectively. Over the same span in radius, the *XMM-Newton* temperature, density, and entropy profiles span $2.7-4$ keV, $0.08-0.01$ cm^{-3}, and $10-100$ keV cm^2, respectively. Clearly, our results from *Chandra* are very consistent with those from *XMM-Newton*.

2.4.3 Hardness analysis

In Fig. 2.11 we show soft (0.5-1 keV) through hard (2-7 keV) cuts in energy space for the adaptively smoothed 150 ksec *Chandra* image. In each panel we overlay the 8.44 GHz radio map in black contours, which for reference is ~ 10 kpc from end-to-end. The previously mentioned 15 kpc linear NE filament becomes fainter at successively harder slices in energy space, and effectively disappears in the rightmost panel. The filament is therefore a soft excess, and is likely to be colder than the surrounding gas. The "butterfly" feature also loses much of its NE-SW extension at higher energies while retaining effectively the same extension along the NW-SE axis that is aligned with the major axis of the BCG stellar isophotes.

Soft X-ray emission along lines of sight that pass through the galaxy midplane suffers more attenuation from the intrinsic hydrogen column than does hard X-ray emission. Moreover, as the line of sight moves away from the projected midplane, the absorbing hydrogen column gets smaller,

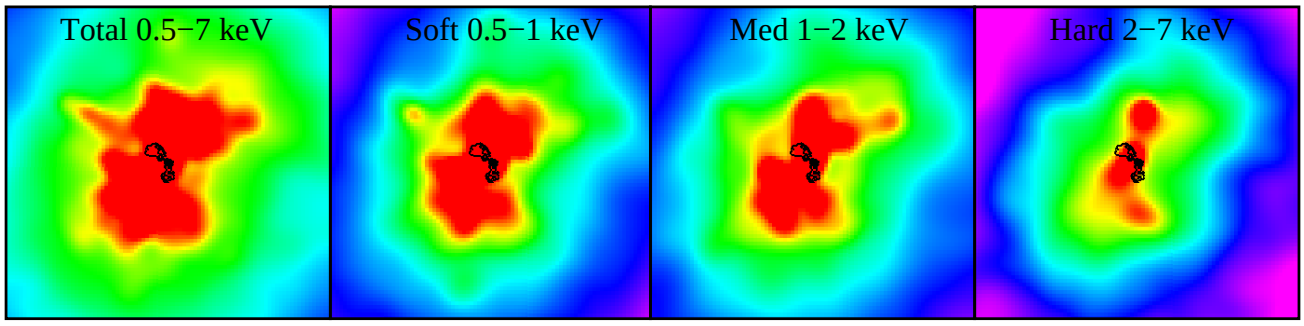

Figure 2.11: 150 ksec adaptively smoothed *Chandra* image of A2597 at various "slices" in energy space, including (from left to right) "total" (0.5-7 keV), soft (0.5-1 keV), "medium" (1-2 keV), and "hard" (2-10 keV) emission. In black contours, we overlay the 8.44 GHz radio contours of PKS 2322-122, which from end-to-end is ~ 10 kpc. Note that the bright linear filament which extends 15 kpc NE from the center in the "total" and "soft" panels is effectively absent in the rightmost "hard" panel. The filament is therefore a soft excess, and is colder than the surrounding gas. The hard X-ray "disk" evident in the rightmost panel is aligned in projection with the isophotal major axis of its host galaxy's stellar component.

resulting in smaller hardness ratios. It is therefore difficult to break the degeneracy between (a) true spatial distribution of soft vs. hard X-ray emitting gas and (b) preferred soft-end absorption by the BCG's hydrogen column. We will therefore not comment on whether or not the apparent hard excess "disk" aligned with the BCG stellar midplane represents a true spatial excess of hotter keV gas. This is certainly possible, and similar hard X-ray disks have been observed before in elliptical galaxies (e.g., Statler & McNamara, 2002). The hard excess associated with the projected midplane could be a reflection of higher local virial temperatures than those at higher galactic latitudes.

2.5 X-ray Spectral Maps

We have used our spatially resolved *Chandra* spectroscopy to create 2D maps of projected gas properties such as temperature and pressure. The combined 150 ksec image was cleaned of contaminating point sources, cropped to include only the inner $80'' \times 80''$ (120×120 kpc), then passed through the `CONTBIN`[1] adaptive binning algorithm described by Sanders (2006). The code locates the brightest pixel in the image and creates a spatial bin around it by including all neighboring pixels of like surface brightness until a user-defined signal-to-noise threshold is met. We set this threshold to be S/N≈ 30, or > 1000 counts. The shape of each spatial bin was constrained so that

[1] `http://www-xray.ast.cam.ac.uk/papers/contbin/`

its length could be at most two times its width (to prevent "stripe"-like bins which would sample an unreasonably large spatial cross section of phase-mixed cluster gas). The result is a spatially binned image that closely follows the surface brightness distribution (see Fig. 2.7*c*). In addition to the contour binned image, the algorithm creates a bin map which we used with J. Sanders' `make_region_files` code to create CIAO-compatible region files for each of the 277 individual spatial bins created for our image by the `CONTBIN` code. The individual `level=2` event files for *Chandra* ObsIDs 6934 and 7329 (which were similarly cleaned of point sources) were then spatially reprojected to identical positions using the merged image as a coordinate reference. The region files created from the bin map were then ported to each of the two event files. A script was used to iteratively extract the source spectrum, background file, and create associated response files (ARF/RMF) for each of the 277 spatial regions on each of the two event files. The corresponding source and background spectra from like regions on the two exposures were then added together using the `mathpha` tool in CIAO, and average responses were created using `addarf` and `addrmf`. This procedure is only viable if the exposures were taken on the same chip (which is true for ObsIDs 6934 and 7329). The summed spectra were then regrouped to 15 count bins, and the `BACKSCAL` and `EXPOSURE` header keywords were updated.

An XSPEC TCL script was used to fit absorbed single temperature `MEKAL` models (`WABS` $\times$ `MEKAL`) simultaneously to the two grouped spectra extracted from each of the matched regions of the two exposures. For each fit, the source redshift was fixed to $z = 0.08$, $N_{\rm H}$ was frozen to the galactic value (2.48×10^{20} cm^{-2}), and kT and $N_{\rm MEK}$ were allowed to vary. The fits were run iteratively to minimize the χ^2 statistic. The best-fit parameters kT, $N_{\rm MEK}$ (effectively the emission measure), gas abundance Z, and their corresponding upper and lower 90% confidence intervals were written to individual text files named for their corresponding spatial bin. J. Sanders' script `paint_output_images` was then used to rescale the spatial bins in the merged 150 ksec `CONTBIN` output image by their corresponding best-fit parameters, producing temperature, emission measure, and abundance maps. A projected "fake pressure" map was then created by multiplying the square root of the emission measure map (which is proportional to but not exactly the density, which requires an uncertain volume assumption) by the temperature (kT) map. The maps were then adaptively smoothed with a variable-width Gaussian kernel to reduce noise.

In Fig. 2.12 we present the projected X-ray temperature map. We overplot the adaptively smoothed X-ray surface brightness contours in black. The color map encodes the best-fit single `MEKAL` gas temperature by the scale at the right of the figure. We map only the innermost $\sim 75 \times 75$ kpc of the cluster. We first note that the overall temperature gradient is reasonably consistent with the projected temperature profile (Fig. 2.10*a*) over this spatial range (e.g., 25″or

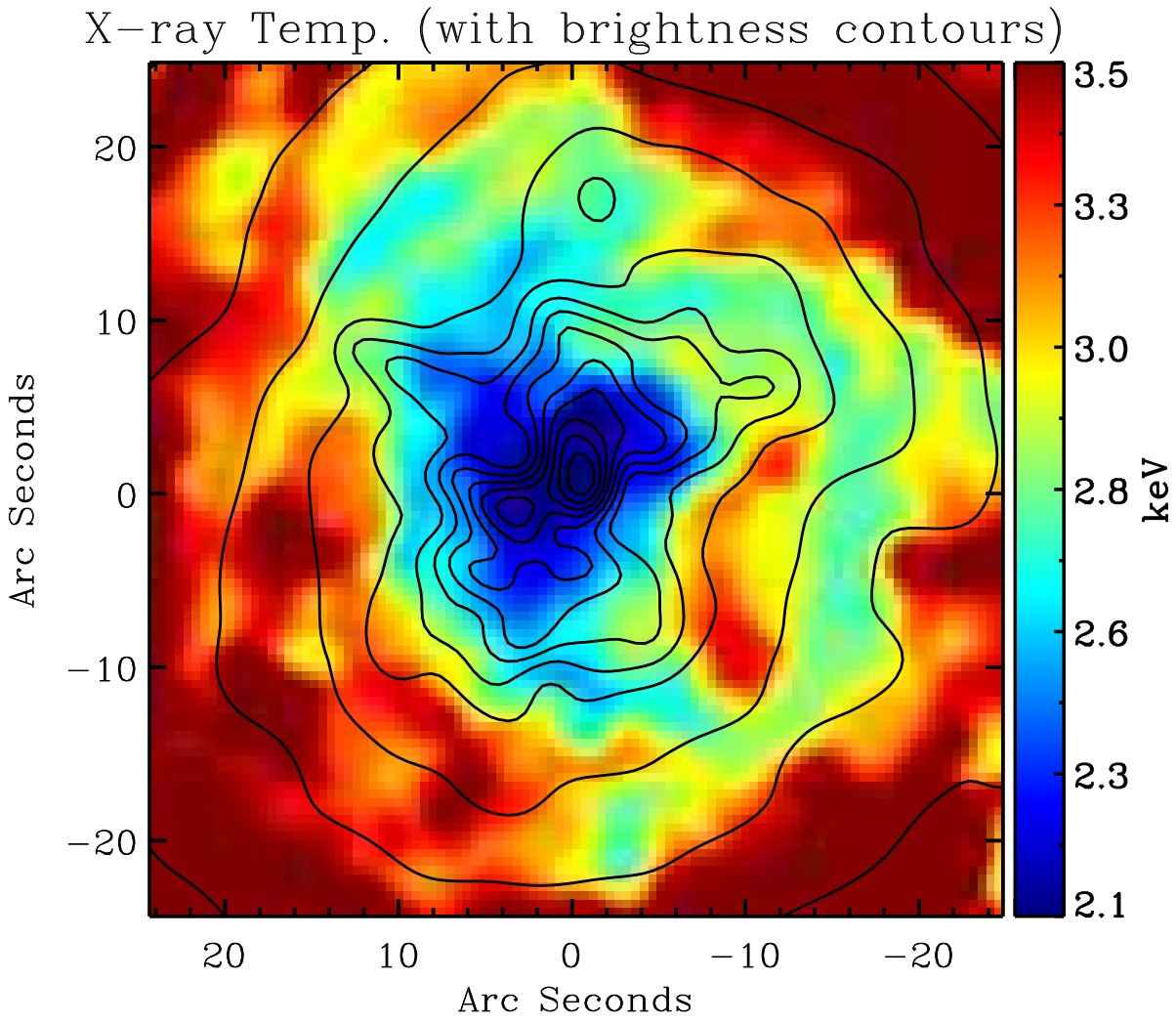

Figure 2.12: X-ray temperature map created from spatially resolved *Chandra* spectroscopy of A2597. The X-ray surface brightness distribution is overlaid in black contours. The best-fit single MEKAL model temperature is encoded via the scaled colorbar at the left of the figure. Note the 10″ "cold filament" extending from the central cold (~ 2.2 keV) feature, as well as the "hot" arc-shaped feature 10″ to the west. These features and their associated physical interpretations are discussed in the text. At the redshift of A2597, 1″ corresponds to ~ 1.5 kpc. East is left, north is up.

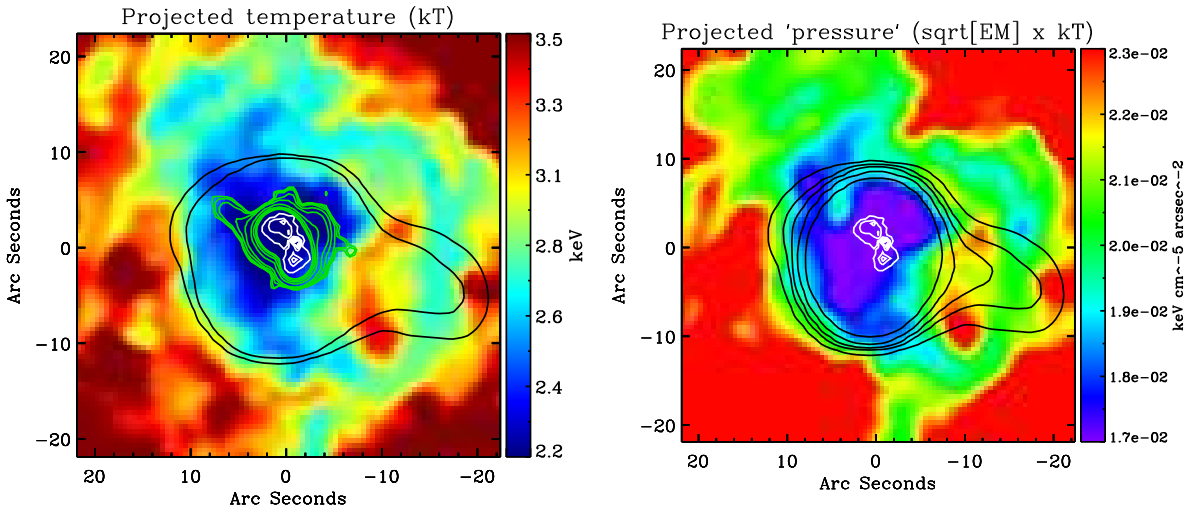

Figure 2.13: (*left*) The same X-ray temperature map shown in Fig. 2.12, with 330 MHz, 1.3 GHz, and 8.4 GHz radio emission overlaid in black, green, and white contours, respectively. (*right*) "Fake pressure" map made by multiplying the temperature (kT) map at *left* with the square root of the emission measure map (effectively the MEKAL normalization). This is a rough proxy for a true pressure map, as the emission measure is proportional to the density. Of course, projection effects have not been accounted for. 330 MHz and 8.4 GHz radio contours are overlaid in black and white, respectively.

~ 37 kpc). The projected profile falls from ~ 3.5 keV at ~ 35 kpc to ~ 2.6 keV in the innermost regions. The outer boundaries of the spectral map are generally $\sim 3.3-3.5$ keV, and the innermost regions fall below < 2 keV. The minor discrepancy on the "cold" end (as compared to our radial profile) is largely due to the radial binning process used to make the radial profiles in Fig. 2.10, as the innermost annuli do not sample the coldest gas in the very center.

The gradient apparent in the 2D projected temperature map is not as smooth as the profile in Fig. 2.10*a*, and is characterized more by an outer "shell" of $\gtrsim 3$ keV gas surrounding a roughly circular region of ~ 2.5 keV gas, and finally an inner region of ~ 2 keV gas within the central $20''$. As can be seen in Fig. 2.7*c*, the spectral extraction regions on this scale are less than a few arcsec in maximum size (owing to high X-ray surface brightness and therefore S/N), so the "sharp-edged" shells we observe are not merely the result of the spatial binning process.

2.5.1 The "cold filament" and "hot arc"

We further observe two significant spatial fluctuations from the "azimuthally averaged" temperature gradient, namely the "triangle-shaped" cold ($\sim 2-2.5$ keV) central feature and the "hot arc" structure $10''$ to the west. As can be seen in comparing the temperature map with the overlaid X-ray surface brightness profiles, the central "cold triangle" is roughly cospatial with the "butterfly" feature we previously described in the X-ray surface brightness image (Fig. 2.3). The feature is primarily characterized by a $10''$ (~ 15 kpc) cold linear filament that is very nearly cospatial with the soft excess linear filament clearly apparent in (Fig. 2.3). There is slight spatial mismatch-match between the features, but this is not surprising given the spatial binning and smoothing processes undertaken during creation of the maps. Inevitably, this results in some loss of spatial information on at least the scale of the spectral extraction bin sizes. Regardless, Figs. 2.11 and 2.12 make it clearly apparent that feature (5) in Fig. 2.4 is a "cold filament". In later sections, we will discuss the physical implications associated with this feature.

In Fig. 2.13*a* and we present the same projected temperature map with 8.44 GHz, 1.3 GHz, and 330 MHz radio emission overlaid in white, green, and black contours, respectively. We see discrete, sharp-edged regions of higher-than-ambient temperature and pressure associated with the previously described "hot arc" feature. In both maps, the "opening" of the feature roughly borders, in projection, the eastern edge of the "western large cavity" (features 1 and 2 in Fig. 2.4). The central axis of the extended western arm of the 330 MHz radio emission corresponds almost exactly with the projected center of the "hot arc" structure, just as it does the western cavity. The 1.3 GHz radio emission features a northeastern extension aligned along the same position angle as the 15 kpc cold filament, seen in the temperature map as a "triangular" cold excess. While the extended 1.3 GHz emission in this area covers only a small spatial fraction of the cold filament, it could be interpreted as evidence of dredge-up of low entropy gas by the propagating radio source. Recall from earlier discussions that this cold filament and the extended 1.3 GHz emission are aligned along the same position angle as the western large cavity, the extended 330 MHz emission, the projected VLBA jet axis, and the high velocity dispersion stream of 10^4 K gas observed in the Oonk *et al.* (2010) data. While the 1.3 GHz emission is cospatial with only the "bottom half" of the cold filament, it isn't necessarily expected to be completely coincident, even in a scenario wherein the jet is responsible for entraining the cold keV gas and creating the filament. The 1.3 GHz emission may sample only a small portion of the real jet, while the remainder of the emission may have cooled off to lower frequencies. The lower frequency 330 MHz emission is not resolved on these scales, so it is difficult to determine whether this may be the case, though it is worth

noting that the 330 MHz emission does show a slight eastern extension at the same radius as the "upper end" of the cold filament, although at a slightly offset position angle. In Fig. 2.13*b* we show the "fake pressure" map, and note a discrete compact region of higher-than-ambient pressure apparently cospatial with the base of the cold filament.

2.6 AGN Feedback Energy Budget

Kiloparsec scale X-ray cavities provide the best known diagnostics for assessing the energy associated with AGN outbursts, and the duty cycle over which these outbursts occur (e.g., Churazov *et al.*, 2002; Bîrzan *et al.*, 2004; Dunn & Fabian, 2006; Rafferty *et al.*, 2006; McNamara & Nulsen, 2007). As is apparent in Fig. 2.4, the central 30 kpc of A2597 is permeated by a network of at least four discrete cavities ranging from 2 to 24 kpc in projected linear extent, as well as X-ray surface brightness excesses, namely the 15 kpc linear filament, which may also be related to propagation of the radio source. In this Section we attempt to decode the relic AGN outburst history by quantitative study of these X-ray features.

2.6.1 Age dating the X-ray Cavities

We consider the simple model adopted by Bîrzan *et al.* (2004) and Rafferty *et al.* (2006) in our estimates of the timescales associated with the X-ray cavities. In this very simple model, X-ray cavity inflation is expected to be initially rapid as the nascent radio jet expands supersonically into the ambient medium. At this stage, cavities excavated by the jet are small, narrow, and younger than the local sound-crossing time, as the strongly shocked ICM gas is found only at the tip of the supersonic propagation front (Heinz *et al.*, 1998; Enßlin & Heinz, 2002; McNamara & Nulsen, 2007). These "infant" cavities would only be associated with minor and spatially small depressions in the X-ray surface brightness, and would be difficult to detect, particularly given a large amount of intervening X-ray gas along the line of sight. The jet decelerates to transonic speeds as its ram pressure equalizes with the ambient ICM pressure, truncating the supersonic inflation stage. The cavity continues to expand subsonically and will eventually "catch up" with the now-decelerated jet on slightly more than a sound crossing time, at which point the buoyant force takes over as the dominant mechanism regulating cavity dynamics.

The buoyant bubble rises amid the ambient pressure gradient and expands adiabatically during its ascent to maintain pressure equilibrium with the surrounding gas. It eventually becomes large enough to cause a detectable deficit in X-ray surface brightness. At this stage, the cavity's

maximum age is set by its terminal velocity in the medium,

$$v_t \approx \sqrt{\frac{2gV}{SC}} \tag{2.7}$$

which is set by the balance of the local buoyant and drag forces. Here, V is the volume of the cavity, S is its cross-sectional area, and g is the local gravitational acceleration. The majority of X-ray cavities (including those in A2597) are cospatial with the BCG stellar isophotes, implying that they rise amid a potential dominated by the BCG. The local gravitational acceleration at radius R from the center of the host galaxy may therefore be inferred from the stellar velocity dispersion σ,

$$g \simeq \frac{2\sigma^2}{R}, \tag{2.8}$$

assuming that the galaxy is an isothermal sphere. The terminal velocity v_t of the cavity is always subsonic, as the Kepler speed $v_{\rm K} = \sqrt{gR}$ is of order the sound speed c_s in the gas

$$c_s = \sqrt{\frac{\gamma kT}{\mu m_{\rm H}}}, \tag{2.9}$$

where $\gamma \simeq 5/3$ is the ratio of specific heats and $\mu \simeq 0.62$ is the mean molecular weight, appropriate for fully ionized gas.

Based on these simple assumptions, three estimates are generally used in age-dating X-ray cavities. The most simple of these is the sound crossing time t_{c_s},

$$t_{c_s} = \frac{R}{c_s} = R\sqrt{\frac{\mu m_{\rm H}}{\gamma kT}}, \tag{2.10}$$

which assumes a direct sonic rise of the bubble along the plane of the sky to its current projected radius R. As the initial stages of cavity inflation are thought to be supersonic, followed by subsonic buoyant rise, this admittedly simple approach may best reflect an "average" of the two stages. Alternatively, if initial inflation is a small fraction of the cavity's age, the buoyant rise time $t_{\rm buoy}$ may be used, which takes drag forces into account. Following the discussion of the terminal

buoyant velocity above, $t_{\rm buoy}$ is given by

$$t_{\rm buoy} \simeq \frac{R}{v_t} \simeq R\sqrt{\frac{SC}{2gV}}. \tag{2.11}$$

Finally, cavity age is constrained by the time it takes for gas to refill the bubble's "wake", which can be roughly estimated by the time it would take a bubble of radius r to rise through its own projected diameter,

$$t_{\rm refill} = 2\sqrt{\frac{r}{g}}. \tag{2.12}$$

Bîrzan *et al.* (2004) made all three estimates for the two M01 ghost cavities in A2597 (features 1 and 3 in Fig. 2.4), using the early short *Chandra* observation. So as to provide an independent check of their results using the deeper X-ray data, we follow their procedure almost exactly, and repeat their calculations for the M01 ghost cavities, the western large cavity (features 1 and 2), as well as the newly detected cavities (4) and (6) (as labeled in Fig. 2.4). Like Bîrzan *et al.* (2004), we adopt the A2597 BCG stellar velocity dispersion of $\sigma \approx 224 \pm 19$ km s^{-1} from Smith *et al.* (1990) in our calculation of the local gravitational acceleration g. Unlike Bîrzan *et al.* (2004), we use the kT inferred from the cavity positions on our X-ray temperature map (Fig. 2.12) in calculating the sound speed in the X-ray gas. We choose to use the 2-D temperature map over our 1-D radial temperature profile (Fig. 2.10*a*), because A2597 is azimuthally anisotropic in X-ray temperature (not to mention surface brightness) on these scales (see e.g. the cold filament and "hot arc" in Fig. 2.12). Furthermore, in calculating the pV work associated with each cavity, we use the projected density profile (Fig. 2.10*b*) to estimate the pressure nkT at the radius of each cavity. The results of these calculations are given in Table 2.3. Our results are generally consistent with Bîrzan *et al.* (2004), though we find marginally higher cavity ages for all three estimates, owing to our use of deeper X-ray data, slight differences in cavity size estimates, and the differing pressure and temperature estimations discussed previously.

Nonetheless, our results are roughly consistent with those of Bîrzan *et al.* (2004), given these highly uncertain calculations. For example, in age dating the M01 western ghost cavity we find $t_{c_s} \approx 27$ Myr, $t_{\rm buoy} \approx 88$ Myr, and $t_{\rm refill} \approx 66$ Myr, while Bîrzan *et al.* (2004) finds 26, 66, and 86 Myr, respectively. Of course, none of these estimates account for projection effects, and assume that the bubble rises purely in the plane of the sky. This results in underestimation of cavity age by generally less than a factor of two (Bîrzan *et al.*, 2004; Rafferty *et al.*, 2006; McNamara & Nulsen,

Table 2.3. **Spatial Properties and Energetics of X-ray Morphological Features**

Label (1)	Name (2)	R (D) (kpc) (3)	r (kpc) (4)	pV ($\times 10^{57}$ ergs) (5)	t_{c_s} ($\times 10^7$ yr) (6)	$t_{\rm buoy}$ ($\times 10^7$ yr) (7)	$t_{\rm refill}$ ($\times 10^7$ yr) (8)	$P_{\rm cav}$ ($\times 10^{42}$ erg s^{-1}) (9)
1	M01 western "ghost" cavity	24	4.8	3.1	2.7	8.8	6.6	6.52
2	C05 "X-ray tunnel"	(18)	1.5	5.25	...	...	...	...
1+2	Western "large cavity"	9	9	35.9	1.0	1.4	5.6	170.6
3	M01 northern "ghost" cavity	21	6.6	7.0	2.7	6.1	7.3	16.5
4	Eastern "ghost" cavity	35	3.6	0.79	3.8	17.8	6.9	1.05
6	Filament base cavity	9	2.3	0.30	1.1	2.7	2.8	1.73

Note. — (1) Label of morphological feature that corresponds to that assigned in Fig. 2.4*a*; (2) "name" given to the corresponding feature; (3) projected radial distance (length) of the feature from the radio core to the estimated center (edge) of the feature; (4) estimated radius of the feature (for the "C05 X-ray tunnel" we give the largest and smallest radii); (5) estimated work associated with cavity assuming subsonic inflation; (6) estimated age of the cavity if it rises at the sound speed (e.g., the sound crossing time), calculated by $t_{c_s} = R/c_s = R\sqrt{\mu m_{\rm H}/\gamma kT}$; (7) estimated buoyant, subsonic cavity rise time calculated by $t_{\rm buoy} \approx R\sqrt{SC/2gV}$; (8) estimated time needed to refill the displaced cavity volume calculated by $t_{\rm refill} = 2\sqrt{r/g}$. See §2.6.1 for more details on these calculations. All estimated values are highly uncertain and rely on several assumptions discussed in the text. All estimated timescales ignore projection effects and assume that the cavity's rise trajectory is in the plane of the sky; (9) X-ray cavity power esimated by assuming $P_{\rm cav} \approx 4pV/\langle t\rangle$, where $\langle t\rangle$ is the average of the three cavity age estimates. Here we have assumed the cavity to be filled with relativistic plasma, so that its enthalpy can be approximated as $4pV$.

2007).

Note that we perform independent calculations for features (1) and (2) (the M01 ghost cavity and CO5 X-ray tunnel, respectively), and then repeat the calculations for the "western large cavity" which is effectively these two features put together. We define the true borders of the western large cavity to define a projected area that is slightly *smaller* than features (1) and (2) added together. This is due to residual X-ray emission found at the "base" of the X-ray tunnel (and therefore the cavity), possibly suggestive of gas which has begun to refill the wake of the buoyantly rising cavity. The true 10σ deficit associated with the western large cavity is slightly offset from the radio core, suggesting that the bubble may have buoyantly risen. We define its eastern border to be offset from the core by ~ 9 kpc. The residual X-ray emission at the base of the cavity can best be seen in the left-most panel of Fig. 2.18.

2.6.2 Energy budget

In column (9) of Table 2.3 we calculate the mean instantaneous power of each cavity $P_{\rm cav}$,

$$P_{\rm cav} = \frac{4pV}{\langle t \rangle} \tag{2.13}$$

where $\langle t \rangle$ is the average of the cavity ages estimated in the above Section (columns 6, 7, and 8 of Table 2.3). We have assumed the cavities are filled with a relativistic plasma, such that their enthalpy can be approximated as $4pV$. The (roughly) estimated instantaneous power of the western large cavity (features 1+2) is 1.7×10^{44} ergs s^{-1}, which is of order the X-ray luminosity of A2597 and comparable to similar estimates made for the X-ray cavities in Hydra A (Wise *et al.*, 2007). In the context of that cool core cluster, this power has been shown to be capable of offsetting radiative losses associated with a cooling flow with mass deposition rates exceeding $> 100\ M_{\odot}$ yr^{-1} (David *et al.*, 2001; Wise *et al.*, 2007). The sum of all cavity thermal energies in A2597, which we estimate to be $\sim pV$, ranges from $(1.6-4.4) \times 10^{58}$ ergs, depending on whether you count the M01 and C05 cavity and tunnel separately, or as one large cavity. This serves as a rough estimate on the energy injected by the AGN into the ambient gas in the past 200 Myr. These estimated energies are very close to the inferred mechanical energy of the central 8.4 GHz radio source, which Sarazin *et al.* (1995) estimated to be 9×10^{57} ergs. It appears that, at least to within an order of magnitude and ignoring timescales and ages (for the moment), mechanical input from the radio source is largely capable of accounting for the energy budget inferred from rough measurements of the X-ray cavities.

Adopting a mass-to-energy conversion efficiency of $\epsilon = 0.1$, and assuming that the energy associated with the X-ray cavities is provided by the AGN, we estimate the BH mass accretion rate implied by this mean instantaneous power to be

$$\dot{M}_{\rm acc} \sim \frac{P_{\rm cav}}{\epsilon c^2} \sim 0.003-0.03\ M_{\odot}\ {\rm yr}^{-1}. \tag{2.14}$$

Rafferty *et al.* (2006) made a similar estimate for A2597, finding a value of $\sim 0.01\ M_{\odot}$ yr^{-1}. Using the stellar velocity dispersion and K-band luminosity of the host, they estimated the mass of the central BH to be $\sim 3 \times 10^8\ M_{\odot}$, for which the corresponding Edddington accretion rate would be $\sim 10\ M_{\odot}$ yr^{-1}. Whether using our results or those from Rafferty *et al.* (2006), this simple estimate suggests that the accretion rate is deep within the sub-Eddington regime. Similar lines of argument have been made for other CC clusters, with similar results. Even Hydra A, which hosts one of the

most powerful AGN in the Universe, is estimated in the same way to be strongly sub-Eddington by two orders of magnitude (e.g., Wise *et al.* 2007).

2.6.3 Pressure budget

The total mechanical pressure associated with the 8.4 GHz source was estimated to be on the order of $p_{8.4\ \mathrm{GHz}} \sim 10^{-9}$ dyn cm^{-2} (Sarazin *et al.*, 1995). As noted previously, it appears that the 8.4 GHz source may be overpressured with respect to the ambient thermal gas, whose pressure we estimated to be $p_{\mathrm{X-ray}} \approx 5.5 \times 10^{-10}$ dyn cm^{-2}. Using a radio spectral index of α = –2.7 calculated with the 1.3 GHz and 330 MHz sources, Clarke *et al.* (2005) estimated that the extended 330 MHz emission filling the western large cavity (Fig. 2.6) is associated with a minimum magnetic field strength of $B_{330\ \mathrm{MHz}}$ = 29 μG and a non-thermal pressure of $p_{330\ \mathrm{MHz}} \approx 5 \times 10^{-11}$ dyn cm^{-2}. Here, the "X-ray tunnel" was assumed to be a prolate cylinder, the relativistic ions and electrons were assumed to have equal energies, and the radio plasma was assumed to occupy the X-ray cavity with a filling factor of unity. At the general radius of the large western cavity (where the 330 MHz extended emission ends), we estimate the X-ray pressure to be 4×10^{-10} dyn cm^{-2}, an order of magnitude higher than the estimated pressure of the 330 MHz source. A population of low energy electrons not sampled by the 330 MHz emission may contribute the dominant fraction of pressure support to the cavity.

2.6.4 Timescale budget

Based on synchrotron loss timescales and assuming a steep spectral index down to 10 MHz, Sarazin *et al.* (1995) and Clarke *et al.* (2005) estimated the lower limit lifetimes of the 8.4 GHz and 330 MHz sources to be $\tau_{8.4\ \mathrm{GHz}} \gtrsim 5 \times 10^6$ yr and $\tau_{330\ \mathrm{MHz}} \gtrsim 8 \times 10^6$ yr, respectively. Clarke *et al.* (2005) also estimated a buoyant rise time (e.g., Enßlin & Heinz, 2002) of $\tau_{\mathrm{buoy,330\ MHz}} > 5 \times 10^7$ yr for the 330 MHz source, assuming it was associated with a buoyant lobe of plasma rising at 60% of the sound speed (assumed to be c_s = 350 km s^{-1}) in the plane of the sky. That the estimated synchrotron lifetime for the 330 MHz is shorter than the estimated buoyant rise time may be suggestive of in situ re-acceleration of electrons within the western large cavity (Clarke *et al.*, 2005), though these highly uncertain age estimates do not allow for more robust interpretation.

Each of these estimated ages is significantly shorter than the largest estimated age for an X-ray cavity, which is 1.8×10^8 yr (for feature 4 in Fig. 2.4, the eastern "ghost" cavity). This suggests that the oldest X-ray cavities were not excavated by the current epoch of radio activity, but are

instead associated with a previous period in the AGN duty cycle. There is ample evidence that cycling times between the triggering of radio activity, the onset of quiescence, and the subsequent re-ignition of activity are always on the order of $10^7 - 10^8$ yr, and radio sources can rarely live longer than this unless there is re-acceleration of the electron population (e.g., Parma *et al.* 1999). The fact that no low frequency radio emission is observed to be cospatial with the oldest ghost cavity is consistent with the scenario wherein the previous epoch of activity excavated the oldest X-ray structures, which then buoyantly rose, perhaps during a period of quiescence. The youngest X-ray cavities would then be associated with the "current" (or at least recently completed) epoch of activity. The smallest estimated cavity age is that for the western large cavity, at 1×10^7 yr. This is fairly close to the estimated age of the 330 MHz source which fills the cavity (8×10^6 yr, see above). Whether the 8.4 GHz and 330 MHz sources are commonly associated with the same, perhaps current epoch of activity is not clear, because the 330 MHz emission is not resolved on the scale of the 8.4 GHz compact source ($\sim$ 10 kpc). However, as their (roughly) estimated ages are similar, and considering the extended 330 MHz emission is aligned along the same position angle at $\sim$ 20 kpc scales as the "current" VLBA jet on 50 pc scales, it certainly seems possible. That the 1.3 GHz emission seems to be an intermediate case spatially "bridging" the 8.4 GHz and 330 MHz sources (see Fig. 2.6, blue contours) is more evidence in favor of this interpretation. Alternatively, the 330 MHz emission could arise from an earlier period when the jet fed radio plasma down the axis of the western large cavity, before being deflected to the south by interaction with the ambient dense molecular medium. This might account for the sharp bend in the southern 8.4 GHz lobe, a scenario which Koekemoer *et al.* (1999) explores in detail. That work found the ambient dense gaseous medium sufficiently massive to significantly deflect the jet over the radio source lifetime.

2.7 Implications for Cooling, AGN fuelling, and Star Formation

The cooling time for the ambient X-ray medium on the $\lesssim$ 30 kpc scale of the X-ray cavity network is $\sim 3 \times 10^8$ yr (McNamara *et al.*, 2001; Morris & Fabian, 2005). This is close to the typical $\sim 10 - 100$ Myr radio cycling timescale of the AGN duty cycle. The estimated ages of the X-ray cavity network in A2597 are more consistent with a "bubble injection timescale" of $\sim 10^7$ yr. In this section, we discuss our results and their implications in the context of ICM/ISM cooling, and the origin of the cold gaseous reservoirs fuelling both AGN activity and star formation.

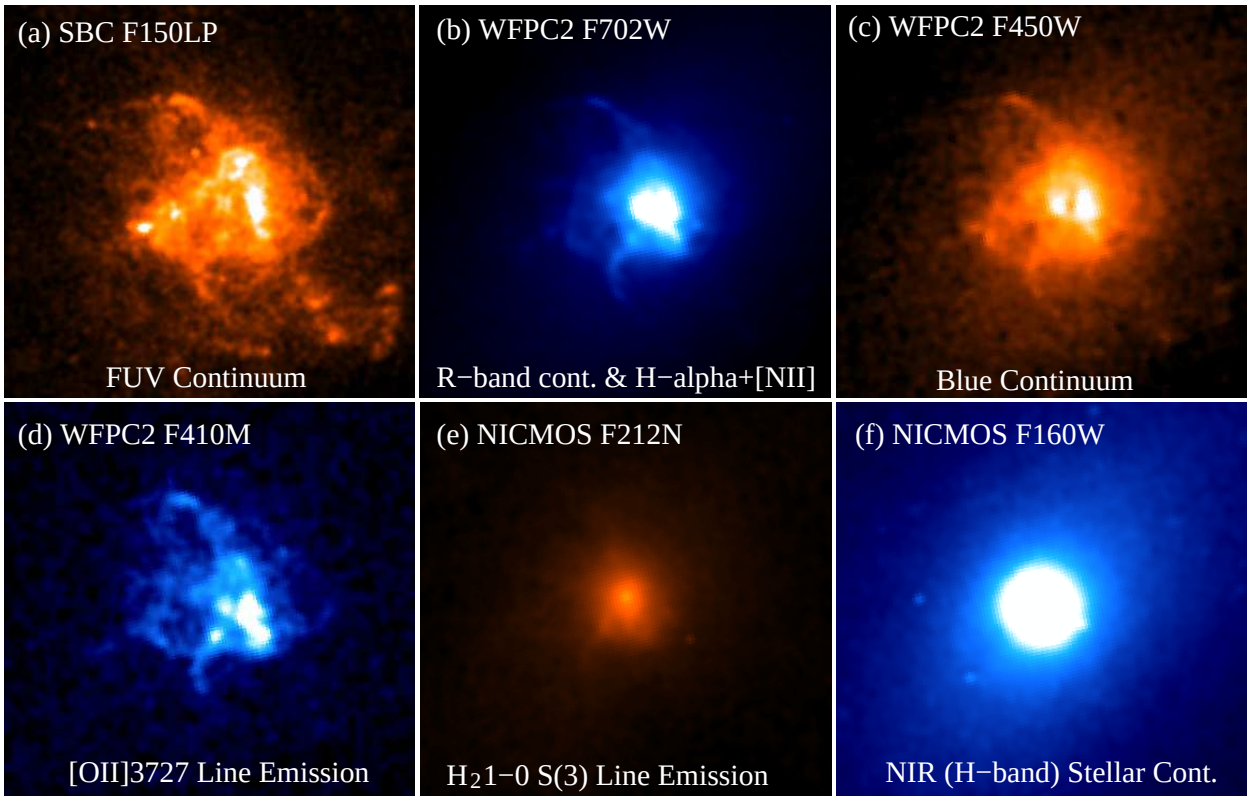

Figure 2.14: *HST* imaging of FUV, optical, NIR, and line emission associated with the ~ 10 kpc-scale nebula at the center of the A2597 BCG. The FOV of each figure is approximately $10'' \times 10''$ (~ 15 kpc$\times$15 kpc). Panel (*a*) is FUV continuum emission, attributed to ongoing star formation, from the ACS SBC F150LP observation of Oonk *et al.* (2011). Lyα emission is not included in the bandpass. Panel (*b*) is *R*-band optical continuum, Hα+[N II], and [S II] emission from Holtzman *et al.* (1996). Panel (*c*), also from Holtzman *et al.* (1996), contains blue optical continuum and a small contribution from [O II]λ3727 Å emission, which dominates the bandpass in the F410M image, from Koekemoer *et al.* (1999), shown in panel (*d*). Panel (*e*) is primarily emission from the 1.956 μm (rest frame) 1-0 S(3) H_2 line, originally published by Donahue *et al.* (2000). Panel (*f*) is *H*-band NIR stellar continuum emission, also from Donahue *et al.* (2000).

2.7.1 The origin of the warm and cold gas

The circumstantial connection between cool core clusters and active warm and cold gas phases in CC BCGs has been known for decades, though consensus has never been reached on the nature of this connection. Relative to BCGs in non-cool core clusters or field gEs, CC BCGs are $\sim 3-4$ times as likely to harbor Hα-bright optical emission line nebulae with complex filamentary morphologies, $10^8 - 10^9$ $M_\odot$ pools of cold molecular gas, low levels of ongoing star formation, and compact central radio sources. The powers of each of these phenomena strongly correlates with ICM cooling rates, and the warm and cold gas reservoirs are almost always cospatial with the

coolest X-ray gas (Hu *et al.*, 1985; Heckman *et al.*, 1989; Crawford *et al.*, 1995; McNamara *et al.*, 2004; Crawford *et al.*, 2005; Fabian, 2003; Rafferty *et al.*, 2006; Salomé *et al.*, 2006; Quillen *et al.*, 2008; O'Dea *et al.*, 2008). This is the case for A2597. One obvious common origin for an intrinsic cool core / CC BCG connection is residual condensation from a rapidly cooling ambient ICM, even at rates that are a few percent of those expected from an uninhibited cooling flow scenario. Reality is more complicated than this, however, as the energetics and ionization sates of the warm and cold ISM phases are rarely consistent with isolated cooling models (see Chapter 1).

Here we consider results from previous sections in the context of the ~ 10 kpc scale emission line nebula in the A2597 BCG, which has been studied extensively for decades (e.g., Heckman *et al.* 1989; McNamara & O'Connell 1993; Voit & Donahue 1997; McNamara *et al.* 1999; Koekemoer *et al.* 1999; Oegerle *et al.* 2001; O'Dea *et al.* 2004; Jaffe *et al.* 2005; Oonk *et al.* 2011). High spatial resolution archival *HST* imaging, shown in Fig. 2.14, reveals its complex filamentary morphology in the FUV and optical (panels *a* through *d* in Fig. 2.14). Deep optical spectroscopy presented by Voit & Donahue (1997) shows the gas temperature, abundance, and electron density to be 9,000-12,000 K, $\sim 0.5 Z_{\odot}$, and $n_e \sim 200$ cm^{-3}, respectively. Koekemoer *et al.* (1999) estimated the pressure associated with the 10^4 K gas on these scales to be

$$p_{\rm nebula} \approx 5.5 \times 10^{-10} \left(\frac{n_e}{200\ {\rm cm}^{-3}}\right) \left(\frac{T}{10^4\ {\rm K}}\right)\ {\rm dyn\ cm}^{-2}. \tag{2.15}$$

Our estimated central X-ray pressure on the same ~ 10 kpc scale is 7×10^{-10} dyn cm^{-2} (see Fig. 2.10*b*), very close to what is inferred for the 10^4 K gas, implying that the two phases are in rough pressure equilibrium. The abundances of the hot X-ray gas and the emission line nebula are approximately the same on these scales, consistent with a scenario in which the former condenses into the latter. Sarazin *et al.* (1995) estimated the pressure of the 8.4 GHz radio source to be $\sim 10^{-9}$ dyn cm^{-2}, which would suggest that the radio lobes are somewhat overpressured with respect to the 10^4 K and 10^7 K ambient gas. Oonk *et al.* (2010) reported high velocity dispersion ($\sim 200-300$ km s^{-1}) streams of H_2 and H II spatially coincident with the projected VLBA jet axis, suggestive of possible mass entrainment by the radio source as it propagates through the dense molecular medium.

Energetics of the nebula

The non-detection of [O III] λ4363 and relatively weak [O III] λ5007 emission almost definitely rules out shocks as the ionizing source for the emission line nebula, a result independently con-

firmed by Voit & Donahue (1997); O'Dea *et al.* (2004); Oonk *et al.* (2011). To recover the observed temperatures, a photoionizing source should be hard and extend into the X-ray, though the small He II/Hβ ratio is indicative of an at best minor role played by photons with energies > 54.4 eV. Photoionization by a young stellar component is the only model which as not been ruled out as the primary heating and ionization source (by e.g., spectral line diagnostics and photon counting exercises, Voit & Donahue 1997; O'Dea *et al.* 2004; Oonk *et al.* 2011).

FUV continuum emission associated with this substantial young stellar component is seen in panel *a* of Fig. 2.14. Estimated star formation rates, as always, vary according to the method used, but range from $2-12$ $M_{\odot}$ yr^{-1} for A2597 (McNamara & O'Connell, 1993; O'Dea *et al.*, 2004; Donahue *et al.*, 2007; Oonk *et al.*, 2011). SFRs estimated from (e.g.) the FUV vs. IR, etc. are not expected to agree given the effects of extinction, and also because these various tracers of star formation sample very different components of the young stellar population. The Balmer sequence in the Voit & Donahue (1997) data is consistent with substantial intrinsic extinction by dust at about one magnitude in V-band (i.e., $A_V \sim 1$). This substantial dust component can be seen in absorption in Fig. 2.14, panel *c*. It is not likely to have condensed from an ambient 10^7 K atmosphere, where grain destruction timescales are shorter than 10^6 yr (e.g., Draine 1978; Dwek & Arendt 1992; Fabian 1994; Koekemoer *et al.* 1999), unless the dust is shielded from interaction with the ambient X-ray gas. Recently, *Herschel* observations revealed the masses and temperatures of these dust components to be 10^7 $M_{\odot}$ and 10^5 $M_{\odot}$ at 50 K and 20 K, respectively (Edge *et al.*, 2010a,b). Donahue *et al.* (2011) recently detected PAH features in A2597 (as well as a number of other CC BCGs). PAH molecule lifetime amid ~ 1 keV gas with density ~ 0.1 cm^{-3} is on the order of hundreds of years due to collisions by suprathermal electrons and ions (Micelotta *et al.*, 2010; Donahue *et al.*, 2011). This confirms that a shielding mechanism is almost certainly required.

The inferred column density of the ionized gas is $N_{\rm HII} \approx 3 \times 10^{19}$ cm^{-2}, however the 21 cm absorption from H I reported by O'Dea *et al.* (1994a) is consistent with a higher neutral column density ($\sim 8 \times 10^{20}$ cm^{-2}), suggesting that the nebula is "ionization-bounded", wherein neutral clouds are sheathed in thin ionized outer layers. This has since become one of the favored "schematics" by which emission line nebulae in CC BCGs are pictured and modeled (see e.g., recent work by Donahue *et al.* 2011; Fabian *et al.* 2011, Mittal et al. 2011, in press). O'Dea *et al.* (1994a) detected narrow (~ 200 km s^{-1}) and broad (~ 400 km s^{-1}) redshifted (~ 300 km s^{-1}) 21 cm absorption components consistent with inwardly streaming clouds of molecular gas. The clumpy and filamentary FUV/optical nebula is further associated with a more diffuse component of NIR-bright vibrational line emission from molecular hydrogen at inferred vibration temperatures of 1,000-2,000 K (panel *e* in Fig. 2.14). Shocks and AGN photoionization have been effectively ruled out

as possible sources for this excitation, as the Hα/H_2 ratios are too low. As mentioned previously, shock and AGN photoionization models have also been ruled out as the possible excitation source for the emission line nebula, given the lack of [O III] λ4363 emission and a lack of radial gradient in ionization state (Voit & Donahue, 1997; O'Dea *et al.*, 2004; Oonk *et al.*, 2011). For the molecular hydrogen, the only model that Donahue *et al.* (2000) could not rule out is UV continuum irradiation from the young stellar component, just as was the case for the emission line nebula (Voit & Donahue, 1997; O'Dea *et al.*, 2004; Oonk *et al.*, 2011). Following this scenario, Donahue *et al.* (2000) estimates the mass of the H_2 component to be $\sim 3 \times 10^9\ M_\odot$.

What we learn from our results

Two results from our spatial analysis of the X-ray emission may carry implications with respect to the origin of the cold gas reservoir in the central BCG that is fuelling current and past epochs of star formation and AGN activity.

That the X-ray emission is elongated along the major axis of the BCG stellar isophotes may have important implications (see Fig. 2.1*b*). As noted by Sarazin *et al.* (1995), one obvious explanation for the elongation is that the keV gas is associated with a small but nonzero amount of angular momentum. Comparison of our *Chandra* image (Fig. 2.3) and the *XMM-Newton* EPIC image from Morris & Fabian (2005) will show that the position angle of the elliptical X-ray isophotes does not twist significantly on any observable scale, even in regions several hundreds of kpc beyond the BCG. Furthermore, at all observable radii, the major axis of the X-ray emission is very closely aligned with the major axis of the BCG stellar isophotes (Fig.2.1*b*), which in turn is elongated along the same general axis over which the A2597 cluster member distribution is extended.

Whether it is through cooling, a gas rich merger, or tidal stripping, gas acquired by a galaxy is expected to coalesce, precess, and settle into a symmetry plane on a few dynamical times of order $10^8 - 10^9$ yr (Gunn, 1979; Tubbs, 1980; Tohline *et al.*, 1982; Habe & Ikeuchi, 1985). The degree to which one can expect the dynamics of the gas to couple to the dynamics of the host galaxy stellar component strongly depends on the net angular momentum associated with these components. In a scenario wherein gas cools and condenses from a relatively static hot atmosphere, one can expect the coupling to be more efficient than a high angular momentum "cold acquisition" scenario in which gas is obtained through a minor or major merger (e.g., Tremblay *et al.* 2007, and references therein).

Whatever the case, if gas in the symmetry plane cools and sheds angular momentum, it can be expected to eventually reach the core and provide a reservoir of fuel for accretion onto the central

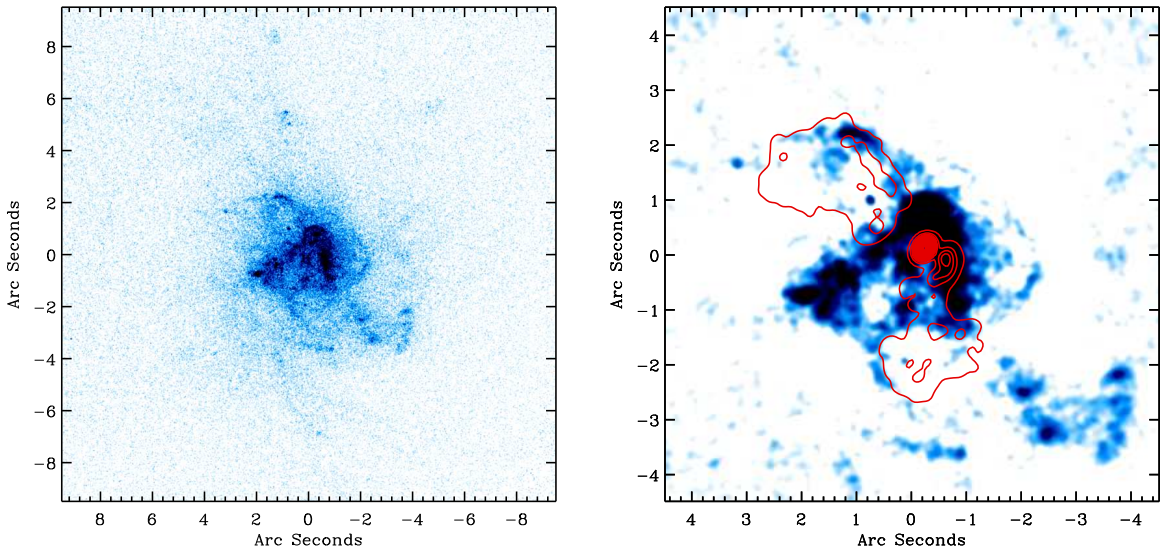

Figure 2.15: *HST* SBC F150LP $\sim$ 8 ksec exposure of FUV continuum emission associated with the A2597 emission line nebula. This image was originally presented and studied in detail by Oonk *et al.* (2011). The raw, unsmoothed data is presented in the panel at *left*. At *right* we present a "zoomed in" residual image obtained by subtracting a highly smoothed version of the image at *left* from a slightly smoothed image, thereby emphasizing the filamentary residual structures. We plot the 8.4 GHz radio contours from Sarazin *et al.* (1995) in red. East is left, north is up. At the redshift of A2597, $1''$corresponds to $\sim$ 1.5 kpc, such that the total FOV of the left panel is $\sim$ 24 kpc, while the FOV of the right panel is $\sim$ 12 kpc on one side.

BH. If the angular momentum of the accreting gas is common over a large range of radius, one might then expect the axis of the jet associated with AGN activity to be perpendicular to the major axis of the accretion reservoir (and, in turn, the BCG stellar isophotes). This appears to be the case in A2597, considering that the projected P.A. of the "current" VLBA jet axis is perpendicular to the major symmetry plane of the host galaxy. Note that we are not suggesting that radio jets, host galaxy symmetry planes, and kpc-scale disks of gas and dust are necessarily expected to be perpendicular. In fact, one can only expect perpendicular jet/disk orientations in the very central regions of the BH sphere of influence, where the dragging of inertial frames will force the angular momentum vector of accreting material to align with the spin axis of the BH on short timescales (e.g., Bardeen & Petterson, 1975). However, the alignment time at > 50 pc is greater than a Hubble time, so no such relationship can be expected (Tremblay *et al.*, 2006).

Nevertheless, the VLBA jet axis on 50 pc scales, the northern 8.4 GHz radio lobe, the extended 1.3 GHz emission, and extended 330 MHz emission are all elongated along the axis that is nearly perpendicular to the major axis of the X-ray isophotes and BCG stellar isophotes. Furthermore, the "cold X-ray filament" and the western large cavity are extended along the same axis. This is

consistent with a scenario in which the hot X-ray gas on 100 kpc scales and the cold accretion reservoir on $\lesssim$kpc scales share the same net angular momentum because they are related through common origin. If the cooling of hot ambient gas is critical to the build up of the host galaxy stellar component, then the fact that the BCG appears to align with the same overall net angular momentum would be consistent with this. Alternatively, more mundane but equally plausible explanations exist. For example, the dynamics of the hot X-ray gas and BCG stellar component could simply reflect the underlying cluster potential in which they have evolved.

Even still, our results are generally consistent with the following "schematic" scenario:

1. Hot keV gas cools and condenses from an ambient hot reservoir into the BCG.

2. This hot gas settles into a symmetry plane of the BCG, cools further, and spirals inward toward the center. This may account for the apparent excess of hard X-ray emission in the major axis of the BCG, as is apparent from Fig. 2.11.

3. The cooling gas reaches the center, forming a cool/cold reservoir on $<$kpc scales, which fuels accretion onto the central black hole, triggering a radio jet. That the apparent PKS 2322-122 jet axis is perpendicular to the major axis of the BCG isophotes and the X-ray gas is circumstantially supportive of this.

4. This jet, whether in present or past epochs, dynamically interacts with the ambient gaseous medium, accounting for the X-ray structures such as the western large cavity and 15 kpc cold X-ray filament. The jet may also interact with the ambient warm/cold medium, accounting for (a) the possible site of triggered star formation along the northern edge of the 8.4 GHz source, (b) the apparent high velocity dispersion stream of molecular gas in the Oonk *et al.* (2010) data, and (c) the deflection of the southern 8.4 GHz lobe.

In Fig. 2.15 we show the *HST* ACS SBC far-ultraviolet image from Oonk *et al.* (2011). Note that there is an ~ 8 kpc "arm" of extended FUV emission at a P.A. of 135°, to the southeast. This extended arm is aligned (in projection) almost exactly with the major axis of the BCG, as well as the major axis of the X-ray isophotes. If the X-ray gas is indeed cooling, settling into the BCG, inspiralling to the center, and providing the reservoir which fuels the AGN, it could also reasonably provide the cold gas fuelling this epoch of ongoing star formation. Tremblay *et al.* (2010) noted a similar correspondence in ages of a young stellar component and a compact central radio source, suggesting that episodes of AGN activity and episodes of star formation stem from common events, namely the infall of gas.

2.7.2 Ages of the young stellar component compared with ages of the X-ray cavity network

Oonk *et al.* (2011), using data from *HST* and the VLT FORS imager, estimated single stellar population ages for the young stellar component (YSP) in A2597. This was done by comparing measured FUV/*U*-band ratios with those predicted from Bruzual & Charlot (2003) simple stellar population models. We show the YSP ages inferred by Oonk *et al.* (2011) in Fig. 2.16 below.

It is important to note that the estimated ages are probably not accurate in the absolute sense, and are better considered in the *relative* sense (e.g., compared with one another). Bearing this in mind, we do note that, at least in the age map, the younger stars are found nearer to the radio source. Looking on smaller scales, there is possible evidence of even younger (5 Myr, "purple" on the map) stars found (a) at the northern edge of the northern radio lobe, and (b) along the projected axis of the host galaxy stellar isophotes. Koekemoer *et al.* (1999) and O'Dea *et al.* (2004) quantitatively investigated the possibility that the blue excess associated with the upper boundary of the northern radio lobe was a site of triggered star formation by the 8.4 GHz jet. Both works found the possibility to be energetically feasible. However, as we cannot offer new data to support or refute the possibility that the propagating jet is triggering star formation by inducing cloud collapse, we will not discuss the specifics here, and instead refer the reader to the above mentioned papers (Koekemoer *et al.*, 1999; O'Dea *et al.*, 2004).

2.8 Implications for AGN Feedback

2.8.1 Persistent star formation amid AGN feedback?

In comparing results from our study to the inferred YSP ages from Oonk *et al.* (2011), we find that the range of young stellar component ages entirely encompasses the inferred age rage of the X-ray cavity network. Oonk *et al.* (2011) found ages for the YSP ranging from $5-700$ Myr old, while our estimates for the X-ray cavity ages range from $10-200$ Myr. Furthermore, estimated ages for the various radio sources at 8.4 GHz, 1.3 GHz, and 330 MHz range from $50-100$ Myr (Clarke *et al.*, 2005). While the Oonk *et al.* (2011) stellar ages are merely rough estimates, they are consistent with those from Koekemoer *et al.* (1999), who performed an independent analysis with different *HST* datasets (WFPC2, in this case).

If these age estimates are even remotely realistic, then the implication is that low levels of star formation ($2-12\ M_{\odot}\ \mathrm{yr}^{-1}$) have managed to persist and survive even amid the AGN feedback-

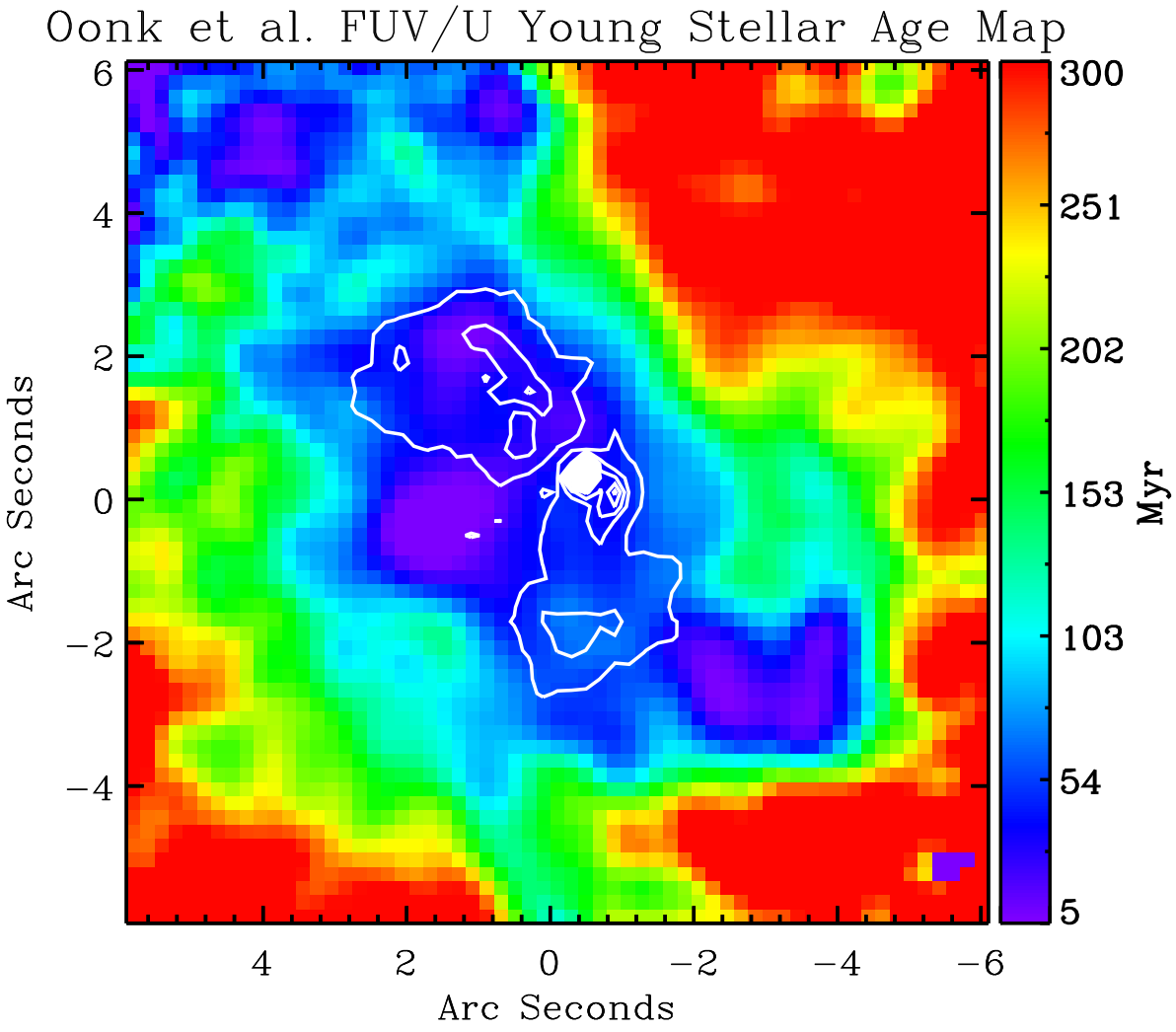

Figure 2.16: Single Stellar Population (SSP) age map from Oonk *et al.* (2011), made by comparing observed FUV/*U*-band ratios (from *HST* and the VLT, respectively), to those predicted from Bruzual & Charlot (2003) models. The inferred ages are more reliable in the relative sense, rather than the absolute sense. Regardless, it is clear that the "youngest" portion of the young stellar component is found nearer to the central 8.4 GHz radio source, which we overlay in white contours.

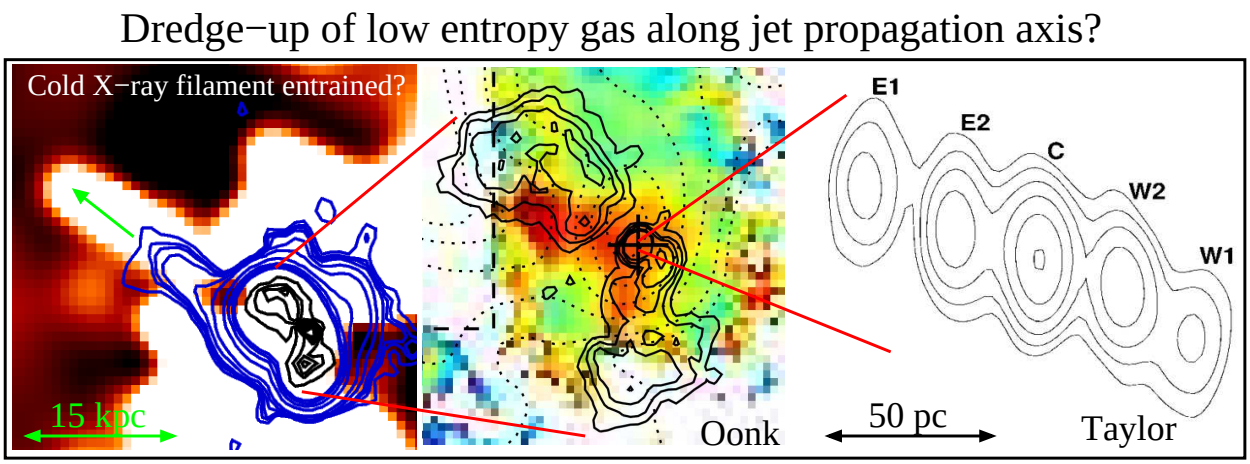

Figure 2.17: 8.4 GHz radio emission, in black, and 1.3 GHz radio emission, in blue, overlaid on the residual X-ray image from Fig. 2.4. The eastern edge of the 1.3 GHz emission is extended along the "bottom half" of the cold X-ray filament. The western edge of the 1.3 GHz emission is extended in the direction along the western large cavity, along with the 330 MHz extended emission, suggestive of a common axis offset from the central 8.4 GHz source. That the 1.3 GHz emission is cospatial with the soft excess X-ray filament may be consistent with a scenario wherein low entropy gas is dredged up by the propagating radio source (either during this epoch of activity or a previous one), as has recently been observed in Hydra A (Gitti *et al.*, 2011). The center panel is a VLT SINFONI Paschen-α velocity dispersion map on the scale of the 8.4 GHz source, from Oonk *et al.* (2010). The higher velocity dispersion gas (in red) is aligned with the projected VLBA small scale jet axis, which we show in the right-most panel from Taylor *et al.* (1999). This could be evidence for entrainment of dense molecular material by the propagating radio source. The FOV is of the left-most panel is approximately $\sim 30 \times 30$ kpc. The panels subsequently "zoom in" from there, to 10×10 kpc and 100×100 pc, respectively.

driven excavation of the X-ray cavities. Furthermore, if the estimated ages of the radio sources are correct, then star formation has been ongoing throughout more than one epoch of AGN activity. Clearly, AGN feedback does not establish an "entropy floor" below which gas cannot cool. The possible site of jet-induced star formation on the leading edge of the northern 8.4 GHz lobe is further evidence of this.

2.8.2 The "cold filament" — Evidence for dredge-up of low entropy gas by radio source

The $\sim$ 15 kpc northeastern soft excess X-ray filament can be considered in the context of multiple possible interpretations. While reserving the caveat that the feature may be of course be of the mundane variety (e.g., foreground object, arising from projection effects and superposition, etc.),

we consider three possible scenarios and their implications here.

1. The cold filament may be consistent with a scenario wherein X-ray gas with low net angular momentum is cooling and condensing from an ambient hot, static atmosphere, as is predicted in inhomogeneous cooling flow models.

2. Two X-ray cavities (features 3 and 4) are detected directly to the north and east of the filament. The filament could arise from displaced keV gas "funneling" down the region separating the cavities, or could arise from one larger cavity disrupting into two, allowing for gas flow down what was formerly the center of the larger cavity.

3. The cold filament may be associated with dredge-up of low entropy gas by the propagating radio source, and "dragged outwards". The main evidence for this is that the filament is aligned along the same position angle as the projected jet axis, and is partly cospatial with 1.3 GHz emission.

The first possible scenario (1), wherein gas condenses as a sheet of cooling gas from an ambient hot atmosphere, may be consistent with inhomogeneous cooling flow models. The cooling flow is always subsonic, though its Mach number will steadily increase inward until it reaches approximately the sound speed. Prior to this point, any growth of thermal instabilities associated with the flow are quickly "smoothed out" by buoyant motions (Balbus & Soker, 1989). The instabilities can persist for longer times as the flow becomes sonic, however, at which point Rayleigh-Taylor and shearing effects can disrupt the homogeneous flow into discrete, thermally unstable clouds which may decouple from the bulk flow. In inhomogeneous cooling flow models, these instabilities, manifest as overdensities, then "lag" behind, persist, and grow. The result is a long-lived, inhomogeneous "rain" of cold gas clouds over a large central region within the CC BCG, which should then pool and collect over a small number of dynamical times. Without being more quantitative, the cold filament may be associated with a "sheet" of cooling gas which has collected as a local overdensity due to persistent thermal instabilities. It is very difficult to be more quantitative in considering this scenario however, as we are limited by the data in our ability to assess the dynamics of the cold filament and other local physical processes at play.

The second scenario (2) is similarly difficult to interpret quantitatively, as projection effects make it impossible to know the exact spatial relationship between the two cavities (features 3 and 4 in Fig. 2.4) and the filament. It is easy to imagine that, if two X-ray bubbles were buoyantly rising side-by-side, a large volume of the displaced ambient keV gas would be preferentially funneled

into a column separating the two cavities. A larger bubble which has disrupted may result in a similar effect. Again, it is difficult to be more quantitative in considering these scenarios, for the reasons discussed above.

While again noting that much of this discussion is pure speculation, we note that scenario (3) is supported by additional observational evidence. In this scenario, the cold filament may arise from dredge-up of cooler, lower entropy gas by the propagating radio source, as has recently been observed in the CC cluster Hydra A (Gitti *et al.*, 2011). We provide a schematic for this scenario and some of this supporting evidence in Fig. 2.17. The cold filament represents a significant spatial deviation from the overall smooth temperature gradient. One explanation for this is that cold gas from the center has been displaced, and "dragged upwards". One obvious mechanism by which such a significant amount of gas could be moved from the center is by a propagating radio source. Incidentally, the position angle of the 15 kpc cold filament is very closely aligned with (1) the extended "arms" of the 1.3 GHz and 330 MHz radio emission and (2) the projected current VLBA jet axis.

Meanwhile, there have been prior suggestions that the "current" jet associated with PKS 2322-122 may be entraining ambient matter. Oonk *et al.* (2010) presented *K*-band integral field (IFU) spectroscopy enabling gas kinematics analysis of the molecular and ionized gas distribution on the scale of the A2597 nebula and the 8.4 GHz radio source. They reported high velocity dispersion ($\sim 200-300$ km s^{-1}) streams of H_2 and H II coincident with the southern edge of the northern 8.4 GHz radio lobe and approximately aligned with the VLBA jet axis. Another high velocity dispersion filament is coincident in projection with the eastern edge of the southern lobe. Oonk *et al.* (2010) considered two possible explanations for these high dispersion features. If PKS 2322-122 is a wide angle tail (WAT), the high velocity filaments may arise from the turbulent wake caused by relative motion of the AGN amid the ambient dense medium. Alternatively, the close projected alignment of the current VLBA jet axis for the northern lobe is suggestive of direct kinematical interaction (e.g., mass entrainment) between the jet and the gas through which it is propagating. In the latter case, the symmetry and asymmetry of the VLBA and 8.4 GHz counterjets, respectively, would require significant deflection of the current jet to account for the position angle mismatch between the 8.4 GHz lobes. A gradual bend in the jet owing to relative motion (consistent with the former scenario) may account for this. Alternatively, sharp deflection of a rapidly decelerating counterjet may possibly arise through interaction with the ambient medium. The site of this possible deflection is not visible in the Oonk *et al.* (2010) velocity maps, though the bright knot of 8.4 GHz radio emission immediately SW of the core may be related. Both scenarios are consistent with the steep lobe spectral index suggestive of dynamical frustration and confinement.

The "bottom half" of the cold filament is cospatial with extended 1.3 GHz radio emission (Fig. 2.17, blue contours). The width of this extended "radio arm" is approximately the width of the filament (~ 2 kpc), though it is slightly offset to the south from the filament's major axis. Of course, the 1.3 GHz emission does not sample the entire jet, regardless of whether or not the filament was "dragged upwards" during this or a previous epoch of activity. As noted previously, the 1.3 GHz emission may sample only a small portion of the real jet, while the remainder of the emission may have aged to lower frequencies. The lower frequency 330 MHz emission is not resolved on these scales, so it is difficult to determine whether this may be the case, though it is worth noting that the 330 MHz emission does show a slight eastern extension at the same radius as the "upper end" of the cold filament, so some part of the jet (relic or otherwise) has made it out to these radii.

As recently done in Gitti *et al.* (2011) for Hydra A, we can roughly estimate the energy that would be required to lift cold gas from the core to the projected height of the filament. To first order, this will be the difference in gravitational potential energy between the two locations. Assuming the local hot ISM is isothermal, hydrostatic, and linear in density with a sound speed $c_s \approx 750$ km s^{-1} (estimated from Eqn. 2.9), this will be

$$\Delta E = \frac{M_{\rm gas}\, c_s^2}{\gamma} \ln\left(\frac{n_{e,i}}{n_{e,f}}\right). \tag{2.16}$$

We very roughly estimate the mass of the displaced X-ray gas (e.g., the mass of the cold filament), $M_{\rm gas}$, by simply scaling general values for X-ray gas mass within ~ 100 kpc (which are usually of order $10^{10}\ M_\odot$). Scaling this down to a radius of 15 kpc, and scaling further to account for the rough "filling factor" of the filament, we arrive at a very conservative range of $10^7 - 10^9\ M_\odot$. The gas density at the bottom and top of the filament ($n_{e,i}$ and $n_{e,f}$, respectively) were estimated from our radial profile in Fig. 2.10. As before, γ was taken to be $5/3$. We find the energy required to "lift" a $10^7\ M_\odot$ filament out to 15 kpc to be 5.4×10^{56} ergs, while the energy required for a $10^9\ M_\odot$ filament is on the order of 10^{58} ergs. These values are comparable to the pV energy of the X-ray cavities listed in Table 2.3, which themselves are diagnostics for AGN power output. Clearly, the AGN has been powerful enough in the past to expend $> 10^{56}$ ergs to excavate 10 kpc scale X-ray cavities. It therefore appears energetically feasible that it could also expend the same amount of energy to entrain and lift cool X-ray gas out to 15 kpc.

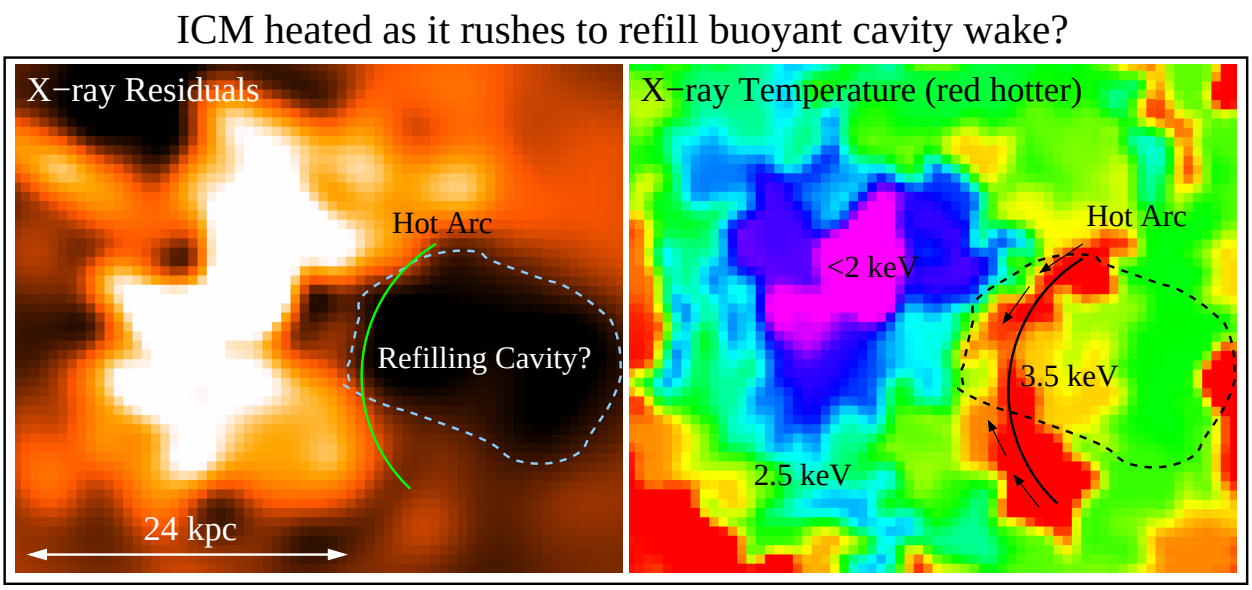

Figure 2.18: "Zoom in" on (*left*) the residual X-ray image presented in Fig. 2.4 and (*right*) the temperature map to highlight the temperature features associated with the western large cavity, which we highlight with a dashed line in both figures. The FOV of both panels is identical. The green and black arcs traces the "hot arc" feature previously described in the temperature map. In the temperature map we draw arrows that illustrate our working interpretation for the "hot arc" feature. In this interpretation, the keV gas displaced by the buoyant rise of the M01 ghost cavity "rushes in" to refill the resulting wake, thermalizing cavity enthalpy by heating the ambient gas > 1 keV above its ambient surroundings.

2.8.3 The "hot arc" — Evidence for thermalization of cavity enthalpy?

In Fig. 2.18 we provide a schematic for a possible interpretation of the "hot arc" feature observed in the X-ray temperature map (see Fig. 2.12). In "effervescent" AGN heating models, the enthalpy (free energy) of a buoyantly rising cavity can be entirely dissipated as the displaced thermal gas rushes to refill its wake (e.g., Churazov *et al.*, 2002; Reynolds *et al.*, 2002; Bîrzan *et al.*, 2004). The enthalpy H of a cavity is merely the $p \times dV$ work required to "inflate" the cavity, plus the thermal energy E within the cavity. That is,

$$H = E + pV = \frac{\gamma}{\gamma - 1} pV, \tag{2.17}$$

where V is the cavity volume, p is the pressure of the radio lobe which displaced the thermal gas, and γ is the ratio of specific heats, dependent on the (unknown) contents of the cavity. Depending on whether the cavity is magnetically dominated or instead filled with relativistic particles, cavity enthalpy is in the range of $2pV - 4pV$. Using this, we can estimate a lower limit on the enthalpy

associated with the western large cavity to be $\sim 7 \times 10^{58}$ erg. We can consider this an estimate of the energy reservoir available to eventually heat the ambient ISM surrounding the cavity.

As the gas refills the cavity, potential energy is converted to kinetic energy, heating the gas by a degree proportional to the potential energy dissipated,

$$\delta U = Mg\delta R \tag{2.18}$$

where M is the mass of the ICM that is displaced by the cavity as it rises through δR, and g is the local gravitational acceleration, as before. Assuming $M = \rho V$, hydrostatic (so that $\rho g = -dp/dR$), and approximately isobaric local conditions (so the pressure gradient $\left[dp/dR\right]$ can be ignored, giving $\delta R = \delta p$), the potential energy dissipation is given by

$$\delta U = V(\rho g)\delta R = -V\frac{dp}{dR}\delta R = -V\delta p. \tag{2.19}$$

The corresponding change in cavity enthalpy is simply given by the first law of thermodynamics,

$$\delta H = T\delta S + V\delta p. \tag{2.20}$$

The cavity is assumed to be entirely adiabatic (non-radiative), so entropy S remains constant and $\delta S = 0$. We therefore see that

$$\delta H = V\delta p = -\delta U, \tag{2.21}$$

meaning the amount of kinetic energy associated with the thermal gas rushing to refill the cavity ($-\delta U$) wake is equal to the enthalpy (free energy) of the cavity. This is the general idea behind "effervescent" cavity heating models like those described by Begelman (2001); Ruszkowski & Begelman (2002).

The net implication is that the $\sim 10^{58}$ erg associated with the western large cavity is available to heat the ambient ICM. Even if only a small fraction of this energy reservoir has so far been tapped, it would certainly be enough to heat the ambient gas on the "inner" boundary of the cavity by ~ 1.5 keV, accounting for the "hot arc" feature in the X-ray temperature map (see, e.g., McNamara & Nulsen 2007, and references therein). This particular result may be one of the very first instances in which cavity enthalpy dissipation is observed to heat the ambient X-ray gas, as is predicted in effervescent AGN feedback models. This is one of the primary results of this thesis.

2.9 Summary & Concluding Remarks

The chief results of this chapter can be summarized as follows

- Our deeper X-ray data confirm that the X-ray emission in the central $60''$ of A2597 exhibits a high degree of spatial anisotropy on the scale of the central brightest cluster galaxy ($\sim 30''$).
- The degree of spatial anisotropy in the X-ray surface brightness distribution increases with decreasing radius from the center of the BCG. At all radii the X-ray emission is extended along the direction of the BCG's isophotal major axis.
- The X-ray emission is permeated by a network of X-ray cavities on $\lesssim 30$ kpc scales. Within this radius, the X-ray surface brightness excesses or deficits with $> 10\sigma$ significance include the (1) "western large cavity" (length ~ 18 kpc), (2) "northern ghost cavity" (diameter ~ 12 kpc), (3) "eastern ghost cavity" (~ 6 kpc), (4) "filament base cavity" (~ 5 kpc), and finally (5) the "X-ray filament" (length ~ 15 kpc).
- The 18 kpc "western large cavity" is cospatial with extended 330 MHz radio emission, and is also aligned along the same position angle as the "X-ray filament", a ~ 3 kpc-scale high velocity dispersion stream of molecular gas, the VLBA jet axis on 50 pc scales, and extended 1.3 GHz radio emission. That the 8.4 GHz source is offset from this common axis suggests that the radio jet has only recently (within the past ~ 50 Myr) been deflected, perhaps by ambient dense gas which has recently been acquired by a cooling flow or a merger.
- Our deeper X-ray data confirm the $> 10\sigma$ significance of a 15 kpc linear soft excess "filament" extending from the central regions toward the northeast. A hardness analysis and our X-ray temperature map are consistent with the interpretation that this is a "cold" filament $\sim 1-1.5$ keV cooler than its immediate surroundings. We suggest that the feature may arise from the dredge-up of low entropy gas by the propagating radio jet, with which it is aligned (in terms of position angle). This scenario is feasible in terms of lower limits on the available energy budget, as inferred from quantitative analysis of the X-ray cavities.
- Our X-ray temperature map reveals a 20 kpc "arc" ~ 1 keV hotter than its immediate surroundings. This feature is cospatial with the eastern boundary of the "western large cavity". We interpret this feature in the context of effervescent AGN heating models, wherein cavity enthalpy is thermalized as ambient keV gas rushes to refill its wake. This may be one of the first instances in which ISM/ICM heating by buoyantly rising X-ray bubbles is observed.

- We find that inferred ages for the young stellar population in the emission line nebula are both younger and older than the inferred ages of the X-ray cavity network and the radio structures which supposedly excavated this cavity network. Low levels (a few $M_{\odot}$ yr^{-1}) of star formation have managed to persist amid AGN feedback. An FUV excess aligned with the northern edge of the radio source may be evidence for compact regions of jet-induced star formation.

3

A Broader Context

Star Formation *and the* AGN Feedback Model

Nature uses as little as possible of anything.
Johannes Kepler, 1571-1630

In this chapter we present results from *Hubble Space Telescope* far ultraviolet (FUV) imaging of the luminous emission-line nebulae in seven CC BCGs associated with an infrared excess. These results were originally published in O'Dea *et al.* (2010), and while we duplicate their presentation here, we augment the original study in two ways: (1) corrections are made to the star formation rates and photon counting exercises. Minor errors are present in the originally published tables (though, importantly, these errors do *not* affect the results or conclusions of O'Dea *et al.* 2010). We also (2) expand discussion of the results, framing them within the larger context of this thesis. We pay particular attention to star formation as it pertains to the AGN feedback model, and elaborate upon our original suggestion (in O'Dea *et al.* 2010) that those sources with elevated star formation rates could be experiencing lower levels of feedback from the AGN.

3.1 Context

As discussed previously, CC BCGs often harbor intense optical emission line nebulae in their central regions. In about half of the cases, low levels ($\sim 1-10\ M_{\odot}\ \mathrm{yr}^{-1}$) of star formation are ongoing amid these warm/cold reservoirs on scales < 30 kpc in clumpy and filamentary distributions that often (but not always) trace the morphology of the emission line nebulae (e.g., O'Dea *et al.* 2004, 2008; Quillen *et al.* 2008; Rafferty *et al.* 2006, 2008; O'Dea *et al.* 2010). In these star forming systems, strong Lyα emission is observed in extended and more diffuse distributions that spatially traces the more compact underlying FUV emission in all observed cases, implying that the latter arises from the former (O'Dea *et al.*, 2004; Baum *et al.*, 2005; O'Dea *et al.*, 2010). In several instances, Lyα and FUV emission is closely tied to the radio morphology suggesting that star formation and associated ionization is present at the edges of radio lobes (see e.g., A2597 in the previous chapter, and A1795, O'Dea *et al.* 2004). As mentioned previously, Lyα and far-ultraviolet continuum observations provide unique constraints on the physical properties of the nebulae in clusters. The far-UV continuum together with optical and infrared observations constrain the star formation history and the properties of young stars associated with the nebula. The Lyα to Hα or Hβ flux ratio is a diagnostic of ionization, metal and dust content (Ferland & Osterbrock, 1985; Binette *et al.*, 1993).

UV emission associated with star formation has been known to exist in CC BCGs for decades (Johnstone *et al.*, 1987; Romanishin, 1987; McNamara & O'Connell, 1989, 1993; McNamara *et al.*, 2004; McNamara, 2004; Hu, 1992; Crawford & Fabian, 1993; Hansen *et al.*, 1995; Allen, 1995; Smith *et al.*, 1997; Cardiel *et al.*, 1998; Hutchings & Balogh, 2000; Oegerle *et al.*, 2001; Mittaz *et al.*, 2001; O'Dea *et al.*, 2004; Hicks & Mushotzky, 2005; Rafferty *et al.*, 2006; Bildfell *et al.*, 2008; Loubser *et al.*, 2009; Pipino *et al.*, 2009). We now know that nearly all BCGs with young stellar populations are in cooling flows (Bildfell *et al.*, 2008; Loubser *et al.*, 2009). However, some BCGs in cooling flows do not have significant star formation (Quillen *et al.*, 2008; Loubser *et al.*, 2009). Hence BCGs exhibiting elevated rates of star formation could be those experiencing a low level of feedback from the AGN. Evidence for residual cooling can be inferred from the reservoirs of cold gas found in BCGs. Alternatively, star formation could also be attributed to stripping from a gas rich galaxy (Holtzman *et al.*, 1996). Recent estimates of condensation and star formations rates show that in a few systems they are in near agreement (e.g., O'Dea *et al.* 2008). Recent work suggests that star formation tends to occur when the central cooling time drops below a critical value (Rafferty *et al.*, 2008; Voit *et al.*, 2008; Cavagnolo *et al.*, 2008). In our study of 62 BCGs with the Spitzer IRAC and MIPS we found that about half of the BCGs in our

sample showed evidence for mid-IR emission produced by star formation (Quillen *et al.*, 2008). The IR emission was typically unresolved by the 8 arcsec (FWHM) PSF of MIPS at 24 μm.

In O'Dea *et al.* (2010) and this chapter, we enlarge the sample of objects studied by O'Dea *et al.* (2004) to include more distant BCGs and those with higher star formation rates (estimated in the IR). Brightest cluster galaxies with high Hα luminosities were chosen from the ROSAT Brightest Cluster Sample (BCS, Ebeling *et al.* 1998). Their Hα luminosities are in the range 10^{42}–10^{43} erg s^{-1}. These galaxies have been observed with the *Spitzer Space Telescope* (Quillen *et al.*, 2008; O'Dea *et al.*, 2008). The FUV *HST* observations presented here allow us to confirm that on-going star formation is present in the BCGs and to determine its spatial scale and morphology (subject to dust extinction).

3.2 Observations

3.2.1 FUV continuum and Lyα images

Observations were obtained with the Solar Blind Channel (SBC) MAMA detector of the Advanced Camera for Surveys (ACS) (Clampin *et al.*, 2004) on the *Hubble Space Telescope* (*HST*) during cycle 11 (program 11230, PI: O'Dea). Each galaxy was observed in two long pass filters, the one containing the Lyα line, the other redward of this line to measure the continuum. The F140LP filter containing the Lyα line was used for all galaxies except the nearer BCGs, Abell 11 and Abell 1664, which were observed using the F125LP filter. The continuum filter chosen was F140LP for objects with redshift $z < 0.11$, F150LP for objects with redshift $0.11 < z < 0.19$ (ZWCL8193, Abell 11, and Abell 1664) and the F165LP filter for the remaining objects with $0.19 < z < 0.31$ (Abell 1835, ZWCL348, RXJ 2129+00, ZWCL3146). Observations were obtained using a 3 point position dither. The exposure time in each filter was 1170s so that the observations in the two filters was approximately one *HST* orbit per galaxy. Observations were taken between March 2008 and February 2009. The long pass filters, F125LP, F140LP, F150LP, and F165LP, have pivot wavelengths of 1438, 1527, 1611 and 1758 Å, respectively, and similar maximum wavelengths of 2000 Å but minimum or cut-off wavelengths of 1250, 1370, 1470 and 1650 Å respectively. The pixel scale for the SBC is approximately $0\farcs034 \times 0\farcs030$/pixel. The camera field of view is $34\farcs6 \times 30\farcs8$. These FUV observations are summarized in Table 3.1.

The ACS/SBC images were reduced with the ACS calibration pipeline producing calibrated drizzled images. Continuum images were shifted to the position of the line images and subtracted from the line images after multiplication by an adjusted corrective factor larger than 1 to take

Table 3.1. **HST FUV Observations of Star Forming CC BCGs**

Source	RA	Dec	z	kpc/″	Line/Cont	Filter
Abell 11	00:12:33.87	-16:28:07.7	0.151	2.60	Line	F125LP
					Cont.	F150LP
Abell 1664	13:03:42.52	-24:14:43.8	0.128	2.26	Line	F125LP
					Cont.	F150LP
Abell 1835	14:01:02.10	+02:52:42.8	0.253	3.91	Line	F140LP
					Cont.	F165LP
ZWCL 348	01:06:49.39	+01:03:22.7	0.254	3.92	Line	F140LP
					Cont.	F165LP
ZWCL 3146	10:23:39.62	+04:11:10.8	0.290	4.32	Line	F140LP
					Cont.	F165LP
ZWCL 8193	17:17:19.21	+42:26:59.9	0.175	2.94	Line	F140LP
					Cont.	F150LP
RXJ 2129+00	21:29:39.96	+00:05:21.2	0.235	3.70	Line	F140LP
					Cont.	F165LP

Note. — *HST* observations obtained under program 11230 (PI: O'Dea). The exposure time in each long pass filter was 1170s. Positions are given in degrees for epoch J2000 and are measured from radio source positions in archival VLA data at 8.5 or 5 GHz. See Table 3.2 for a summary of the archival radio images.

into account the additional continuum photons present in the line images. Our procedure was to increase the correction factor until regions of the image became negative. FUV and continuum subtracted Lyα images are shown in Figures 3.1-3.7. The fluxes of the continuum subtracted Lyα are given in Table 3.3.

3.2.2 Comparison images

Observed at the same time were optical images with the WPFC2 camera on board *HST* using the broad band F606W filter for Abell 1664, ZWCL 8193 and RXJ 2129.6+0005. Visible broad band images observed with WFPC2 were available from the Hubble Legacy Archive for the remaining galaxies in either the F702W filter (Abell 1835) or the F606W filter (ZWCL 348, ZWCL 3146, and Abell 11). The broad band optical images are shown for comparison in Figures 3.3-3.7.

We have overlaid 3μm continuum observations as contours in Figures 3.3-3.7 on the FUV continuum images. These images were taken with the IRAC camera on the *Spitzer Space Telescope* and are described by Egami *et al.* (2006); Quillen *et al.* (2008). We find that the FUV and Lyα emission is located near the center of the brightest cluster galaxies as seen at 3μm.

Chandra X-ray Observatory observations with the (Advanced CCD Imaging Spectrometer (ACIS) were available from the archive for four of the galaxies; Abell 1664, Abell 1835, ZWCL 3146, and RXJ 2129+00. Exposure times are 11, 22, 49, and 12 ks respectively. The event files were binned to 1″pixels and the resulting images smoothed with the *ciao* adaptive smoothing routine *csmooth* using the algorithm by Ebeling *et al.* (2006). Constant surface brightness X-ray contours are shown for these four galaxies in Figures 3.4, 3.5, 3.7 and 3.9 overlaid on the continuum subtracted Lyα images.

Where available, we selected high resolution VLA observations from the NRAO archive. For some sources we chose an additional data set in order to obtain a complementary lower resolution image. The NRAO AIPS package was used for the calibration, imaging, self-calibration, and deconvolution. The properties of the final images are given in Table 3.2. We detected a faint point source in all the BCGs. The flux densities of the point sources are given in Table 3.4. These high resolution observations are not sensitive to very diffuse emission.

Figures 3.3-3.7 have been centered at the location of the central radio sources as measured from VLA archival data at 5 or 8.5 GHz (with positions listed in Table 4.1). Coordinate errors measured from *HST*, *Spitzer Space Telescope* and ACIS *Chandra X-ray Observatory* observations are of order an arcsecond. The FUV and Lyα images lack point sources that could be used to register the images at sub-arcsecond scales.

3.3 Results

3.3.1 UV Morphology

We find that all 7 galaxies observed display extended emission in both FUV continuum and Lyα emission. The FUV continuum is patchy, as was true for Abell 1795 and Abell 2597 (O'Dea *et al.*, 2004). As discussed in that work, the FUV continuum is likely associated with young stars in star clusters. The Lyα morphology contains both clumps and a more diffuse or filamentary component. The diffuse component in seen in Lyα but not in the FUV continuum, e.g., ZWCL 8193 (Figure 3.1). Diffuse or filamentary Lyα was also seen by O'Dea *et al.* (2004) in Abell 1795 and Abell 2597. The association between the Lyα and FUV continuum implies that the source of the FUV

Table 3.2. **VLA Archival Data**

Source	Date	ID	ν (GHz)	Array	CLEAN Beam ($'' \times ''$@$^\circ$)	rms noise (μJy)
Abell 11	6-Jun-1998	AB878	8.46	A/B	0.74×0.38@ 80.7	74
	6-Oct-2002	AL578	1.46	B/C	14.9×7.2 @-71.7	80
Abell 1664	14-Nov-1994	AE099	4.86	C	9.2×4.2 @ -24.7	100
Abell 1835	23-Apr-1998	AT211	4.76	A	0.45×0.39 @ 30.0	47
ZWCL 348	28-May-1994	AK359	4.86	A/B	1.59×0.52 @ -72.2	66
ZWCL 3146	14-Nov-1994	AE099	4.86	C	4.61×4.42 @ 46.3	60
	29-Jan-1997	ACTST	4.86	A/B	1.52×0.47 @ -72.2	50
ZWCL 8193	15-Aug-1995	AM484	8.44	A	0.28×0.23 @ -83.1	180
	27-Jun-1997	AE110	4.86	C	4.29×3.75 @ -34.9	70
RXJ 2129+00	12-Apr-1998	AE117	8.46	A	0.26×0.24 @ -15.0	50
	07-Jul-2002	AH788	4.86	B	1.28×1.20 @ 1.7	35

Note. — The data for ZWCL 8193 has poor absolute flux density calibration.

continuum contributes to the ionization of the Lyα emitting gas.

All our BCGs display asymmetry in the FUV emission. In Abell 11, the FUV continuum and Lyα emission is arranged in an extended clump cospatial with the visible nucleus, with a more diffuse component about 2$''$west of the nucleus (also seen in the optical image). The main clump of emission is slightly offset from the center of the *Spitzer* IRAC 3μm isophotes (see Figure 3.3). In Abell 1664, three large clumps of FUV and Lyα trace the disturbed morphology of the host galaxy as observed in the optical. Additionally, there is a low surface brightness filament of Lyα emission extending ~ 25 kpc to the south of the three bright clumps. This filament is not associated with any optical counterpart in the WFPC2 image or any FUV continuum emission. The 3μm peak, cospatial with the galaxy's nucleus, is also cospatial with the dust lanes in the optical image (see Figure 3.4). Abell 1835 has also been observed by Bildfell *et al.* (2008) who measure a size for the blue star forming region of 19 ± 2 kpc, which is in good agreement with our measurement of ~ 17 kpc for the size of the Lyα emission (Table 3.3). In Abell 1835 the 3μm contours are also not centered on the brightest regions seen the FUV, Lyα or visible band images (see Figure 3.5). For ZWCL 348 the visible and 3μm emission peaks are nearly centered and the FUV emission peaks on the center of the galaxy. However the visible band image shows that the galaxy is disturbed and the outer contours seen at 3μm are not round (see Figure 3.6). The Lyα emission extends eastwards from the nucleus much further than to the west. In ZWCL 3146 the FUV and Lyα emission are centered on the 3μm contours (see Figure 3.7). For ZWCL 8193 there is a nuclear bulge in the

Table 3.3. **Lyα & FUV Continuum Properties**

Source	Aperture Radius ($''$)	Cont. Sub. Lyα Flux (10^{-14} erg cm^{-2} s^{-1})	FUV Flux (10^{-14} erg cm^{-2} s^{-1})	L.A.S. Lyα arcsec (kpc)	L.A.S. FUV arcsec (kpc)	Morphology
Abell 11	2.0	8.8±0.3	18.9±0.2	5.5 (14.5)	4.5 (11.7)	Lopsided, clumpy FUV, similar Lyα
Abell 1664	3.0	7.7±0.4	39.8±0.2	18.0 (40.7)	12.2 (27.6)	Very clumpy & patchy, long filament to S
Abell 1835	2.0	14.4±0.3	22.9±0.2	4.3 (17.0)	3.8 (14.8)	Symmetric "core", outer filaments
ZWCL 348	2.0	9.9±0.3	11.8±0.3	6.4 (24.8)	3.3 (12.9)	Clumpy, patchy, lopsided
ZWCL 3146	3.0	9.3±0.3	17.7±0.2	6.5 (28.1)	5.1 (22.0)	More symmetric, diffuse
ZWCL 8193	2.0	6.3±0.4	42.8±0.2	10.8 (31.8)	8.8 (25.8)	Clumpy, filamentary, lopsided
RXJ 2129+00	2.0	1.9±0.7	2.1±0.7	4.1 (15.3)	2.0 (7.4)	Lyα lopsided "shell", FUV faint

Note. — Fluxes were measured using aperture photometry and an aperture that covers the bulk of the emission visible in Figures 1-7. Errors are from count rate statistics. In general, the morphologies of the Lyα and FUV continuum emission were generally similar (unless otherwise noted), and the FUV emission typically spanned a slightly smaller linear extent than did the Lyα as it is less diffuse and extended. See the associated discussion in Section 3.

optical and 3μm images. However FUV and Lyα emission is brighter north of the nucleus, and has a spiral shape suggesting that a smaller galaxy has been recently disrupted in the outskirts of the BCG (see Figure 3.8). The host galaxy is an elliptical in a rich environment with several nearby dwarf satellites. The disturbed morphology of the host galaxy is suggestive of a recent or ongoing series of minor mergers. RXJ 2129+00 displays Lyα emission which extends on only the north-eastern side of the galaxy. The offset between radio and Lyα peaks is small and so may be due to a registration error in the *HST* image (see Figure 3.9).

"Clumpiness" of FUV emission

We find that most of these BCGs display strong asymmetries or uneven distributions in their star formation as seen from the FUV continuum images (see Fig. 3.2). For these galaxies, 1$''$corresponds to 2–4 kpc (see Table 4.1) thus these asymmetries are on a scale of order 10-50 kpc. On smaller scales, the FUV morphology is generally more clumpy and filamentary than is the associated Ly-alpha component. For the purposes of this thesis, we qualitatively define a "clump" as a compact region of emission a factor of ~ 2 brighter than the surrounding lower surface brightness diffuse component. Abell 11, 1664, ZWCL 8193, and RXJ 2129+00 may be described as "clump-dominated", in which the majority ($> 50\%$) of the FUV flux is associated with compact (< 2 kpc) bright clumps. For example, the majority of FUV emission in Abell 11 is associated with three bright clumps, the largest of which (the northern-most clump) extends ~ 0.6 kpc. The three bright clumps together contribute $>\sim 60\%$ of the total FUV flux from the source. The FUV morphology

of RXJ 2129+00 is almost entirely associated with three small ($\sim$ 0.5 kpc) clumps, and appears to lack a diffuse component. For Abell 1835, ZWCL 348, and ZWCL 3146, the distinction between clumpy FUV emission and the diffuse component is less clear, and the flux seems to more gradually peak toward the center than, for example, ZWCL 8193. Note also that these galaxies are vastly more symmetric on $>$ 20 kpc scales than are the "clump-dominated" BCGs.

The high star formation rates of the galaxies studied here compared to others in the ROSAT BCG sample may be related to the large scale X-ray structure. We will discuss this in more detail in the "X-ray morphology" subsection below . Comparisons between Lyα and existing Hα images (not shown) suggest that there are large variations in emission line ratio. This can be explained either by patchy extinction or with shocks, affecting the intrinsic line ratios.

McNamara (1997) classified the morphology of star forming regions in cooling core BCGs (studied using mainly ground based optical observations) into four classes - point, disk, lobe, and amorphous. McNamara (1997) noted that the disks were very rare and that the amorphous morphologies are the most common. All of the seven BCGs studied here fall in the amorphous class. Why are disks so rare? We note that the star formation occurs over a large spatial scale (7-28 kpc). One possibility is that the stars form before the gas can collapse into a disk. In addition, studies of the kinematics of the optical emission line nebulae in cool core BCGs find that the gas motions are mostly turbulent with very little organized rotation (e.g., Heckman *et al.* 1989; Baum *et al.* 1992; Wilman *et al.* 2006, 2009). Thus, the lack of star forming disks may reflect the lack of systematic rotation in the star forming gas.

Radio Emission

We detect a compact radio point source in all seven of the BCGs. In ZWCL 8193 the radio point source is 3″ from the center of the BCG at the location of FUV-bright debris features and may be associated with a merging galaxy (Figure 3.8). The flux densities and spectral indexes of the unresolved emission are given in Table 3.4. We find that the spectral indexes of the point sources are steep. This suggests that the point sources are not flat spectrum parsec scale beamed jets, but are possibly extended on at least tens of parsec scales. We also include FIRST (Becker *et al.*, 1995) flux densities and NVSS (Condon *et al.*, 1998) flux densities and powers in Table 3.4. The FIRST ($\sim$ 5″) and NVSS ($\sim$ 45″) flux densities are in good agreement indicating that there is very little additional flux density on scales between 5 and 45 arcsec. The mean value of the NVSS log powers for the seven BCGs is log P_ν = 24.33; while A1795 is log P_ν = 24.87 and A2597 is log P_ν = 25.42. The radio powers for the seven BCGs are typical for our sample of 62 (Quillen *et al.*, 2008; O'Dea

Table 3.4. **Radio Properties of the Unresolved Emission**

Source	R.A.	Dec.	ν (GHz)	S_ν (mJy)	α	FIRST S_ν (mJy)	NVSS S_ν (mJy)	NVSS log P_ν (W Hz^{-1})
Abell 11	00:12:33.87	-16:28:07.7	8.46	21.3	-0.79	···	94.3	24.66
			1.46	85.6	···	···	···	···
Abell 1664	13:03:42.52	-24:14:43.8	4.86	14.5	-0.74	···	36.4	24.09
Abell 1835	14:01:02.10	+02:52:42.8	4.76	11.2	-0.84	31.3	39.3	24.75
ZWCL 348	01:06:49.39	+01 03 22.7	4.86	1.1	-0.93	3.5	~ 1.4	23.31
ZWCL 3146	10:21:03.79	+04 26 23.4	4.86	0.6	-1.56	~ 4.2	7.1	24.14
ZWCL 8193[1]	17:17:19.21	+42 26 59.9	8.44	64.8	-0.58	132.5	133.5	24.94
			4.86	89.2	···	···	···	···
RXJ 2129+00	21:29:39.96	+00:05:21.2	8.46	4.4	-0.86	24.3	25.4	24.48
			4.86	7.1	···	···	···	···

Note. — Cols. 2 and 3. The right ascension and declination (J2000) of the unresolved radio source. Col 4. The frequency of observation. Col 5. The flux density of the point source in mJy. See Table 3.2 for details pertaining to these archival VLA observations. Col 6. The spectral index of the point source. We have used (1) the reprocessed archival data for Abell 11, ZWCL 8193 and RXJ 2129+00, (2) the reprocessed archival data and the FIRST flux densities for Abell 1835, ZWCL 348. and ZWCL 3146, and (3) the reprocessed archival data and the NVSS flux density for Abell 1664. The spectral index is defined such that $S_\nu \propto \nu^\alpha$. Col 7. The integrated flux density at 1.4 GHz from VLA FIRST (Becker *et al.*, 1995). Col 8. The integrated flux density from NVSS (Condon *et al.*, 1998). Col 9. The power at 1400 MHz in the rest frame of the source using the NVSS flux density.

et al., 2008).

We detect faint jets in RXJ 2129+00 and Abell 1835. In RXJ 2129+00 the jet extends about $1''$ to the SE of the core and has a flux density of 1.9 mJy at 8.46 GHz. The jet in Abell 1835 has a total extent of about $1''.5$, and seems to start initially oriented to the West but then curves toward the NW. The jet flux density is 2.3 mJy at 4.76 GHz. For these two we have overlayed radio contours on the images showing Lyα emission so the orientation of the radio emission can be seen. In neither galaxy are the radio jets clearly associated with Lyα emission or lying near line emitting filaments as was true for the nearer galaxies Abell 1795 and Abell 2597 (O'Dea *et al.*, 2004). We suggest that the more powerful radio sources in Abell 1795 and 2597 are able to trigger star formation in their environments, while the weaker radio sources studied here are not. The lack of FUV emission aligned with the radio jet indicates that scattered AGN light (which would be aligned with the jet) does not contribute significantly.

Govoni *et al.* (2009) have found a faint, diffuse "mini-halo" around the BCG in A1835 which extends for several hundred kpc. The diffuse radio emission suggests that the AGN was much more active in the past and/or that A1835 has experienced a cluster merger (e.g., Murgia *et al.* 2009).

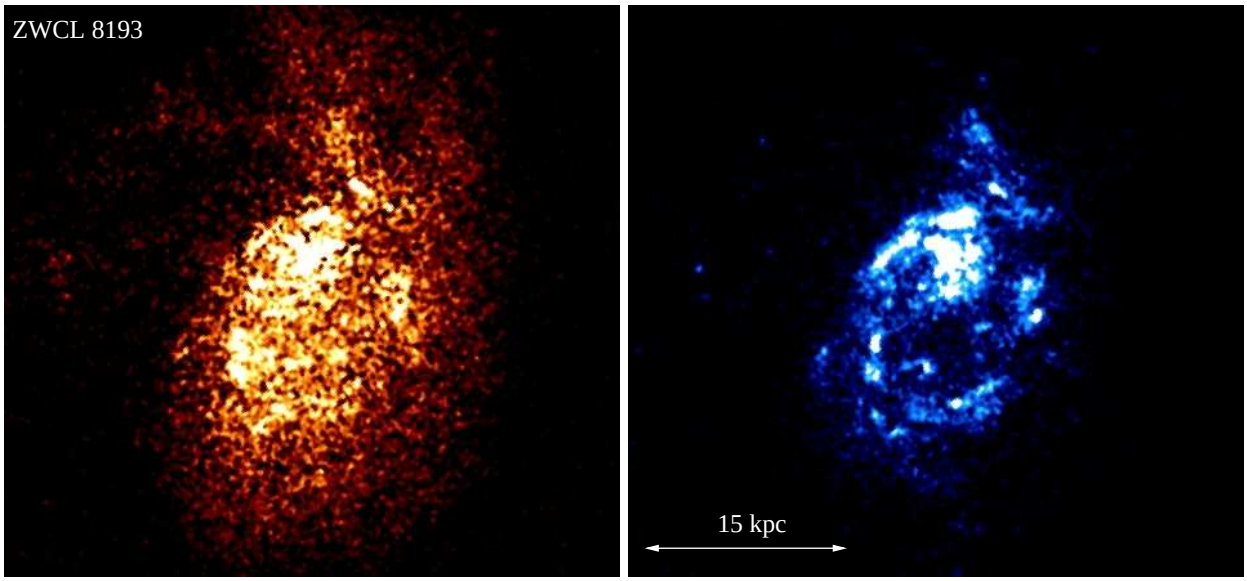

Figure 3.1: Comparison of continuum-subtracted Lyα and FUV continuum images for ZWCL 8193. In general, the Lyα is more diffuse, extended, and smoothly distributed than is the underlying FUV continuum, which is more tightly arranged in clumpy and filamentary morphologies. The FUV continuum likely traces localized sites of star formation, which in turn photoionizes the smoother and more extended Lyα halos.

X-ray Morphology

Here we discuss the X-ray structure and its relation to the BCG in the four sources for which we have X-ray imaging. For Abell 1664, the outer 3μm isophotes extend to the south-west where there is excess X-ray emission (see Figure 3.4). The asymmetric X-ray morphology was also noted by Kirkpatrick *et al.* (2009). Abell 1835 also displays asymmetric X-ray structure (see Figure 3.5, and also Schmidt *et al.* 2001). Though the FUV and Lyα emission are centered on the 3μm contours in ZWCL 3146, again the X-ray emission is lopsided, extending south-east of the nucleus (see Figure 3.7). RXJ 2129+00 also displays asymmetric X-ray emission contours extending to the south-west (see Figure 3.9).

We find that the four BCGs with X-ray imaging display asymmetries in the X-ray emission with Abell 1664 previously noted by Kirkpatrick *et al.* (2009). We also see offsets between the BCG and the peak in the X-ray emission for all sources, ranging from 5 kpc for RXJ 2129+00 to 13 kpc for Abell 1835, with a median offset of $\sim$ 10 kpc for all four.

In their study of 48 X-ray luminous galaxy clusters, Bildfell *et al.* (2008) observed similar significant offsets between the centroid of the brightest X-ray contour and that of the BCG. That

work found a median offset of 14 kpc in their sample (and an average of 44 kpc). Sanderson *et al.* (2009) found that line emitting BCGs all lie in clusters with an offset of < 15 kpc in their sample of 65 X-ray selected clusters. Loubser *et al.* (2009), in their sample of 49 optically selected BCGs, found even larger offsets on average (median 27 kpc, mean 53 kpc). The offset of the BCG from the peak of the cluster X-ray emission is an indication of how close the cluster is to the dynamical equilibrium state, and decreases as the cluster evolves (Katayama *et al.*, 2003). Our BCGs have offsets which are below the median for optically selected BCGs (Bildfell *et al.*, 2008; Loubser *et al.*, 2009) and are consistent with the trend for BCGs in cooling flows to have small offsets $\lesssim 10$ kpc (Bildfell *et al.*, 2008; Sanderson *et al.*, 2009) (but not seen by Loubser *et al.* 2009).

Comparison to CO and Hα observations

Emission from CO remained unresolved at a resolution of 6″ for Abell 1835 and ZWCL 3146 (Edge & Frayer, 2003). The Spitzer MIPS observations of these BCGs did not spatially resolve the 24μm emission (Quillen *et al.*, 2008; Egami *et al.*, 2006). However, the IRAC observations of Abell 1664 and ZWCL 8193 did resolve regions of very red color centered on the nucleus with a size of a few arc seconds (Quillen *et al.*, 2008). For comparison the point spread function FWHM for IRAC camera is 1.″7 at 3 μm (IRAC band 1) and 2.″2 at 8 μm (IRAC band 4) and for MIPS is 7″at 24 μm. Our *HST* FUV continuum images show that the star formation regions in these galaxies extend over a range of roughly 2 to 12 arcseconds, corresponding to 7-28 kpc (Table 3.3). These sizes are consistent with the upper limits from the CO and Spitzer MIPS observations.

Abell 1664 has been observed using integral field spectroscopy by Wilman *et al.* (2006) in the Hα line. The continuum subtracted Lyα emission image resembles the Hα image shown as Figure 2 by Wilman *et al.* (2006), with a bright spot about 2″from the nucleus to the south west. The bright spot we see just north of the nucleus does correspond to an Hα emission feature. However the Ly emission is brighter north west of the nucleus rather than north east of the nucleus as is true in Hα. It is likely that a more detailed comparison will reveal a large variation in Lyα to Hα ratio suggesting either large variations in extinction or shock emission as photoionization models to predict a narrower range of intrinsic emission ratios (Ferland & Osterbrock, 1985, 1986).

In A1835, the Hα and Lyα are both elongated along a NW-SE direction (Figure 3.5. We also see a dust lane along that orientation in the WFPC2 F702W image. The Hα integral field spectroscopy by Wilman *et al.* (2006) shows a velocity shear of ~ 250 km s^{-1} along that direction which they suggest may be due to rotation.

Wilman *et al.* (2006) also observed ZWCL 8193 and detected Hα emission at the galaxy center

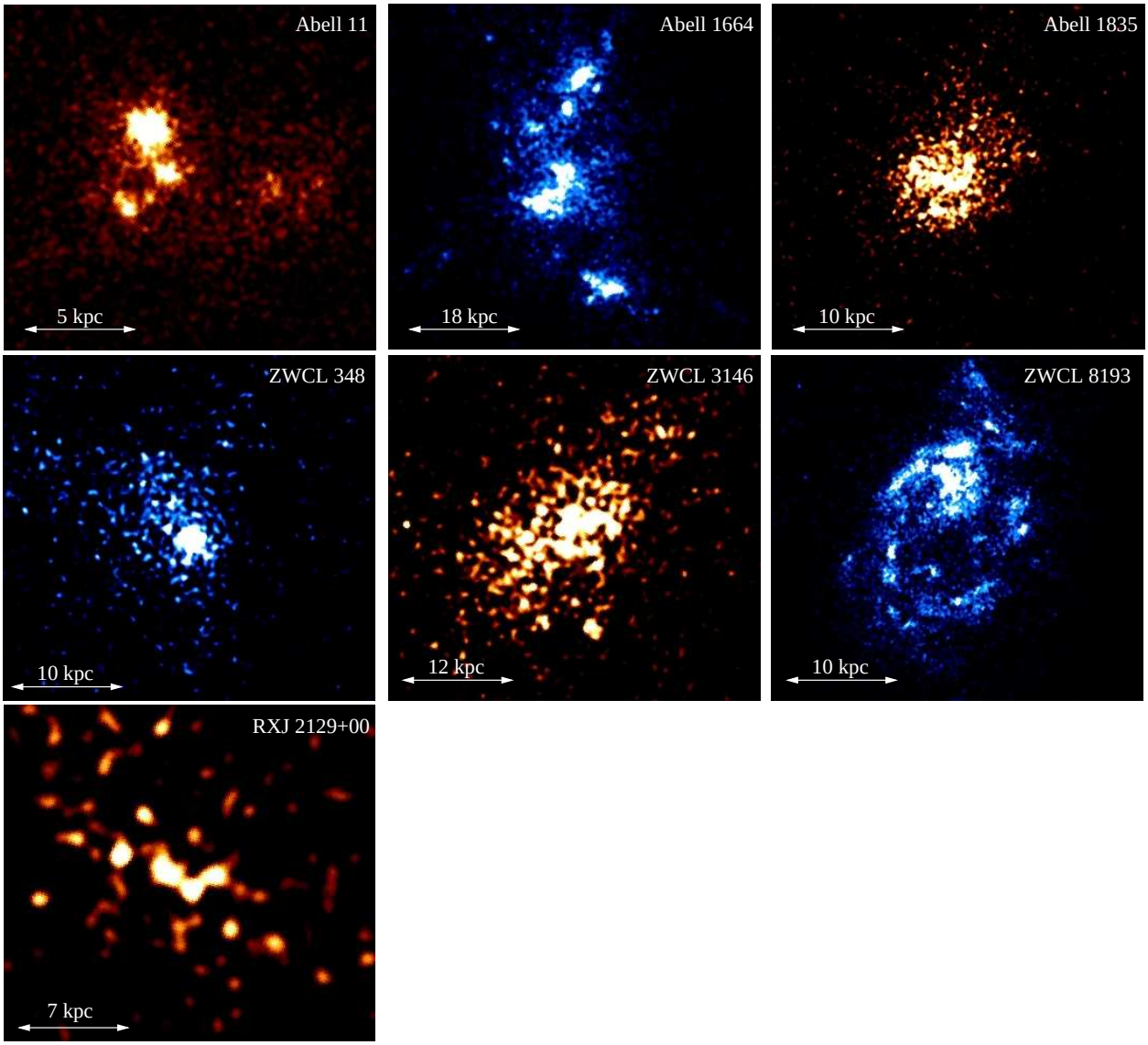

Figure 3.2: *HST*/ACS FUV images of the BCGs in our sample. Many exhibit clumpy and filamentary morphologies on < 10 kpc scales and general asymmetries on > 20 kpc scales. Abell 11, 1664, ZWCL 8193, and RXJ 2129+00 may be described as "clump-dominated", in which the majority ($> 50\%$) of the FUV flux is associated with compact bright clumps (as opposed to the lower surface brightness diffuse component). East is left, North is up.

Table 3.5. **Star Formation & Cluster Properties**

Source (1)	M_{H_2}) ($\times 10^{10} M_\odot$ yr^{-1}) (2)	SFR$_{\rm IR}$ ($M_\odot$ yr^{-1}) (3)	SFR$_{\rm H\alpha}$ ($M_\odot$ yr^{-1}) (4)	SFR$_{\rm FUV}$ ($M_\odot$ yr^{-1}) (5)	Balmer Dec ($F\left[H\alpha/H\beta\right]$) (6)	Central Entropy (KeV cm^2) (7)	Central Cooling Time (Gyr) (8)
Abell 11	1.1	35	9.7	5.5	...	...	...
Abell 1664	1.9	15	5.6	4.65	5.2	14.40	0.81
Abell 1835	7.9	125	40.5	14.66	5	11.44	0.58
ZWCL 348		52	15.5	7.65	4.27	...	...
ZWCL 3146	7.0	67	47.1	16.0	3.7	11.42	0.59
ZWCL 8193	1.5	59	7.6	6.34	5.9	...	...
RXJ 2129+00		13	2.3	1.11	> 2	21.14	0.82

Note. — (1) Source name; (2) Molecular gas mass estimates. For Abell 11, Abell 1665, Abell 1835, and ZWCL 3146, these values are taken from Edge (2001), and have been corrected to the value of the Hubble constant used in this thesis. The ZWCL 8193 molecular mass is from Salomé & Combes (2003). Note also that Egami *et al.* (2006) detected 10^{10} $M_\odot$ of warm molecular hydrogen in ZWCL 3146; (3) Infrared estimated star formation rates, from O'Dea *et al.* (2008) (except for Abell 1835 and ZWCL 3146, which are from Egami *et al.* 2006). The O'Dea *et al.* (2008) star formation rates are estimated from the 8 and 24 μm fluxes presented by Quillen *et al.* 2008; (4) Hα-derived star formation rates, estimated from the limited-aperture observations of Crawford *et al.* (1999) (long slit of width 1.″3). In the case of ZWCL 348, the Hα flux is from the Sloan Digital Sky Survey archive (3″ diameter fiber); (5) FUV-derived star formation rates, from this chapter. These rates have been updated and supersede those presented in O'Dea *et al.* (2010). Neither the Hα or UV based star formation rate estimates have been corrected for internal extinction; (6) Central entropies and (7) cooling times, from Cavagnolo *et al.* (2009).

and in two clumps about 3″ north of the galaxy (see their Figure 17). Their Hα emission more closely resembles our FUV continuum image, though the Hα emission is stronger near the galaxy than north of the galaxy and we see stronger continuum emission north of the galaxy than near the galaxy center. The Hα kinematics are complex. Our Lyα image shows diffuse emission over a region that is about twice the area than the Hα emission. The Lyα emission exhibits a tail curving to the east from the north and almost looks like a spiral galaxy.

3.3.2 Estimated Star Formation Rates

Pipino *et al.* (2009) used optical and NUV colors of BCGs to demonstrate that the UV light is produced by a young rather than old stellar population. We use the FUV continuum flux to estimate star formation rates in these galaxies. The continuum flux was first corrected for Galactic extinction. Extinction correction was done using Galactic extinction at the position of each BCG and the extinction law by Cardelli *et al.* (1989) (as done in Table 5 by O'Dea *et al.* 2004 for Abell 1795 and Abell 2597). We then compared the count rate predicted for the observed filter by the STSDAS synthetic photometry package SYNPHOT for a spectrum produced by STARBURST99[1] (Leitherer *et al.*, 1999; Vázquez & Leitherer, 2005). More details on this method of star formation

[1]http://www.stsci.edu/science/starburst99/

rate estimation can be found in Chapter 4 and in Tremblay *et al.* (2010).

The UV continuum estimated star formation rates are listed in Table 3.5. We compare the UV continuum estimated star formation with those based on the limited aperture Hα fluxes by Crawford *et al.* (1999) (using 1.″3 wide slit) or spectroscopic measurements from the Sloan Digital Sky Survey archive (using a 3″diameter fiber) and those estimated from infrared observations with the *Spitzer Space Telescope* by Egami *et al.* (2006); Quillen *et al.* (2008); O'Dea *et al.* (2008). Neither the UV continuum estimated or Hα estimated star formation rates have been corrected for internal extinction. This Table also lists molecular gas masses by Edge (2001); Salomé & Combes (2003).

Balmer decrements are available for most of the galaxies considered here and range from $\sim 3-5$ (Crawford *et al.*, 1999), see Table 5. Assuming an intrinsic Hα/Hβ theoretical line ratio of 2.86 ("case B" recombination, Osterbrock 1989), the observed Balmer decrement allows us to estimate the color excess associated with the internal extinction in the source, following the parameterization of Cardelli *et al.* (1989):

$$E\left(B-V\right)_{\mathrm{H}\alpha/\mathrm{H}\beta} = \frac{2.5\times\log\left(2.86/R_{\mathrm{obs}}\right)}{k(\lambda_\alpha)-k\left(\lambda_\beta\right)} \tag{3.1}$$

where $R_{\mathrm{obs}} = F\left(\mathrm{H}\alpha\right)/F\left(\mathrm{H}\beta\right)$ is the observed flux ratio, and the extinction curves at Hα and Hβ wavelengths are $k(\lambda_\alpha)\approx 2.63$ and $k\left(\lambda_\beta\right)\approx 3.71$, respectively, as given by Cardelli *et al.* (1989). One caveat is that if processes other than recombination (e.g., shocks, cosmic ray heating) contribute to Hα, the intrinsic Hα/Hβ ratio would be higher than the theoretical "Case B" value and the estimated extinctions would be upper limits. With this possibility in mind, the upper-limit intrinsic optical extinction is $E(B-V)\sim 0.6$ for a Balmer decrement of 5, corresponding to an extinction in the FUV of $A_{\mathrm{FUV}}\sim 5.5$ and therefore a correction factor of 160 to the measured flux.

We note from Table 3.5 that IR star formation rates exceed those estimated in Hα and these exceed those estimated from the FUV continuum. This would be consistent with patchy but significant levels of extinction. The correction factor estimated for the UV photometry of 160 for a Balmer decrement of 5 is vastly higher than that required to make up the deficit of star formation rates estimated between the UV and (e.g.) the IR. Large levels of extinction are also likely because of the high molecular gas content in these galaxies and the dust lanes seen in the optical images. Previous comparisons by Hu (1992) between Hα and Lyα flux suggested modest extinctions intrinsic to the cluster of order $E(B-V)\approx 0.09-0.25$. This was done assuming an unabsorbed Lyα/Hα ratio of 13 for photoionization and collision models (Ferland & Osterbrock, 1986). However the

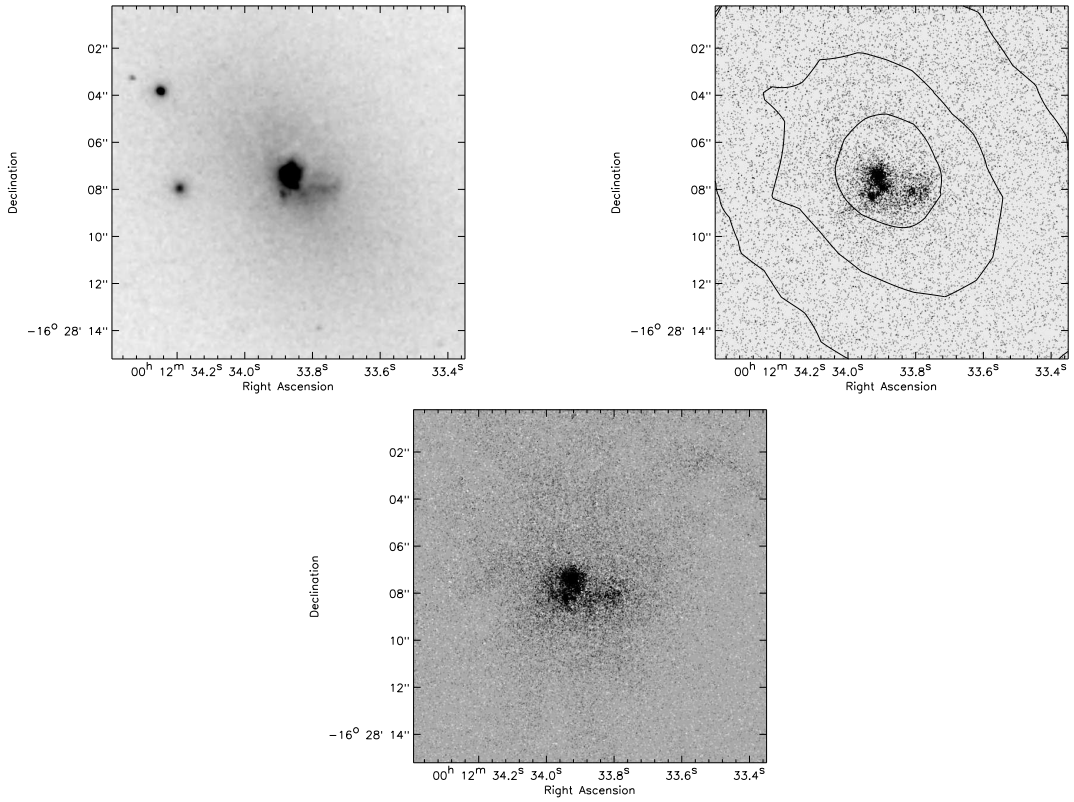

Figure 3.3: Abell 11. (upper left) *HST* WFPC2 F606W optical image. Note the dust lane. (upper right) *HST* SBC FUV continuum image with 3μm *Spitzer* IRAC band 1 contours overlayed. Contour separation is a factor of two in surface brightness. (bottom) Continuum subtracted *HST* SBC Lyα image of Abell 11. At the redshift of Abell 11 (z = 0.151), 1$''$ corresponds $\sim$ 2.6 kpc.

BCGs considered by Hu (1992) were not chosen via their Hα luminosity. As Hα luminosity is correlated with both molecular gas mass and infrared luminosity (O'Dea *et al.*, 2008) it is perhaps not surprising that the sample considered here would have higher estimated internal extinctions than the same considered by Hu (1992).

In short, FUV estimated star formation rates are generally $\sim$ 3 to $\sim$ 12 times lower than those estimated from the *Spitzer* observations. Balmer decrements and molecular gas observations suggest that internal extinction could be extremely high in some regions. The discrepancy between the estimated star formation rates and the internal extinction correction factor from the Balmer decrement suggest that internal extinction is patchy. As the infrared estimated star formation rate is least sensitive to extinction, it can be considered the most accurate, and suggests that about 90% of the FUV continuum has been absorbed. When taking patchy extinction into account, the discrepancy between star formation rates estimated at different wavelengths may be reconciled. Moreover, even

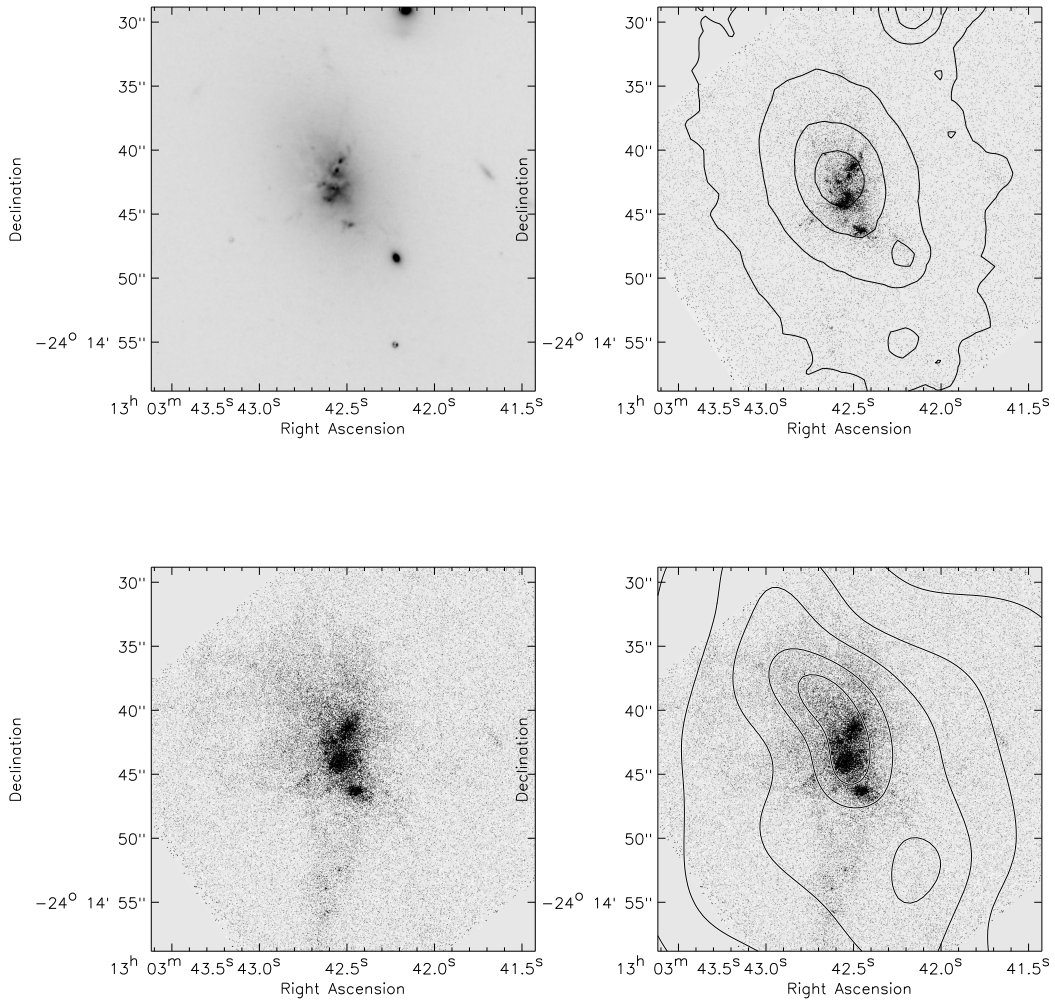

Figure 3.4: Abell 1664. (*upper left*) *HST* WFPC2 F606W optical image of Abell 1664. Note the dust lane. (*upper right*) *HST* SBC FUV continuum image with 3μm *Spitzer* IRAC band 1 contours overlayed. Contour separation is a factor of two in surface brightness. (*lower left*) Continuum subtracted *HST* SBC Lyα image of Abell 1664. (*lower right*) Continuum subtracted Lyα image with *CXO* X-ray contours. The peak of the Lyα emission is cospatial with that of the X-ray emission, although a second peak in the X-ray is detected to the southwest where there is a deficit of Lyα. At the redshift of Abell 1664 (z = 0.128), 1$''$corresponds $\sim$ 2.3 kpc.

when accounting for internal extinction, a one-to-one correspondence between star formation rates measured in the UV and IR are not necessarily expected, as the associated star formation indicators in those wavelength regimes may probe different properties and timescales associated with the young stellar component (e.g., Johnson *et al.* 2007).

O'Dea *et al.* (2008) found that in gas-rich star forming BCGs the nominal gas depletion time scale is about 1 Gyr. Since star formation is not highly efficient, it seems likely that 1 Gyr is an upper limit to the life time of the star formation. Pipino *et al.* (2009) suggest that the star formation in BCGs is relative recent with ages less than 200 Myr. Thus, a typical star formation rate of 50 $M_\odot$ yr^{-1} would result in a total mass of less than 10^{10} $M_\odot$ which is a small fraction of the total stellar mass in a BCG (e.g., von der Linden *et al.* 2007) as also noted by, e.g., Pipino *et al.* (2009).

O'Dea *et al.* (2008) noticed a discrepancy between the infrared estimated star formation rates and the size of the star forming regions. Here we have confirmed that the star forming regions are not large and remain under 30 kpc. This puts the galaxies somewhat off the Kennicutt relation (Kennicutt Jr., 1998) but (as shown by O'Dea *et al.* 2008 in their Figure 8) only by a modest factor of a few. While we confirm the discrepancy we find that it is small enough that it could be explained by other systematic effects such as an overestimate of the H_2 mass. The CO to H_2 conversion factor is suspected to be uncertain by a factor of a few (e.g., Israel *et al.* 2006). Thus, there may be no significant discrepancy between the size of the star forming regions as measured in the FUV and that predicted with the Kennicutt relation.

3.3.3 Is the young stellar population sufficient to ionize the nebula?

The fact that the Lyα morphology closely traces that of the underlying FUV continuum emission suggests that the latter provides at least a significant fraction of ionizing photons for the former, and that the nebula is ionized locally. Here we explore this argument more quantitatively, in considering whether the observed FUV continuum is consistent with a sufficient number of hot stars required to ionize the nebula. This question can be addressed using simple arguments outlined by Zanstra (1929) and employed in similar contexts by (e.g., Baum & Heckman 1989a; O'Dea *et al.* 2004). We assume a case B recombination scenario (Osterbrock, 1989), in which the medium is optically thin to Balmer photons but optically thick to Lyman photons, and that in 10^4 K gas, $\sim 45\%$ of all Balmer photons will emerge from the nebula as Hα photons. We further assume that all ionizing photons that are emitted by the stars are absorbed by the gas. This makes our estimate a rough lower limit, as in reality, a significant fraction of ionizing photons will escape, increasing the number of required stars.

Table 3.6. **Can Hot Stars Ionize the Nebulae?**

Source (1)	Hα Luminosity (erg s^{-1} cm^{-2}) (2)	$Q_{required}$ (photons s^{-1}) (3)	SFR($Q_{required}$) ($\dot{M}_\odot$ yr^{-1}) (4)	$\left(\frac{SFR_{FUV}}{SFR[Q_{required}]}\right)$ (5)
Abell 11	...	...	...	...
Abell 1664	6.38×10^{41}	4.64×10^{53}	2.12	2.17
Abell 1835	1.68×10^{42}	1.22×10^{54}	5.58	2.09
ZWCL 348	1.95×10^{42}	1.41×10^{54}	6.47	0.94
ZWCL 3146	3.29×10^{42}	2.39×10^{54}	1.10	1.13
ZWCL 8193	2.79×10^{42}	2.03×10^{54}	9.29	0.58
RXJ 2129+00	3.33×10^{40}	2.42×10^{52}	1.11	8.1

Note. — Results of a photon-counting exercise designed to determine whether there are sufficient hot stars present (giving rise to the underlying FUV continuum) to ionize the emission-line nebula. We have used the Zanstra (1931) method relating the Hα emission line luminosity with the number of ionizing photons required to give rise to that luminosity, assuming all ionizing photons are absorbed in 10^4 K gas obeying a case B recombination scenario. (1) Source name; (2) Hα luminosities in erg s $^{-1}$ cm^{-2}, from Crawford *et al.* (1999) excepting ZWCL 348, whose Hα luminosity is from the SDSS archive; (3) number of ionizing photons, per second, required to ionize the nebula, as estimated using the Zanstra (1931) method described in section 3.3; (4) star formation rate required to power the nebula, estimated by comparing $Q_{required}$ with a STARBURST99 model calculating the number of photons with energies greater than 13.6 eV for a 10^7 yr old starburst assuming a continuous star formation rate of 1 $M_\odot$ yr^{-1} and an IMF with an upper mass cutoff of 100 $M_\odot$ and slope α = 2.35; (5) Comparing the value calculated in column (4) with the "observed" star formation rate as estimated by comparing our FUV photometry with the same STARBURST99 model. A ratio greater than 1 indicates that enough ionizing photons are present from the young stellar population to ionize the nebula. Obviously, there are significant uncertainties associated with these estimates. As such, this is meant only as an order-of-magnitude exercise. That the ratios are all of order unity indicates that the FUV emission due to the young stellar population is of sufficient strength to power the emission-line nebula.

Given these assumptions, the number of ionizing photons required to power the nebula can be estimated via its observed Hα luminosity using the Zanstra (1929) method, which relates the emission-line luminosity to $Q_{\rm tot}$, the total number of photons with energies greater than 13.6 eV needed, per second, to ionize the nebula:

$$Q_{\rm tot} = \frac{2.2 L_{\rm H\alpha}}{h\nu_{\alpha}} \text{ photons s}^{-1} \tag{3.2}$$

where $L_{\rm H\alpha}$ is the total nebular Hα luminosity, h is Planck's constant, ν_{α} is the frequency of the Hα line, and 2.2 is the inverse of the 0.45 Balmer photon to Hα photon ratio assumed above.

For each galaxy in our sample (save Abell 11, for which we do not have an Hα luminosity) we have calculated this value and scaled it in terms of a required star formation rate as predicted by the same STARBURST99 models used to calculate the star formation rates based on the FUV continuum. We present these results in Table 3.6. In every case the ratio of the observed star formation rate to that required by the Zanstra method is of order unity, suggesting that the FUV continuum provides a significant fraction of ionizing photons for the nebula. Note that it is likely that stellar photoionization is not the only source of energy for cooling flow nebula (e.g., Voit & Donahue 1997). This result is consistent with the notion that the nebula is ionized locally by the young stars embedded within it, as supported by the similar morphologies of the Lyα emission and FUV continuum emission. O'Dea *et al.* (2004) undertook a similar exercise in their study of the cool core clusters Abell 1795 and Abell 2597, finding that there were enough hot stars present to within a factor of a few. That work also estimated the degree to which a hidden quasar ionizing continuum would contribute ionizing photons, finding that a modest AGN luminosity could contribute $\sim 10\%$ of what was required.

3.4 Discussion

In this chapter we have presented high angular resolution images in FUV continuum and Lyα of 7 BCGs selected on the basis of IR emission which suggested the presence of significant star formation. We confirm that the BCGs are actively forming stars. This confirms that the IR excess seen in these BCGs is indeed associated with star formation. Our observations are consistent with a scenario in which gas which cools from the ICM fuels the star formation (O'Dea *et al.*, 2008; Bildfell *et al.*, 2008; Loubser *et al.*, 2009; Pipino *et al.*, 2009). The FUV continuum emission extends over a region $\sim 7-28$ kpc (largest linear size) and even larger in Lyα. Both continuum

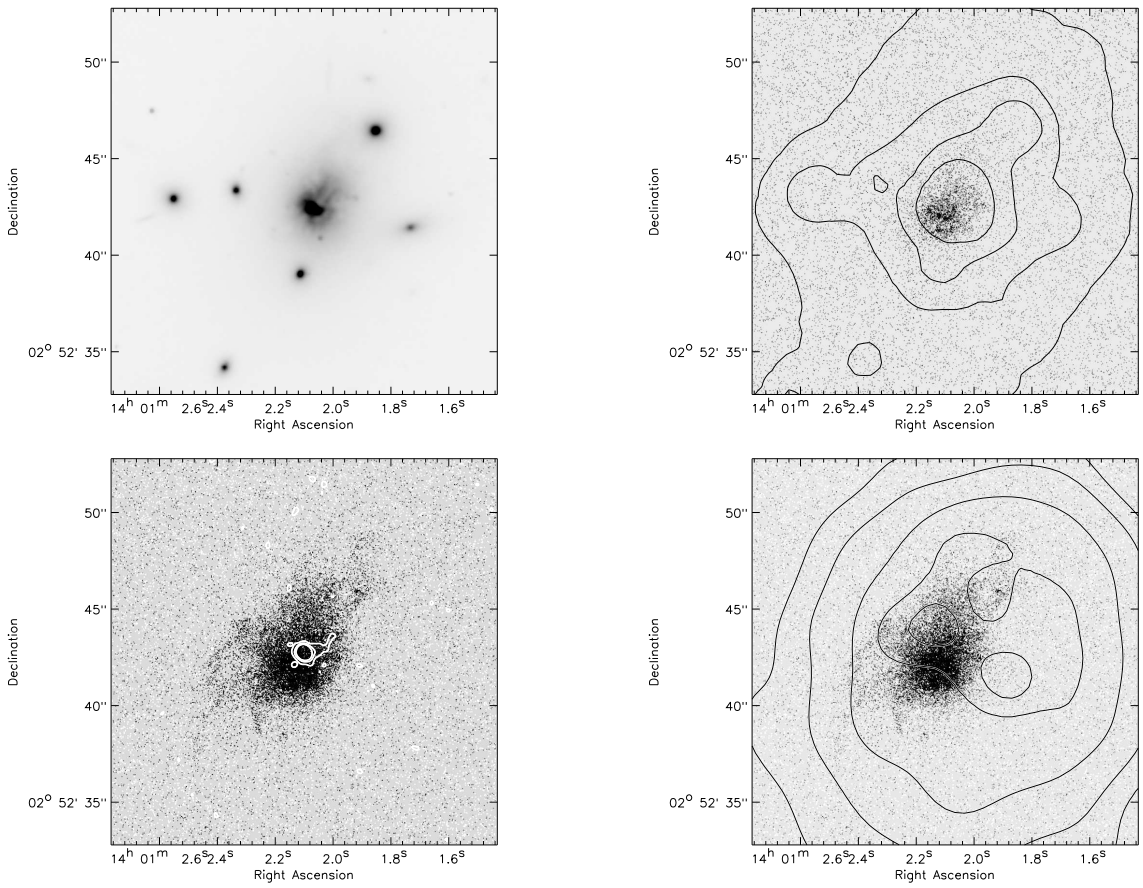

Figure 3.5: Abell 1835. (*upper left*) *HST* WFPC2 *R*-band (F702W) image of Abell 1835. Note the dust lane. (*upper right*) *HST* SBC FUV continuum image overlayed with *Spitzer* IRAC 3μm contours. (*lower left*) Continuum subtracted *HST* Lyα image of Abell 1835 (gray scale) with 5 GHz VLA radio contours. There is no obvious relation between the Lyα and the radio jet. (*lower right*) Continuum subtracted Lyα image with *Chandra* X-ray contours. As in Abell 1664, the two peaks in X-ray emission are offset from the peak in the Lyα emission. At the redshift of Abell 1835 ($z = 0.253$), $1''$corresponds to ~ 4 kpc.

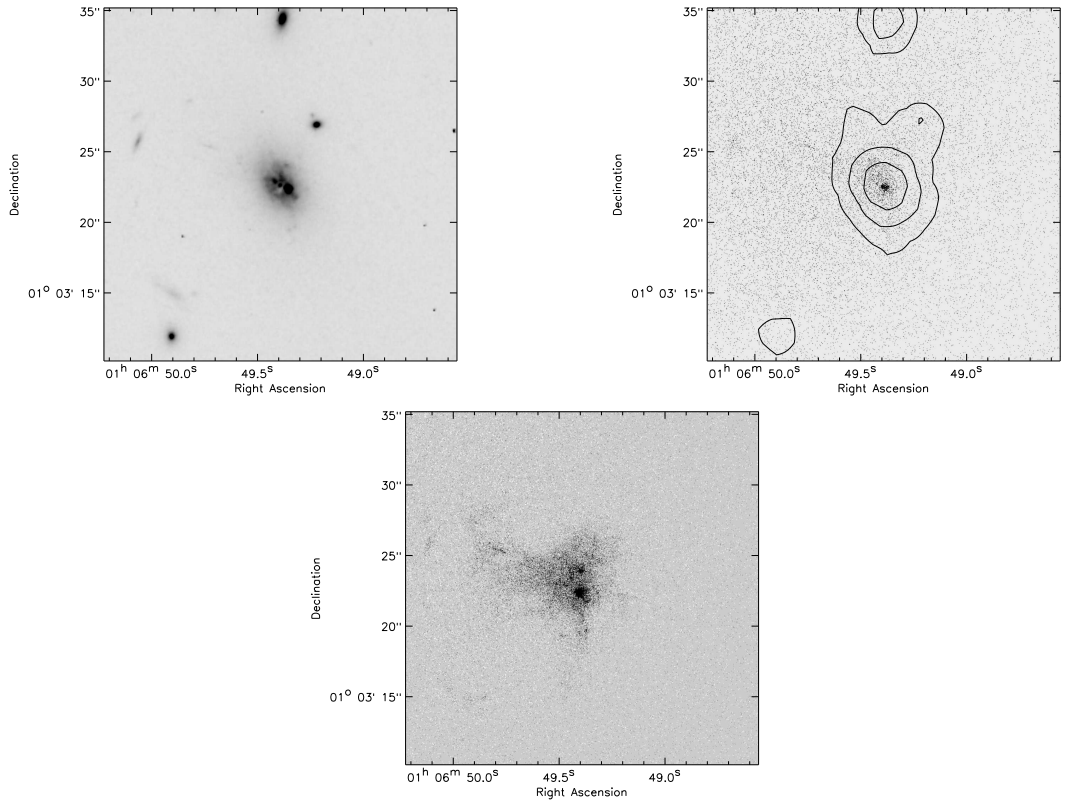

Figure 3.6: ZWCL 348. (*upper left*) optical *HST* WFPC2 F606W image of ZWCL 348. Note the dust lane. (*upper right*) FUV *HST* SBC continuum image overlayed with 3μm contours. (*bottom*) Continuum subtracted *HST* SBC Lyα image of ZWCL 348. At the redshift of ZWCL 348 (z = 0.254), 1$''$corresponds to $\sim$ 4 kpc.

and line emission contains clumps and filaments, but the Lyα emission also contains a diffuse component.

Star formation rates estimated from the FUV continuum range from about 3 to 12 times lower than those estimated from the infrared. However, both the Balmer decrement in the central arcsec, the presence of dust lanes seen in the optical images, and the detection of CO in these galaxies suggest that there are regions of dense gas and high extinction within the central 10-30 kpc. Thus, the lower star formation rates estimated in the FUV are consistent with the expected internal extinction.

We find that the young stellar population required by the FUV observations would produce a significant fraction of the ionizing photons required to power the emission line nebula.

We find unresolved radio emission in each of the seven BCGs. In addition, Abell 1835 and RXJ 2129+00 also exhibit weak kpc scale jets. The unresolved radio emission in ZWCL 8193 is offset

from the center of the BCG by 3 arcsec and may be associated with a merging galaxy. These BCGs tend to have fairly compact (< 1 kpc), weak, steep spectrum radio structures. The hypothesis that the radio source are confined to the sub-kpc scale by dense gas (as originally suggested for GPS and CSS sources, e.g., Wilkinson *et al.* 1984; van Breugel *et al.* 1984; O'Dea *et al.* 1991, 1998) could be tested via VLBI observations. On the other hand, the radio properties could be explained if nuclear fueling has been reduced by a previous AGN activity cycle and we are now seeing the galaxies following a period of relative AGN quiescence. It is tempting to also account for the high star formation rate with a period of low feedback. Rapid cooling in the IGM fueling the current high star formation may be due to a previous reduction in energy deposited into the IGM. Kirkpatrick *et al.* (2009) find that cooling rates could be high enough to fuel the star formation in Abell 1664. Similar cooling rates have been estimated for most of the other galaxies in our sample (O'Dea *et al.*, 2008).

We note that there is FUV continuum and Lyα emission in Abell 1795 and Abell 2597 which is closely associated with the radio sources - suggesting a contribution from jet induced star formation (O'Dea *et al.*, 2004). However, the radio jets in Abell 1835 and RXJ 2129+00 show no relationship with the FUV emission. While both Abell 1795 and Abell 2597 host star formation, it is at a lower level than estimated for the 7 of our sample. In addition the 7 BCGs studied here generally harbor less powerful radio sources than those in Abell 1795 and Abell 2597. The combination of higher SFR and lower radio power in our BCGs suggests that the radio sources have a smaller relative impact on the triggering and/or properties of the star formation and associated emission line nebulae. Further, the lack of FUV emission aligned with the radio jets indicates that the contribution from scattered AGN light is small.

We have also noted that most of our galaxies exhibit asymmetries in their distribution of star formation, and four of our sources exhibit ~ 10 kpc spatial offsets between the peak of the X-ray emission and the BCG. Feedback from an AGN (from jets and bubbles) might account for these offsets, however it is worth noting that these sources are supposedly experiencing a "low state" of Feedback (as inferred from their compact, weak radio sources). The observed spatial offsets do not correspond with any observable signature of AGN feedback, past or present. We should also note that Abell 2597 (Chapter 2), which clearly exhibits strong signatures of recent or ongoing feedback, features a BCG core and X-ray surface brightness peak that are aligned with one another. Cluster mergers could account for the spatial offsets observed in our sources, as could residual "gas sloshing" which remains long-lived even after virialization of the cluster. Disturbances in the ICM could lead to higher cooling rates in the gas as the cluster relaxes and slowly evolves to equilibrium (e.g., Russell *et al.* 2010, and references therein).

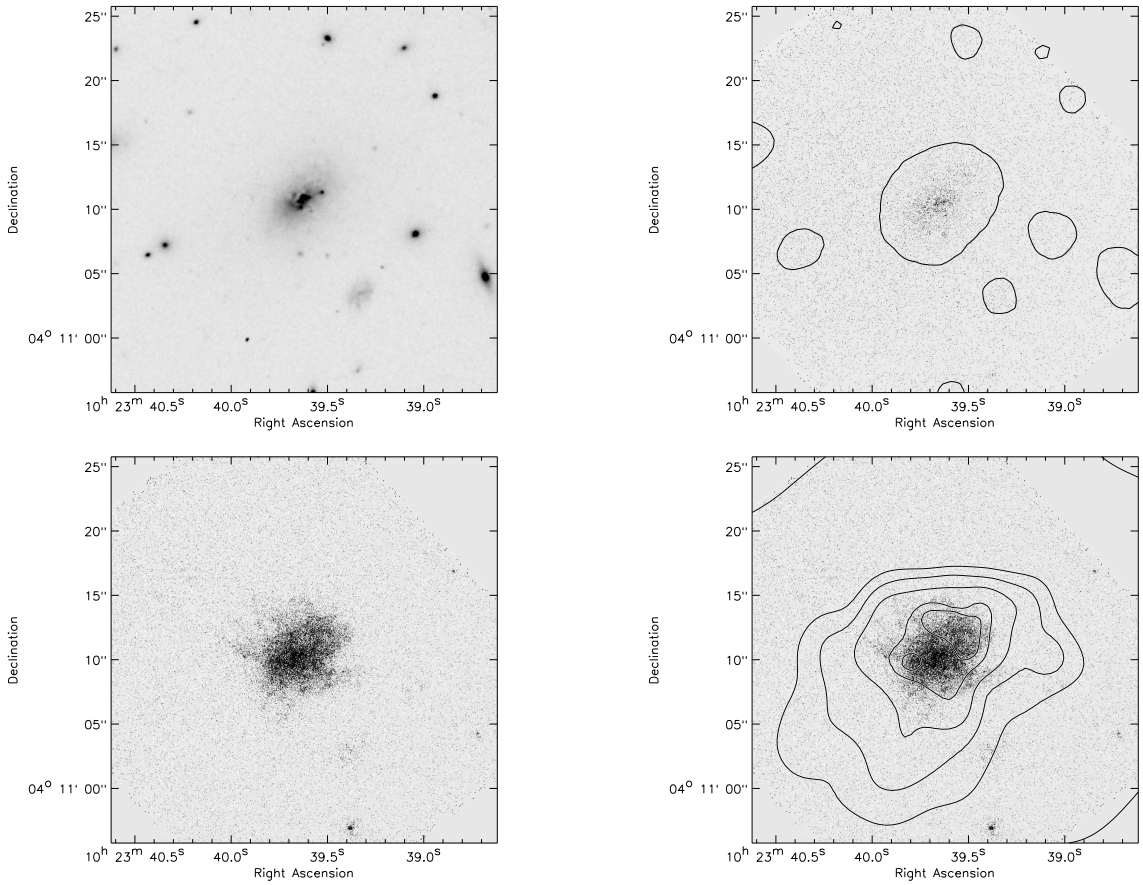

Figure 3.7: ZWCL 3164. (*upper left*) Opitcal *HST* WFPC2 F606W image of ZWCL 3146. (*upper right*) *HST* SBC FUV continuum image overlayed with 3μm contours. (*lower left*) Continuum subtracted *HST* SBC Lyα image of ZWCL 3146. (*lower right*) Continuum subtracted Lyα image with X-ray contours. Note the asymmetry in the X-ray emission. At the redshift of ZWCL 3146 (z = 0.290), 1$''$corresponds to $\sim$ 4.3 kpc.

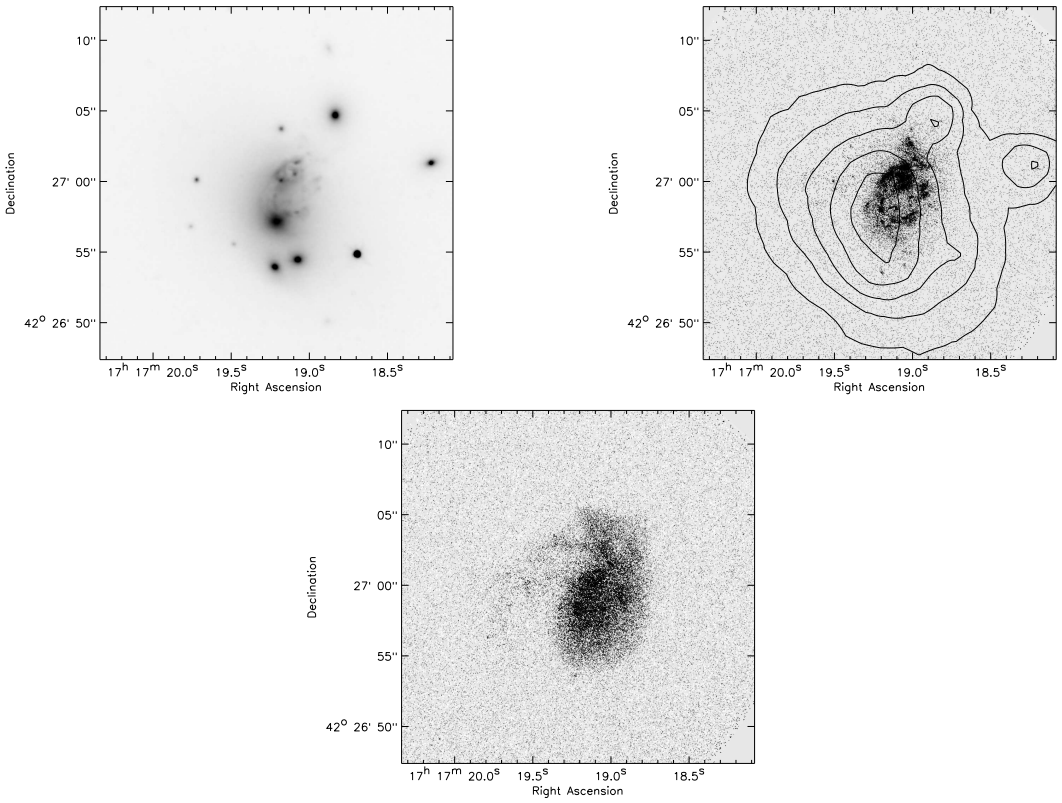

Figure 3.8: ZWCL 8193. (*upper left*) *HST* WFPC2 F606W image of ZWCL 8193. Note the dust lane. (*upper right*) *HST* SBC FUV continuum image overlayed with 3μm contours. (*bottom*) Continuum subtracted *HST* SBC Lyα image of ZWCL 8193. The Lyα filament has a spiral appearance. At the redshift of ZWCL 8193 (z = 0.175), 1$''$corresponds to $\sim$ 3 kpc.

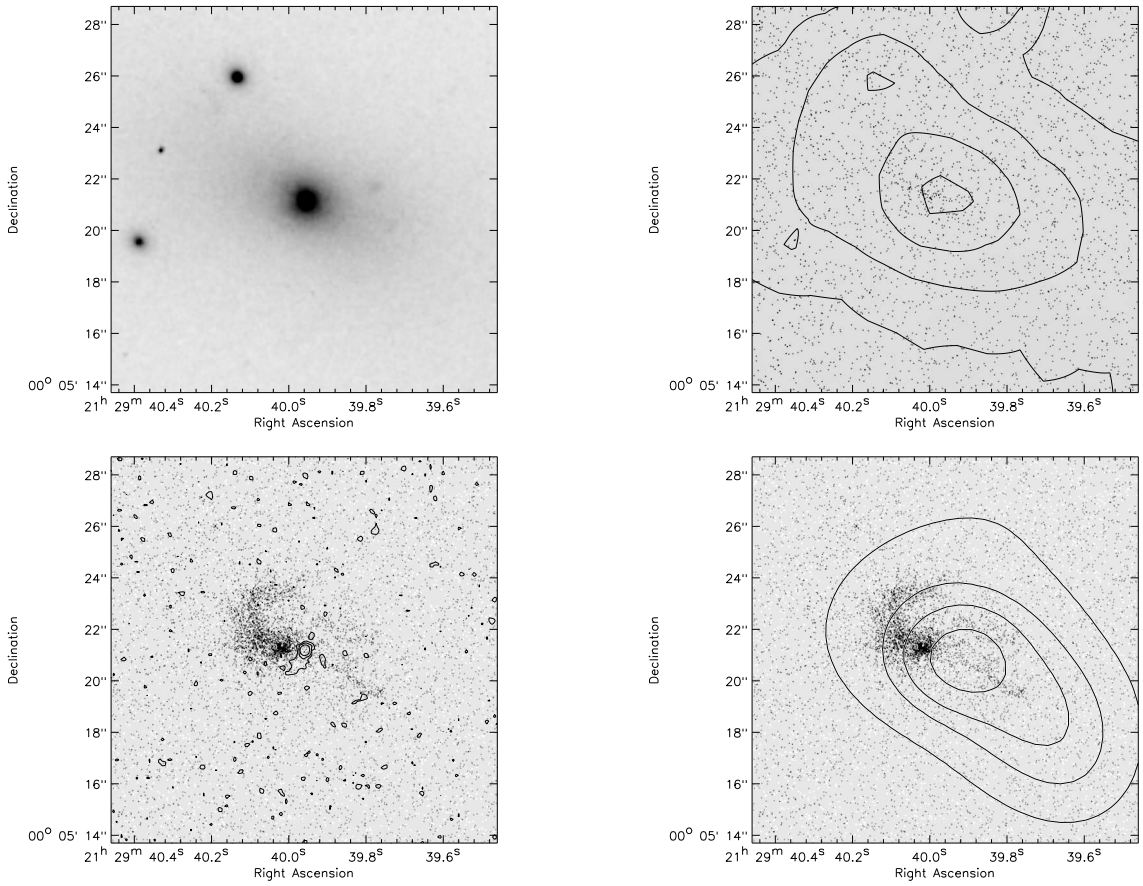

Figure 3.9: RXJ 2129+00. (*upper left*) Optical *HST* WFPC2 F606W image of RXJ 2129+00. (*upper right*) *HST* SBC FUV continuum image overlayed with 3μm contours. (*lower left*) Continuum subtracted *HST* Lyα image of RXJ 2129+00 overlayed with 8 GHz VLA radio contours. (*lower right*) Continuum subtracted Lyα image with X-ray contours. At the redshift of RXJ 2129+00 (z = 0.235), 1$''$corresponds to $\sim$ 3.7 kpc.

4

Comparison Study

Star Formation & AGN Activity *in a* Field Galaxy

I refuse to answer that question on the grounds that I don't know the answer.
Douglas Adams, 1979

We have thus far framed our discussion of star formation and AGN triggering/feedback in the context of the cluster cooling flow model. Of course, not all galaxies are in clusters, and the cooling flow model may ultimately prove to be incorrect. It is therefore important to consider star formation and AGN triggering in a purely observational, model-independent context. The powerful radio galaxy 3C 236 shares many similarities with the BCG in Abell 2597, including (1) direct observational evidence of episodic AGN activity, (2) a powerful, compact central radio source, and (3) compact regions of ongoing star formation. There is a fundamental difference between the two sources, however: 3C 236 is a field galaxy, and therefore resides in a poor environment. As such, it serves as an important "comparison source" with which we may compare our results from previous chapters.

4.1 Context

Galaxies occupy a heavily bimodal distribution in color-magnitude space, wherein young, predominantly disk -dominated galaxies reside in a 'blue cloud' and evolve onto a characteristically quiescent, bulge-dominated 'red sequence' (e.g., Bell *et al.* 2004; Faber *et al.* 2007). The underdensity of galaxies in the 'green valley' separating these populations implies that cloud-to-sequence evolution is swift, requiring a cessation of star formation more rapid than would be expected in passively evolving systems (e.g., Cowie *et al.* 1996). Quasar- and radio-mode feedback models (see Section 1.4) have been proposed as mechanisms by which star formation may be truncated by the heating and expulsion of gas (Silk & Rees, 1998; Hopkins *et al.*, 2005; Croton *et al.*, 2006; Schawinski *et al.*, 2006), as it is now known that quasar activity was two orders of magnitude more common at redshifts $z \sim 2$ than at the present time (e.g., Schmidt *et al.* 1991). This, considered in the context of declining star formation rates in massive galaxies at $z \sim 2$ (e.g., Pérez-González *et al.* 2008), along with the emerging consensus that most populations of galaxies harbor quiescent black holes at their centers (hereafter BHs, e.g, Kormendy & Richstone 1995), supports the notion that all bright galaxies go through several active phases (e.g., Haehnelt & Rees 1993; Cavaliere & Padovani 1989). In this scenario, the quenching of star formation via feedback from active galactic nuclei (AGN) may be one of the primary drivers of cosmic downsizing (e.g., Cowie *et al.* 1996; Scannapieco *et al.* 2005, and references therein).

The relationship between the AGN duty cycle and the regulation of host galaxy stellar evolution is far more complicated, however, as it can play competing roles at successive stages of galactic evolution. AGN activity has been associated not only with quenching star formation on large scales, but also triggering it via ISM cloud compression from the propagating relativistic jets associated with radio galaxies (e.g, the so-called "alignment effect", Rees 1989; Baum & Heckman 1989b; Daly 1990; McCarthy 1993; Best *et al.* 2000; Privon *et al.* 2008). Moreover, it is natural to expect a correlated (but not necessarily causal) relationship between AGN activity and star formation. The tight relationship between BH mass and host galaxy bulge velocity dispersion (Magorrian *et al.*, 1998; Ferrarese & Merritt, 2000; Gebhardt *et al.*, 2000) implies that the growth of the BH and the galaxy bulge are tightly coupled (e.g., Kauffmann & Haehnelt 2000; Ciotti & van Albada 2001). It is therefore expected that, throughout the process of hierarchical galaxy formation, gas infall due to major mergers or tidal stripping from a gas-rich companion can fuel not only AGN, but also the growth of the host galaxy stellar component via infall-induced starbursts (e.g., Di Matteo *et al.* 2005). A significant fraction ($\sim$ 30%) of nearby powerful radio galaxies exhibit evidence of infall-induced starbursts near their nuclei (Smith & Heckman, 1989; Allen *et al.*, 2002;

Baldi & Capetti, 2008; Tremblay *et al.*, 2009), suggesting that the phenomenon is both common and comperable to the lifetime of the radio source ($\sim 10^7 - 10^8$ yr, e.g., Parma *et al.* 1999). The AGN/starburst connection is therefore likely real and fundamental to galaxy evolution itself, and its characterization has been a major pursuit of the past two decades (e.g., Barnes & Hernquist 1991; Silk & Rees 1998; Fabian 1999; Di Matteo *et al.* 2005; Hopkins *et al.* 2005; Springel *et al.* 2005; Silverman *et al.* 2008; Quillen & Bland-Hawthorn 2008).

A key discriminant in understanding the nature and evolution of the AGN/starburst connection may be found in some radio galaxies whose morphology is clear evidence for multiple epochs of AGN activity. Several such examples have been observed (e.g., 3C 219 – Bridle *et al.* 1986; Clarke *et al.* 1992, 0108+388 – Baum *et al.* 1990), and have come to constitute a new class of "double-double" radio sources, representing $\sim 5-10\%$ of predominantly large (> 1 Mpc) radio galaxies (e.g., Schoenmakers *et al.* 2000a,b). Double-doubles are characterized by outer ('older') and inner ('younger') radio sources propagating outwards amidst the relic of the previous epoch of activity. This apparently repetitive activity is thought to be a consequence of the AGN fuel supply having been interrupted, whether by exhaustion, smothering, or disturbance, at some time in the past (Baum *et al.*, 1990). This scenario is consistent with models of radio galaxy propagation (e.g., Kaiser *et al.* 2000; Brocksopp *et al.* 2007). The relative ages of the radio sources (and therefore the timescale over which the engine was cut off and re-ignited) can be estimated using size estimates from radio maps coupled with a dynamical model for the jets and radio spectral energy distributions (SEDs) of the radiating electrons (Schoenmakers *et al.*, 2000a,b; O'Dea *et al.*, 2001).

4.1.1 An important test case: 3C 236

The nearby ($z = 0.1005$) double-double radio galaxy 3C 236 is an important test case in studies of the AGN/starburst connection, and is the basis of both this chapter and a previous study by O'Dea *et al.* (2001). 3C 236 is a powerful double-double with a relic edge-brightened FR II (Fanaroff & Riley, 1974) radio source whose deprojected linear extent exceeds 4 Mpc, making it the second largest known radio galaxy (only J1420-0545 is larger, Machalski *et al.* 2008), and even one of the largest objects in the universe (Schilizzi *et al.*, 2001). Its inner young Compact Steep Spectrum (CSS) source, whose apparent origin is cospatial with the nucleus, is only 2 kpc in extent and is morphologically reminiscent of a young classical double. Anecdotally, 3C 236 was initially classified as a pure CSS source before it was associated years later with the massive relic FR II source (R. Laing, private communication). The jet propagation axes of both the Mpc- and kpc-scale sources are aligned to within $\sim 10^\circ$ of one another (as projected on the sky). See Fig. 4.1

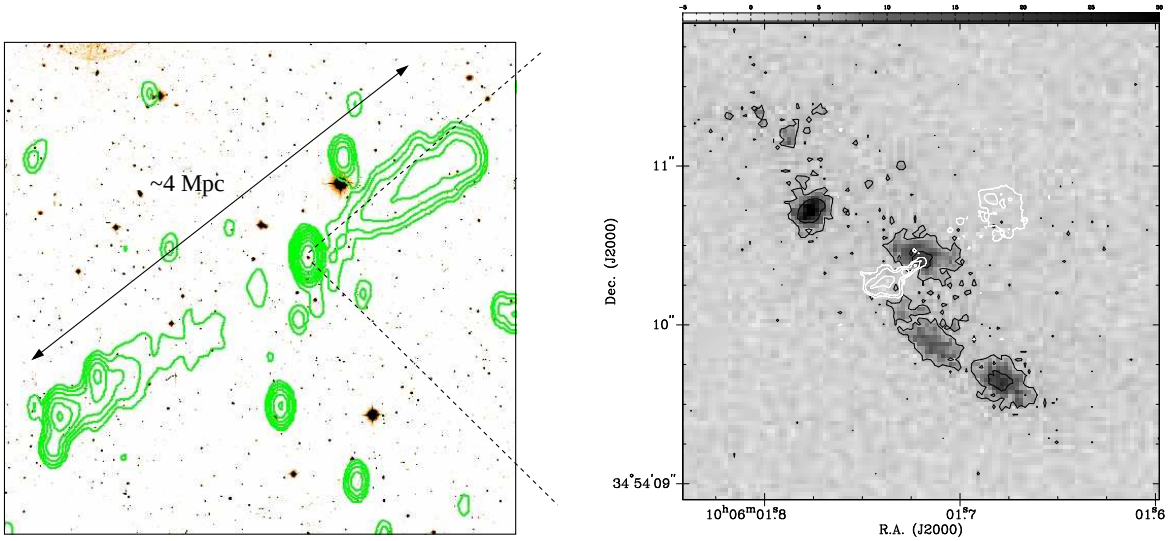

Figure 4.1: The two radio sources associated with 3C 236. (a) 326 MHz WSRT radio contours (in green, from Mack *et al.* 1997) of the "relic" radio emission associated with 3C 236, overlayed on SDSS imaging of the same region of sky. The deprojected size of the jet is ~ 4.5 Mpc, making it the largest known radio galaxy and one of the largest objects in the universe. (b) Global VLBI 1.66 GHz radio contours of the central 2 kpc CSS ("young") radio source from Schilizzi *et al.* (2001), overlayed on *HST*/STIS NUV imaging of the star forming knots described by O'Dea *et al.* (2001). The jet axes of the Mpc- and kpc- scale radio sources are aligned on nearly the same position angle.

for radio contour overlays of both sources, using 326 MHz Westerbork Synthesis Radio Telescope (WSRT) and 1.66 GHz Global Very Long Baseline Interferometry (VLBI) Network radio mapping from Mack *et al.* (1997) and Schilizzi *et al.* (2001) for the relic and CSS sources, respectively.

In addition to its rare radio morphology, 3C 236 is also unique in that its nuclear dust complex is made up of an inner circumnuclear dusty disk that is somewhat misaligned with an apparently separate outer dust lane (Martel *et al.*, 1999; de Koff *et al.*, 2000; Tremblay *et al.*, 2007). The total dust mass in the complex is estimated to be $\sim 10^7$ $M_\odot$, based on *Hubble Space Telescope* (*HST*) absorption maps and IRAS luminosities (de Koff *et al.*, 2000). In Fig. 4.2 we present a 1.6 μm / 0.7 μm absorption map of the dust complex, originally presented in Tremblay *et al.* (2007) and made via division of *HST*/NICMOS and WFPC2 data from Martel *et al.* (1999) and Madrid *et al.* (2006), respectively.

The work by O'Dea *et al.* (2001) studied *HST* NUV and optical imaging of the central few arcsec of 3C 236, finding four knots of blue emission arranged in an arc along the dust lane in the galaxy's nucleus. Their original NUV data is presented in greyscale with black contours in Fig. 4.1(*b*). The lack of an obvious spatial relationship between the knots and the CSS source suggests that the starbursts are infall-induced rather than jet-induced. Martel *et al.* (1999) had

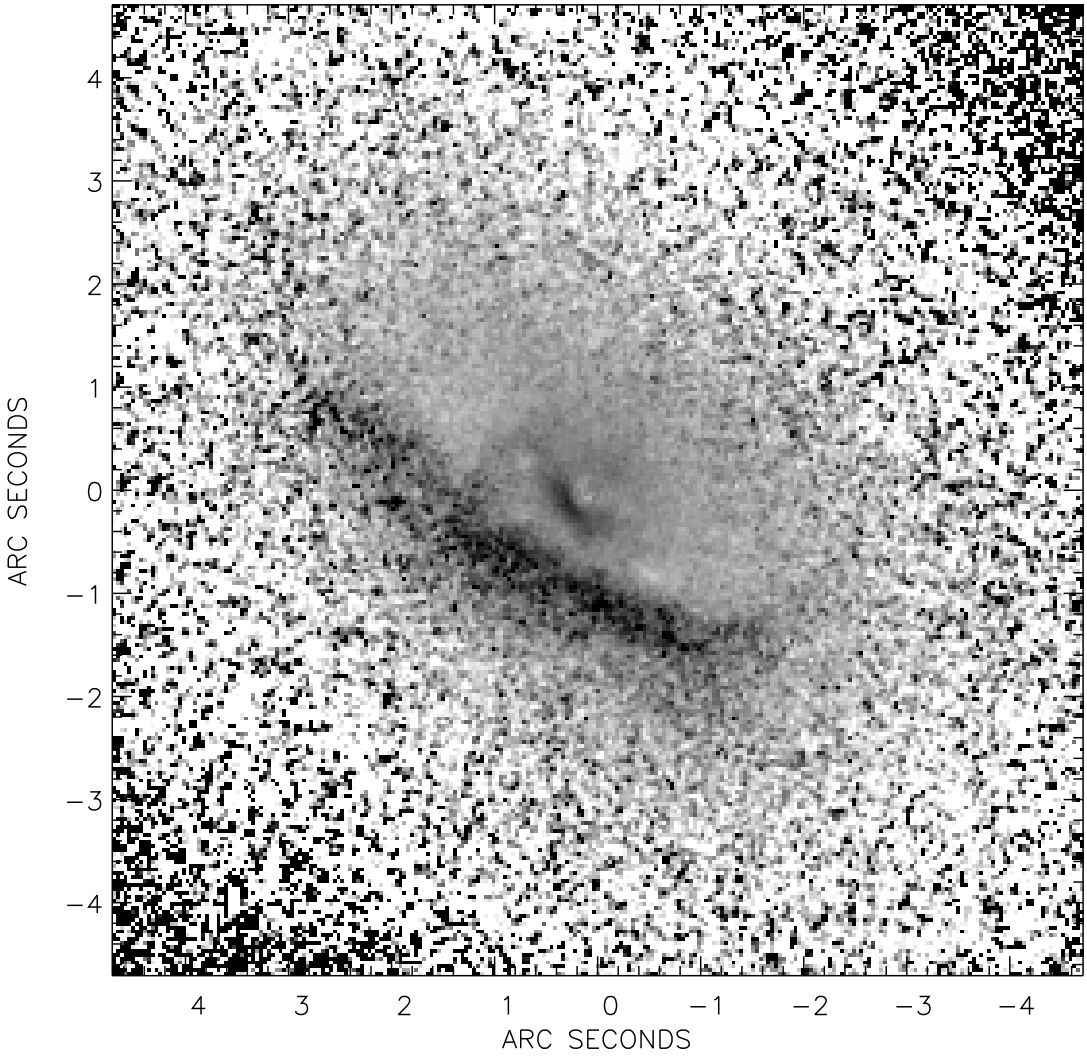

Figure 4.2: 1.6 μm / 0.7 μm colormap of the outer lane and inner dusty disk in the nucleus of 3C 236, made via division of *HST*/NICMOS and WFPC2 data from Martel *et al.* (1999) and Madrid *et al.* (2006), respectively. This absorption map was originally presented in Tremblay *et al.* (2007).

Table 4.1. **Summary of Observations of 3C 236**

Observatory (1)	Instrument (2)	Aperture (3)	Filter/Config. (4)	Waveband/Type (5)	Exp. Time [Orbits] (6)	Reference (7)	Obs. Date (8)	Comment (9)
				NEW OBSERVATIONS				
HST	ACS	HRC	F330W	*U*-band Imaging	2516s [1]	*HST* 9897	21 Oct 2003	SF Knots
HST	ACS	HRC	F555W	*V*-band Imaging	2612s [1]	*HST* 9897	22 Oct 2003	Dust Lanes
HST	ACS	SBC	F140LP	FUV Imaging	6900s [3]	*HST* 9897	21 Oct 2003	SF Knots
HST	STIS	NUV-MAMA	F25SRF2	NUV Imaging	2520s[1]	*HST* 9897	19 Oct 2003	SF Knots
				ARCHIVAL OBSERVATIONS				
HST	WFPC2	PC1	F702W	*R*-band Imaging	4×140s	*HST* 5476	7 May 1995	Galaxy
HST	WFPC2	PC1	F555W	*V*-band Imaging	2×300s	*HST* 6384	12 Jun 1996	Galaxy & Dust
HST	STIS	NUV-MAMA	F25SRF2	NUV Imaging	1440s	*HST* 8275	03 Jan 1999	SF Knots
HST	NICMOS	NIC2-FIX	F160W	NIR Imaging	1152s	*HST* 10173	02 Nov 2004	Host Isophotes

Note. — A summary of the new and archival observations used in our analysis. (1) Facility name; (2) instrument used for observation; (3) configuration of instrument used; (4) filter used; (5) corresponding waveband and specification of whether the observation was imaging or spectroscopy; (6) exposure time (if the observatory is *HST*, the corresponding number of orbits also appears in brackets); (7) corresponding reference for observation. If the observatory is *HST*, the STScI-assigned program number is listed; (8) date of observation; (9) comment specific to observation.

also detected the knots of emission in their *HST R*-band imaging, albeit to a lesser degree as the knots are very blue. O'Dea *et al.* (2001) used their photometry in comparison with stellar population synthesis models to estimate upper limits to the ages of the individually resolved star forming knots (seen in Fig. 4.1*b*). They found disparate ages between the clumps of emission, finding two to be relatively young with ages of order $\sim 10^7$ yr, while the other two were estimated at $\sim 10^8 - 10^9$ yr old, comparable to the estimated age of the giant relic radio source. O'Dea *et al.* (2001) argued that 3C 236 is an "interrupted" radio galaxy, and has undergone two starburst episodes approximately coeval with the two epochs of radio activity observed on Mpc- and kpc-scales. That work motivated follow-up observations with *HST* at higher sensitivity and spatial resolution, the results of which we present in this chapter.

We organize this chapter as follows. In section 4.2 we describe the new and archival data presented in this chapter, as well as the associated data reduction. In section 4.3 we present our results, including a comparison of our photometry with stellar population synthesis models, following (in the interests of consistency) the analysis strategy used in O'Dea *et al.* (2001). We discuss our results in section 4.4, focusing on the role played by the AGN/starburst connection in the special test-case environment of 3C 236. We summarize this work and provide some concluding remarks in section 4.5.

4.2 Observations & Data Reduction

We present *Hubble Space Telescope* observations of the nucleus of 3C 236 obtained as part of the Cycle 12 GO program 9897 by O'Dea and collaborators. These consist of U- and V-band imaging with the Advanced Camera for Surveys (ACS) High Resolution Channel (HRC), FUV imaging with the ACS Solar Blind Channel (SBC), and NUV imaging with the Space Telescope Imaging Spectrograph (STIS). Below we describe the specifics of each new observation presented in this chapter, and provide a brief description of the archival imaging and spectroscopy that we also include in our analysis. We also describe the steps taken to reduce the data. A summary of the new and archival *HST* observations utilized in this work can be found in in Table 4.1.

4.2.1 Cycle 12 ACS and STIS imaging

Our *HST*/ACS observations were designed to enable high sensitivity multicolor photometry allowing for construction of an SED of the blue knots previously observed in 3C 236 (O'Dea *et al.*, 2001). The FUV, NUV, U-, and V-bands were chosen so as to provide multiple constraints on a young blue stellar population, while also enabling consistency checks and estimates on the amount of intrinsic reddening. At the redshift of 3C 236 (z = 0.1005), the U- and V- bands are located just blue-ward and red-ward of the 4000 Å break, respectively. Exposure times were chosen to permit detection of the knots at adequate signal-to-noise (S/N) over a range of possible ages and intrinsic properties. Three orbits (6900 s) were obtained for the SBC FUV image using the F140LP long pass filter. We obtained one orbit each ($\sim$ 2500 s) for the HRC U- and V-band images using the F330W and F555W filters, respectively. The F140LP long pass filter on ACS SBC ranges from $\sim$ 1350 Å (with a hard cutoff) to $\sim$ 2000 Å with a pivot wavelength of 1527 Å. The SBC Multi-anode Microchannel Array (MAMA) has a spatial resolution of $\sim$0.″034 $\times$ 0.″030 per pixel and a nominal field of view of 34.″6$\times$30.″1. The SBC achieves a peak efficiency of 7.5% at 1250 Å. The F330W and F555W filters on ACS HRC have central wavelengths (filter widths) of 3354 (588) Å and 6318 (1442) Å respectively. The HRC has a pixel scale of 0.″028 $\times$0.″025 per pixel and its field of view is 29″$\times$26″. It reaches a peak efficiency of 29% at $\sim$ 6500 Å.

We have also obtained one orbit (2520 s) of NUV imaging with the Cs_2Te MAMA detector on STIS. The F25SRF2 filter has a central wavelength of 2320 Å and a FWHM of 1010 Å, which permits geocoronal [O I]λ1302+1306 Å contamination in its bandpass, though its contribution is far lower than the detector background and is not expected to affect our results. The F25SRF2 cutoff does not permit geocoronal Lyα emission. The NUV-MAMA has a pixel scale of 0.″024 and

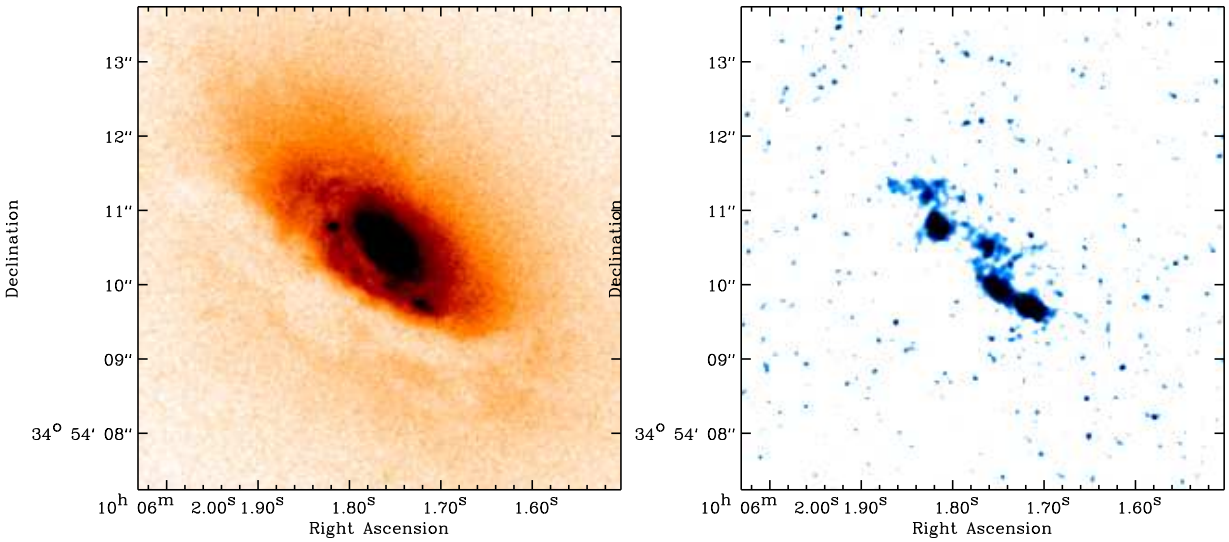

Figure 4.3: (*left*) 2500 s *V*-band exposure of the nucleus of 3C 236, using *HST*/ACS HRC with the broadband F555W filter. The outer dust lane is seen in white, while three of the four knots of star formation are seen to the south and west of the nucleus along the inner dusty disk, whose position angle is slightly offset from that of the outer.(*right*) combined 6900 s *HST*/ACS SBC FUV (F140LP) image of the star forming knots observed along the inner dust structure of 3C 236. The image has been smoothed with a two pixel Gaussian kernel. North is up, east is left. The two images are on the same scale. At a redshift of $z \sim 0.1$, $1''$corresponds to ~ 1.8 kpc.

a field of view of $25'' \times 25''$.

4.2.2 Archival data

In this chapter we make use of archival *HST* Wide-Field Planetary Camera 2 (WFPC2) imaging in *V*- and *R*-band (F555W and F702W filters, respectively) obtained as part of the 3CR snapshot programs by Sparks and collaborators (de Koff *et al.*, 1996; McCarthy *et al.*, 1997; Martel *et al.*, 1999). We also use the 1440 s STIS NUV-MAMA F25SRF2 image of 3C 236, which formed the basis of the study by O'Dea *et al.* (2001), and was formally presented as part of a data paper by Allen *et al.* (2002). The *H*-band image obtained with the *HST* Near-Infrared Camera and Multiobject Spectrograph (NICMOS2) in SNAP program 10173 (PI: Sparks, Madrid *et al.* 2006; Tremblay *et al.* 2007; Floyd *et al.* 2008) was used for fits to the host galaxy isophotes. Imaging and spectroscopy from the Sloan Digital Sky Survey (SDSS) is also used (York *et al.*, 2000; Adelman-McCarthy *et al.*, 2008).

4.2.3 Data reduction

The previously unpublished *HST* data presented in this chapter were reduced using the standard On-the-Fly Recalibration (OTFR) pipeline provided as part of the Multi-mission Archive at Space Telescope (MAST). For ACS, the OTFR pipeline combines calibrated and flatfielded dithered exposures using the `multidrizzle` routine with the default parameters. The task calculates and subtracts a background sky value for each exposure, searches for additional bad pixels not already flagged in the data quality array, and drizzles the input exposures into outputs that are shifted and registered with respect to one another. From these drizzled exposures a median image is created, which is then compared with original input images so as to reject cosmic rays on the drizzled median. More information on the specifics of `multidrizzle` can be found in Koekemoer *et al.* (2002).

We have not performed post-pipeline processing on the two one-orbit ACS HRC drizzled images (U- and V-band), as for the purposes of this work we are concerned primarily with high surface brightness emission near the center of the galaxy, and the results from the OTFR pipeline were sufficiently free of cosmic rays and hot pixels to be deemed "science ready". For the three-orbit ACS SBC data, we combined the three individual calibrated and flatfielded files manually using `multidrizzle` with the default parameters. The single 6900s output image was left unrotated with respect to North so as to avoid associated pixel interpolation errors in our photometry. Information regarding the reduction of the archival data utilized in this chapter can be found in the appropriate references cited in section 4.2.2.

4.3 Results

In Fig. 4.3 we present the ACS/HRC V-band (at left in red) and ACS/SBC FUV (at right in blue) images in panels (a) and (b), respectively. The two images are aligned and on the same scale, with east left and north up. At the redshift of 3C 236, $1''$corresponds to ~ 1.8 kpc. In Fig. 4.4(*a*) we present the same data in Fig. 4.3 as an overlay, with the FUV contours rendered in black on the V-band image for a clearer sense of the spatial relationship between the blue star forming knots (seen in the FUV) and the dust complex (seen in V-band). We have labeled each blue knot following the scheme in O'Dea *et al.* (2001) to allow for easier comparison of results. In the original STIS NUV image discussed in O'Dea *et al.* (2001) (see Fig. 4.1*a*), knots "3" and "4" appeared to be separate, individually resolved regions of emission. In our new higher sensitivity and spatial resolution imaging with ACS we detect these two regions as one filament of emission that extends $\sim 1''$. In

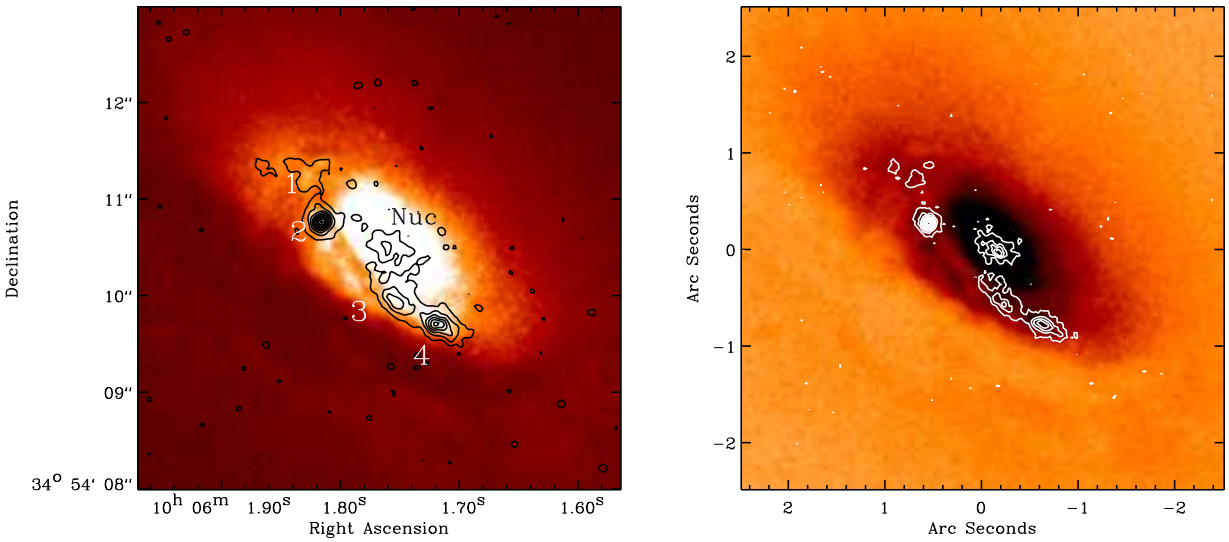

Figure 4.4: (*a*) ACS HRC *V*-band image of the nucleus of 3C 236 with ACS SBC FUV contours (smoothed with a two pixel Gaussian). The knots of star formation along the inner dust structure have been labeled so as to be consistent with O'Dea *et al.* (2001). That work detected knots "3" and "4" as two distinct compact regions of emission in their STIS MAMA NUV imaging, while we detect one continuous filament of emission in our more sensitive and higher spatial resolution FUV imaging. So as to maintain consistency with O'Dea *et al.* (2001) while making this clear we refer to this patch as "knot 3+4" throughout this chapter. (*b*) The same HRC *V*-band image (with colors inverted to better emphasize the outer dust lane) with STIS S25SRF2 NUV contours. The knots of star formation are nearly morphologically identical in both the FUV and NUV, though the higher sensitivity of ACS is evident in the FUV contours at left, which highlight lower surface brightness features in the knots. Both panels are aligned and on the same scale. East is left, north is up. At the distance of 3C 236, 1″corresponds to 1.8 kpc.

the interests of consistency we have nonetheless named this region with the two labels "3" and "4" originally assigned in O'Dea *et al.* (2001), and will hereafter refer to the filament as "Knot 3+4" when discussing both regions as a whole. As in O'Dea *et al.* (2001), we will also refer to the "nuclear" FUV emission, seen in Fig. 4.4 as the contour cospatial with the nucleus in the underlying *V*-band. In Fig. 4.4(*b*) we overplot the STIS S25SRF2 NUV contours on the same *V*-band image (with colors inverted to highlight the continuum deficit due to the outer dust lane). The blue emission is morphologically nearly identical in both the FUV and NUV, although the higher sensitivity (and longer exposure time) of the ACS data is evident in the FUV contours of Fig. 4.4(*a*), which map lower surface brightness features than are seen in Fig. 4.4(*b*). We utilize the ACS/HRC *U*-band image in our analysis, though do not present the image in a figure as it appears nearly identical to the knots in Figs. 4.3(*b*) and 4.4.

We present an analysis of these new data in the subsections below, framed in the context of past results from O'Dea *et al.* (2001).

4.3.1 The outer lane and inner dusty disk

In Fig. 4.3(*a*) a significant deficit of galaxy continuum due to a dust lane extends ~ 10 kpc and runs in a northeast-to-southwest direction south of the nucleus at a position angle of $\sim 50°$. A steep brightness and color gradient defines a ridge north of the outer lane, giving way to an inner circumnuclear disk of gas and dust whose major axis is oriented $\sim 30°$ (offset $\sim 20°$ from the outer lane). It is not apparent whether the lane and disk are disjoint structures or a continuous, warped distribution of gas and dust. de Koff *et al.* (2000) estimated the mass of dust in the complex to be $\sim 10^7$ $M_\odot$, corresponding to a gas mass $\sim 10^9$ $M_\odot$ given the standard gas-to-dust ratio from the literature (Sodroski *et al.*, 1994).

4.3.2 Properties of the star forming knots

We have measured the total flux from each knot of star formation in the SBC FUV image (Fig. 4.3*b*) as well as the STIS NUV (Fig. 4.4*b*) and HRC *U*-band images. We have also measured the HRC *V*-band flux for knots 2, 4, and the blue emission associated with the nucleus. We have not performed *V*-band photometry for knots 1 and 3 as they are not clearly detected in this band (see Fig. 4.3*a*). Fluxes were measured from the drizzled images using the `apphot` package in IRAF. The default drizzled pixel units for ACS are in electrons s^{-1}, which scales to counts by a factor of the gain. As this is corrected for in the pipeline's calibration stage, "counts" and "electrons" can be considered equivalent for the purposes of this study, regardless of the instrument being discussed. Count rates were summed in an aperture whose radius was chosen based on the size of the source being measured. Background count rates measured through an aperture of the same radius were subtracted from the sum. Photometric conversion into flux units was applied by scaling the residual (source minus background) value by the inverse sensitivity (the PHOTFLAM keyword), converting the value from electrons s^{-1} to flux units in erg cm^{-2} s^{-1} $Å^{-1}$. Statistical 1σ uncertaintes were calculated from the measured count rates. The absolute photometric calibration of the ACS SBC, ACS HRC, and STIS MAMA is 5%, 2%, and 5%, respectively[1]. Our photometry was corrected for galactic extinction using the scaling relation by Cardelli *et al.* (1989) and a color excess $E(B-V) = 0.011$, as listed in the NASA/IPAC Extragalactic Database (NED). Summed

[1]Maybhate, A., et al. 2010, "ACS Instrument Handbook", Version 9.0 (Baltimore: STScI).

and galactic extinction corrected counts were also converted to magnitudes normalized to the *HST* VEGAMAG system, defined such that the magnitude of Vega is zero in all *HST* bandpasses.

As estimates on the *intrinsic* color of each knot is required in our analysis, and as each star forming knot is likely embedded in a great deal of dust, we have also corrected all photometry for estimated internal extinction. We had originally proposed for and received STIS low dispersion long-slit spectroscopy to allow measurement of the Balmer decrement (Hα / Hβ flux ratio) in a 2$''$slit aligned with the knots, however a pointing error rendered the data unusable. In lieu of this, we use the measured Balmer decrement from Buttiglione *et al.* (2009), who presented line fluxes for 3C 236 using available Sloan Digital Sky Survey (SDSS) spectroscopy.

Assuming an intrinsic Hα/Hβ theoretical line ratio of 2.86 (i.e., a "case B" recombination scenario is assumed, Osterbrock 1989), the observed Balmer decrement allows us to estimate the color excess associated with the internal extinction in the source, following the parameterization of Cardelli *et al.* (1989) as described in Atek *et al.* (2008):

$$E\left(B-V\right)_{\mathrm{H}\alpha/\mathrm{H}\beta} = \frac{2.5 \times \log\left(2.86/R_{\mathrm{obs}}\right)}{k(\lambda_{\alpha}) - k\left(\lambda_{\beta}\right)} \tag{4.1}$$

where $R_{\mathrm{obs}} = F\left(\mathrm{H}\alpha\right)/F\left(\mathrm{H}\beta\right)$ is the observed flux ratio, and the extinction curves at Hα and Hβ wavelengths are $k(\lambda_{\alpha}) \approx 2.63$ and $k\left(\lambda_{\beta}\right) \approx 3.71$, respectively, as given by Cardelli *et al.* (1989). The Balmer decrement for 3C 236 measured by Buttiglione *et al.* (2009) of $R_{\mathrm{obs}} \approx 4.54$ yields an $E\left(B-V\right)_{\mathrm{H}\alpha/\mathrm{H}\beta} \approx 0.465$. The spatial resolution of the SDSS spectroscopy, while lower than that of *HST*, nonetheless allows for a reasonably believable estimate of the internal extinction in the nucleus. In Fig. 4.5 we present the SDSS data for 3C 236, with a "zoom in" on the Hα and Hβ lines in Fig. 4.5(*b*). As for the purposes of this study we are primarily interested in the spectroscopy solely for the Balmer decrement, we do not fit any of the lines and instead use only the analysis from Buttiglione *et al.* (2009). We do note that a narrow Hα absorption feature appears to be superimposed over the Hα+[NII] lines, and possibly offset from the peak in the emission in velocity space. Hα absorption has been associated with hot stars (Robinson *et al.*, 1990), though we cannot confidently associate the feature with anything specific in the nucleus, as the spectrum is spatially blended over that size scale.

Moreover, the lower spatial resolution of SDSS prohibits us from quantifying how patchy the extinction may or may not be on size scales of a few kpc (of order the scale over which the knots are distributed). It is not unreasonable to think that one knot may be more deeply embedded in the dust disk (and thus more significantly reddened) than another. Regardless, we expect that any

Table 4.2. **Photometry of the Blue Knots in 3C 236**

Source (1)	FUV Flux erg s^{-1} cm^{-2} (2)	$m_{\rm F140LP}$ (FUV) (mag) (3)	$m_{\rm FS25SRF2}$ (NUV) (mag) (4)	$m_{\rm F330W}$ (U-band) (mag) (5)	$m_{\rm FUV}-m_{\rm NUV}$ (6)	$m_{\rm FUV}-m_{U-{\rm band}}$ (7)	$m_{\rm NUV}-m_{U-{\rm band}}$ (8)
CORRECTED FOR GALACTIC EXCTINCTION							
Knot 1	8.305×10^{-18}	22.204 ± 0.025	22.165 ± 0.023	22.074 ± 0.015	0.039 ± 0.034	0.130 ± 0.029	0.091 ± 0.027
Knot 2	1.771×10^{-17}	21.382 ± 0.017	21.840 ± 0.019	21.731 ± 0.013	-0.459 ± 0.025	-0.349 ± 0.021	0.109 ± 0.023
Knot 3	1.134×10^{-17}	21.866 ± 0.021	21.865 ± 0.020	21.498 ± 0.012	0.001 ± 0.029	0.368 ± 0.024	0.367 ± 0.023
Knot 4	1.670×10^{-17}	21.427 ± 0.017	21.788 ± 0.019	21.813 ± 0.013	-0.361 ± 0.025	-0.386 ± 0.021	-0.025 ± 0.023
Knot 3+4	2.836×10^{-17}	20.871 ± 0.013	20.961 ± 0.013	20.835 ± 0.009	-0.090 ± 0.018	0.036 ± 0.0158	0.126 ± 0.016
Nucleus	9.207×10^{-18}	22.092 ± 0.024	21.613 ± 0.017	20.359 ± 0.007	0.480 ± 0.029	1.733 ± 0.025	1.254 ± 0.018
All	9.037×10^{-17}	19.612 ± 0.008	19.703 ± 0.007	19.125 ± 0.004	-0.091 ± 0.010	0.487 ± 0.008	0.579 ± 0.008
CORRECTED FOR GALACTIC & INTERNAL EXTINCTION							
Knot 1	4.240×10^{-16}	17.934 ± 0.025	18.141 ± 0.023	19.711 ± 0.015	-0.207 ± 0.034	-1.777 ± 0.029	-1.570 ± 0.027
Knot 2	9.044×10^{-16}	17.112 ± 0.017	17.817 ± 0.019	19.369 ± 0.013	-0.705 ± 0.025	-2.258 ± 0.021	-1.552 ± 0.023
Knot 3	5.790×10^{-16}	17.596 ± 0.021	17.841 ± 0.020	19.136 ± 0.012	-0.246 ± 0.029	-1.540 ± 0.024	-1.294 ± 0.023
Knot 4	8.674×10^{-16}	17.157 ± 0.017	17.764 ± 0.019	19.451 ± 0.013	-0.607 ± 0.025	-2.294 ± 0.021	-1.687 ± 0.023
Knot 3+4	1.448×10^{-16}	16.601 ± 0.013	16.937 ± 0.013	18.473 ± 0.009	-0.336 ± 0.018	-1.872 ± 0.0158	-1.535 ± 0.016
Nucleus	4.701×10^{-16}	17.822 ± 0.024	17.589 ± 0.017	17.997 ± 0.007	0.232 ± 0.029	-0.175 ± 0.025	-0.407 ± 0.018
All	4.614×10^{-15}	15.342 ± 0.008	15.680 ± 0.007	16.762 ± 0.004	-0.337 ± 0.010	-1.420 ± 0.008	-1.082 ± 0.008

Note. — Photometry of the blue star forming regions in 3C 236. We have presented our results corrected only for galactic extinction, and then again with galactic and internal extinction corrections applied. The internal extinction correction was estimated from the Balmer decrement using SDSS spectroscopy (see section 3 and Table 4.5). 1σ uncertainties have been derived from count rate statistics. The table does not include the systematic errors due to the absolute photometric calibration of the instruments, which are 5%, 2%, and 5% for the ACS SBC (FUV), ACS HRC (U-band), and STIS MAMA (NUV), respectively. (1) Source name; (2) measured FUV flux of each blue source from the ACS SBC F140LP image; (3) apparent brightness of the FUV emission in the *HST* VEGAMAG system; (4) apparent brightness in the NUV; (5) apparent brightness in the U-band; (6) FUV-NUV color; (7) FUV-U-band color; (8) NUV-U-band color. Larger (more positive) color values correspond to redder colors.

variation in reddening between knots due to unresolved patchy extinction will be reasonably small when compared to the overall intrinsic reddening in the nucleus. Were this not the case, we would expect to see more severe color gradient shifts in the absorption map presented in Fig. 4.2. Instead, the colors of the outer lane and inner disk appear to be quite uniform over their projected lengths.

In Table 4.2 we present the results from our photometric analysis, including measured FUV flux, magnitudes, and colors for each knot. The data are presented first with only galactic extinction corrections applied, and then again with both galactic and internal extinction corrections applied. These corrections are given in Table 3. As the colors are always computed in magnitudes as "shorter wavelength"–"longer wavelength", larger (more positive) values correspond to redder knots. As in O'Dea *et al.* (2001), we find that the knots vary relatively significantly in comparing colors that have *not* been corrected for internal extinction (columns 6, 7, and 8 in the upper half of Table 2). We note that knots 1 and 3 are significantly redder than 2 and 4. In correcting the colors using our estimate for internal extinction, however, we find that all knots are intrinsically very blue,

Table 4.3. **Extinction Corrections**

Band	Galactic Extinction $A(\lambda)_{\rm Gal}$ (mags)	Internal Extinction $A(\lambda)_{{\rm H}\alpha/{\rm H}\beta}$ (mags)
FUV (F140LP)	0.1011	4.270
NUV (F25SRF2)	0.0953	4.025
U-band (F330W)	0.0559	2.362
V-band (F555W)	0.0292	1.232

Note. — Estimated and calculated corrections to photometry due to galactic and internal extinction. Galactic extinction estimated using $E(B-V) = 0.011$ and the law by Cardelli *et al.* (1989). Internal extinction calculated from the Balmer decrement $F({\rm H}\alpha)/F({\rm H}\beta)$ as measured by Buttiglione *et al.* (2009) from SDSS spectroscopy, using the method described in Osterbrock (1989) and in §4.3.3.

as expected. The sole exception is the UV-bright emission that is cospatial with the nucleus, which lies significantly redward of the "dust disk knots" in color space, even after the internal extinction correction has been applied. This could be due to an older stellar population or patchy extinction leading to higher reddening along the line of sight toward the nuclear UV emission (or both).

Again, we are unable to quantify whether or not there may be patchy extinction on scales finer than the SDSS spatial resolution. As there is vastly more dust in the nucleus than in regions of the galaxy a few kpc outward from the dust complex (determined from our colormap in Fig. 4.2), we find it likely that we have systematically undercorrected for internal extinction. However, a knot that is more heavily extincted than we have corrected for will be intrinsically bluer and therefore younger. Uncertainty therefore lies far more on the "young end" of age estimates than it does on the old, and we are able to estimate upper limits to the ages of the knots as done in O'Dea *et al.* (2001). We describe these results in the section below.

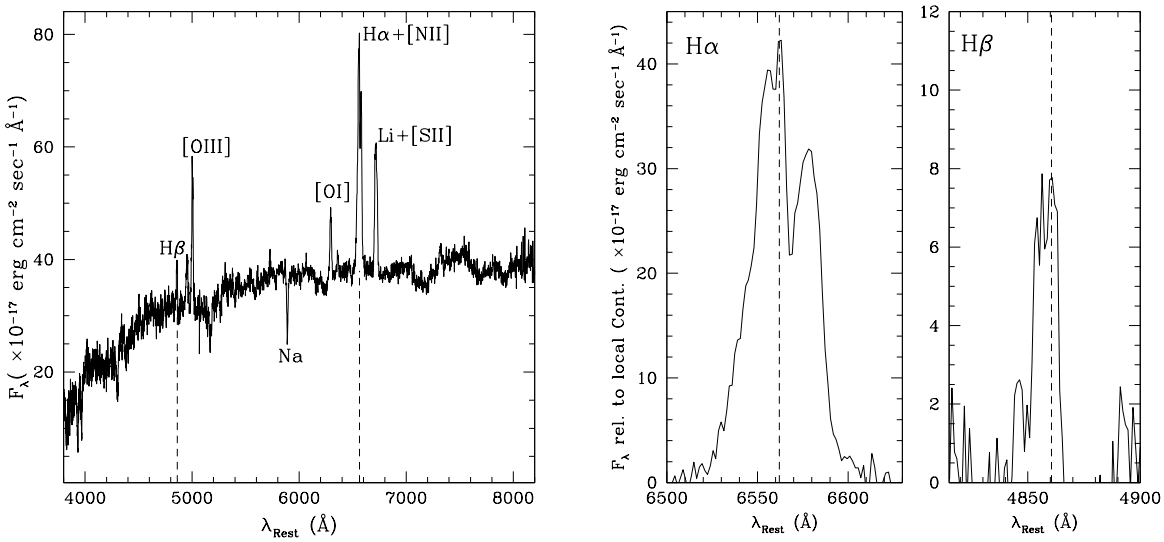

Figure 4.5: (*left*) Sloan Digital Sky Survey (SDSS) spectroscopy of the host galaxy of 3C 236. Significant emission and absorption lines have been labeled, and the positions of Hα and Hβ, the lines most relevant for our purposes, have been marked with vertical dashed lines. The spectrum has been shifted to the rest frame using the known redshift of 3C 236 at z = 0.1. (*right*) "Zoom in" of the Hα and Hβ lines from the spectrum normalized to their local continuum. SDSS data are of sufficient spectral resolution to resolve the two [NII] lines at 6548 Å and 6583 Å about Hα at 6563 Å (marked with a vertical dashed line). Buttiglione *et al.* (2009) measured the Balmer decrement $F_{\mathrm{H}\alpha}/F_{\mathrm{H}\beta}$ = 4.54. See Table 4 for other emission line measurements.

4.3.3 Comparison of photometry with stellar population models

We have compared our photometry with evolutionary models from the stellar population synthesis code STARBURST99[2] (Leitherer *et al.*, 1999; Vázquez & Leitherer, 2005). The package incorporates Geneva evolutionary tracks as well as Padova asymptotic giant branch stellar models, and is now widely used for its effectiveness in accounting for all stellar phases contributing to the SED of a young stellar population from the FUV to the NIR. Several simulations were run, with parametric variations in stellar initial mass function (IMF), heavy element abundance, mass range, and whether or not the starburst continuously formed stars at a star formation rate (SFR), or whether it was instantaneous (wherein the starburst is modeled by a delta function, and the resulting population is allowed to age through time).

Simulation results were *K*-corrected to the redshift of 3C 236 using its luminosity distance of $\sim$ 457 Mpc. The corrected model spectra were then convolved through the relevant *HST* filter

[2]http://www.stsci.edu/science/starburst99/

transmission curve using the photometric synthesis code SYNPHOT[3] in the STSDAS IRAF package. These corrected and convolved models could then be directly compared with our extinction-corrected photometry.

An inherent challenge in comparing our data to predictive population synthesis models lies in the fact that we cannot know for certain what the absolute intrinsic color of each star forming knot is. As our internal extinction correction is based solely on the Balmer decrement as measured from (relatively) low spatial resolution SDSS spectroscopy, we are able to at best make a rough correction for internal reddening. As such, running several simulations with slight variations in model parameters was largely an exploratory exercise in which we qualitatively characterized how much a model might shift in color-color space given slight changes in, for example, the IMF or heavy element abundance. In general, these variations were found to be small enough such that our uncertain photometry would be unable to discriminate between subtly different models.

Ultimately, however, we are most interested in the rough ages of the knots as this study focuses on a possible coeval relationship between the blue star forming regions and the reignition of radio activity in the central engine. Model variations are such that our order-of-magnitude age estimates are largely independent of slight changes in model parameters. Moreover, slight variations in our estimate for the internal extinction would not affect the shape of the observed SED so much that we'd associate it with a significantly older or younger starburst. As such, we will focus our discussion on the "best fit" model we have found, with the caveat that all results presented in this section are uncertain and highly dependent upon the intrinsic SEDs of the knots, which we can only roughly estimate.

It is also important to note that there is line contamination in our broad-band filters that we have not corrected for, and it is necessary to quantify how much this might affect our results, particularly for the FUV emission in the nucleus. In Table 4.4 we list intensities of selected bright emission lines (both directly measured from SDSS spectroscopy as analyzed by Buttiglione *et al.* 2009, and estimated using line ratios from Dopita *et al.* 1997, measured in the M87 nucleus). In column (3) of the table we remark on whether or not the line falls within a passband used in our observations. Relative to this work, there is significant uncertainty associated with these line fluxes given the mismatch between SDSS resolution and fiber placement and the blue star forming regions we're interested in. Moreover, there are even greater uncertainties in the estimated UV line strengths (as they are derived from ratios measured for the nucleus of M87, not 3C 236). We therefore use these fluxes only to roughly address the possible impact of line contamination

[3]http://www.stsci.edu/hst/HST_overview/documents/synphot/

on our results. There are relatively bright lines contaminating our optical and UV passbands, namely [OIII]λ5007 (in ACS HRC F555W) and CIVλ1549 (in ACS SBC F140LP and STIS NUV-MAMA). However, correcting for this contamination would not change the overall shape of the SED relative to the comparison STARBURST99 model (which itself includes stellar and nebular emission, and as mentioned above, has been redshifted and convolved through the appropriate bandpass). Even correcting the photometry by as much as a factor of two would not affect the age estimate we'd ultimately end up making, both for the knots in the dusty disk as well as for the nuclear FUV emission. We therefore do not correct our photometry for line contamination, given the uncertainties mentioned above, and because it ultimately does not affect our results.

In Fig. 4.6 we present the main result of this chapter, in which we compare the SEDs of the blue star forming knots as measured in our data with the synthetic SEDs generated by STARBURST99. We plot four "snapshot" epochs of our best-fit model, normalized to a continuous star formation rate of 1 $M_\odot$ yr^{-1}, a Salpeter (1955) IMF of slope $\alpha = 2.35$, upper and lower mass limits of 100 $M_\odot$ and 1 $M_\odot$, respectively, and solar abundances where $Z = 0.020$. These "snapshot" epochs are 1 Myr (lowest line in blue), 10 Myr (second-to-lowest SED in green), 100 Myr (second highest in yellow) and 1 Gyr (top SED in red). As discussed previously, other star formation models were tested, but are not plotted in Fig. 4.6 as variation in overall SED slope and normalization was minimal.

In black we overplot the measured SEDs of the blue star forming knots, as well as the blue emission in the nucleus, using our photometry as corrected for galactic and internal extinction. Individual knots are identified as per the legend in the upper right corner of Fig. 4.6, using the naming convention for the knots outlined in Fig. 4.4(*a*). The black symbols on each SED mark the central wavelengths of the (from left to right) FUV, NUV, *U*-, and *V*-band *HST* filters, respectively. As mentioned in the previous section, we were only able to obtain *V*-band flux measurements for knots 2, 4, and the blue emission associated with the nucleus (as they were the only regions clearly detected in the *V*-band image).

The ages of the blue knots cospatial with the dusty disk

We find the SEDs of knots 1, 2, 3, and 4 to best match the 10^7 yr model SED. Still, significant variation in color exists among each knot, whose flux in a particular bandpass can vary by as much as a factor of five with respect to the others. Moreover, the SEDs compare somewhat inconsistently with the model (green 10 Myr line in Fig. 4.6), as there is an apparent deficit of emission in the FUV, an excess in the NUV, and another deficit in the U-band (with respect to the model).

These variations are due to (1) truly intrinsic differences between the colors of the knots, (2)

patchy extinction, and/or (3) globally under- or over-correcting for extinction. While we lack the ability to quantitatively discriminate between these scenarios, we find it naturally likely that a combination of all three work to produce the observed variations. It is also important to note that we are studying UV emission in a very dusty environment that is optically thick to UV photons. The UV emission that we do see is therefore likely emitted on the near side of the clouds with respect to our line of sight, and we know little of the regions of the bursts that are more deeply embedded in the dusty disk. Nevertheless, we can confidently state that the observed SEDs of the knots are more consistent with a $10^7 - 10^8$ yr old starburst than they are with a 10^6 or 10^9 yr old starburst (as modeled by STARBURST99, anyway).

The age of the UV emission cospatial with the nucleus

Along these lines, we find the nuclear emission to most closely match the 1 Gyr SED, though there is a deficit in its FUV flux with respect to the model (top-most red 1 Gyr line). Assuming that the FUV emission in the nucleus is indeed associated with a 1 Gyr old starburst (an assumption we discuss below), it is possible (and even likely) that this FUV deficit is due to an undercorrection for internal extinction to the nucleus. Such an undercorrection would affect the FUV flux the most, while the *V*-band flux would remain relatively unchanged. The net result would be a steepening of the slope on the blue end, such that the SED of the nucleus might more closely correspond with that of the 1 Gyr model. Moreover, while we cannot quantify how patchy the extinction may be over these scales (as we have discussed several times previously), it is reasonable to imagine the extinction being greater in the nucleus than it is on the edge of the dusty disk, given the inclination of the disk is more edge-on than face-on, such that the nucleus would be farther down the line of sight than the edge of the disk (Tremblay *et al.*, 2007). Regardless, we do not expect that heavier extinction toward the nucleus (in comparison with the knots in the disk) would alter the shape of the nuclear SED so much that it would better correspond with a different age.

Of course, it is important to estimate how much the AGN may contribute to the FUV emission in the nucleus. 3C 236 is a low-excitation radio galaxy (LEG). Moreover, it lacks broad lines indicative of a deficit of ionizing photons from the accretion disk (Buttiglione *et al.*, 2009), suggesting that the accretion region is obscured along our line of sight (i.e., Urry & Padovani 1995). Contribution from the AGN to the nuclear FUV emission would therefore come in the form of scattered light, which we do not expect to contribute significantly to the overall UV excess (certainly not to a degree that would affect our order-of-magnitude age estimates). Holt *et al.* (2007) similarly fit stellar population models to their ground-based SED for 3C 236, finding that a good

Table 4.4. **Emission Line Ratios & Radio Measurements**

Measurement (1)	Value (2)	In Passband? (3)	Reference (4)
MEASURED INTENSITIES			
Log L(Hα)	41.13	No	1
Hβ / Hα	0.22(4)	F555W	1
[OIII]λ5007 / Hα	0.57(2)	F555W	1
[OI]λ6364 / Hα	0.30(3)	No	1
[NII]λ6584 / Hα	0.69(1)	No	1
[SII]λ6716 / Hα	0.49(2)	No	1
[SII]λ6731 / Hα	0.35(3)	No	1
Log L(178 MHz)	33.56	N/A	2
Log L(5 GHz)	31.62	N/A	3
ESTIMATED UV LINE INTENSITIES			
Lyα / Hα	$\sim$ 6.7	No	
CIV λ1549 / Hα	$\sim$ 1.2	F140LP, NUV-MAMA	4
HeII λ1549 / Hα	$\sim$ 0.3	F140LP, NUV-MAMA	4
NIII]λ1750 / Hα	$\sim$ 0.1	F140LP, NUV-MAMA	4
CIII]λ1909 / Hα	$\sim$ 0.3	NUV-MAMA	4
MgII λ2798 / Hα	$\sim$ 0.1	F330W	4

Note. — (1) De-reddened logarithm of luminosity in erg s^{-1} or line ratio (with respect to Hα); (2) measured value, with errors parenthetically presented as percentages; (3) remark if the line (at the redshift of 3C 236) falls into one of the *HST* passbands used in this study; (4) reference. UV line intensities were estimated using measured ratios from the nucleus of M87. Significant uncertainties are associated with these estimates.

References. — (1) Buttiglione *et al.* (2009); (2) Spinrad *et al.* (1985); (3) Buttiglione *et al.* (2010); (4) Dopita *et al.* (1997)

fit required a red power-law component, suggestive that the UV excess is not likely associated with scattered light from the AGN and is instead a young, reddened stellar population. Moreover, no point source is visible in any *HST* imaging of the nucleus, and *Spitzer Space Telescope* IR spectroscopy obtained for 3C 236 (*Spitzer* programs 20719 and 40453 by PI Baum and collaborators) does not show evidence for a hidden quasar continuum (although formal presentation of these data is forthcoming in future papers). Hence, we expect the majority of the FUV emission in the nucleus to be due to stellar continuum from young stars, whose age we have estimated to be $\sim 10^9$ yr old.

The ages of the knots in context of other works

To summarize, we conclude from Fig. 4.6 that the four star forming knots cospatial with the dusty disk are of order $\sim 10^7$ yr old, while the stars in the nucleus are older, with an age of $\sim 10^9$ yr old. In Table 5 we present the star formation rates associated with our "best fit" STARBURST99 continuous star formation model. We also list the mass range required for an instantaneous burst model to reproduce the observed fluxes, while noting that the continuous model is a better match to our data. Nevertheless, the mass ranges we estimate are consistent with those predicted by the instantaneous burst models of O'Dea *et al.* (2001). Our estimated SFRs are also consistent with those derived from the O'Dea continuous star formation models, and are always on the order of a few $M_\odot$ yr^{-1}. See Table 3 in O'Dea *et al.* (2001) to compare both their derived SFRs and masses with our results.

Unlike this work, O'Dea *et al.* (2001) compared their photometry to Bruzual & Charlot stellar population synthesis models (Bruzual A. & Charlot, 1993; Charlot & Longhetti, 2001) absent an estimate for internal extinction (the required data was not available at the time). They found bimodality in the ages of the knots, wherein knots 1 and 3 were measured to be young, of order $\lesssim 10^7$ yr old, and 2 and 4 were estimated at $\lesssim 10^8 - 10^9$ yr old. In contrast, we estimate a nearly uniform age distribution among the knots in the dust disk of $\sim 10^7$ yr old, while the FUV emission in the nucleus is likely to be $\sim 10^9$ yr. The difference in results between this work and that of O'Dea *et al.* (2001) likely arises from (1) different data sets (2) the lack of internal extinction correction in the O'Dea work (none was available at the time), and (3) comparison with Bruzual & Charlot models vs. STARBURST99 models in this work. Whatever the case, the age upper limits we estimate for our knots are consistent with the "young" knots 1 and 3 from O'Dea *et al.* (2001). That work also clearly emphasizes that the older ages estimated for knots 2 and 4 are merely upper limits, and entirely dependent upon the intrinsic colors of the knots.

The work by Holt *et al.* (2007) also estimated the ages of the star forming regions in 3C 236 by fitting young stellar population models to a ground-based SED from the ESO Very Large Telescope (VLT). Their results are consistent both with O'Dea *et al.* (2001) and this work, estimating similar ages for the stellar populations. In examining stellar absorption features, they further rule out models with ages $\gtrsim 1.0$ Gyr, as those models overpredict the depth of the Ca II feature.

The work by Koekemoer *et al.* (1999) performed a similar age dating exercise for the centrally dominant radio-loud elliptical galaxy in the cooling flow cluster Abell 2597. Much like 3C 236, that object possesses a compact radio source, a significant filamentary dust lane, and a network of clumpy knots and filaments of blue continuum, which Koekemoer *et al.* (1999) interpreted to be sites of recent star formation. Using single-burst Bruzual & Charlot models, that work derived ages for the knots of $\sim 10^7 - 10^8$ yr, comparable to the inferred age of the compact radio source.

4.4 Discussion

4.4.1 Dynamics of the gas and dust in 3C 236

As discussed in section 3.1 and seen in Fig. 4.3(*a*), 3C 236 possesses both an outer filamentary dust lane and an inner circumnuclear disk whose semi-major axes are misaligned with one another by $\sim 15^\circ$ (Martel *et al.*, 1999; de Koff *et al.*, 2000; O'Dea *et al.*, 2001). These morphologies are strongly indicative of a galaxy that has recently acquired gas from a companion, suggesting that the outer lane is dynamically young. Below we motivate this assertion using simple dynamical arguments.

Gas and dust acquired through mergers or tidal stripping is expected to coalesce on a dynamical timescale ($\sim 10^8$ yr, e.g. Gunn 1979; Tubbs 1980) and precess about a symmetry plane of the host galaxy, finally settling into it on a precession timescale of order a Gyr (e.g., Tohline *et al.* 1982; Habe & Ikeuchi 1985). During this time the gas will dissipate angular momentum and fall inward toward the nucleus at a rate dependent upon the structure of the potential well and the star formation efficiency of the gas (Barnes, 1996; Bekki & Shioya, 1997). In the scenario proposed by Lauer *et al.* (2005), filamentary distributions of dust that have not yet reached the nucleus would be classified as lanes, which might be thought of as transient structures that would eventually form a nuclear disk if given sufficient time (e.g., Tremblay *et al.* 2007, and references therein).

The recent study by Tremblay *et al.* (2007) lent evidence in support of this scenario. That work described a dichotomy between dusty lanes and disks in a sample of low-redshift ($z < 0.3$) 3CR radio galaxies (including 3C 236), finding round nuclear dusty disks to preferentially reside in round

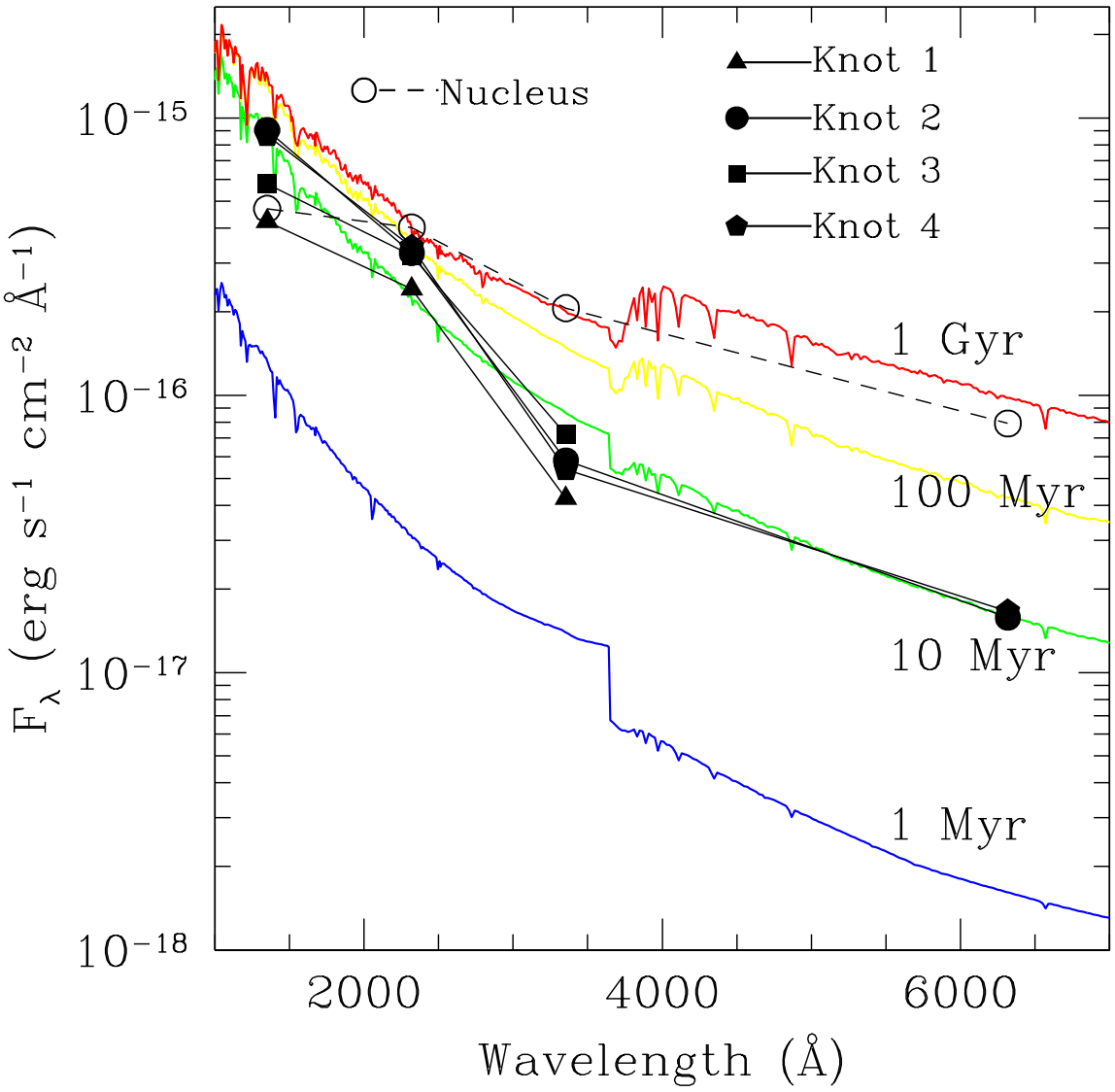

Figure 4.6: SEDs of the blue star forming knots as measured in our data, compared with synthetic SEDs as predicted by STARBURST99 stellar population synthesis models. We plot four "snapshot" epochs of one standard STARBURST99 model, normalized to a continuous star formation rate of 1 $M_\odot$ yr^{-1}, a Salpeter IMF of slope α = 2.35, upper and lower mass limits of 100 $M_\odot$ and 1 $M_\odot$, respectively, and solar abundances where Z = 0.020. Other continuous star formation models were tested, but are not plotted here as variation in overall SED slope and normalization was minimal. In black we overplot the fluxes of the blue star forming knots, as well as the red nucleus, using our photometry as corrected for galactic and internal extinction (using the Balmer decrement). Individual knots are identified as per the legend in the upper right corner, using the naming convention for the knots described in Fig. 4.4.

Table 4.5. **Estimated Star Formation Parameters**

Source (1)	Est. Required SFR ($M_\odot$ yr^{-1}, Cont. Model) (2)	Est. Required Mass Range (Log $M_\odot$, Inst. Model) (3)
Knot 1	0.69	7.3 – 8.7
Knot 2	1.47	7.7 – 9.0
Knot 3	0.94	7.5 – 8.8
Knot 4	1.41	7.7 – 9.0
Knot 3+4	2.36	7.9 – 9.2
Nucleus	0.47	7.4 – 8.7
All	7.51	8.4 – 9.7

Note. — (1) Source identifier; (2) Estimated star formation rates (SFRs) using the "best fit" STARBURST99 "snapshot" epoch as determined based on Fig. 4.6 and as described in §4.2. We have chosen the 10^7 year SED as the "best fit" for all of the knots, and the 10^9 yr SED for the nucleus. The chosen STARBURST99 model for this estimate is normalized to a continuous star formation rate of 1 $M_\odot$ yr^{-1}, a Salpeter IMF of slope α = 2.35, upper and lower mass limits of 100 $M_\odot$ and 1 $M_\odot$, respectively, and solar abundances where Z = 0.020. Other models were tested, but those results are not presented here as variation was minimal, and the SFR for each knot is generally of order ~ 1 $M_\odot$ yr^{-1} regardless of the model. (3) Required mass range of an instantaneous starburst triggered $10^7 - 10^8$ yr ago. The STARBURST99 parameters used are the same as in (2), except the starburst is modeled as a delta function at time zero, rather than forming continuously with a star formation rate.

to boxy host galaxies, depending on their inclination with respect to the line of sight. Conversely, filamentary dust lanes which had not yet settled into the nucleus were found to reside exclusively in host galaxies with disky isophotes. Numerical simulations of dissipational mergers have shown that rotationally supported, disky systems are typically the result of gas-rich mergers, while boxy galaxies are often formed through dry (gas-poor) mergers (e.g., Barnes 1996; Bekki & Shioya 1997; Khochfar & Burkert 2005). Past studies of both radio-loud and radio-quiet ellipticals have shown that dust lanes are very often misaligned with the major axis of their host galaxy isophotes, while the opposite is true for dusty disks (e.g., Tran *et al.* 2001, and references therein). These results support a scenario in which nuclear dusty disks are native to the host galaxy pre-merger, while dust lanes are far younger structures, having recently been externally acquired through tidal stripping or a merger (Tremblay *et al.*, 2007).

3C 236 appears to contain *both* an outer dust lane and inner dusty disk. Moreover, the outer dust lane is slightly misalinged with the major axis of the host galaxy isophotes over a projected $4''$ linear extent centered about the nucleus. We mark the isophotal structure of the host in Fig. 4.7(*a*), in which we have plotted isocontours on 1.6 μm (analog of *H*-band) *HST*/NICMOS imaging from Madrid *et al.* (2006). In Fig. 4.7(*b*) we present a "zoomed in" view of the colormap originally presented in Fig. 4.2, with contours marking the misalinged outer lane and inner dusty disk. Note how the dusty disk appears to be better aligned with the major axis of the inner host galaxy isophotes than the lane (Figs. 4.7*a* and (*b*) are on the same scale). In Figs. 4.7(*c*) and (*d*) we plot isophote major axis position angle (P.A.) and isophotal ellipticity, respectively, as a function of semi-major axis. These data stem from fits to the NICMOS *H*-band isophotes using the IRAF task `ellipse`, originally performed by Donzelli *et al.* (2007) and analyzed by Tremblay *et al.* (2007). Note from Fig. 4.7(*c*) that the isophotes are lopsided, particularly to the southeast between $\sim 2''$and $4''$from the nucleus. The asymmetric isophotes are indicative of a stellar population that has yet to fully relax dynamically, suggesting a recent minor merger has taken place.

Framed in the context of the results discussed above, the dual dust morphologies in 3C 236 present strong evidence of the host galaxy having recently ($\sim 10^9$ yr) acquired gas from a companion. Following the scenario discussed by Tremblay *et al.* (2007), the inner dusty disk may have been native to the host galaxy *before* the recent gas acquision event, while the outer lane may be been externally acquired as a result of that event, and is still in the process of migration toward the nucleus.

As dust traces molecular gas accretion reservoirs that fuel AGN activity, this scenario works naturally with the notion that 3C 236 is an "interrupted" radio source. de Koff *et al.* (2000) estimated the mass of dust in the lane and disk to be $\sim 10^7$ $M_\odot$, corresponding to a gas mass of

$\sim 10^9$ $M_\odot$. Such a significant gas mass could supply fuel to the AGN for a long period of time, allowing the radio galaxy to grow to its very large size (4 Mpc). The relic radio source also lends an unrelated argument in favor of a scenario in which a large fraction of the gas mass was native to the host galaxy *prior* to whatever event cut off or smothered the AGN activity for a period of time (ostensibly the same event responsible for depositing new gas into the system). *Some* significant fuel source was clearly necessary to power such a large radio jet, though it is not clear whether that original source is still present and observed in the form of the inner disk, or whether the original source was exhausted and the dust we observe now traces a newly deposited accretion reservoir. Imagining for a moment that the inner dust disk is old and native to the host "pre-interruption", it is plausible to imagine the inner disk being perturbed, cutting off the BH fuel supply, then resettling back toward the nucleus after a short period of time ($\sim 10^7$ yr), reigniting AGN activity. During this time the young, newly acquired dust from the "interruption" event would begin to settle into a filamentary lane, and begin migration inwards toward the nucleus on a much larger timescale (a few times $\sim 10^9$ yr).

The nature of this "interruption" event is not clear. The host galaxy of 3C 236 is in a very poor environment and has no obvious group members within 0.5 Mpc (based on a statistical correction for background contamination, Zirbel 1997). This, combined with the fact that the isophotes of 3C 236, while lopsided, are not highly irregular, suggests that the event was likely a minor merger. In this scenario, the presumably dust-rich and small donor galaxy would have been fully consumed by the much larger 3C 236. Were the event a major merger, one would expect to see more irregularity in the isophotes, as the "dynamically young" dust, the CSS radio source, and the fact that one can still detect the relic radio source even given synchrotron cooling timescales ($\sim 10^8 - 10^9$ yr) require the merger event to have happened relatively recently (no more than $10^7 - 10^8$ yrs ago). A major merger of nearly equal-mass galaxies would likely result in structural irregularities that would last much longer than that timescale.

4.4.2 Star formation in the nucleus in the context of the relic radio source

Canonical estimates based on synchrotron cooling timescales would suggest that the relic ~ 4 Mpc FR II radio source is not older than a few times 10^8 yr (e.g., Parma *et al.* 1999). O'Dea *et al.* (2001) attempted to better constrain the age of the relic source, arguing that a lower limit to its age $t_{\rm min,relic}$ could be estimated using simple dynamical arguments:

$$t_{\rm min,relic} \simeq 7.8 \times 10^6 \left(\frac{v_{\rm lobe}}{c}\right)^{-1} \ {\rm yr} \tag{4.2}$$

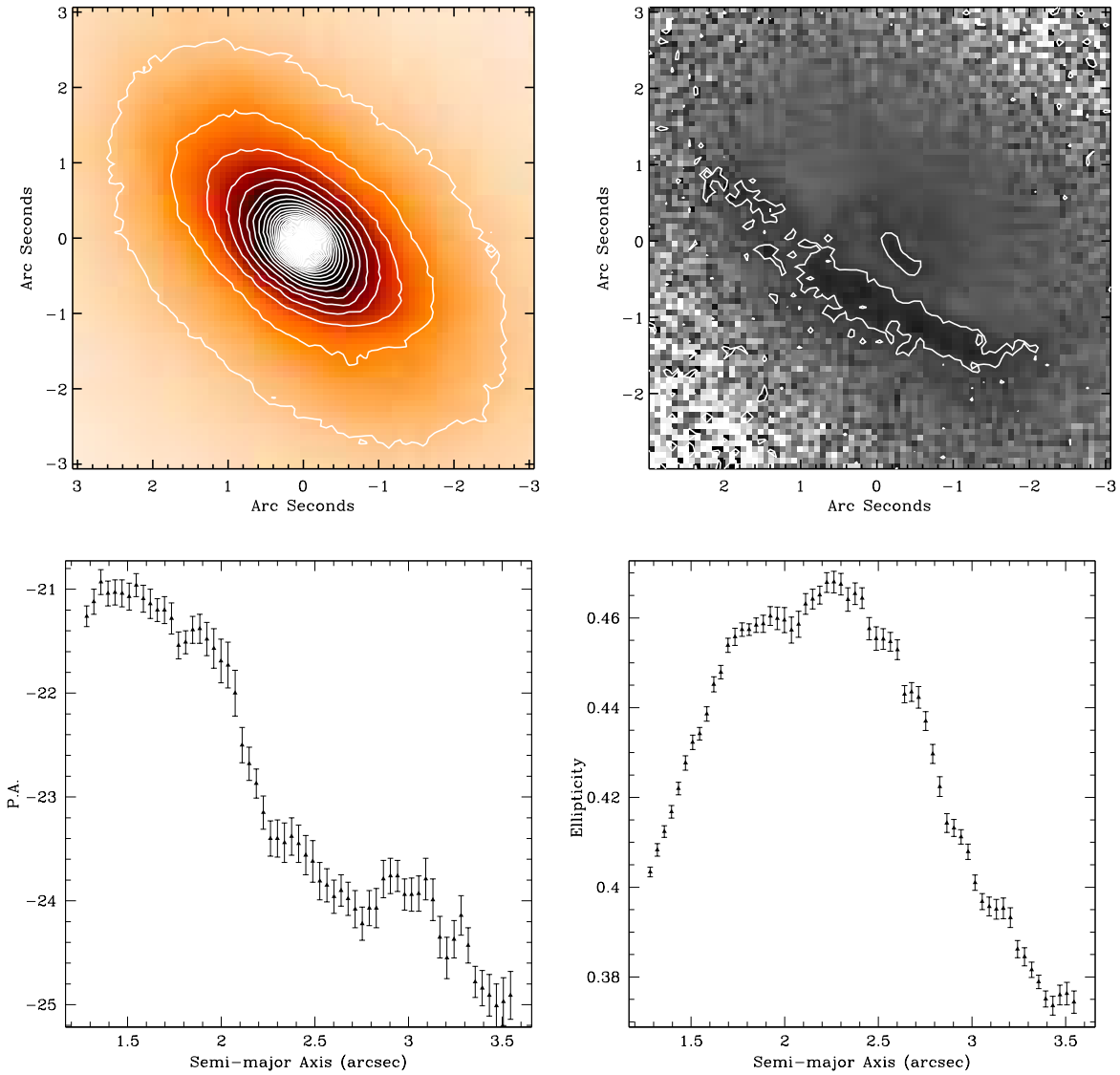

Figure 4.7: (*top left*) *HST*/NIC2 1.6 μm image of 3C 236 with highlighted isophotal contours. (*top right*) 1.6 μm / 0.702 μm (*H*/*R*-band) colormap of the dusty disk in the nucleus of 3C 236, made via division of *HST*/NIC2 and WFPC2 data. Evidence for two disparate dust structures are seen in the colormap. The position angles of the outer dust lane and the inner disk-like structure are offset by $\sim 10^{\circ}$. (*bottom left*) Semi-major axis position angles (P.A.) of ellipses fit to the *HST*/NIC2 *H*-band isophotes using the IRAF routine `ellipse`. The plot shows a several sigma twist in the isophotes between $1''$and $3''$, which is also visibly evident in the contours of the image at top left. (*bottom right*) Ellipticity of the fit isophotes from `ellipse` over the same scale.

where v_{lobe} is the lobe propagation speed. Using a canonical expansion speed of $\sim 0.03c$ (e.g., Alexander & Leahy 1987), O'Dea *et al.* (2001) estimated the dynamical age of the relic source to be 2.6×10^8 yr. This would make for an old radio source, near to the time when synchrotron cooling would render the lobes unobservable at higher frequencies as the electrons age. Of course, the relic source associated with 3C 236 is among the largest in the universe, so the fact that it's likely old is not surprising.

If the double-double radio source indeed arises from episodic activity in the AGN, at some stage in the life of 3C 236 its nucleus would have entered a dormant phase and halted the collimation of its jets. This would have deprived the hot-spots of their energy supply on a timescale of order the nucleus-to-hotspot traversal time of the jet material ejected prior to the shut down of the AGN, assuming it advanced relativistically (e.g., Baum *et al.* 1990; Kaiser *et al.* 2000; Schoenmakers *et al.* 2000a,b). The production of "young electrons" in the hotspots by magnetohydrodynamical (MHD) turbulence or Fermi acceleration in the Mach disk is thought to cease when the hotspot is no longer fed by a jet, meaning the electron population will begin to age once the last of the remaining jet material has arrived (e.g., Jones *et al.* 1999, and references therein). If one believes radio spectral ageing techniques, then the ages of the youngest electrons in the lobe added to the jet traversal time from the nucleus to the hotspot should be of order the timescale over which the nucleus has been dormant. O'Dea *et al.* (2001) estimated this timescale to be $\sim 10^7$ yr, an order of magnitude younger than the 2.6×10^8 yr dynamical age of the relic source.

Note that the ages estimated by these two techniques need not agree, as the ages of the youngest electrons in the lobe will correspond to the time when jet propagation ceased, but tell us nothing about how long the nucleus may have been active. Moreover, all of these age estimates in the radio are heavily dependent upon assumptions such as the propagation speed and the true source of young electrons. Indeed, the active phase corresponding to the creation of the relic radio source may have been far longer lived than the dynamical age of the relic source itself. We cannot know for certain how much of the lobes may have already cooled past the point of observability. Observations at lower frequencies may be enlightening in this regard.

As discussed in section 3.3.2, we have estimated the age of the nuclear starburst to be $\sim 10^9$ yr old, given the previously discussed caveats and noting that it may be younger if we have under-corrected for internal extinction to the nucleus. Nevertheless, the approximate ages of the nuclear starburst and the ~ 4 Mpc relic source are just close enough to warrant noting that they might *possibly* be related to a common gas infall event. Having said that, we again stress that this is only a possibility, and we are unable to draw conclusions relating to such a connection in light of the significant uncertainties involved.

4.4.3 The star forming knots in the context of the CSS radio source

O'Dea *et al.* (2001) used arguments similar to those discussed in the above section to estimate the age of the central CSS radio source, operating under the assumption that it was young and not "old and frustrated" (a reasonable assumption, especially in light of recent results on CSS sources, e.g. Holt *et al.* 2009). Their estimate for its age $t_{\rm min,CSS}$ was given by

$$t_{\rm min,CSS} \simeq 3.2 \times 10^3 \left(\frac{v_{\rm lobe}}{c}\right)^{-1} \ {\rm yr}, \tag{4.3}$$

where using the same lobe advance speed they found the age of the CSS source to be very young indeed, of order $\sim 1.0 \times 10^5$ yr. As discussed in section 3.3, we have estimated that the star forming knots cospatial with the dusty disk are $\sim 10^7$ yr old.

4.4.4 Is the recent episode of star formation coupled to the rebirth of radio activity in 3C 236?

If the recent episode of star formation in the disk were directly related to the event resulting in reignition of radio activity giving birth to the CSS source, we would not necessarily expect a one-to-one correspondence among their ages. The dynamical time on scales of a few kpc, where the star forming knots are located, is far longer than the dynamical time on sub-pc scales where the AGN is fuelled. In this context, the difference in estimated ages of the star forming knots and the CSS source would constrain the timescale over which the gas is transported from kpc to sub-kpc scales. This can't be any longer than the age of the young stars ($\sim 10^7$ yr), which corresponds not only with the dynamical time on kpc scales but also the estimated dormancy period of the nucleus.

The recent work by Wuyts *et al.* (2009) discusses the merger-driven models of Hopkins *et al.* (2006) in the context of internal color structure in massive star forming galaxies. They find internal color gradients to be strongest during the merger phase, with blue star formation expected on scales outside a few kpc (approximately where we observe the star formation in 3C 236). In their previously mentioned work, Koekemoer *et al.* (1999) derived ages to star forming knots in Abell 2597 that were closely related to the inferred merger and AGN fuelling timescales giving rise to the compact radio source in that galaxy.

Our observations have yielded similar results, and seem to suggest one possible "story" for the history of 3C 236. In considering its double-double radio morphology in the context of its dynamically young dust complex and recently triggered compact starbursts, we suggest that 3C 236

has undergone multiple epochs of AGN activity due to a non-steady supply of fuel to the central engine. We suggest that the period of activity related to the 4 Mpc relic source was ended when the fuel supply to the central engine was cut off, whether by exhaustion, strangulation, or disturbance. After a subsequent $\sim 10^7$ yr dormant phase, infalling gas from a minor merger event reached kpc scales, where a starburst was triggered via cloud-cloud collisions amid collapse. The gas not involved in star formation reached the nucleus after a subsequent dynamical time, triggering reignition of the AGN and giving birth to the CSS radio source.

We hesitate to make further suggestions relating to the star formation in the nucleus and its possible connection with the relic source, nor will we suggest whether or not the outer filamentary dust lane and inner disk are two distinct structures with different histories (i.e., recently acquired vs. native to the host pre-merger). We have argued in section 4.1 that discriminating between the two scenarios may shed light on whether the AGN "interruption" event was due to actual *exhaustion* of its fuel supply, or only dynamical *disturbance* of its fuel supply. Whatever the case, the results of this work and those of O'Dea *et al.* (2001) strongly suggest that the transport of gas to the nucleus of 3C 236 has been significantly nonsteady over the past Gyr, giving rise to a unique galaxy that acts as an important test case in studies of the AGN/starburst connection.

4.5 Summary

We have presented follow-up *HST* ACS and STIS observations of the radio galaxy 3C 236, described by O'Dea *et al.* (2001) as an "interrupted" radio source. The galaxy is associated with a massive relic ~ 4 Mpc FR II radio source (making it one of the largest objects in the universe), as well as an inner 2 kpc CSS "young" radio source. This "double-double" radio morphology is evidence for multiple epochs of AGN activity, wherein the BH fuel supply is thought to have been exhausted or cut off at some time in the past, and has only recently been reignited.

We present *HST* FUV, NUV, U-, and V-band imaging of four star forming knots, previously described by O'Dea *et al.* (2001), that are arranged in an arc along the outer edge of the galaxy's circumnuclear dust disk (which itself is surrounded by a misaligned outer filamentary dust lane). We have also detected blue emission cospatial with the nucleus itself. We describe these observations in detail, as well as the steps taken to reduce the data. We present photometry of the blue knots, and discuss our efforts to correct the data for internal extinction to the source using the Balmer decrement available from archival SDSS spectroscopy.

We compare the measured four-color SEDs of the star forming knots to synthetic SEDs from

STARBURST99 stellar population synthesis models, with the ultimate goal of roughly estimating the ages of the knots. We find that the four knots cospatial with the outer edge of the dusty disk are likely $\sim 10^7$ yr old, while the FUV emission cospatial with the nucleus is likely older, at $\sim 10^9$ yr old (with the caveat that undercorrection for internal extinction in the nucleus would lower this limit). We argue that the ages of the young knots are suggestive of a causal connection with the young central radio source.

We frame these results in the context of 3C 236 as an apparently "interrupted" radio galaxy. Our results are generally consistent with those of O'Dea *et al.* (2001), and we argue along similar lines that the transport of gas in the nucleus of 3C 236 is nonsteady, wherein the active phase giving rise to the 4 Mpc relic source was cut off by exhaustion or disturbance of the AGN fuel supply. We suggest that this lead to a dormant period punctuated by a minor merger event, and the subsequent infalling gas triggered not only a new episode of star formation, but also ushered the galaxy into a new active phase giving rise to the young CSS radio source.

Results such as these support the natural argument that infalling gas largely fosters the relationship between the growth of the AGN and that of its host galaxy stellar component. In time, that relationship may evolve from mutual growth to the regulation of the latter by the former through quenching from AGN feedback. As infalling gas is a critical component in merger-driven hierarchical models, the triggering of AGN may be fundamental to galaxy evolution itself. In this way, the relevance of 3C 236 might extend beyond studies of episodic activity in radio galaxies to studies of AGN in the context of galaxy evolution as a whole.

4.6 Context: 3C 236 compared with A2597

Though they reside in very different environments, 3C 236 and Abell 2597 (the subject of Chapter 2) share important similarities and equally important differences. It is useful to summarize these, and in so doing, assess the role that may be played by environment in shaping the various observed properties of the two systems.

- 3C 236 is a field galaxy (i.e., in a poor environment), with no detected group members or companions within 0.5 Mpc. A2597 resides in a rich cluster associated with a cool core. High resolution X-ray spectroscopy is consistent with a moderately strong cooling flow.

- Both 3C 236 and the A2597 BCG exhibit evidence of episodic radio activity: 3C 236 is a double-double radio source (outer 4 Mpc relic source, inner 2 kpc CSS source), and PKS

2322-122 in the A2597 BCG is a ~ 10 kpc CSS source with a network of X-ray cavities suggestive of inflation by at least one previous active episode.

- 3C 236 possesses a relic, 4 Mpc FR II radio source with an upper age limit estimated at $\sim 10^8$ yr. A2597 is far more compact in terms of radio structure, though it does possess what *could* be considered a relic low-frequency source ~ 20 kpc in length. The morphology of this low frequency radio source can be considered more "FR I-like" than "FR II-like".

- In A2597, low frequency 330 MHz emission, offset in position angle from the 8.4 GHz CSS source, is observed to be cospatial with the largest of these X-ray cavities. Ghost X-ray cavities not associated with radio emission are also detected at more distant clustercentric radii.

- The estimated duty cycle for 3C 236, by simple age estimates for the "old" relic source and the "young" CSS source, is $\sim 10^7$ yr (see the discussion in this Chapter), while quantitative analysis of the X-ray cavity network and radio structures in A2597 suggests the AGN duty cycle is of order $10^7 - 10^8$ yr.

- Both sources harbor compact FUV emission, inferred to arise from ongoing star formation, in clumpy and filamentary morphologies spanning the central few (< 10) kpc. In A2597, the FUV emission spatially traces the morphology of the emission line nebula. In 3C 236, the clumpy FUV emission is cospatial in projection with an outer filamentary dust lane, as well as with the nucleus, surrounded by an inner dusty disk offset in position angle from the major axis of the outer dust lane.

- The compact knots of star formation in 3C 236 are estimated to be 10^7 yr and 10^9 yr old, respectively. The estimated age range of the young stellar component in A2597, as inferred from FUV and U-band observations, is 5×10^6 to 6×10^8 yr.

- The FUV-derived star formation rates for the compact knots are similar for both sources (a few $M_\odot$ yr^{-1}), and correspond to a similar total mass of new stars added to each galaxy (on the order of $\sim 10^6\ M_\odot$).

- Both sources can be considered "low excitation" galaxies, with respect to their optical spectra.

- While both sources are dusty (as inferred from optical observations), 3C 236 possesses a far more structured and "kinematically settled" dust complex, which includes the outer filamentary dust lane and an inner dusty disk. There is a small position angle offset between these two structures. A2597 harbors a far more morphologically "disturbed" dust lane spanning an axis that is nearly perpendicular to the BCG isophotal major axis (in contrast with 3C 236).
- While 3C 236 and A2597 share important similarities in the FUV, optical, and radio, they are extremely different in the X-ray. This is not surprising, as 3C 236 is not associated with a cluster and is not embedded within a hot X-ray atmosphere, whereas A2597 is a strong, X-ray bright cool core cluster.

The strong similarities between the two sources immediately suggests that a cooling flow is not exclusively required to provide the gaseous reservoir fuelling star formation and AGN activity in A2597. Having said that, recent star formation and recently triggered AGN activity can be simply understood in the context of infalling gas, regardless where it came from. Presumably, 3C 236 acquired the gas reservoir which is fuelling the current episode of AGN activity and star formation from a merger-driven "cold accretion" scenario. Gas acquired through a merger or tidal stripping is expected to coalesce in a symmetry plane of the host galaxy and slowly flow inwards. Similar behavior can be expected of a cooling flow scenario, with the main exception being that the gas is hot as it is acquired, and may be associated with less net angular momentum than cold, dusty gas acquired through a merger. Ultimately, we are not in a position to comment further on the role of mergers vs. cooling flows in providing the gaseous reservoirs found in the centers of CC BCGs. X-ray spectroscopy of A2597 is consistent with a moderately strong cooling flow, so if the model is correct, that cooling gas certainly needs to go *somewhere*. On the other hand, 3C 236 almost certainly had to acquire its gas reservoir through a merger. Perhaps the kpc-scale settled dust complex in 3C 236 and the lack of such a dust complex in A2597 can be understood in the context of cold vs. hot accretion scenarios.

5

THE EPOCH OF CLUSTER ASSEMBLY

Distant FR I Radio Galaxies *as* Cluster Beacons

On their backs were vermiculite patterns that were maps of the world in its becoming.
CORMAC MCCARTHY, 2006

Galaxy clusters are thought to assemble at redshifts $1 < z < 2$, though to date, very few (of order tens) have been detected in this redshift range (which has appropriately been named the "cluster desert"). This is not necessarily surprising, given the difficulties associated with extending typical galaxy cluster selection methods (e.g., X-ray surveys) to these depths. The problem is compounded because spectroscopic confirmation of candidate clusters in the "desert" is made extremely difficult when the 4,000 Å break is redshifted beyond 10,000 Å (at $z = 1.5$). In this chapter, we present a search for FR I radio galaxy candidates at $1 < z < 2$. As discussed in Chapter 1, FR Is are ubiquitously associated with cD ellipticals in local galaxy clusters, though no FR Is are (officially) known to exist beyond $z > 1$, given (a) the tight redshift-luminosity correlation and (b) the low(er) luminosities of FR Is vs. FR IIs, which are generally found at higher redshifts. As we will discuss

below, there are (possibly) ways around this, and the detection of candidate FR I sources at these distances may act as "beacons" for the assembling protoclusters they may be associated with.

Probing the epoch of cluster assembly will be critical to an understanding of the cosmological evolution of cool cores, and the "entropy history" of clusters in general. As discussed in Section 1.5, FR I radio galaxies seem to require "hot mode" accretion with low accretion rates. Locating FR Is at high-z, particularly those associated with clusters or protoclusters, would argue for the presence of such fuelling modes in this redshift range. A large population of $1 < z < 2$ FR I could be considered surprising and contrary to expectations, as merger-driven hierarchical models are thought to dominate structure growth at these early epochs. Finally, the detection of high-z clusters is critically important for cosmological models, as the cluster mass function at high redshifts constrains ΛCDM cosmology. At the moment, our understanding suffers badly from poor statistics, as existing X-ray satellites are incapable of extending X-ray cluster selection methods to these depths. Moreover, future X-ray missions such as *WFXT* are either in their infancy and a long way off, or have been abandoned altogether (see the regrettable recent cancellation of the *IXO* mission). It is therefore necessary to find *other* ways by which high redshift clusters can be found, and this chapter presents one such method. The results in this chapter were originally published in Chiaberge *et al.* (2009), and have since been put to use in the possible detection of candidate protoclusters at $z \sim 1.8$ (Chiaberge *et al.*, 2010).

5.1 Context

Extended, 100 kpc scale radio emission associated with radio galaxies has long been classified into two morphological groups: "edge-darkened" Fanaroff-Riley class I (FR I) objects with (often) two "plume-like" jets, and edge-brightened FR II objects characterized by bright terminal hotspots and the absence of an obvious counterjet (Fanaroff & Riley, 1974). FR I galaxies typically have a radio power lower than that of FR II sources, with the FR I/FR II break set at $L_{178\ \mathrm{MHz}} \sim 2 \times 10^{33}$ erg s^{-1} Hz^{-1}. However, the transition is rather smooth, and both radio morphologies are observed in the population of sources whose luminosities are near this break (e.g., Bridle, 1984). The FR I/FR II break (at low redshifts) also depends on the luminosity of the host galaxy, as shown by Owen & Ledlow (1994); Ledlow & Owen (1996). Whether this arises from an intrinsic relationship or is merely the result of selection effects is still not obvious (Scarpa & Urry, 2001). From the optical point of view, FR Is are invariably associated with the most massive galaxies in the local universe (e.g., Zirbel, 1996; Donzelli *et al.*, 2007), thus they are also most likely to be linked with the most

massive black holes in the local universe. Furthermore, FR Is are usually located at the center of massive clusters (see e.g. Owen *et al.*, 1996, for a review). On the other hand, at low redshifts, FR IIs are generally found in regions of lower density, while (critically) *some* FR II reside in richer groups or clusters at redshifts higher than ~ 0.5 (Zirbel, 1997).

The discovery (or *confirmed absence*) of high redshift (hereafter "high-z") FR Is will greatly inform our understanding of several major unsolved problems specific to observational dichotomies in radio galaxies (see Chapter 1), in addition to studies of assembling protoclusters at $1 < z < 2$. However, flux-limited samples of radio galaxies such as the 3CR and its deeper successors (the 6C and 7C catalogs) are limited by the tight redshift-luminosity correlation, i.e. the well known Malmquist bias. This, along with the steep luminosity function of these objects, gives rise to a selection bias resulting in detection of high luminosity sources only at high redshifts and low power sources exclusively at low redshift. It is therefore unsurprising that, in the above mentioned catalogs, all "high z" objects are FR II sources (or QSOs), while FR Is are only found at $z < 0.2$. Indeed, besides possibly one of the two candidates discussed in Snellen & Best (2001a), no FR I radio galaxies are known to exist at $z > 1$. Nevertheless, there is evidence that the population of radio-loud AGN substantially increases with redshift up to $z \sim 2-2.5$ (e.g. Ueda *et al.*, 2003). Thus, if FR I galaxies do in fact exist at high redshift, they might be significantly more abundant at $z > 1$ than in the local universe. Sadler *et al.* (2007) find that, in the redshift range $0 < z < 0.7$, radio galaxies with radio powers $P_{1.4\ \mathrm{GHz}} < 10^{25}$ W Hz^{-1} undergo significant cosmic evolution. Their result is consistent with a pure luminosity evolution law similar to that followed by star forming galaxies over a similar redshift range. The discovery of low power radio galaxies at higher redshifts will clearly also inform our understanding of the cosmological evolution of radio galaxies as compared to "normal" galaxies.

The role of FR Is in the framework of the unification scheme for radio-loud AGN is a significant matter of debate (see Chapter 1 for a slightly more comprehensive review). In particular, the lack of low redshift "FR I quasars[1]" (with the possible exception of a few peculiar objects, such as the broad-lined FR I 3C 120, e.g., Eracleous & Halpern 1994; García-Lorenzo *et al.* 2005), has yet to be fully understood. It is possible that most (if not all) FR Is intrinsically lack a broad line region and are possibly powered by (relatively) radiatively inefficient accretion disks (e.g. Baum *et al.*, 1995; Falcke *et al.*, 2004; Fabian *et al.*, 2006). This picture is also supported by the discovery that the large majority of FR I hosts have faint unresolved nuclei in *HST* images. The flux and luminosities of these nuclei show a tight correlation with those of the radio cores (Chiaberge *et al.*,

[1]We define FR I quasars to be radio galaxies associated with objects showing broad emission lines in their UV-optical spectrum.

1999). The existence of such a correlation is explained in terms of a single emission mechanism (non-thermal synchrotron radiation produced at the base of the relativistic jet) for both the radio and optical bands (Chiaberge *et al.*, 1999). On the other hand, work by Heywood *et al.* (2007) claims that FR I quasars are prevalent in the Universe, based on the analysis of a sample of QSOs in the redshift range $0.36 < z < 2.5$ selected from the 7C survey, using both their low-frequency flux density and optical spectral properties. However, some of the results from that work are still unclear. For example, these authors show evidence for the existence of "high-power" FR I QSO, whose nature has yet to be completely understood. A search for "bona fide" *low power* radio galaxies at $1 < z < 2$ will clearly inform a better understanding of the FR I-QSO phenomenon and its role in the AGN unification framework.

From the point of view of the environment, FR I radio galaxies are found in giant ellipticals often located at the center of clusters of galaxies. Finding high-z FR I with properties similar to those found in the local universe may represent a breakthrough for studies of the evolution of galaxies and clusters. Using radio galaxies as "beacons" for high-z clusters is not a new idea. In the recent past, high-z radio galaxies have often been used in searches for protoclusters and massive galaxies at the epoch of their formation (e.g. Pentericci *et al.*, 2001; Zirm *et al.*, 2005; Miley & De Breuck, 2008). However, these studies used high power sources with extremely high redshifts ($z > 2$). These objects are rare (in terms of detection frequencies), and their connection to radio galaxies in the local Universe is not clear. It is also not obvious whether their protocluster environment will have virialized by $z \gtrsim 2$, given the difficulties associated with the X-ray detection of their ICM. Powerful FR IIs have the disadvantage of exhibiting strong emission from the nucleus and powerful relativistic jets, which may strongly influence the properties of the host galaxy and may hamper studies of the environment, particularly in the X-ray band (e.g Fabian *et al.*, 2003). As FR Is are less powerful AGNs, they are more similar to "normal" inactive galaxies than FR IIs, and enable an easier investigation of the surrounding environment. FR Is with distorted morphologies have been used in previous cluster searches, but only out to a redshift $z < 1$ (Blanton *et al.*, 2000). To date, only a handful (less than 10) of X-ray confirmed clusters are known at $z > 1$, none of which have redshifts higher than $z = 1.45$ (see Rosati *et al.*, 2002, for a review). The clusters associated with our FR I candidates may in fact represent the "missing link" between the protoclusters at redshifts > 2 and the well studied clusters of galaxies at $z < 1$.

In this chapter, we present a search for FR I radio galaxies between $1 < z < 2$ by taking advantage of the large collection of multiwavelength data gathered via the Cosmic Evolution Survey (hereafter COSMOS, Scoville *et al.* 2007). In section 5.2 we give an overview of our method, and in section 5.3 we describe our selection procedure in detail. In section 5.4 we discuss a few

peculiar objects for which the optical counterpart identification is uncertain, and in section 5.5 we discuss our candidate high-z FR Is from the point of view of their radio morphology and local environment. We conclude by presenting several high-z galaxy cluster candidates discovered using our newly developed selection procedure. In section 5.6 we give a summary of this chapter, draw conclusions, and outline future prospects. Throughout this chapter we normalize all listed magnitudes to the Vega system.

5.2 Overview of our search for high-z FR Is

The search for FR I radio galaxy candidates between $1 < z < 2$ is performed using selection criteria that span multiple wavelengths. As pointed out in the previous section, flux limited samples of radio galaxies include low power sources at low redshift only. The 3C sample, arguably the best studied sample of radio galaxies, includes FR I radio galaxies only out to $z \sim 0.2$ (because its flux limit is set to 9 Jy at 178 MHz). Deeper catalogs may include a larger number of distant FR Is, but flux-limited searches based on these catalogs are highly inefficient given the dominant population of faint radio sources associated with e.g. nearby starburst galaxies. In other words, if we were to use deep flux-limited samples, we would find a large fraction of sources with a radio flux that is typical of (e.g.) FR Is at $z \sim 1$, but which are in fact low-z starburst galaxies (or even possibly bright FR IIs at $z > 2$). We would find very few "true" high-z FR Is using these samples. In order to select "bona fide" FR I candidates, it is therefore crucial that our search discriminate not only by radio power, but also by properties across multiple bands.

We focus our search within the overlapping fields of the Very Large Array Faint Images of the Radio Sky at Twenty-centimeters (VLA FIRST) survey (Becker *et al.*, 1995) and the cross-spectrum Cosmic Evolution Survey (COSMOS, Scoville *et al.* 2007). The COSMOS field, a $1.4^\circ \times 1.4^\circ$ square centered at R.A.=10:00:28.6, DEC=+02:12:21.0 (J2000) is entirely covered by FIRST. The COSMOS region was selected because its equatorial position allows for observations from northern- and southern-hemisphere observatories, as well as for its low and uniform galactic extinction $\left(\langle E\,(B-V)\rangle \simeq 0.02 \text{ mag}\right)$ and lack of very bright radio, UV, and X-ray sources. This 2 square degree region of the sky has been extensively imaged across the spectrum with deep observations from most of the major space- and ground-based observatories, yielding a rich dataset of over 2 million galaxies in multiple bands. The specific COSMOS datasets used in our selection procedure consist of 1.4 GHz radio imaging from the VLA (Schinnerer *et al.*, 2007), as well as optical images taken with *HST*'s Advanced Camera for Surveys (ACS/WFC, Koekemoer *et al.* 2007)

in the F814W filter (similar to *i*-band), K_s-band from the Kitt Peak National Observatory (KPNO, Capak *et al.* 2007), optical bands from Subaru (Taniguchi *et al.*, 2007), and *i* and *u*-bands from the Canada-France-Hawaii Telescope (CFHT, Capak *et al.* 2007). We also make use of less sensitive imaging across multiple optical bands from the *Sloan Digital Sky Survey* (SDSS, York *et al.* 2000) Data Release 5 (DR5).

Our search procedure begins with the FIRST survey at 1.4 GHz. The low resolution FIRST data allow us to easily start our selection procedure based on the "total" radio flux. FIRST was initially conceived as a radio sky counterpart to the Palomar Observatory Sky Survey (POSS I), and so encompasses over 10,000 square degrees of the North Galactic Cap (which includes the full COSMOS field), imaged in 3 minute snapshots with 2×7 3-MHz frequency channels centered at 1.365 and 1.435 GHz in the VLA's B-configuration (Becker *et al.*, 1995). Post-pipeline radio maps have a resolution of $5''$, and the detection threshold of the survey is of order ~ 1 mJy with a typical RMS of 0.15 mJy. At redshift $z = 1.5$, $5''$ corresponds to 40 kpc. Since FR I radio galaxies (in the local Universe, at least) exhibit jet structures at a few times 100 kpc scales, very little morphological information is discernible from the 1.4 GHz FIRST images. However, higher resolution maps would have the disadvantage of missing some of the extended, lower surface brightness regions, therefore the FIRST survey is the right catalog with which to begin our search.

At the 1 mJy detection threshold of the survey, ~ 90 sources per square degree are detected. The low angular resolution of FIRST is compensated for by the VLA-COSMOS survey (Schinnerer *et al.*, 2007), which has a resolution of $1''.5 \times 1''.4$, corresponding to ~ 12 kpc for a source at $z = 1.5$, and a 1σ detection threshold of 10 μJy. We therefore use the FIRST images only to obtain the total radio flux of the sources. We use the deeper and higher resolution VLA-COSMOS data to study the actual radio structure of the sources that meet our initial flux selection and derive their position, as detailed in the next section.

It is worth reiterating that "step one" of our search for FR Is is not based on *morphology*, but rather on *radio flux*. However, we do use the radio morphology to exclude FR IIs. Therefore, at the end of our selection process, we are left with a sample of low power radio sources that are FR I candidates, and whose radio morphology still has to be determined in greater detail.

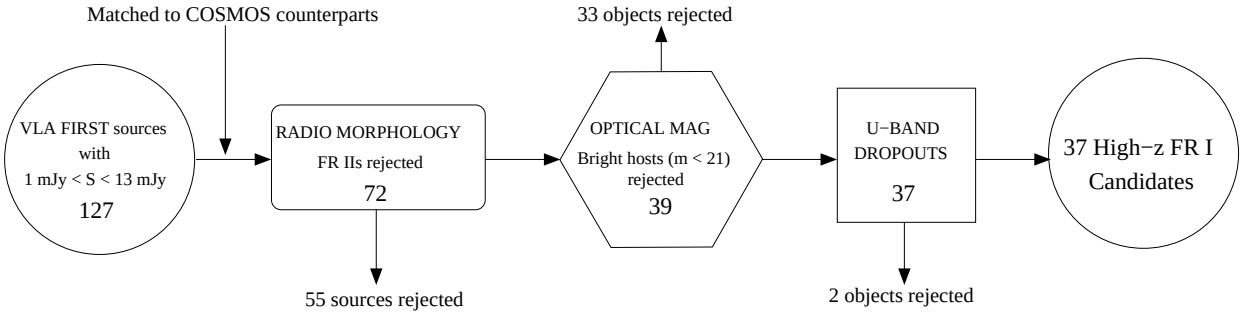

Figure 5.1: Flow-chart describing our selection procedure. The number of sources that survive each rejection step is reported inside each box. See text for more details.

5.3 Selection Procedure

Assumptions

Our search depends upon the assumption that the FR I/FR II break luminosity at $L_{1.4\ \mathrm{GHz}} \sim 4 \times 10^{32}$ erg s^{-1} Hz^{-1} (assuming a spectral index α_r = 0.8 between 1.4 GHz and 178 MHz) does not change with redshift. Moreover, we assume that the photometric properties of high-*z* FR I host galaxies are similar to those of FR II hosts in the same range of redshift. Note that photometric redshifts for COSMOS sources are already available in the literature (Mobasher *et al.*, 2007). Photometric redshifts have proven to be statistically reliable for a large population of objects, but for single objects (AGN in particular), uncertainties associated with photometric redshifts can be (very) large. Therefore, we use photometric redshifts only as a confidence check (see Sect.5.5), and never used the published z_{phot} in the confirmation or rejection of a candidate. That is, no objects meeting our selection criteria are rejected based on photometric redshift value. Based on these two basic assumptions outlined above, we describe our selection procedure here. A flow-chart describing our selection procedure is shown in Fig 5.1.

1. **Radio selection: flux limits.** We select FIRST radio sources inside the COSMOS field whose 1.4 GHz total flux corresponds to that expected for FR Is at $1 < z < 2$. To that end, we require that our candidate sources reside in a narrow bin of $L_{1.4}$. The limits of this "allowable" 1.4 GHz luminosity range ($L_{1.4,\mathrm{min}}$, $L_{1.4,\mathrm{max}}$) are set such that the objects we select have a total radio power typical of FR Is. That is, the radio power must be significantly *above* the level of radio activity produced by "non radio-loud AGN" and starburst galaxies[2] in the target redshift bin, but safely *below* the FR I/FR II break. Based on these criteria, we calculate $L_{1.4,\mathrm{min}}$ and $L_{1.4,\mathrm{max}}$ in terms

[2]Starburst galaxies typically have $L_{1.4} < 10^{30}$ erg s^{-1} Hz^{-1}.

of flux limits $F_{1.4,\mathrm{min}}$ and $F_{1.4,\mathrm{max}}$. We set $F_{1.4,\mathrm{min}}$ to correspond to the flux observed from a source of radio power $L_{1.4,\mathrm{min}}$ at $z = 2$ (e.g. the faintest of the objects we're searching for), and set $F_{1.4,\mathrm{max}}$ to the flux of a source of brightness $L_{1.4,\mathrm{max}}$ at $z = 1$ (e.g. the very brightest sources we wish to find). The observed flux of the $\nu = 1.4$ GHz Fanaroff-Riley break luminosity for each value of z can be derived using

$$F_\nu(\nu_0) = \frac{L_\nu(\nu_0)(1+z)^{1-\alpha}}{4\pi D_L^2}, \tag{5.1}$$

where $L_\nu(\nu_0)$ is the luminosity of the FR I/FR II break at ν_0. We assume a spectral index $\alpha = 0.8$. In the formula, a factor of $(1+z)$ accounts for the passband and another of $(1+z)^{-\alpha}$ makes up the K correction. The flux of the FR I/FR II break at $z = 1$ is $F_{1.4} \sim 26$ mJy. However, we set our upper "allowable flux" limit F_{max} a factor of two fainter than this (to 13 mJy) to ensure that, at the end of the process, we select "bona fide" FR I candidates and avoid accidentally selecting FR IIs near the break luminosity. Any FR IIs that do "slip by" are rejected during step 2, in which we make rejections based on radio morphology. The flux of the break at $z = 2$ is ~ 10 mJy, and so we set our lower limit F_{min} to be an order of magnitude fainter (at 1 mJy). This corresponds to the detection threshold of the FIRST survey. We searched the FIRST database (`http://sundog.stsci.edu/`) for radio sources possessing integrated 1.4 GHz fluxes between 1 mJy and 13 mJy within the COSMOS field. The number of sources that match our flux criteria is 131. Clearly, a selection based on flux only allows the presence of both $z < 1$ "faint" sources and $z > 2$ "powerful" sources. The next selection steps are designed to reject most of the objects that fall outside our preferred redshift range.

2. **Radio selection: morphology.** The sources selected at step 1 are individually examined for large-scale radio morphology. Those candidates featuring clearly "edge-brightened" radio structures are rejected so as to filter out more powerful FR II sources at redshift $z > 2$ which have passed our initial flux selection. Though the FIRST imaging is at very low resolution, it typically suffices for the identification of classical doubles, as edge-brightened lobes or hotspots of FR IIs are found on $>$100 kpc scales, translating to $> 11''$ at $z = 2$. As a result of this, a significant number of pairs of radio sources that were counted as two "single" objects at the previous step are now recognized to be "double" sources. Twenty-two of those FR IIs are identified. In Fig. 5.2 we show three examples of such sources. Note that these account for 44 "single" FIRST radio sources. We then check the VLA-COSMOS radio maps to make sure that objects that appear as compact in the FIRST images are not smaller "double" FR II radio sources. Eleven FR IIs are identified using VLA-COSMOS

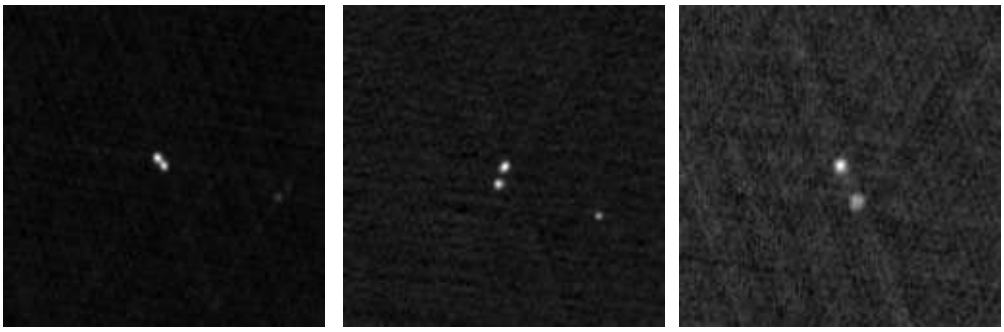

Figure 5.2: Examples of sources showing a clear double (FR II) morphology that were rejected during our selection step 2. The objects are the FIRST sources J095908+024809 (left), J100217+012220 (center) J100245+024534 (right). The size of each image is 5'x5', as obtained from the FIRST image cutouts archive.

radio maps, for a total of 55 such objects rejected based on their radio morphology.

3. **Optical selection: magnitude.** In order to set constraints on the host galaxies' photometric properties, the next step involves the identification of the optical counterparts of the radio sources. Therefore, for our sample, the optical counterpart identification is part of our selection process. We simply blink the COSMOS-VLA radio data with the optical *HST*-COSMOS image, registered on the same WCS frame. Despite the short exposure time (single orbit observations), the *HST*-COSMOS images represent the best available data for identifying the optical counterparts. The significantly higher angular resolution (compared to the ground based optical data) allows for more certainty in the identification of optical counterparts. In most cases, it is straightforward to identify the host galaxy, since the position of the radio core is well set by the VLA-COSMOS images, and the beam size is small enough that only one galaxy is found at the same position on the *HST* image. We will discuss a few peculiar cases for which the optical counterparts are not easily detected in section 5.4. We also unambiguously identify the host galaxy for 24 FR IIs. We check the COSMOS source catalog at the coordinates corresponding to the radio sources that match the first two selection steps and we obtain the magnitudes for each "surviving" candidate at the various available bands.

We set a lower limit in optical (*i*-band) magnitude to reject fairly bright, low redshift galaxies with intrinsically less powerful radio emission (e.g., possible star forming galaxies). In this step we make use of the assumption that the properties of the host galaxies of FR Is are similar to those of FR IIs, as is the case for low-redshift radio galaxies. The *K*-band magnitude of an FR II radio galaxy at $1 < z < 2$ does not exceed $M_K \sim 17$ (e.g. Willott *et al.*, 2003), and the typical $I-K$ color of FR II hosts is ~ 4 or higher. This sets a lower limit to the *i*-band magnitude of ~ 21. In Fig. 5.3 we plot the *i*-band magnitude against the radio flux for the sources with an optical

counterpart. Note that not all of the FR IIs are plotted in the diagram: some of the FRIIs are left out because either the host galaxy is not detected in the optical, or it cannot be identified because it lies somewhere between the location of the two radio hotspots and multiple galaxies are present in the same region. For the candidate FRIs that do not have an optical counterpart but for which the host galaxy is seen in the IR (see Sect 5.4), we plot the magnitude of the closest optical source. This can be interpreted as a rough lower limit to the magnitude of its would-be optical counterpart, and is completely irrelevant from the point of view of our selection procedure (as we do not discard optically faint objects).

Note that, as a result of the magnitude limit, most of the host galaxies of our candidates are not detected in the Sloan Digital Sky Survey. This step in the selection process is only intended to reject those host galaxies that are unreasonably brighter or "bluer" than typical radio galaxies in the target redshift range. Importantly, setting a limit in *i*-band ensures that we are not rejecting galaxies that are fainter than "normal" radio galaxies in *K*-band. With this selection step we only filter out bright nearby galaxies, and we keep distant and intrinsically red objects. Thirty-three objects are rejected at this stage because of the host galaxy optical brightness.

One object with $m_I < 21$ (object 236[3]) is not rejected because it appears to be "stellar-like" in the *HST* image. Since it completely lacks an extended host galaxy, the magnitude of the point source we observe can be considered as a lower limit to the magnitude of the host. The nature of this source is unclear: one possibility is that it is a QSO that resides in the redshift range $1 < z < 2$. In that case, because of its low radio power, it *could* be a "unique" FR I-QSO (see Section 5.5). Alternatively, it could be a high-power radio-loud QSO located at a redshift much higher than 2 (see below).

4. **Optical selection: *U*-band dropouts.** As the last step in the selection process, we ensure that objects with redshifts significantly higher than 2 are excluded from the sample. This is primarily because the radio power of such objects would exceed the FR I/FR II break. We check the deep COSMOS ground-based images, rejecting two sources that are detected in *V* and *B*-band, but which are *not* detected in *U*-band. These "*U*-band dropouts" are typically galaxies located at a redshift significantly higher than our range of interest, with a lower limit at $z \sim 2.5$ (e.g. Giavalisco, 2002).

At the end of the selection process we are left with 37 candidates, which we list in Table 5.1. The Table reports, for each source, the radio flux at 1.4 GHz, the magnitude of the optical counterpart

[3]Not to be confused with 3C 236, the subject of Chapter4. The labeling for this candidate was merely coincidental.

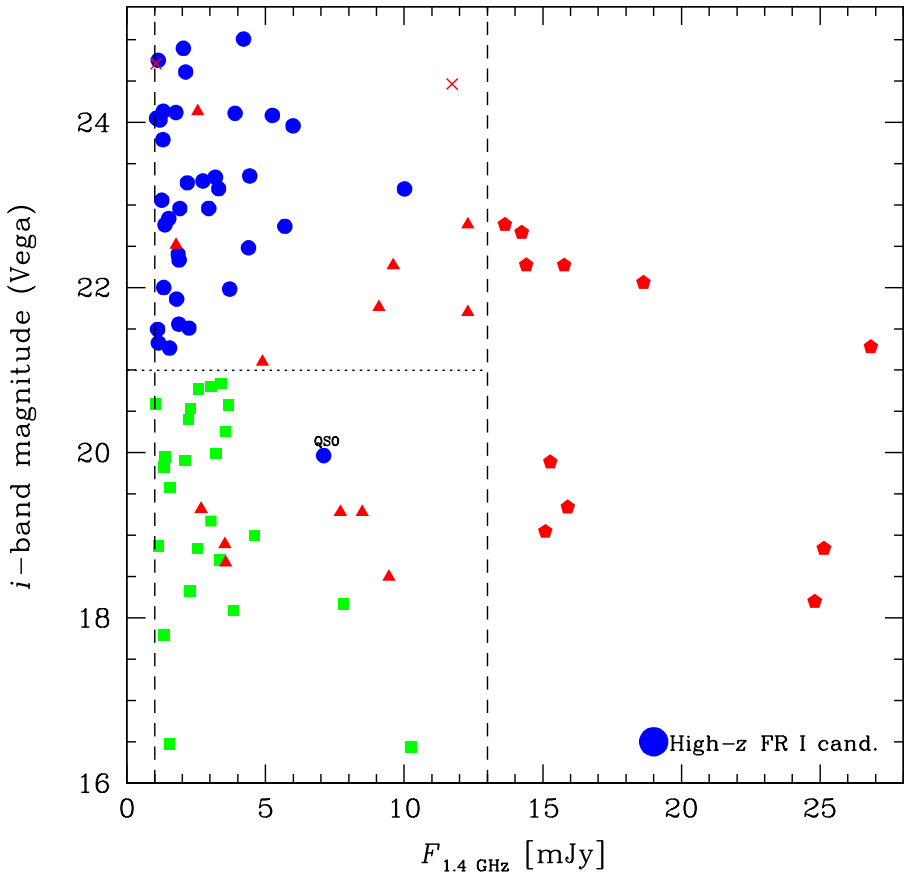

Figure 5.3: Optical *i*-band magnitude plotted against the radio flux at 1.4 GHz. Only the sources for which a host galaxy is clearly detected are plotted. The two vertical dashed lines are the radio flux limits for the selection process at step 1. The horizontal line represents our lower limit for the optical selection (step 3). Circles are the FR I candidates, triangles are rejected because of their FR II radio morphology, pentagons are rejected by radio flux, squares are rejected by host galaxy magnitude and crosses are *u*-band dropouts. Note that the QSO is not rejected despite its bright optical magnitude (see text).

in K_s−, V− and i–bands (normalized to the Vega system), the photometric redshift of the source as it appears in the COSMOS catalog (Mobasher *et al.*, 2007), and a qualitative description of the observed radio and optical morphologies.

Radio and optical images for each of the FR I candidates are shown in Figs. 5.4, 5.5, 5.6, 5.7 and 5.8. The radio data at 1.4 GHz (in orange) are taken from the VLA-COSMOS survey (Schinnerer *et al.*, 2007). The optical images (in blue) are from the *HST*-COSMOS programs (GO 9822, GO 10092) and were taken using *HST*/ACS in *i*-band (Koekemoer *et al.*, 2007), unless mentioned otherwise.

In the following section we discuss issues related to the optical counterpart identifications. Note that the identification of the optical counterparts is part of our selection process at steps 3 and 4. In fact, we look both at the shallow SDSS images (mainly to check that no optical counterpart is found, as prescribed by our selection step 2) and at the deeper ground based images from the COSMOS collaboration (to identify the optical counterpart). In the next section we describe a few peculiar cases of objects with no detected optical counterpart, but which are clearly detected in the IR.

5.4 IR identifications

As mentioned above, identification of optical counterparts was difficult for a few cases. This is because (1) no obvious optical source cospatial with the radio core is seen, or (2) it is not clear whether we are seeing a group of galaxies or a single irregularly shaped object. In six cases, the peak of the optical emission is not coincident with the peak of the radio core. This is clearly evident for candidates 5, 7, 22, 32, 39 and 228 (see Figs. 5.5, 5.6, and 5.7). For object 5, a very low surface brightness object is only tentatively detected in the ACS image, even after significant smoothing. For object 22, the optical counterpart is also not clearly identified, as three to four relatively bright galaxies are present in the ACS image, none of which aligns with the peak of the radio core. For objects 7, 39 and 228 no optical counterpart is detected anywhere near the location of the radio source. For object 32, an optical source is clearly seen in the Subaru *i*-band image, but it is located $\sim 2''$ E of the radio source. However, in all of these cases, *Spitzer Space Telescope*/IRAC images taken as part of the COSMOS program (Sanders *et al.*, 2007) clearly reveal the host galaxy at the location of the radio source. In Fig. 5.9 we show the *Spitzer* images at 3.6 μm, together with the radio contours that indicate the location of the FR I candidate. Clearly, the optical magnitude listed in Table 5.1 for the objects that are only identified in the IR should be considered a rough lower

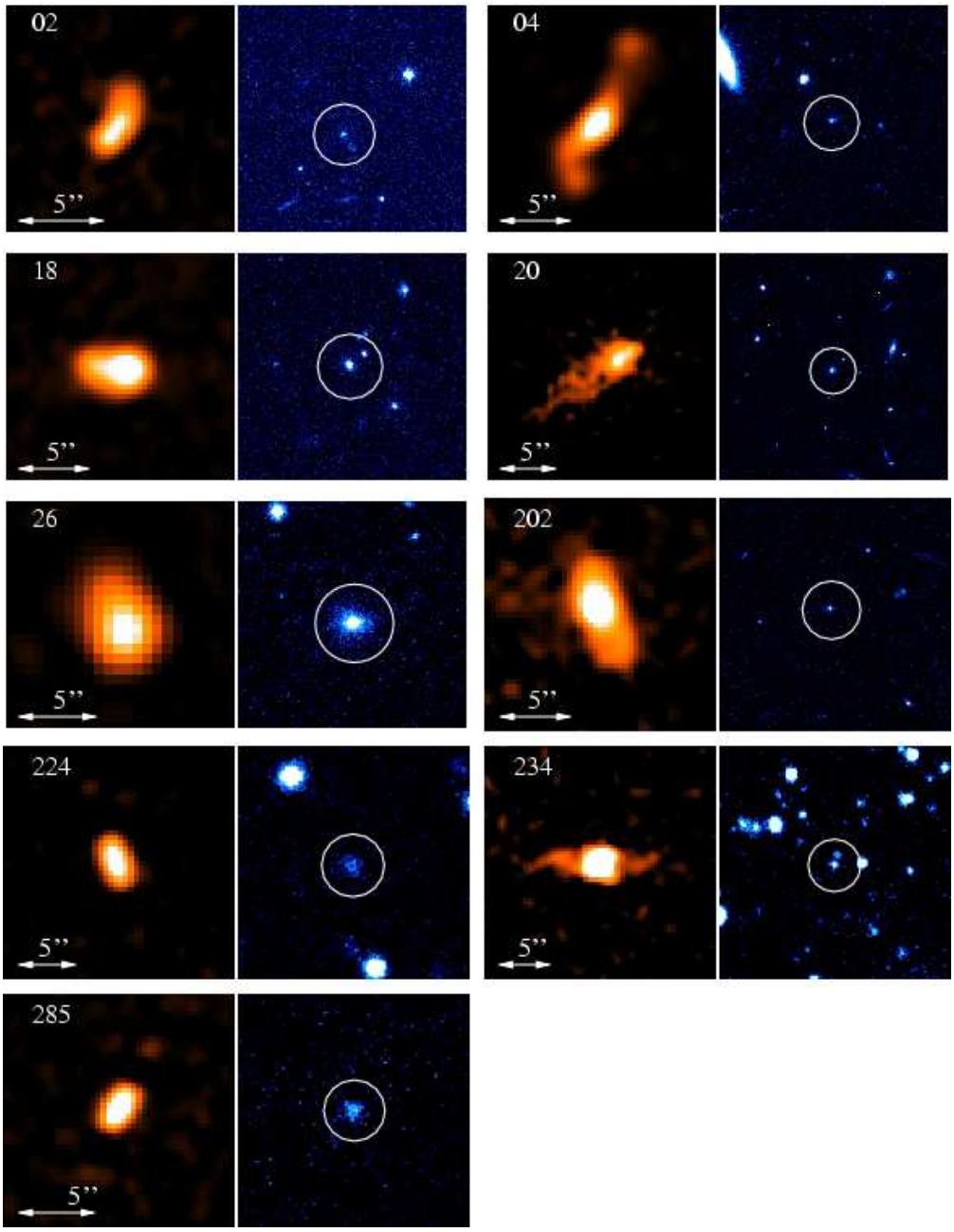

Figure 5.4: FR I candidates with extended 1.4 GHz radio morphology. In these images, 5” corresponds to a linear scale of $\sim$ 40 kpc at z = 1.5. For each object, the image in the left panel are from VLA-COSMOS survey, while in the right panel we show the *HST*-COSMOS ACS images (F814W), except for 234 and 285 where the Subaru *i*-band image is shown.

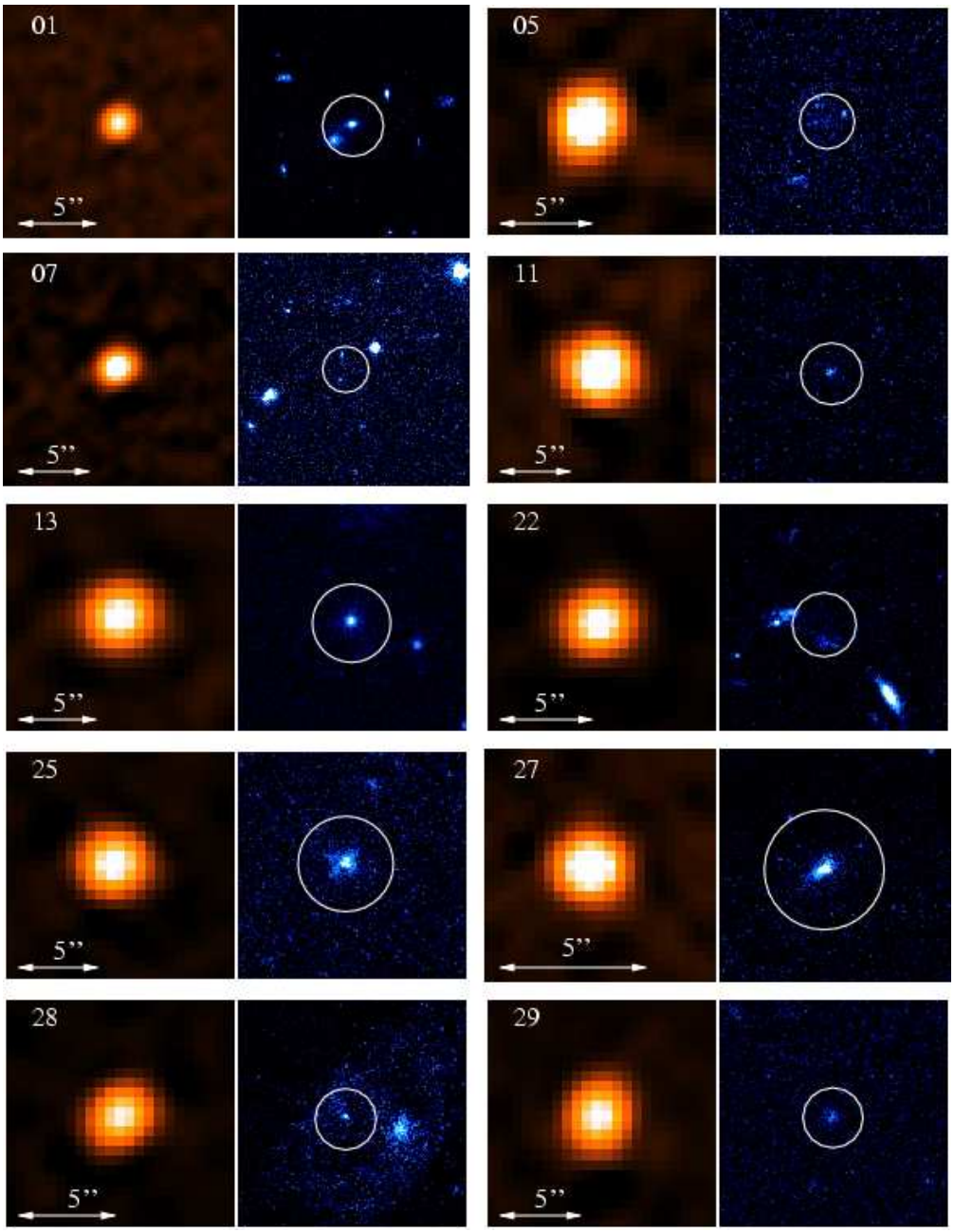

Figure 5.5: FR I candidates with compact (only slightly resolved at the resolution provided by the VLA images) radio morphology. For each object, the image in the left panel is from VLA-COSMOS survey, while in the right panel we show the *HST*-COSMOS ACS images (F814W), except for objects 32 and 37 where the Subaru *i*-band image is shown, since the *HST* image is not available for those two objects.

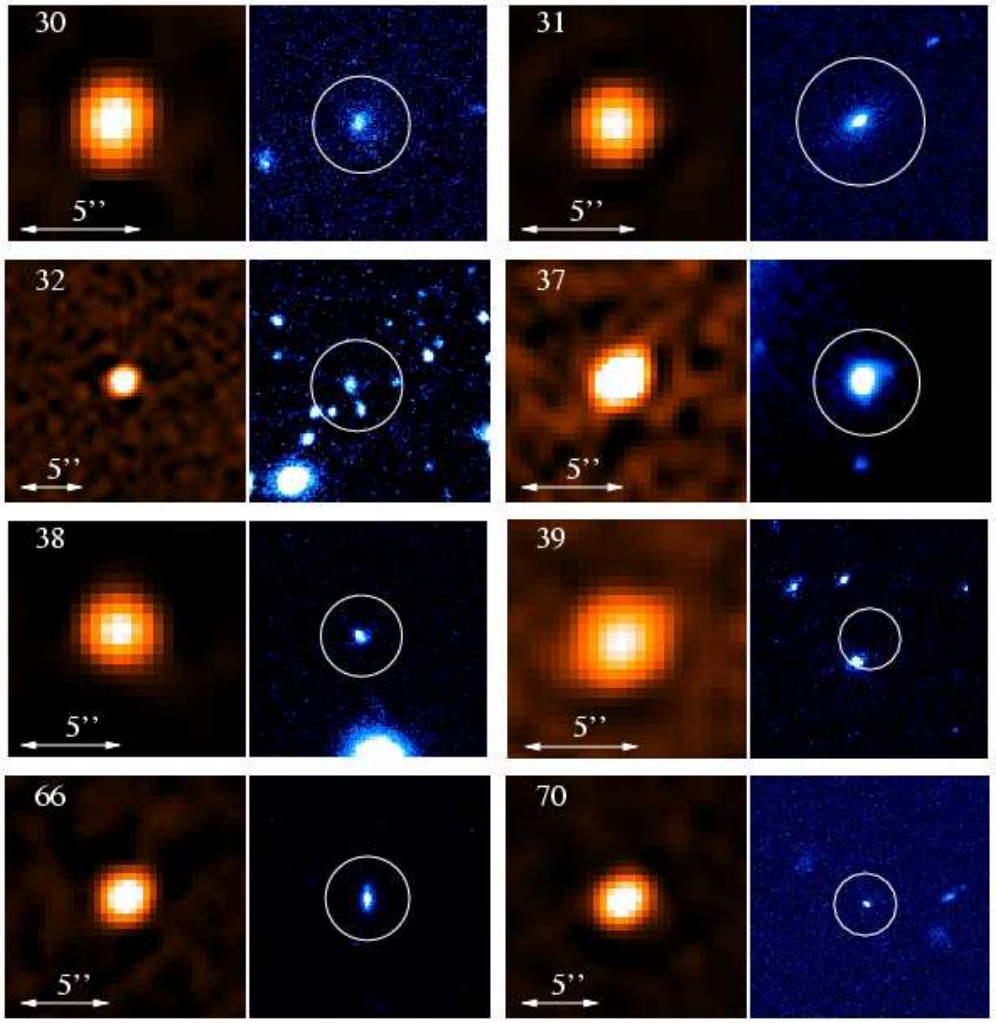

Figure 5.6: FR I candidates with compact (only slightly resolved at the resolution provided by the VLA images) radio morphology. For each object, the image in the left panel is from VLA-COSMOS survey, while in the right panel we show the *HST*-COSMOS ACS images (F814W), except for objects 32 and 37 where the Subaru *i*-band image is shown, since the *HST* image is not available for those two objects.

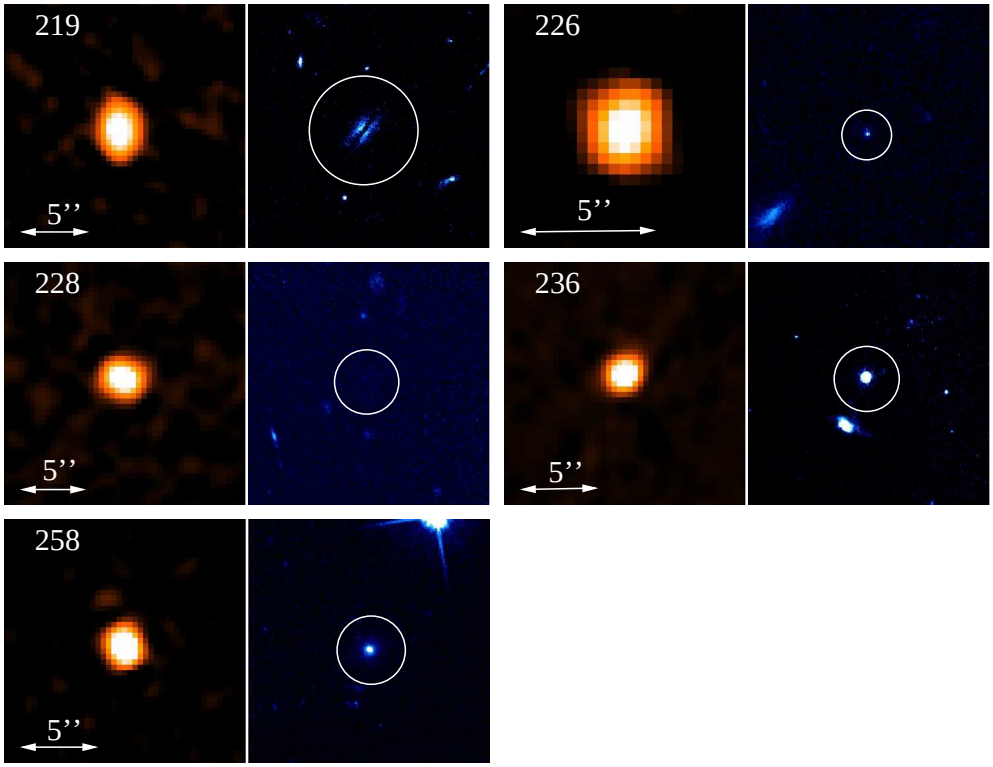

Figure 5.7: FR I candidates with compact (only slightly resolved at the resolution provided by the VLA images) radio morphology. For each object, the image in the left panel is from VLA-COSMOS survey, while in the right panel we show the *HST*-COSMOS ACS images (F814W), except for objects 32 and 37 where the Subaru *i*-band image is shown, since the *HST* image is not available for those two objects.

limit, since it has been derived from the COSMOS catalog from the optical object closest to the radio source.

The lack of an optical counterpart, together with the *clear detection* of an IR counterpart is certainly interesting. The absence of the object in the ACS image might be explained by the fact that the host galaxy is a very low surface brightness object, thus the short exposure time of the *HST* images would prohibit its detection. However, we would then expect to detect it in the deeper ground based images. This cannot be clearly established, mostly because of confusion problems. In the IR Spitzer images, the elliptical host is more easily seen, since it dominates the emission with respect to the bluer surrounding galaxies that disappear in the IR. An alternate scenario is that these are higher redshift objects, not visible in the optical because of Hydrogen absorption (*i*-band dropouts). In this case, the bluer galaxies seen in the optical data around the position corresponding to the radio source would not be at the same redshift as the host galaxy of the radio source. For

Table 5.1. **High-Redshift FR I Radio Galaxy Candidates**

ID (1)	K_s Mag (2)	V Mag (3)	I Mag (4)	$S_{20\ \mathrm{cm}}$ (mJy) (5)	z_{phot} (6)	Radio Morphology (7)	Optical Morphology (8)
01	17.710	24.423	21.860	1.79	0.94	Compact	Smooth
02	19.279	25.835	24.047	1.08	1.59	Extended	Compact
03	21.014	25.583	25.008	4.21	1.59	Unresolved	Compact
04	18.872	25.473	23.957	5.99	1.85	Extended	Compact
05	18.991	24.449	23.789	1.30	2.08	Compact	–
07	20.072	24.942	23.777	1.14	1.09	Compact	–
11	19.716	26.994	24.750	1.13	1.05	Compact	Compact
13	18.670	24.711	22.835	1.51	1.21	Compact	Compact
16	18.668	24.860	22.741	5.70	1.10	Unresolved	Smooth
18	19.015	24.316	22.479	4.39	0.93	Extended	Complex
20	18.276	24.594	21.998	1.33	0.98	Extended	Compact
22	19.698	24.043	23.288	2.74	1.51	Compact	–
25	18.787	24.952	23.266	2.18	1.40	Compact	Complex
26	17.631	24.908	22.332	1.88	1.30	Extended	Smooth
27	18.722	24.279	22.957	1.91	1.39	Compact	Complex
28	20.158	25.127	24.118	1.77	1.23	Compact	Compact
29	21.099	25.341	24.610	2.12	1.03	Compact	Compact
30	18.360	25.812	23.055	1.26	1.15	Compact	Complex
31	18.456	23.948	21.981	3.71	0.88	Compact	Smooth
32	20.214	25.095	24.134	1.31	2.17	Compact	Compact
34	19.105	25.152	24.082	5.25	2.04	Unresolved	Compact
36	18.606	24.782	23.335	3.19	1.42	Unresolved	Complex
37	18.176	22.388	21.556	1.87	1.26	Compact	Smooth
38	19.489	24.603	23.193	10.01	1.15	Compact	Complex
39	18.405	25.268	22.759	1.37	1.36	Compact	–
52	17.928	23.132	21.266	1.54	0.84	Unresolved	Complex
66	18.149	23.637	21.493	1.11	0.80	Compact	Smooth
70	19.521	24.766	24.109	3.90	2.75	Compact	–
202	19.706	26.376	24.049	1.08	1.24	Extended	Compact
219	18.256	24.517	22.402	1.85	1.20	Compact	Complex
224	18.636	25.414	23.196	3.31	1.40	Extended	Compact
226	19.879	25.225	24.027	1.19	2.04	Compact	Compact
228	19.379	27.163	24.894	2.04	1.45	Compact	–
234	18.724	25.399	23.350	4.43	1.42	Extended	Complex
236	17.461	20.594	19.965	7.10	1.23	Compact	QSO
258	17.860	23.190	21.508	2.24	1.07	Compact	Compact
285	19.018	24.022	22.958	2.95	1.24	Extended	Complex

Note. — (1) Object ID; (2) K_s-band apparent magnitude in the Vega system; (3) V-band apparent magnitude (Vega). The magnitude for the objects identified in the IR only are that of the closest optical counterpart; (4) I-band apparent magnitude (Vega). The magnitude for the objects identified in the IR only are that of the closest optical counterpart (Capak *et al.*, 2007); (5) Integrated radio flux at 20 cm (mJy) from the FIRST survey; (6) Photometric redshift z_{phot}, calculated by Mobasher *et al.* (2007); (7) Qualitative characterization of radio morphology, based on VLA-COSMOS image. This classification reflects whether the corresponding image of this target is located in Figs. 5.4, 5.5, 5.6, 5.7, 5.8 ; (8) Qualitative characterization of the morphology of the optical counterpart to the radio source, based on inspection of the ACS I-band image. The optical morphology classification for the host galaxies detected only in the IR is omitted.

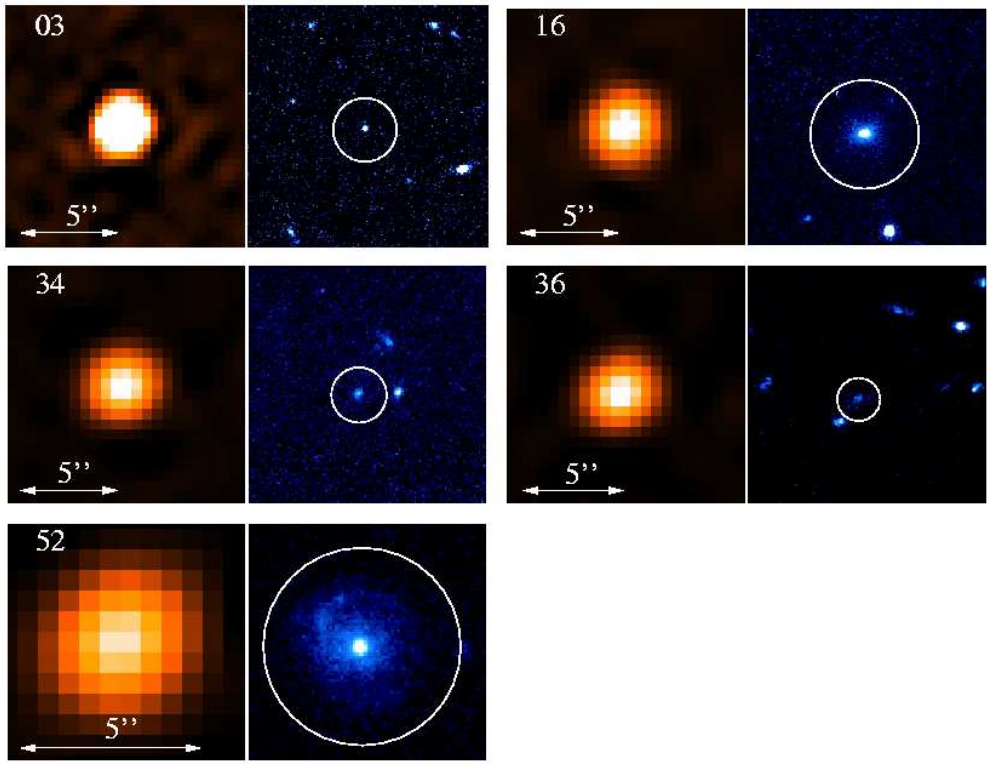

Figure 5.8: FR I candidates with unresolved radio morphology (the FWHM of the source is consistent with the beam width of the VLA image). For each object, the image in the left panel is from VLA-COSMOS survey. In the right panel we show the *HST*-COSMOS ACS images (F814W)

an *i*-band dropout, the redshift of the host would be around $z \sim 6$, therefore these objects would be very high power radio sources that should not be included in our sample. Further investigation is needed to assess their nature. It is also worth noting that for those objects with uncertain optical identification, $z_{\rm phot}$ is most likely derived from one of the galaxies surrounding the real host.

5.5 Results and discussion

5.5.1 The $K-z$ relation

Radio galaxies are known to obey the so-called $K-z$ relation (Lilly & Longair, 1982), a correlation between the infrared *K*-band magnitude and redshift, up to at least $z \sim 4$. The origin of the $K-z$ relation is still unclear, and it is possible that it is just the result of selection effect (Lacy *et al.*, 2004). Our selection criteria make use of the optical-IR properties of the hosts of known powerful radio galaxies, which obey the $K-z$ relation. However, while it is important to reject "bright"

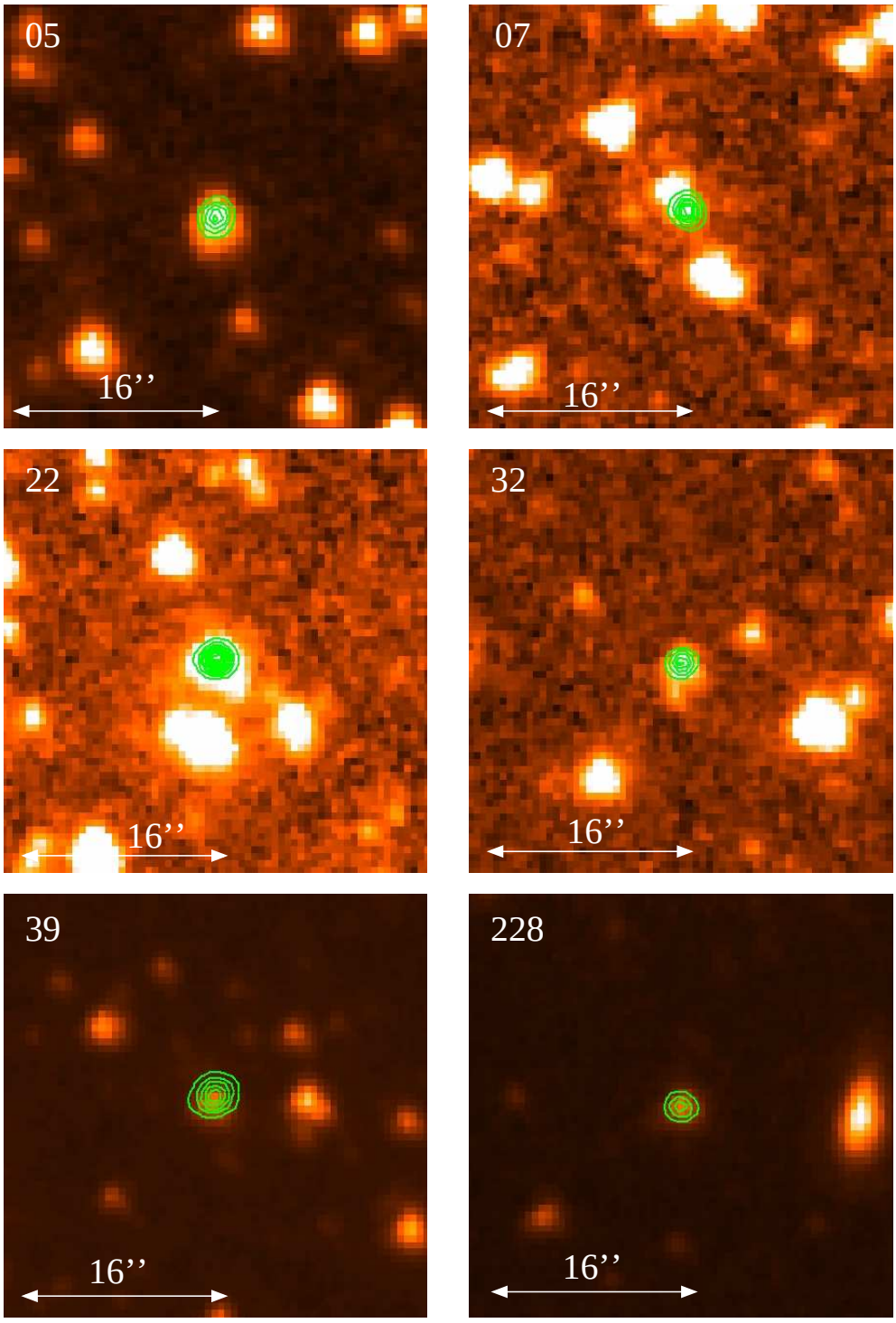

Figure 5.9: Objects identified using *Spitzer* IR images. The radio contours are overplotted onto the 3.6μm image to show the location of the source.

optical hosts in order to eliminate nearby galaxies from the sample, our selection criteria do not impose any lower limit to the K-band flux of the hosts. In other words, objects that lie significantly above or below the $K-z$ relation are included in our final sample, if they exist at all.

In Fig. 5.10 we plot the K_s-band magnitude of our FR I candidates' optical counterparts vs. their photometric redshift $z_{\rm phot}$, as derived from the COSMOS photometric catalog by Mobasher *et al.* (2007). The FR I candidates are plotted as filled circles. The objects with $m_I < 21$ are plotted as squares. The candidates morphologically identified as FR IIs are not plotted, as in this chapter we only focus on FR Is.

In addition to our candidates, we also plot in Fig 5.10 (as empty circles) the galaxies from the 3CRR, 6C, and 7C catalogs of radio sources (Willott *et al.*, 2003). Whereas for our FR I candidates we plot K_s-band magnitude vs. *photometric* redshift, for the Willott *et al.* (2003) data we plot K-band magnitude vs. *spectroscopic* redshift. The brightness difference between K- and K_s- bands is typically less than a tenth of a magnitude, therefore the minor differences that arise from comparing photometric measurements in these two bands are not a concern.

As expected from our selection criteria, the objects plotted as squares are relatively nearby galaxies (judging from the Figure, at least). With only a few exceptions, the FR I candidates approximately reside in the correct redshift bin and lie on or slightly above the $K-z$ relation. One outlier (object 70) is at $z_{\rm phot} = 2.75$, which is unexpected because our selection procedure should exclude galaxies at $z \gtrsim 2.5$ (u-band dropouts), hence the photometric redshift for object 70 may be incorrect (this would not be surprising). A few objects are ~ 2 K-band magnitudes fainter than the average of the galaxies of Willott *et al.* (2003). These might also be objects for which the photometric redshift is incorrect. Alternatively, they might be a population of radio galaxies associated with fainter hosts. A few objects with ~ 2 K-band magnitudes fainter than the bulk of the radio galaxy population is in fact observed at low redshifts as well.

In the following section we describe the FR I candidates, focusing on their radio morphology, properties of their host, and on their Mpc-scale environment.

5.5.2 Radio Morphology

Here we examine the structure of the 1.4 GHz emission for those 37 FR I candidates appearing as filled circles in Fig. 5.10. Even at the resolution of the VLA-COSMOS, survey most of our targets appear as compact radio sources. Nine of them show a discernible radio morphology on scales larger than $\sim 5''$, which corresponds to a projected physical scale of ~ 40 kpc at $z = 1.5$. We show the 1.4 GHz VLA-COSMOS maps of these nine sources in Fig 5.4 (left panels), alongside

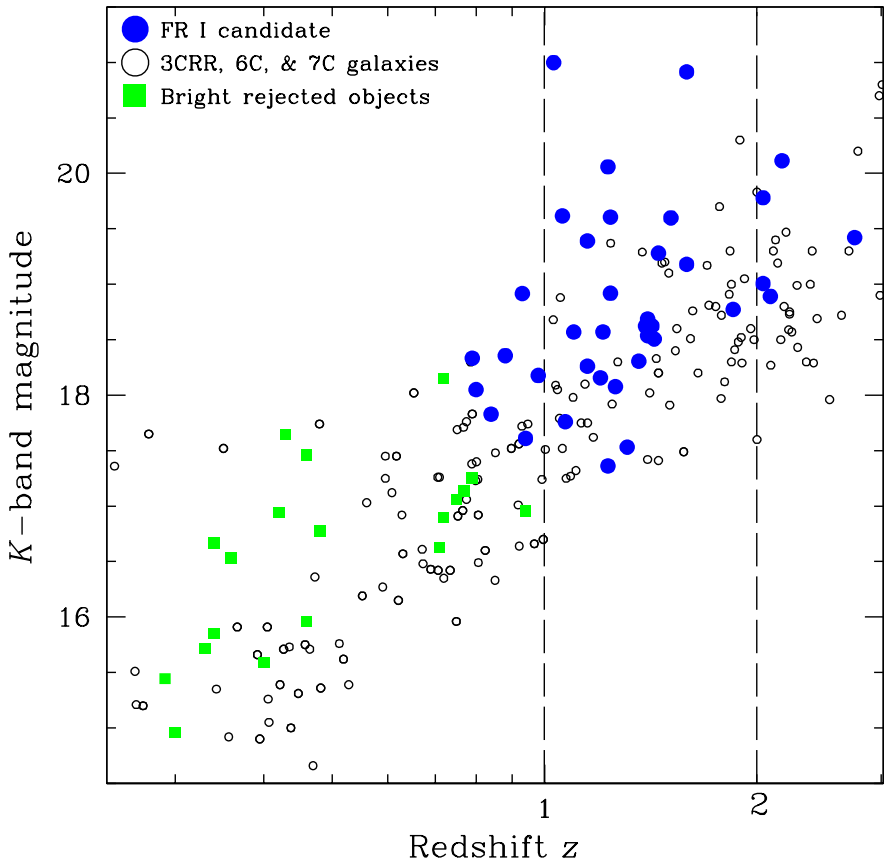

Figure 5.10: The $K-z$ relation for radio galaxies. 3C, 6C and 7C sources from Willott *et al.* (2003) are plotted as open circles. Our FR I candidates are filled circles. Objects rejected by host galaxy optical magnitude are plotted as squares.

the *i*-band *HST*/ACS imaging of their optical counterparts (right panels). The optical counterparts are marked with white circles in the *HST* images.

Even among those sources with extended radio morphology, only two (objects 04 and 234) exhibit the radio morphology of "bona fide" FR Is, in which the surface brightness peaks near the center of the source, and extended jets are visible. In objects 02, 18 and 202 the jet seems to be one-sided and curved, similar to many "asymmetric" nearby FR I galaxies (at least as they appear in shallow observations with poor spatial resolution, e.g., 3C 66B and 3C 129, van Breugel & Jagers 1982). Objects 18 and 26 have a radio morphology similar to so-called "core-jet" compact radio sources (Conway *et al.*, 1994), in which the visible jet component is nearly as bright as the

radio core. The absence of a counter jet in these objects might be due to relativistic beaming effects if the jet axis is nearly aligned with the observer's line of sight.

Object 20 has a very peculiar morphology. It shows a bright compact component, with a possible jet extended roughly to the N-W. The "small-scale" morphology is embedded in a larger scale structure with lower surface brightness, similar to an elongated "lobe". Its peculiar morphology also roughly resembles an FR II lobe, in which the brightest region is the so-called "hot-spot", usually interpreted as the location where the relativistic jet impacts the ISM (or IGM/ICM). We checked to see whether a "counter-lobe" was present at some large distance along the NW-SE direction. No radio source that could be reasonably interpreted as the "counter-lobe" is found, even if we allow the counter jet to be bent at a reasonably large angle. This, especially when considering the clear correspondence of the brightest radio component with a galaxy in the *HST* image, allows us to confidently rule out the possibility of this being an FR II hotspot.

All other 28 sources are slightly resolved (Figs. 5.5, 5.6, and 5.7) or unresolved (Fig 5.8). As stated previously, these observations are at 1.4 GHz, which at $z = 1.5$ corresponds to 3.5 GHz in the rest frame. The emission at that frequency is dominated by the central region of the radio source, where young, high energy electrons reside and emit synchrotron radiation up to high radio frequencies with flat ($\alpha \lesssim 0.5$) radio spectra. Extended radio components like jets and lobes have steeper indices, thus the emission rapidly drops as frequency increases. It may therefore be that we simply do not detect extended, low surface brightness radio jets and lobes for the majority of our candidates given the high rest frame radio frequency of the observations and the intrinsic faintness of the extended regions.

Note also that the size of the radio sources with "FR I-like" structures is smaller than the typical size scales for FR Is at low redshift. Whereas the largest structure we observe among our 37 candidates is of order 100 kpc from end to end (candidate 04, Fig. 5.4), FR Is in the nearby universe are known to exhibit larger morphologies, up to a several hundreds of kpc, and in a few cases even Mpc (e.g. B2 1108+27, NGC 6251 Perley *et al.*, 1984).

Although it is likely that the non-detection of large-scale structures is a result of the high frequency at which the COSMOS observations are performed, it is also possible that our high-z FR I candidates are intrinsically small. In fact, even the higher power FR IIs in this redshift range appear smaller than their lower redshift counterparts. From the work by e.g. Kapahi (1985); Gopal-Krishna & Wiita (1987); Kapahi (1989) it is known that the projected linear distance between the hotspots appears to scale roughly as $(1+z)^{\sigma}$, where σ is between 1 and 2.

Interestingly, Drake *et al.* (2004) have found a population of infrared-bright radio sources that morphologically resemble the so-called compact steep spectrum (CSS) sources (see (O'Dea *et al.*,

1998), for a review). CSS objects are believed to be young radio sources that will eventually evolve in the large, powerful FR II radio galaxies. The sources of Drake *et al.* (2004) are at least 1 dex less powerful than normal CSS sources, and the derived expansion velocities of the radio sources are also significantly smaller. From the analysis of their overall properties, these authors claim that those "mini" radio sources will not evolve into either FR IIs or FR Is, but will instead lose their radio-loudness and will become radio quiet FIR-luminous AGNs. Should our candidates be intrinsically small, they might "fill the gap" between the powerful CSS sources and the radio-faint sources of Drake *et al.* (2004), from the point of view of their radio properties. It is therefore possible that most of our targets are simply the progenitors of the FR Is we observe in the local universe.

In summary, unlike nearby FR Is, the vast majority of our candidates exhibit very little extended morphology in the radio band. Clearly, it will be necessary in future papers to determine whether this is due to (1) the high radio frequency at which the observations were made, (2) the faintness of the extended jets and plumes, or (3) the fact that our objects may be intrinsically small and possibly young radio sources. The Extended Very Large Array (EVLA) and Atacama Large Millimeter/Submillimeter Array (ALMA) will achieve a signal-to-noise and spatial resolution that enables detailed studies of these faint and distant objects.

5.5.3 Host Galaxies and environment

Optical images for each of the candidates are shown in Figs. 5.4, 5.5, 5.6, 5.7, and 5.8. The photometric properties of the hosts, as derived by Capak *et al.* (2007), are reported in in Table 5.1.

Despite the images being single orbit *HST* exposures, we attempt to classify the hosts into four different classes based on optical appearance: (1) smooth ellipticals, (2) complex, (3) compact and (4) unresolved. A more detailed study will be performed when deeper images are obtained. Class 1 are objects of apparent elliptical shape, with very little or no disturbed morphology; class 2 are objects that appear to be interacting with close companions and/or show irregular morphologies; class 3 are barely resolved galaxies small enough to prohibit morphological classification; and class 4 includes the object that we classify as a possible QSO, i.e., a point source (object 236, Fig. 5.11).

From visual inspection of the images of the 31 sources with optical counterparts, 6 of our objects appear as smooth ellipticals, 10 are complex, 14 are compact, and 1 is unresolved (stellar-like). The resolution of the images of the 6 host galaxies that are only detected in the IR does not allow us to derive any morphological classification. It is worth noting the high fraction of objects

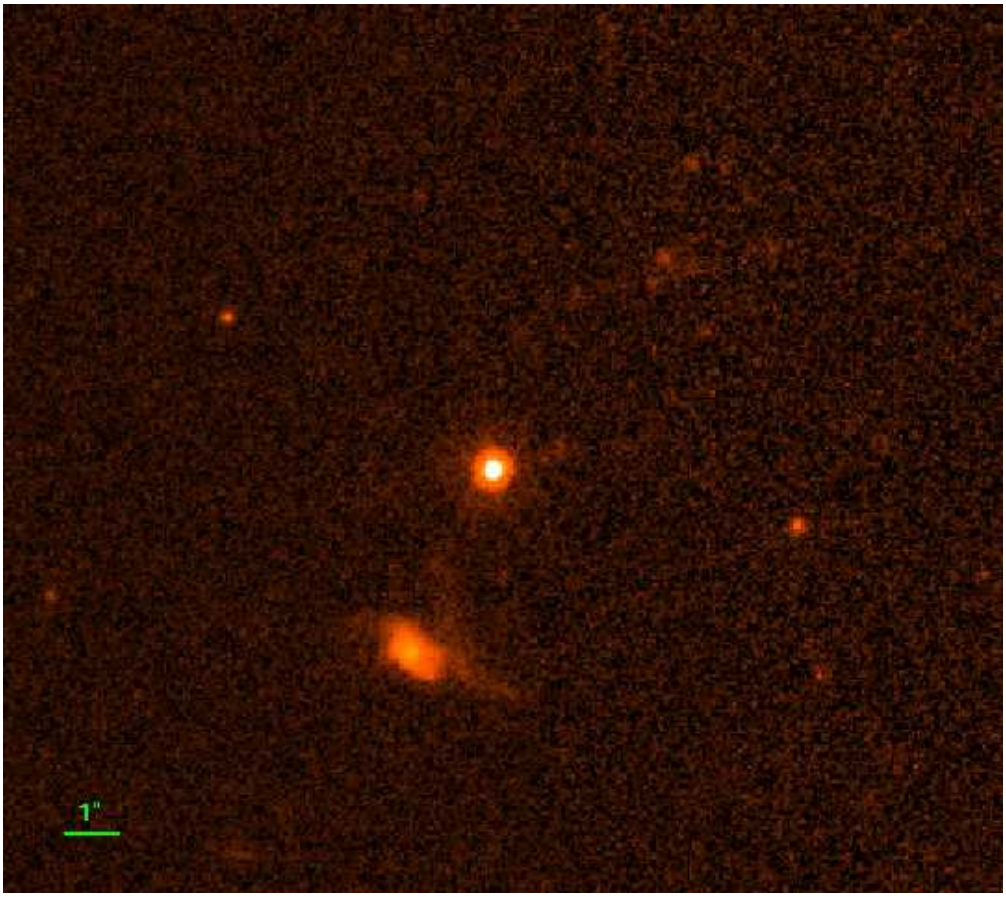

Figure 5.11: *HST*/ACS F814W image of target 236. The optical counterpart of this object appears as "stellar-like". This might be an example of a low power radio galaxy associated with a QSO. This figure was created by Dr. Marco Chiaberge.

with complex optical morphologies among our FR I candidates. This appears to be at odds with low redshift FR Is, the large majority of which are hosted by undisturbed ellipticals or cD galaxies (Zirbel, 1996). However, the larger fraction of complex morphologies in our sample may simply reflect the different stage of evolution of the host, that might still be in a very active merging phase at $1 < z < 2$.

Little can be said about the compact galaxies. Because of the short exposure times of the *HST* data, we may simply be seeing the core of the galaxies and miss the extended regions of lower surface brightness. Alternatively, these might be intrinsically smaller objects, which would contrast with local FR I hosts that appear to be invariably associated with giant ellipticals at the centers of clusters.

The presence of one stellar-like optical counterpart is also intriguing. We interpret this object as

a compact nucleus (possibly the AGN) outshining the host galaxy. This is consistent with QSOs, though scaled down in luminosity by a few orders of magnitude. However, it has been established that at low redshifts, no FR Is belonging to the 3CR (Spinrad *et al.*, 1985) or B2 (Colla *et al.*, 1970) samples are associated with host galaxies of this kind. Most importantly, from the point of view of the physics of their active nucleus, none appear to possess broad lines in the optical spectrum[4]. Recently, Zamfir *et al.* (2008) did not find FR I-QSO in a large sample of SDSS-FIRST/NVSS quasars, reinforcing the idea that FR I-QSOs are extremely rare in the local universe.

Clearly, this "nucleated" galaxy needs further investigation aimed at determining its nature as a (possible) quasar through the detection of broad permitted lines in its rest-frame optical spectrum. However, even if the unresolved object was spectroscopically confirmed as a QSOs, the fraction of FR I quasars in our sample (1/37) would be significantly lower than the fraction of FR II quasars in the same range of redshift, which is around 40% (e.g. Willott *et al.*, 2000). A possible scenario is that the smaller fraction of FR I-QSO as compared to the fraction of FR II-QSO simply results from the dependence of such a fraction on luminosity (Willott *et al.*, 2000). This may reflect a reduction of the opening angle of the "obscuring torus" as luminosity decreases (the so called "receding-torus" model). Alternatively, most high-z FR Is may intrinsically lack a significant broad emission line region and thermal disk emission, as may be the case for FR Is in low-z samples (e.g. Chiaberge *et al.*, 1999). These issues can be further explored with deep *HST* imaging aimed at determining the nature of the hosts. Spectroscopy with 8 m class telescopes to can also determine the presence or absence of any broad emission lines.

Although our sample cannot be considered statistically complete, the selection criteria are not biased against the presence of QSOs. Instead, the selection based on the radio flux at 1.4 MHz is somewhat biased in favor of core-dominated, relativistically beamed objects, and none of the objects that were rejected because their optical i-band magnitude exceeds our selection limit were point sources. The existence of a large number of FR I-QSOs at intermediate-to-high redshifts has been noted by Heywood *et al.* (2007). This would imply a strong evolution in the physical properties of radio galaxies with FR I radio morphology, since FR I-QSOs are essentially absent at low redshifts. However, besides the different selection criteria, the objects of Heywood *et al.* (2007) are mostly high power sources, while here we focus on radio galaxies of the same power as low-z FR Is. It is therefore possible that at high-z, the FR I break shifts towards higher radio powers.

An in-depth analysis of the properties of the objects in our sample and, and the associated im-

[4]This is true with one exception: 3C 120, a peculiar object with FR I radio morphology associated with an S0 host showing a spiral-like structure. However, 3C 120 is formally not part of the 3CR catalog of Spinrad *et al.* (1985).

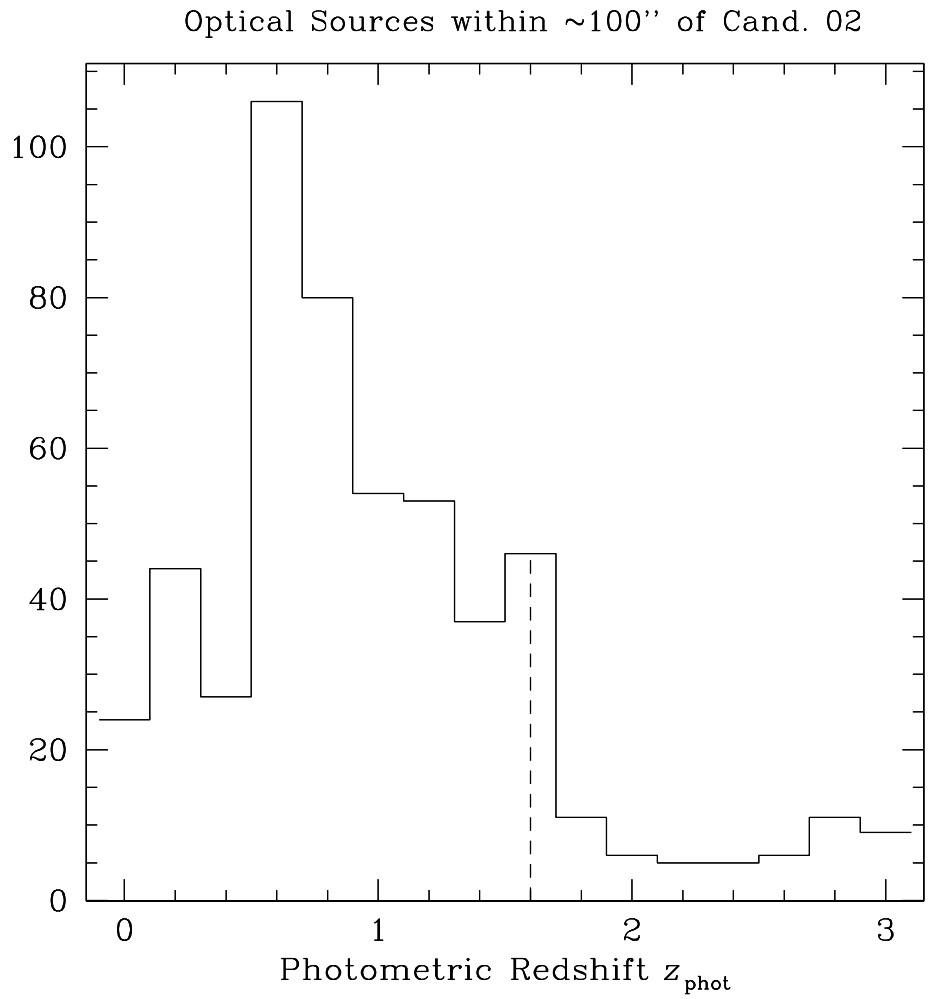

Figure 5.12: Photometric redshifts distribution of optical sources in the COSMOS catalog within $100''$ of candidate 02. The vertical dashed line marks the photometric redshift of the candidate FR I. A peak in the redshift distribution corresponding to the redshift of our source is evident, and may be interpreted as the presence of an overdensity of galaxies at the redshift of the FR I candidate.

plications for the AGN unification scheme, will be the subject of future work (see, for example Chiaberge *et al.* 2010). However, the limited morphological information we have at this stage seems to show that FR I-QSO represent a tiny fraction of the low-power FR I radio galaxies population at $1 < z < 2$.

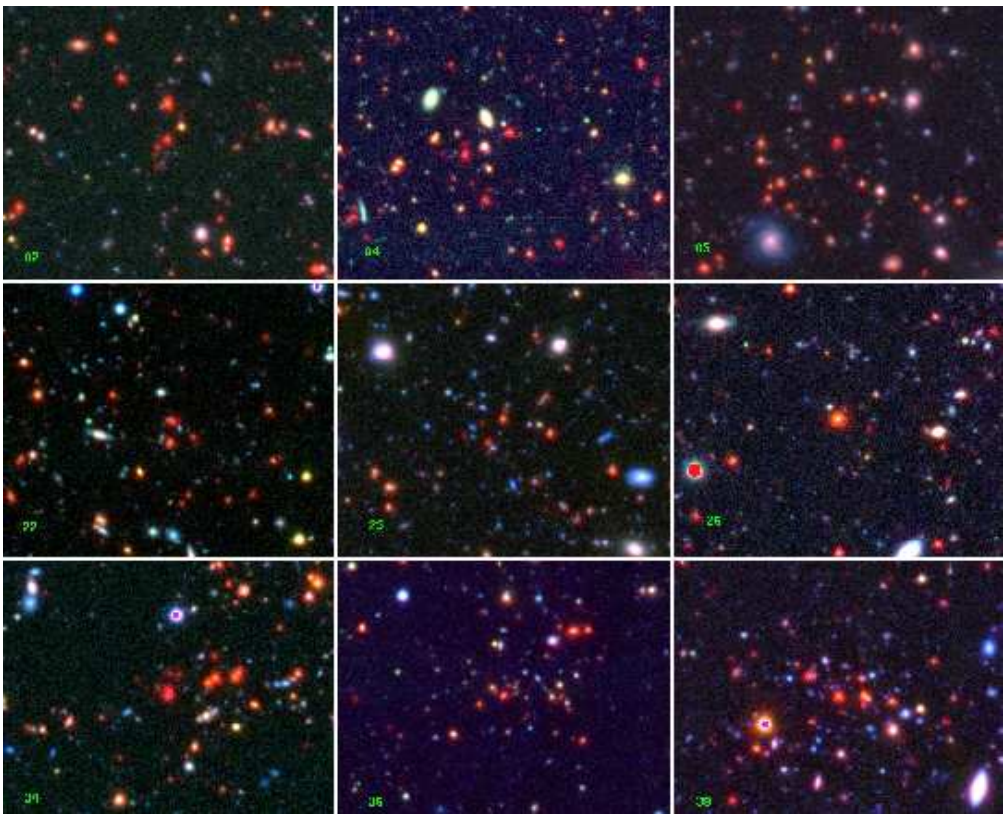

Figure 5.13: RGB images of nine cluster candidates found around our high-*z* FR I candidates. The "color" images are obtained using *Spitzer* data at 3.6μm for the R channel, z-band for the G channel, and V-band for the B channel. The projected scale of each image is $\sim 110'' \times 90''$. This figure was created by Dr. Marco Chiaberge.

5.5.4 FR I candidates as tracers of high-*z* galaxy clusters?

One of the motivations for our high-*z* FR I radio galaxy search is to locate high-*z* clusters of galaxies. In the local universe, $\sim 70\%$ of the entire population of FR Is is associated with cD-like galaxies (Zirbel, 1996), and almost all low-*z* FR Is reside in clusters of various richness (Zirbel, 1997). Only ~ 15 clusters are known to exist between $1 < z < 2$, thus a large sample of FR Is may easily double the number of clusters in that redshift range, assuming that the environment of FR Is does not significantly change with redshift. Although we defer a systematic search for clusters to **?** and other forthcoming papers, in this section we qualitatively explore the Mpc environments of our candidate FR Is, so as to probe the possibility that their host galaxies reside in clusters (or protoclusters).

We use two methods in our search for cluster candidates. First, we search the COSMOS catalog for the photometric redshift of objects that are located inside a region of projected radius 1 Mpc

from the FR I candidate. Only in the case of object 02 do we find qualitative evidence for an overdensity of galaxies around its photometric redshift, which we interpret as indicative of the *possible* presence of a group or a cluster. In Fig. 5.12 we show the photometric redshift distribution of optical sources within $100''$ (corresponding to a projected radius of 855 kpc at $z = 1.6$) of candidate 02. The vertical dashed line marks the photometric redshift of the FR I candidate. A peak in the redshift distribution corresponding to the redshift of our source is evident. However, the low detection rate obtained with the above method is not surprising. Our FR I candidates are quite possibly among the brightest cluster members, while an L^* galaxy at $z \sim 1.5$ is expected to have $m_i \sim 24$. Thus, the COSMOS optical images are in fact not deep enough to detect a significant number of cluster galaxies at redshifts $z > 1$. Even when they are detected in the images, their photometric redshift can be highly uncertain because of the large errors on the photometry of such faint objects.

Another more effective method is to search for extremely red objects around our FR I candidates. Although there is still some level of degeneracy between objects that are intrinsically red and redshifted objects, this method seems to lead to more promising results, even at the qualitative level presented here. In Fig. 5.13 we show nine cluster candidates found with the latter method. We produced RGB "color" images using *Spitzer* data at 3.6μm for the R channel, z-band for the G channel, and V-band for the B channel.

We are in the process of creating observational programs (specifically with the Very Large Telescope) designed to spectroscopically confirm the redshift of the (possible) BCGs in these cluster candidates. More details on these proposed programs cam be found in Chiaberge *et al.* (2010). Sensitive and high spatial resolution optical/NIR imaging and spectroscopy will be needed for a better understanding of these candidate clusters. WFC3 on *HST* is ideal for this (at least in terms of imaging), and proposals are in the process of being submitted. The launch of a next-generation X-ray telescope would greatly improve these studies, enabling detailed analysis of any hot ICM plasma that may have virialized by these epochs. In a forthcoming paper by Chiaberge, and collaborators (including the Author), we will study the *Chandra*-COSMOS data and attempt to detect candidate cluster ICMs using stacking techniques.

5.6 Summary & Conclusions

In this chapter, we have outlined our search for $1 < z < 2$ FR I radio galaxy candidates in the COSMOS field. Previously, no low power FR I radio galaxies were known to exist in this red-

shift bin, save for one (or possibly two) candidates in the HDF North (Snellen & Best, 2001b). Flux-limited samples are not suitable for finding low-power radio galaxies at high-z because of the tight redshift-luminosity correlation. Therefore, we used a 4-step, multi-wavelength selection process. This started with a radio flux selection, and used radio morphology and optical magnitude constraints to further narrow the sample of candidates.

The photometric redshift of the bulk of our FR I candidates are in the expected range $1 < z_{\rm phot} < 2$. These redshifts must be confirmed with spectroscopic observations using at least an 8 m class telescope, future larger instruments, or space-based observations that take advantage of the lower background. We note that, since this initial pilot study, one such spectroscopic confirmation has been obtained (Chiaberge *et al.*, in preparation).

In most cases, the radio images presented in this chapter show objects with compact morphologies. These might be intrinsically young sources that will eventually evolve into the giant FR I radio galaxies observed at low redshifts. Alternatively, extended emission may not detected because of the rest-frame high frequency at which the observations were taken. Further investigation is needed to address this issue. Chiaberge and collaborators (including the Author) are currently planning low-frequency radio observations aimed at detecting extended emission from "older" electron populations associated with these sources. These, combined with deep, high resolution data at higher wavelengths ($\sim$ 8 GHz), will enable the derivation of the radio spectral index for these sources and allow us to better study their morphology.

The short one-orbit *i*-band *HST* observations used in our selection process are not suitable for a detailed morphological study of the host galaxies. However, the data do exhibit a wide array of discernible morphologies, ranging from smooth ellipticals to complex interacting systems. A few of our candidates appear to be compact, and one is stellar-like. This object might belong to a population of FR I-QSOs that are effectively absent in the local Universe. However, the fraction of low-power FR I-QSOs in our sample appears to be significantly lower than the overall fraction of FR II-QSOs in the same redshift bin. Optical-IR spectroscopy of the source is needed to assess the nature of this candidate QSO.

Although the images from the COSMOS survey are not suitable for the detection a large fraction of cluster galaxies at $z > 1$, the environment of several of our FR I candidates shows evidence for the presence of a cluster. This is apparent when the IR images from *Spitzer* are used in concert with the optical ground-based data, resulting in a significant number of "red" objects surrounding the host galaxies of our FR I candidates.

The search presented in this chapter is a pilot study, and finds objects to be observed with existing and future high-resolution, sensitive instruments. The Extended Very Large Array (EVLA)

and ALMA, for example, will provide crucial information on the radio morphology of our sources, and will enable a better understanding of whether or not our candidates are intrinsically small and "progenitors" of the local FR I population. With WFC3 on *HST*, it is now possible to study in greater detail the properties of the host galaxies and their cluster environment in the optical and IR. This will have important consequences with regards to our understanding of the most massive galaxies, clusters of galaxies, and their origins. Several such proposals are now in the pipeline. Clearly, these studies will be complemented and further expanded should *JWST* eventually launch. We can also continue to hope that a future high sensitivity X-ray mission will launch[5].

[5]The Author regretfully acknowledges the recent cancellation of the *IXO* mission, as well as the recently announced proposal to terminate funding for *JWST*.

6

LOOKING AHEAD

Summary, Conclusions, & Future Work

Modern science has been a voyage into the unknown, with a lesson in humility waiting at every stop. Our common sense intuitions can be mistaken. Our preferences don't count. We do not live in a privileged reference frame. Knowledge is preferable to ignorance. Better by far to embrace the hard truth than a reassuring fable.

CARL SAGAN, 1997

6.1 Summary

In this thesis, we have presented two independent studies broadly unified within the context of star formation as it pertains to cool core clusters of galaxies, the triggering of AGN activity, and the associated energetic feedback that may play a critical role in heating the ambient environment on tens to hundreds of kiloparsec scales. A comparison study of episodic star formation and AGN activity in a field galaxy was then provided so as to better understand the role played by hot X-ray gas accretion and by mergers in triggering these phenomena. Finally, we broadened the context of this thesis by describing a search for high redshift FR I radio galaxies which may act as observable "beacons" for assembling protoclusters. In this Chapter, we distill the various results from these independent studies into a summary, so as to succinctly assess the "lessons learned". First, however, it is important to revisit the questions posed at the conclusion of Chapter 1:

- *What role does AGN feedback play in regulating star formation and the entropy of the ICM?*
- *What is the role of star formation in regulating the physics of the warm and cold ISM phases in CC BCGs?*
- *How can we disentangle the roles played by cooling flows and mergers in depositing the gas reservoirs which fuel episodes of star formation and AGN activity?*
- *How might we find assembling protoclusters at high redshift, so as to study the cosmic evolution of (e.g.) the cool core phenomenon?*

Recall that it was never our goal to *answer* these questions, but rather to better understand the questions themselves. Below, we provide a summary of the main results presented in each chapter (save for the first, which is introductory), so as to assess how we may have broadened our understanding of the above issues.

6.1.1 Summary of Chapter 2

In this chapter, we presented a multiwavelength study of the cool core cluster Abell 2597. The bulk of our analysis was based upon a new 150 ksec *Chandra* image of the highly anisotropic X-ray emitting gas associated with the central brightest cluster galaxy. These new data, in concert with a rich suite of archival data including *HST* imaging of ongoing star formation in A2597, enable a "unified", cross-spectrum interpretation of this canonical CC cluster, particularly in the context of

AGN feedback and its effects on the warm and cold gas phases in the central BCG.

The question posed for Chapter 2:

What role does AGN feedback play in regulating star formation and the entropy of the ICM?

Itemized summary of results:

- Our deeper X-ray data confirm that the X-ray emission in the central $60''$ of A2597 exhibits a high degree of spatial anisotropy on the scale of the central brightest cluster galaxy ($\sim 30''$).

- The degree of spatial anisotropy in the X-ray surface brightness distribution increases with decreasing radius from the center of the BCG. At all radii the X-ray emission is extended along the direction of the BCG's isophotal major axis.

- The X-ray emission is permeated by a network of X-ray cavities on $\lesssim 30$ kpc scales. Within this radius, the X-ray surface brightness excesses or deficits with $> 10\sigma$ significance include the (1) "western large cavity" (length ~ 18 kpc), (2) "northern ghost cavity" (diameter ~ 12 kpc), (3) "eastern ghost cavity" (~ 6 kpc), (4) "filament base cavity" (~ 5 kpc), and finally (5) the "X-ray filament" (length ~ 15 kpc).

- The 18 kpc "western large cavity" is cospatial with extended 330 MHz radio emission, and is also aligned along the same position angle as the "X-ray filament", a ~ 3 kpc-scale high velocity dispersion stream of molecular gas, the VLBA jet axis on 50 pc scales, and extended 1.3 GHz radio emission. That the 8.4 GHz source is offset from this common axis suggests that the radio jet has only recently (within the past ~ 50 Myr) been deflected, perhaps by ambient dense gas which has recently been acquired by a cooling flow or a merger.

- Our deeper X-ray data confirm the $> 10\sigma$ significance of a 15 kpc linear soft excess "filament" extending from the central regions toward the northeast. A hardness analysis and our X-ray temperature map are consistent with the interpretation that this is a "cold" filament $\sim 1-1.5$ keV cooler than its immediate surroundings. We suggest that the feature may arise from the dredge-up of low entropy gas by the propagating radio jet, with which it is aligned (in terms of position angle). This scenario is feasible in terms of lower limits on the available energy budget, as inferred from quantitative analysis of the X-ray cavities.

- Our X-ray temperature map reveals a 20 kpc "arc" ~ 1 keV hotter than its immediate surroundings. This feature is cospatial with the eastern boundary of the "western large cavity". We interpret this feature in the context of effervescent AGN heating models, wherein cavity enthalpy is thermalized as ambient keV gas rushes to refill its wake. This may be the first instance in which evidence for ISM/ICM heating by cavity enthalpy dissipation is observed in an X-ray temperature map. This could be a very important piece of evidence in favor of effervescent AGN feedback models.

- We find that inferred ages for the young stellar population in the emission line nebula are both younger and older than the inferred ages of the X-ray cavity network and the radio structures which supposedly excavated this cavity network. The net implication is that low levels of star formation (a few $M_{\odot}$ yr^{-1}) have managed to persist amid energetic feedback from the AGN. An FUV excess aligned with the northern edge of the radio source may be evidence for compact regions of jet-induced star formation.

The "flagship results" from Chapter 2: *Our X-ray spectral analysis reveals both direct and circumstantial evidence of ISM/ICM heating by a radio-mode, effervescent AGN feedback mechanism. The most compelling piece of evidence is the "hot arc" feature seen in the X-ray temperature map. The X-ray surface brightness map reveals evidence of dredge-up of low entropy X-ray gas by the propagating radio source. Low levels of star formation have managed to persist amid the feedback-driven excavation of the X-ray cavity network. Moreover, compact regions of star formation may have been triggered by the propagating radio source. The mass, timescale, and energy budgets associated with the hot, warm, and cold gas phases, as well as many other properties of A2597, are consistent with a general "AGN heated cooling flow" scenario.*

6.1.2 Summary of Chapter 3

In this Chapter we presented *HST* imaging of FUV continuum and Lyα emission from seven CC BCGs selected on the basis of an IR excess suggestive of elevated star formation rates.

The question posed for Chapter 3:

What is the role of star formation in regulating the physics of the warm and cold ISM phases in CC BCGs?

Itemized summary of results:

- We confirm that the IR excess associated with our sample of CC BCGs is associated with low levels (a few $M_{\odot}$ yr^{-1}) of ongoing star formation on $\lesssim$ 30 kpc scales, as revealed by our *HST* FUV imaging.
- Star formation rates estimated from the FUV are 2 to 10 times lower than those estimated from the IR. In all cases, the Balmer decrement is consistent with a level of internal extinction that is sufficient (but not strictly or exclusively required) to account for the difference.
- The young stellar population required to account for the observed FUV continuum emission can fully contribute an adequate number of ionizing photons required to power the Lyα and Hα-bright emission line nebulae (in terms of luminosity, not ionization states).
- Unresolved, weak radio sources are observed in each of the seven BCGs. Additionally, A1835 and RXJ 2129+00 exhibit weak kpc-scale jets.
- The combination of higher SFR and lower radio power is consistent with a scenario wherein a low state of AGN feedback allows for increased residual condensation from the ambient X-ray atmosphere, accounting for the elevated star formation rates.
- We observe kpc-scale offsets between the peak of the X-ray surface brightness profile and the brightest regions of FUV emission in several of our sources. AGN feedback is not expected to cause this offset. It may be due to residual "sloshing" of hot-phase gas, which can remain long-lived even after virialization of the cluster. Disturbances in the ICM could lead to higher cooling rates in the gas as the cluster relaxes and slowly evolves to equilibrium. This may account for the elevated star formation rates.

The "flagship results" from Chapter 3: *Even at low levels, star formation provides a dominant contribution to the ionizing photon reservoir required to power the observed luminosities of the emission line nebula. Our seven CC BCGs were selected on the basis of an IR excess assumed to be associated with an elevated star formation rate. We confirm that this is the case, and also note that each of these possess only weak, compact radio sources. The combination of higher SFR and lower radio power suggests that the radio source has a smaller relative impact on the properties of the star forming regions. It may be indirectly related, however, in that a low mode of AGN feedback may allow for increased residual condensation from the ambient hot atmosphere, thereby accounting for the higher star formation rates*.

6.1.3 Summary of Chapter 4

In Chapter 4, we presented *HST* ACS and STIS observations of the radio galaxy 3C 236, described by O'Dea *et al.* (2001) as an "interrupted" radio source. The galaxy is associated with a relic ~ 4 Mpc FR II radio source (making it one of the largest objects in the universe), as well as an inner 2 kpc CSS "young" radio source. This "double-double" radio morphology is evidence for multiple epochs of AGN activity, wherein the BH fuel supply is thought to have been exhausted or cut off at some time in the past, and has only recently been reignited. 3C 236 is a field galaxy that is not associated with a galaxy cluster, and so our analysis of star formation and AGN triggering in this source serves as a comparison study for the results presented in Chapters 2 and 3.

The question posed for Chapter 4:

How can we disentangle the roles played by cooling flows and mergers in depositing the gas reservoirs which fuel episodes of star formation and AGN activity?

Itemized summary of results:

- We confirm the presence of four bright knots of FUV emission in an arc along the edge of the inner circumnuclear dust disk in the galaxy's nucleus, as well as FUV emission cospatial with the nucleus itself. We interpret these to be sites of recent or ongoing star formation.
- We estimate the ages of the knots by comparing our extinction-corrected photometry with stellar population synthesis models. We find the four knots cospatial with the dusty disk to be young, of order $\sim 10^7$ yr old. The FUV emission in the nucleus, to which we do not expect scattered light from the AGN to contribute significantly, is likely due to an episode of star formation triggered $\sim 10^9$ yr ago.
- We argue that the young $\sim 10^7$ yr old knots stem from an episode of star formation that was roughly coeval with the event resulting in reignition of radio activity, creating the CSS source.
- The $\sim 10^9$ yr old stars in the nucleus may be associated with the previous epoch of radio activity that generated the 4 Mpc relic source, before being cut off by exhaustion or interruption.
- The ages of the knots, considered in the context of both the disturbed morphology of the nuclear dust and the double-double morphology of the "old" and "young" radio sources, present evidence for an AGN/starburst connection that is possibly episodic in nature.

- We suggest that the AGN fuel supply was interrupted for $\sim 10^7$ yr due to a minor merger event and has now been restored. The resultant non-steady flow of gas in the disk is likely responsible for both the new episode of infall-induced star formation and also the multiple epochs of radio activity.

- 3C 236 shares many similarities with A2597 (evidence for episodic AGN activity, compact knots of star formation at comparable rates). We discuss their differences as they may pertain to (a) accretion from an ambient hot X-ray atmosphere (in the case of A2597) and (b) cold accretion through a minor merger (in the case of 3C 236). Ultimately, we are not in a position to comment further on the role of mergers vs. cooling flows in providing the gaseous reservoirs found in the centers of CC BCGs. X-ray spectroscopy of A2597 is consistent with a moderately strong cooling flow, and does not exhibit strong evidence for a recent minor or major merger. On the other hand, 3C 236 almost certainly had to acquire its gas reservoir through a merger. While the strong similarities between the two sources suggests that a cooling flow is not exclusively required to provide the gaseous reservoir fuelling star formation and AGN activity in A2597, the few but important differences between the two sources could be understood in the context of cold vs. hot accretion scenarios.

The "flagship results" from Chapter 4: *An AGN/starburst connection may be causally related by a discrete gas infall event, likely stemming from a minor merger. A non-steady flow of gas to the nucleus can account for the apparent episodic activity, in terms of both AGN triggering and star formation. 3C 236 shares many similarities with A2597, although the lack of a kpc-scale, settled dusty disk in A2597 might be due to a very different gas accretion history (i.e., from residual ICM cooling, rather than a merger).*

6.1.4 Summary of Chapter 5

In Chapter 5 we broadened the context of this thesis with a search for high redshift radio galaxies as observable "beacons" for assembling protoclusters. The work outlines a new method by which these "beacons" may be used to probe the "cluster desert" of $1 < z < 2$, where galaxy clusters are thought to assemble, but are extremely difficult to detect with typical selection methods.

The question posed for Chapter 5:

How might we find assembling protoclusters at high redshift, so as to study the cosmic evolution of (e.g.) the cool core phenomenon?

Itemized summary of results:

- Our search yields 37 low-power radio galaxy candidates that are possibly FR Is. Each of these candidates has a photometric redshift between $1 < z < 2$. Spectroscopic confirmation of these photometric redshifts will be required, as they are often unreliable.
- We show that a large fraction of our low luminosity candidate radio galaxies display a compact radio morphology that does not correspond to the FR I morphological classification. Whether they are too distant to detect extended, possibly FR I-like radio emission is not known. Deeper radio observations will be needed.
- The candidates are apparently associated with galaxies that show clear signs of interactions, at odds with the typical behavior observed in low-*z* FR I hosts.
- The compact radio morphology might imply that we are observing intrinsically small and possibly young objects that will eventually evolve into the giant FR Is we observe in the local universe.
- One candidate is associated with a point-like optical counterpart. This might belong to a population of FR I-QSOs, which would represent a small minority of the overall population of high-*z* FR Is.
- A search for candidate $1 < z < 2$ clusters using our candidate FR I radio galaxies yields nine weak possibilities that warrant follow-up observations.

The "flagship results" from Chapter 5: *Our multiwavelength selection process yielded 37 low-power radio galaxy candidates that are possibly FR Is. The photometric redshift of the bulk of our FR I candidates are in the expected range* $1 < z_{\rm phot} < 2$*, which would place them within the epoch of cluster assembly. Nine* $1 < z < 2$ *FR I candidates are associated with local optical/IR overdensities which may be indicative of association with a cluster, protocluster, or group.*

6.2 Caveats and disclaimers

Of course, we could never hope to address all of the known issues related to cool core clusters in this thesis. Rather, we have focused on a very small subset of the science pertaining to episodic

star formation and AGN activity, the role played by the environment on these phenomena, and the impact these phenomena have on each other and their environment. So as to not "lose the forest for the trees", it is important to at least briefly mention those critical pieces of understanding which we have only barely mentioned or ignored completely.

- **We have effectively ignored transport processes in the intracluster medium**. Processes like thermal conduction might be critical in dictating the observed properties of the ICM. In many cases its effects are strong enough to offset radiative cooling, negating the need for (e.g.) AGN heating, though debate is ongoing as to whether or not conduction can establish *stable* temperature gradients which are sufficiently long-lived (see Chapter 1).

- **We have not adequately explored the role played by mergers in the context of our results and the cool core/non-cool core dichotomy**. We tangentially address this issue in Chapter 4 with our CC BCG/field radio galaxy comparison study, but it only scratches the surface. A subset of the community believes that the cooling flow model is incorrect in almost every respect, and that may indeed be the case (see the discussion in Chapter 1). Many believe that mergers can instead account for the pools of warm/cold gas in CC BCGs. Much more work is needed, and we are not necessarily in a position to favor one scenario over another in the context of our results.

- **We have focused only on a small sample of nearby cool core clusters**. In Chapter 3 we demonstrated that star formation plays an important role in determining the properties of the warm/cold gas phases in CC BCGs. While this has been known for decades (see the references in that chapter), the conclusions drawn from our small subsample of CC BCGs, preferentially selected on the basis of elevated star formation rates, cannot be extended into a general, wide-reaching conclusion. A comprehensive study of larger, more representative samples of CC and, critically, non-CC clusters, groups, and field galaxies is needed.

- **Just because our results are consistent with a particular model does not mean that the model is correct**. Many of our results, particularly those presented in Chapters 2 and 3, are consistent with the general "AGN heated cooling flow" scenario. This does not, however, mean that cooling flows are exclusively *required* to account for the warm/cold gas phases, star formation, and AGN activity. Instead, mergers may be responsible for depositing these gas reservoirs, though we do not adequately explore this possibility (see the relevant point above).

- **We have not addressed several critically important aspects, issues, and phenomenon related to CC BCGs.** This is obvious, as no thesis (except an *extremely* long one!) could address *all* aspects of CC BCGs. In our case, we have concerned ourselves only with a very small subset of the issues. For example, we have barely discussed the spectacular and highly mysterious emission line filaments that are very commonly observed in the cores of CC BCGs, including in A2597. These filaments are poorly understood, and it is not known (1) how they are formed, (2) what powers their luminosities and calibrates their emission line ratios, and (3) what keeps them long-lived. Debate continues as to whether or not the filaments are "lifted outwards" by the radio source or are "falling inwards" from a cooling flow, perhaps down "tubes" of magnetic fields (an emerging majority favors some version of the latter scenario). See Chapter 1 for an abridged review of the many other critical aspects of BCGs which we do not address.

This is an incomplete summary of the various caveats and disclaimers we could list. For more detailed considerations concerning complexities in interpreting our results, etc., see the discussion sections in each of the previous chapters.

6.3 What have we learned?

How have the results from this thesis broadened our understanding of cooling flows, AGN feedback, and CC BCGs?

6.3.1 A thought experiment

Consider this thought experiment: suppose we insist on interpreting the results from Chapters 2 through 4 *strictly* and *exclusively* in the context of the "AGN heated cooling flow" model. In other words, suppose we wish to make the following *"definitive statement"*:

> "*All results from Chapters 1 through 4 can be explained in terms of hot X-ray gas accretion and radio source feedback*[1]."

[1]We stress that we're not *actually* making this statement; it's merely a thought experiment.

What is consistent with this statement?

Many of our results are indicative of AGN heating via direct kinematical interaction between a propagating radio source and the hot ($10^7 < T < 10^8$ K) and warm/cold phases ($10 < T < 10^4$ K) of the ISM in CC BCGs. This is strong evidence that *AGN feedback is real*, in that the AGN clearly returns energy to the ambient medium, influencing it in dramatic, observable ways. This has been known for years (see, for example, the highly compelling X-ray, radio, and optical images of Perseus in Figs. 1.4 and 1.6). In this thesis, we have presented similarly compelling evidence for directly observed AGN feedback in A2597. This evidence includes:

- The mere existence of spatially anisotropic temperature structures in the X-ray temperature map is evidence for AGN heating. Otherwise, one might simply expect the gas to become cooler towards the center of the BCG in a "smooth" way, as the temperature of the gas reflects the relatively "smooth" underlying gravitational potential.

- The western large cavity in A2597 is almost exactly cospatial in projection with extended 330 MHz radio emission, suggestive of a causal, intrinsic connection between the two features.

- The western large cavity is aligned along the same position angle as (1) the cold X-ray filament, (2) the high velocity dispersion stream of molecular gas, (3) the extended arms of the 1.3 GHz emission, and (4) the VLBA jet axis on 50 pc scales (see Fig. 2.17). This is strong (albeit circumstantial) evidence that the 15 kpc cold X-ray filament arises from dredge-up of low(er) entropy X-ray gas by the radio jet. We have shown that the jet can supply the energy required to lift the estimated mass of the filament out to these distances. Mass entrainment by a radio jet is a form of AGN feedback.

- Timescale and energy budgets associated with the various X-ray cavities and the 8.4 GHz and 330 MHz radio sources are consistent with one another. In other words, the ages and energies associated with the X-ray cavity network can be roughly accounted for by the ages and energies associated with the radio sources.

- The steep radio spectral index of the 8.4 GHz source, together with its bent morphology, is indicative of dynamical confinement by the ambient warm gaseous medium through which the radio source is propagating.

- Futhermore, a compact blue excess spatially associated with the leading edge of the northern 8.4 GHz lobe might be indicative of star formation triggered by the propagating radio source.

- We have also presented compelling evidence that the hot X-ray emitting ISM in the A2597 BCG is heated as it rushes to refill the wake of the buoyant large western cavity, as is predicted in effervescent AGN feedback models. This particular result may be one of the very first instances in which cavity enthalpy dissipation is actually observed to heat the ambient X-ray gas. We would argue that this is one of the most exciting "flagship results" presented in this thesis.

We have also presented results which are consistent with the interpretation that (1) ambient hot X-ray gas cools and condenses into the CC BCG and (2) directly provides the gaseous fuel reservoir for both star formation and the triggering of AGN activity. The evidence for this that is exclusive to this thesis includes includes:

- The spatial elongation of the hot X-ray gas aligns with the major axis of the A2597 BCG stellar isophotes, as well as an extended ~ 8 kpc arm of FUV emission associated with ongoing star formation. The radio jet axis is perpendicular to this axis. This is consistent with a scenario wherein (1) gas condenses from the ambient X-ray atmosphere, (2) settles into a BCG equipotential, and (3) flows inward, fuelling star formation and AGN activity. Note that these results do not necessarily *require* this explanation, but they are *consistent* with it.

- Without exception, those CC BCGs in Chapter 3 with higher star formation rates possessed lower power, unresolved radio sources, while those with lower star formation rates possessed higher power, extended radio sources.

- The combination of higher SFR and lower radio power is consistent with a scenario wherein a low state of AGN feedback allows for increased residual condensation from the ambient X-ray atmosphere, accounting for the elevated star formation rates.

What is not consistent with this statement?

- If the "hot arc" in A2597 is indeed evidence of ICM heating by cavity enthalpy dissipation, why do we not see more "hot arcs" associated with other similarly sized cavities in CC clusters (e.g., Perseus, Hydra A, etc.)?

- Several of the CC BCGs presented in Chapter 3 exhibit kpc-scale offsets between the peak of the X-ray surface brightness and the peak of the FUV emission. It is not clear that AGN

outflows could exclusively account for these offsets, as they are observed in clusters which are supposedly experiencing a "low state" of feedback.

- Moreover, if the gaseous reservoirs fuelling star formation and AGN activity were provided by a cooling flow, to first order one might expect the coolest X-ray gas to be cospatial with sites of star formation and the radio core. For those CC BCGs exhibiting the X-ray/FUV spatial offset, this is not the case, yet they still have elevated star formation rates.

- It is also worth noting that 3C 236 is a field galaxy with no nearby companions, and is not surrounded by an ambient atmosphere of rapidly cooling X-ray gas. Nevertheless, it shares *many* characteristics with A2597, such as compact central CSS radio sources, knots of star formation with SFRs on the order of a few $M_{\odot}$ yr^{-1}, and signatures of episodic AGN activity (the 4 Mpc relic source in 3C 236 and the ghost cavities in A2597). Clearly, while a cooling flow can account for the reservoirs of cold gas in CC BCGs (in terms of the baryon budget, at least), it may not not strictly *required*. In general, mergers are an obvious mechanism by which gas can be deposited into a galaxy, fuelling an episode of star formation and AGN activity. A2597 does not exhibit particularly strong evidence in favor of a recent minor or major merger, while other CC BCGs do exhibit evidence of mergers (e.g., NGC 4696/Centaurus). The roles played by cooling flows vs. mergers is still not clear, and far more work is needed.

6.3.2 The major conclusions of this thesis

We conclude this section by simply listing what we believe to be the three main conclusions of this thesis.

1. **AGN feedback is real, and likely plays a dominant role in regulating the pathway of entropy loss from hot ambient medium to cold gas to star formation.**

2. **AGN feedback does not establish an impassable "entropy floor" below which gas cannot cool. Some star formation manages to persist even in regions directly affected by feedback.**

3. **Star formation plays an important role in dictating the properties of the warm and cold ($\lesssim 10^4$ K) gas phases in CC BCGs**.

6.4 Why is this Important?

Why are cool cores and CC BCGs important?

The 2010 Astrophysics Decadal Survey names a better understanding of the "cosmic dawn", beginning with the epoch of reionization, as a chief priority of the coming decade. The growth of the first stars, galaxies, and black holes at these early epochs was very likely driven and mediated by the cooling and coalescence of gas in dark matter halos (e.g., Silk 1977; Rees & Ostriker 1977). Given the extreme redshifts involved, these systems are not directly observable (at least not with the current generation of space- and ground-based facilities). Brightest Cluster Galaxies in cool core clusters provide critical tests for galaxy formation and evolution models, because they provide a low-redshift, observable analog to cooling processes thought to drive structure growth at early epochs.

Why is AGN Feedback important in a the broad context?

As discussed at length in Chapter 1, the addition of "anti-hierarchical" quenching of star formation is required in merger-driven hierarchical galaxy formation models in order to account for the decades-old "over cooling problem", wherein star formation is effectively catastrophic and grows hierarchically along with structure. This is inconsistent with fundamental observations, including the bright-end truncation of the galaxy luminosity function and the bimodality of galaxies in color-magnitude space.

The need for this anti-hierarchical growth mode can be broadly contextualized as a need to explain the "cosmic downsizing" phenomenon, wherein the dominant contributors to the star formation rate density shifts from high mass galaxies to low mass galaxies with increasing cosmic time. The net implication is that more massive galaxies form at higher redshifts, and less massive galaxies form at lower redshifts — this "big-to-small" behavior is not predicted in cosmological models based upon hierarchical, "big-to-bigger" growth.

Moreover, the $M_{\rm BH}-\sigma$ relation (Magorrian *et al.*, 1998; Ferrarese & Merritt, 2000; Gebhardt *et al.*, 2000), if real, suggests that the growth of black holes and their host galaxy stellar components is not only *tightly coupled*, but also *self calibrating*. To first order, it seems possible that if the $M_{\rm BH}-\sigma$ is intrinsic, it must be fostered by mutual growth amid gas coalescing in newly formed galaxies. However, a second-order effect may be needed to account for the apparent tight calibration. A feedback loop arising from AGN triggering is a natural and promising possibility.

When we consider (1) the correspondence of the epoch of peak quasar activity with the onset of declining star formation rates, and (2) evidence that black hole growth is as anti-hierarchical as

the cosmic evolution of star formation rate densities, a scenario emerges wherein AGN feedback may be one of the primary mechanisms by which cosmic downsizing operates. The notion that AGN feedback may partly account for several major outstanding questions in modern astrophysics is attractive for obvious reasons, though much work remains to be done.

6.5 The Future

Promising though it is, AGN feedback is still largely a black box. It has been invoked to solve various problems by quenching star formation on global scales, but there is mounting evidence, some of which has been presented in this thesis, that star formation may be *triggered* by AGN, or at least persist at low levels amid AGN feedback. We still do not understand the microphysics regulating the possible feedback loop, nor do we even truly understand how radio jets form, propagate, and dissipate energy. Even if AGN feedback is the "solution" to the cooling flow problem, it is becoming clear that yet *another* heating mechanism is required to calibrate the observed ionization states of the cold gas reservoirs in brightest cluster galaxies. Finally, we must at least appreciate the irony that a large and vibrant community (including the Author) has formed around the study of the cooling flow model which fails, in almost every respect, to match observations. Are we seriously underestimating the importance of transport processes like thermal conduction in regulating the entropy of the ICM? Mergers are among the most important drivers of hierarchical structure growth, but what specific, subtle roles might they play in cool core vs. non-cool core clusters? What is a cool core, really? There is little doubt that the pathway of entropy loss from hot primordial baryons to the cold reservoirs from which stars form is of fundamental significance in the Universe. However, we must temper our certainty with humility. As Dr. Chris O'Dea, a good friend and the adviser of this Ph.D. Thesis once warned, "*it was a mistake in the past to think we understood cooling flows and it would be a mistake now to do it again*."

We conclude this thesis with five fundamental, outstanding questions that are critical to a better understanding of clusters, the galaxies within them, and even the Universe as a whole.

- *What mechanisms regulate the entropy of the ICM?*
- *How might environmental factors regulate the triggering of AGN?*
- *How might AGN outbursts contribute to differences between observed and predicted scaling relations in clusters?*

- *What physical processes or mechanisms dictate the presence or absence of a cool core?*
- *How does a BCG, its stellar component, and its central black hole grow during the epoch of cluster assembly? How might this growth differ from that of field galaxies?*

Over the past two decades, *HST*, *Chandra*, and *XMM-Newton* have brought about a paradigm shift in our understanding of cooling flows in galaxy clusters, and this will be among their greatest legacies. The emergence of the next generation of observatories may trigger yet another paradigm shift. Yet, while the now-onlining ALMA is sure to yield scientific returns of extraordinary value, continued investment in space-based facilities like *JWST* will be needed to foster a scientific future as bright as the past. We have so much more to learn. It is worth risking hyperbole to always remind ourselves that, barely more than a century ago, we believed the Universe to be permeated by a "luminiferous ether". Imagine what we'll believe tomorrow.

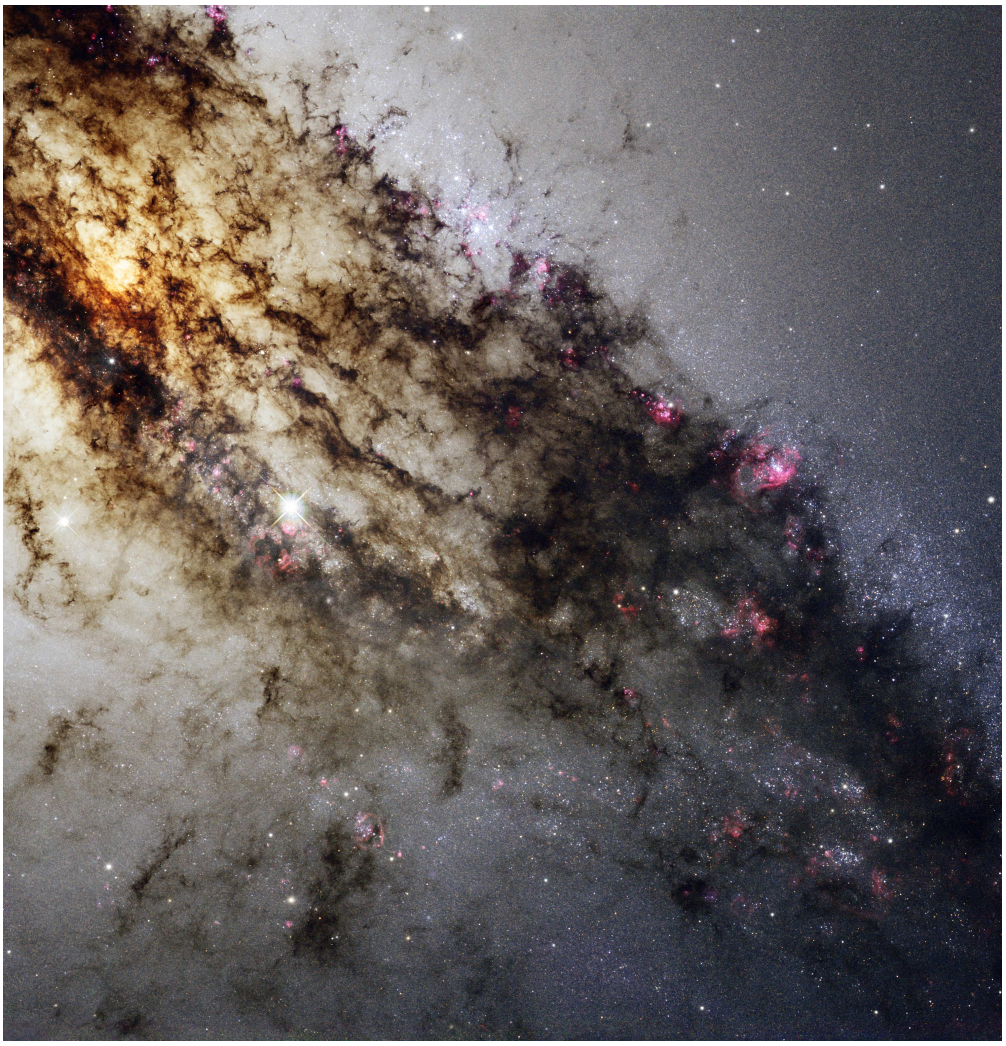

Figure 6.1: *HST* Wide Field Camera 3 (WFC3) observation of the nearby powerful radio galaxy Centaurus A, illustrative of the current state of the art in space-based astronomical imaging. Continued investment in both ground- and space-based observatories will be needed to foster the coming decades of discovery. The *Hubble Space Telescope* inspired the Author to pursue astronomy as a career. We conclude this thesis with a wish that the next generation of scientists is similarly inspired by the next generation of Great Observatories. (Credit: NASA, ESA, STScI/AURA, R. O'Connell and the WFC3 Scientific Oversight Committee).

References

Abell G. O., 1958, ApJS, 3, 211

Abell G. O., Corwin H. G., Jr., Olowin R. P., 1989, ApJS, 70, 1

Adelman-McCarthy J. K., others , 2008, ApJS, 175, 297

Alexander P., Leahy J. P., 1987, MNRAS, 225, 1

Allen M. G. et al., 2002, ApJS, 139, 411

Allen R. J., 1969, A&A, 3, 382

Allen S. W., 1995, MNRAS, 276, 947

Antonucci R., 1993, ARA&A, 31, 473

Antonucci R., 1999, Advances in Space Research, 23, 1139

Antonucci R. R. J., 1984, ApJ, 278, 499

Arnaud K. A., 1996, in G. H. Jacoby & J. Barnes (ed.), *Astronomical Data Analysis Software and Systems V*, vol. 101 of *Astronomical Society of the Pacific Conference Series*, pp. 17–+

Arnaud M., 2005, in F. Melchiorri & Y. Rephaeli (ed.), *Background Microwave Radiation and Intracluster Cosmology*, pp. 77–+

Arnaud M., Evrard A. E., 1999, MNRAS, 305, 631

Arnaud M., Rothenflug R., Boulade O., Vigroux L., Vangioni-Flam E., 1992, A&A, 254, 49

Atek H., Kunth D., Hayes M., Östlin G., Mas-Hesse J. M., 2008, A&A, 488, 491

Baan W. A., Haschick A. D., Burke B. F., 1978, ApJ, 225, 339

Balbus S. A., Soker N., 1989, ApJ, 341, 611

Baldi R. D., Capetti A., 2008, A&A, 489, 989

Ball R., Burns J. O., Loken C., 1993, AJ, 105, 53

Bardeen J. M., Petterson J. A., 1975, ApJ, 195, L65+

Barnes J., 1996, in Bender R., Davies R. L. (eds.), *New Light on Galaxy Evolution*, vol. 171 of *IAU Symposium*, pp. 191–+

Barnes J. E., Hernquist L. E., 1991, ApJ, 370, L65

Barthel P. D., 1989, ApJ, 336, 606
Barthel P. D., 1994, in G. V. Bicknell, M. A. Dopita, & P. J. Quinn (ed.), *The Physics of Active Galaxies*, vol. 54 of *Astronomical Society of the Pacific Conference Series*, pp. 175–+
Batcheldor D., Robinson A., Axon D. J., Perlman E. S., Merritt D., 2010, ApJ, 717, L6
Bauer F. E., Fabian A. C., Sanders J. S., Allen S. W., Johnstone R. M., 2005, MNRAS, 359, 1481
Baum S. A., 1987, *Extended optical emission line gas in powerful radio galaxies*, Ph.D. thesis, Maryland Univ., College Park.
Baum S. A., Heckman T., 1989a, ApJ, 336, 681
Baum S. A., Heckman T., 1989b, ApJ, 336, 681
Baum S. A., Heckman T. M., Bridle A., van Breugel W. J. M., Miley G. K., 1988, ApJS, 68, 643
Baum S. A., Heckman T. M., van Breugel W., 1992, ApJ, 389, 208
Baum S. A., Laor A., O'Dea C. P., Mack J., Koekemoer A. M., 2005, ApJ, 632, 122
Baum S. A., O'Dea C. P., 1991, MNRAS, 250, 737
Baum S. A., O'Dea C. P., Murphy D. W., de Bruyn A. G., 1990, A&A, 232, 19
Baum S. A., Zirbel E. L., O'Dea C. P., 1995, ApJ, 451, 88
Becker R. H., White R. L., Helfand D. J., 1995, ApJ, 450, 559
Begelman M. C., 2001, ApJ, 551, 897
Begelman M. C., Fabian A. C., 1990, MNRAS, 244, 26P
Bekki K., Shioya Y., 1997, ApJ, 478, L17+
Bell E. F. et al., 2004, ApJ, 608, 752
Benson A. J., Bower R. G., Frenk C. S., Lacey C. G., Baugh C. M., Cole S., 2003, ApJ, 599, 38
Bertschinger E., Meiksin A., 1986, ApJ, 306, L1
Best P. N., Kaiser C. R., Heckman T. M., Kauffmann G., 2006, MNRAS, 368, L67
Best P. N., Röttgering H. J. A., Longair M. S., 2000, MNRAS, 311, 23
Bicknell G. V., 1995, ApJS, 101, 29
Bildfell C., Hoekstra H., Babul A., Mahdavi A., 2008, MNRAS, 389, 1637
Binette L., Dopita M. A., Tuohy I. R., 1985, ApJ, 297, 476
Binette L., Wang J., Villar-Martin M., Martin P. G., Magris C. G., 1993, ApJ, 414, 535
Bîrzan L., Rafferty D. A., McNamara B. R., Wise M. W., Nulsen P. E. J., 2004, ApJ, 607, 800
Blandford R. D., Payne D. G., 1982, MNRAS, 199, 883
Blandford R. D., Znajek R. L., 1977, MNRAS, 179, 433
Blanton E. L., Gregg M. D., Helfand D. J., Becker R. H., White R. L., 2000, ApJ, 531, 118
Blanton E. L., Sarazin C. L., McNamara B. R., Wise M. W., 2001, ApJ, 558, L15
Blundell K. M., Rawlings S., 2001, ApJ, 562, L5

Böhringer H., Voges W., Fabian A. C., Edge A. C., Neumann D. M., 1993, MNRAS, 264, L25

Bower R. G., Benson A. J., Malbon R., Helly J. C., Frenk C. S., Baugh C. M., Cole S., Lacey C. G., 2006, MNRAS, 370, 645

Branduardi-Raymont G., Fabricant D., Feigelson E., Gorenstein P., Grindlay J., Soltan A., Zamorani G., 1981, ApJ, 248, 55

Bregman J. N., David L. P., 1988, ApJ, 326, 639

Bridle A. H., 1984, AJ, 89, 979

Bridle A. H., Perley R. A., Henriksen R. N., 1986, AJ, 92, 534

Brighenti F., Mathews W. G., 2003, ApJ, 587, 580

Brocksopp C., Kaiser C. R., Schoenmakers A. P., de Bruyn A. G., 2007, MNRAS, 382, 1019

Bruzual G., Charlot S., 2003, MNRAS, 344, 1000

Bruzual A. G., Charlot S., 1993, ApJ, 405, 538

Burns J. O., 1990, AJ, 99, 14

Burns J. O., Hallman E. J., Gantner B., Motl P. M., Norman M. L., 2008, ApJ, 675, 1125

Buttiglione S., Capetti A., Celotti A., Axon D. J., Chiaberge M., Duccio Macchetto F., Sparks W. B., 2009, ArXiv e-prints

Buttiglione S., Capetti A., Celotti A., Axon D. J., Chiaberge M., Macchetto F. D., Sparks W. B., 2010, A&A, 509, A6+

Capak P. et al., 2007, ApJS, 172, 99

Capetti A., Balmaverde B., 2010, *A New View of the Origin of the Radio-Quiet/Radio-Loud AGN Dichotomy?*, pp. 175–+

Cardelli J. A., Clayton G. C., Mathis J. S., 1989, ApJ, 345, 245

Cardiel N., Gorgas J., Aragón-Salamanca A., 1998, Ap&SS, 263, 83

Carlstrom J. E., Holder G. P., Reese E. D., 2002, ARA&A, 40, 643

Cavagnolo K. W., Donahue M., Voit G. M., Sun M., 2008, ApJ, 683, L107

Cavagnolo K. W., Donahue M., Voit G. M., Sun M., 2009, ApJS, 182, 12

Cavaliere A., Fusco-Femiano R., 1976, A&A, 49, 137

Cavaliere A., Padovani P., 1989, ApJ, 340, L5

Chandran B. D. G., Rasera Y., 2007, ApJ, 671, 1413

Charlot S., Longhetti M., 2001, MNRAS, 323, 887

Chen Y., Reiprich T. H., Böhringer H., Ikebe Y., Zhang Y.-Y., 2007, A&A, 466, 805

Chiaberge M., Capetti A., Celotti A., 1999, A&A, 349, 77

Chiaberge M., Capetti A., Macchetto F. D., Rosati P., Tozzi P., Tremblay G. R., 2010, ApJ, 710, L107

Chiaberge M., Macchetto F. D., Sparks W. B., Capetti A., Allen M. G., Martel A. R., 2002, ApJ, 571, 247

Chiaberge M., Tremblay G., Capetti A., Macchetto F. D., Tozzi P., Sparks W. B., 2009, ApJ, 696, 1103

Churazov E., Brüggen M., Kaiser C. R., Böhringer H., Forman W., 2001, ApJ, 554, 261

Churazov E., Sunyaev R., Forman W., Böhringer H., 2002, MNRAS, 332, 729

Cimatti A., Dey A., van Breugel W., Hurt T., Antonucci R., 1997, ApJ, 476, 677

Ciotti L., van Albada T. S., 2001, ApJ, 552, L13

Clampin M. et al., 2004, in P. Amico, J. W. Beletic, & J. E. Belectic (ed.), *Scientific Detectors for Astronomy, The Beginning of a New Era*, vol. 300 of *Astrophysics and Space Science Library*, pp. 555–563

Clarke D. A., Bridle A. H., Burns J. O., Perley R. A., Norman M. L., 1992, ApJ, 385, 173

Clarke T. E., Kronberg P. P., Böhringer H., 2001, ApJ, 547, L111

Clarke T. E., Sarazin C. L., Blanton E. L., Neumann D. M., Kassim N. E., 2005, ApJ, 625, 748

Cohen M. H., Ogle P. M., Tran H. D., Goodrich R. W., Miller J. S., 1999, AJ, 118, 1963

Colla G. et al., 1970, A&AS, 1, 281

Condon J. J., Cotton W. D., Greisen E. W., Yin Q. F., Perley R. A., Taylor G. B., Broderick J. J., 1998, AJ, 115, 1693

Conselice C. J., Gallagher J. S., III, Wyse R. F. G., 2001, AJ, 122, 2281

Conway J. E., Myers S. T., Pearson T. J., Readhead A. C. S., Unwin S. C., Xu W., 1994, ApJ, 425, 568

Cowie L. L., Barger A. J., Bautz M. W., Brandt W. N., Garmire G. P., 2003, ApJ, 584, L57

Cowie L. L., Binney J., 1977, ApJ, 215, 723

Cowie L. L., Fabian A. C., Nulsen P. E. J., 1980, MNRAS, 191, 399

Cowie L. L., Songaila A., Hu E. M., Cohen J. G., 1996, AJ, 112, 839

Crawford C. S., Allen S. W., Ebeling H., Edge A. C., Fabian A. C., 1999, MNRAS, 306, 857

Crawford C. S., Edge A. C., Fabian A. C., Allen S. W., Bohringer H., Ebeling H., McMahon R. G., Voges W., 1995, MNRAS, 274, 75

Crawford C. S., Fabian A. C., 1993, MNRAS, 265, 431

Crawford C. S., Fabian A. C., Johnstone R. M., Arnaud K. A., 1989, MNRAS, 236, 277

Crawford C. S., Hatch N. A., Fabian A. C., Sanders J. S., 2005, MNRAS, 363, 216

Croton D. J., others , 2006, MNRAS, 365, 11

Daly R. A., 1990, ApJ, 355, 416

David L. P., Bregman J. N., Seab C. G., 1988, ApJ, 329, 66

David L. P., Nulsen P. E. J., McNamara B. R., Forman W., Jones C., Ponman T., Robertson B., Wise M., 2001, ApJ, 557, 546

David L. P., Slyz A., Jones C., Forman W., Vrtilek S. D., Arnaud K. A., 1993, ApJ, 412, 479

de Koff S., Baum S. A., Sparks W. B., Biretta J., Golombek D., Macchetto F., McCarthy P., Miley G. K., 1996, ApJS, 107, 621

de Koff S. et al., 2000, ApJS, 129, 33

De Villiers J., Hawley J. F., Krolik J. H., Hirose S., 2005, ApJ, 620, 878

De Young D. S., Roberts M. S., 1974, ApJ, 189, 1

Di Matteo T., Springel V., Hernquist L., 2005, Nature, 433, 604

Donahue M., de Messières G. E., O'Connell R. W., Voit G. M., Hoffer A., McNamara B. R., Nulsen P. E. J., 2011, ArXiv e-prints

Donahue M., Horner D. J., Cavagnolo K. W., Voit G. M., 2006, ApJ, 643, 730

Donahue M. et al., 2007, ApJ, 670, 231

Donahue M., Mack J., Voit G. M., Sparks W., Elston R., Maloney P. R., 2000, ApJ, 545, 670

Donahue M., Voit G. M., 1991, ApJ, 381, 361

Donzelli C. J., Chiaberge M., Macchetto F. D., Madrid J. P., Capetti A., Marchesini D., 2007, ApJ, 667, 780

Dopita M. A., Koratkar A. P., Allen M. G., Tsvetanov Z. I., Ford H. C., Bicknell G. V., Sutherland R. S., 1997, ApJ, 490, 202

Draine B. T., 1978, ApJS, 36, 595

Drake C. L., Bicknell G. V., McGregor P. J., Dopita M. A., 2004, AJ, 128, 969

Dunn R. J. H., Fabian A. C., 2006, MNRAS, 373, 959

Dunn R. J. H., Fabian A. C., Taylor G. B., 2005, MNRAS, 364, 1343

Dursi L. J., Pfrommer C., 2008, ApJ, 677, 993

Dwek E., Arendt R. G., 1992, ARA&A, 30, 11

Ebeling H., Edge A. C., Bohringer H., Allen S. W., Crawford C. S., Fabian A. C., Voges W., Huchra J. P., 1998, MNRAS, 301, 881

Ebeling H., White D. A., Rangarajan F. V. N., 2006, MNRAS, 368, 65

Edge A. C., 2001, MNRAS, 328, 762

Edge A. C., Frayer D. T., 2003, ApJ, 594, L13

Edge A. C. et al., 2010a, A&A, 518, L46+

Edge A. C. et al., 2010b, A&A, 518, L47+

Edwards L. O. V., Hudson M. J., Balogh M. L., Smith R. J., 2007, MNRAS, 379, 100

Egami E. et al., 2006, ApJ, 647, 922

Enßlin T. A., Heinz S., 2002, A&A, 384, L27
Eracleous M., Halpern J. P., 1994, ApJS, 90, 1
Faber S. M., others , 2007, ApJ, 665, 265
Fabian A. C., 1994, ARA&A, 32, 277
Fabian A. C., 1999, MNRAS, 308, L39
Fabian A. C., 2003, MNRAS, 344, L27
Fabian A. C., Johnstone R. M., Sanders J. S., Conselice C. J., Crawford C. S., Gallagher J. S., III, Zweibel E., 2008, Nature, 454, 968
Fabian A. C., Nulsen P. E. J., 1977, MNRAS, 180, 479
Fabian A. C., Sanders J. S., Crawford C. S., Ettori S., 2003, MNRAS, 341, 729
Fabian A. C. et al., 2000, MNRAS, 318, L65
Fabian A. C., Sanders J. S., Taylor G. B., Allen S. W., Crawford C. S., Johnstone R. M., Iwasawa K., 2006, MNRAS, 366, 417
Fabian A. C., Sanders J. S., Williams R. J. R., Lazarian A., Ferland G. J., Johnstone R. M., 2011, ArXiv e-prints
Fabian A. C., Voigt L. M., Morris R. G., 2002, MNRAS, 335, L71
Falcke H., Körding E., Markoff S., 2004, A&A, 414, 895
Fanaroff B. L., Riley J. M., 1974, MNRAS, 167, 31P
Ferland G. J., Fabian A. C., Hatch N. A., Johnstone R. M., Porter R. L., van Hoof P. A. M., Williams R. J. R., 2008, MNRAS, 386, L72
Ferland G. J., Fabian A. C., Hatch N. A., Johnstone R. M., Porter R. L., van Hoof P. A. M., Williams R. J. R., 2009, MNRAS, 392, 1475
Ferland G. J., Osterbrock D. E., 1985, ApJ, 289, 105
Ferland G. J., Osterbrock D. E., 1986, ApJ, 300, 658
Ferrarese L., Merritt D., 2000, ApJ, 539, L9
Floyd D. J. E. et al., 2008, ApJS, 177, 148
Forman W., Jones C., 1982, ARA&A, 20, 547
Forman W. et al., 2007, ApJ, 665, 1057
Forman W., Kellogg E., Gursky H., Tananbaum H., Giacconi R., 1972, ApJ, 178, 309
Forman W. et al., 2005, ApJ, 635, 894
Fruscione A. et al., 2006, in *Society of Photo-Optical Instrumentation Engineers (SPIE) Conference Series*, vol. 6270 of *Presented at the Society of Photo-Optical Instrumentation Engineers (SPIE) Conference*
García-Lorenzo B., Sánchez S. F., Mediavilla E., González-Serrano J. I., Christensen L., 2005,

ApJ, 621, 146
Gebhardt K. et al., 2000, ApJ, 539, L13
Giacconi R., Gursky H., Kellogg E., Schreier E., Tananbaum H., 1971, ApJ, 167, L67+
Giacconi R. et al., 2002, ApJS, 139, 369
Giavalisco M., 2002, ARA&A, 40, 579
Gitti M., Nulsen P. E. J., David L. P., McNamara B. R., Wise M. W., 2011, ApJ, 732, 13
Gopal-Krishna , Wiita P. J., 1987, MNRAS, 226, 531
Govoni F., Murgia M., Markevitch M., Feretti L., Giovannini G., Taylor G. B., Carretti E., 2009, A&A, 499, 371
Griffith M. R., Wright A. E., 1994, VizieR Online Data Catalog, 8027, 0
Gunn J. E., 1979, in *Active Galactic Nuclei*, pp. 213–225
Gunn J. E., Gott J. R., III, 1972, ApJ, 176, 1
Gursky H., Kellogg E., Murray S., Leong C., Tananbaum H., Giacconi R., 1971, ApJ, 167, L81+
Gursky H., Schwartz D. A., 1977, ARA&A, 15, 541
Habe A., Ikeuchi S., 1985, ApJ, 289, 540
Haehnelt M. G., Rees M. J., 1993, MNRAS, 263, 168
Hansen L., Jorgensen H. E., Norgaard-Nielsen H. U., 1995, A&A, 297, 13
Hardcastle M. J., Evans D. A., Croston J. H., 2006, MNRAS, 370, 1893
Hardcastle M. J., Evans D. A., Croston J. H., 2007, MNRAS, 376, 1849
Hardcastle M. J., Harris D. E., Worrall D. M., Birkinshaw M., 2004, ApJ, 612, 729
Harris D. E., Cheung C. C., Biretta J. A., Sparks W. B., Junor W., Perlman E. S., Wilson A. S., 2006, ApJ, 640, 211
Haynes M. P., Brown R. L., Roberts M. S., 1978, ApJ, 221, 414
Heckman T. M., Baum S. A., van Breugel W. J. M., McCarthy P., 1989, ApJ, 338, 48
Heinz S., Reynolds C. S., Begelman M. C., 1998, ApJ, 501, 126
Heywood I., Blundell K. M., Rawlings S., 2007, MNRAS, 381, 1093
Hicks A. K., Mushotzky R., 2005, ApJ, 635, L9
Hine R. G., Longair M. S., 1979, MNRAS, 188, 111
Holt J., Tadhunter C. N., González Delgado R. M., Inskip K. J., Rodriguez J., Emonts B. H. C., Morganti R., Wills K. A., 2007, MNRAS, 381, 611
Holt J., Tadhunter C. N., Morganti R., 2009, MNRAS, 400, 589
Holtzman J. A. et al., 1996, AJ, 112, 416
Hopkins P. F., Hernquist L., Cox T. J., Di Matteo T., Robertson B., Springel V., 2005, ApJ, 630, 716

Hopkins P. F., Hernquist L., Cox T. J., Di Matteo T., Robertson B., Springel V., 2006, ApJS, 163, 1

Hopkins P. F., Richards G. T., Hernquist L., 2007, ApJ, 654, 731

Hu E. M., 1992, ApJ, 391, 608

Hu E. M., Cowie L. L., Wang Z., 1985, ApJS, 59, 447

Hudson D. S., Mittal R., Reiprich T. H., Nulsen P. E. J., Andernach H., Sarazin C. L., 2010, A&A, 513, A37+

Hutchings J. B., Balogh M. L., 2000, AJ, 119, 1123

Israel F. P., Tilanus R. P. J., Baas F., 2006, A&A, 445, 907

Jackson N., Rawlings S., 1997, MNRAS, 286, 241

Jaffe W., Bremer M. N., Baker K., 2005, MNRAS, 360, 748

Jaffe W., Bremer M. N., van der Werf P. P., 2001, MNRAS, 324, 443

Jetha N. N., Sakelliou I., Hardcastle M. J., Ponman T. J., Stevens I. R., 2005, MNRAS, 358, 1394

Johnson B. D. et al., 2007, ApJS, 173, 392

Johnstone R. M., Fabian A. C., Nulsen P. E. J., 1987, MNRAS, 224, 75

Jones T. W., Ryu D., Engel A., 1999, ApJ, 512, 105

Kaiser C. R., Binney J., 2003, MNRAS, 338, 837

Kaiser C. R., Schoenmakers A. P., Röttgering H. J. A., 2000, MNRAS, 315, 381

Kaiser N., 1986, MNRAS, 222, 323

Kapahi V. K., 1985, MNRAS, 214, 19P

Kapahi V. K., 1989, AJ, 97, 1

Katayama H., Hayashida K., Takahara F., Fujita Y., 2003, ApJ, 585, 687

Kauffmann G., Haehnelt M., 2000, MNRAS, 311, 576

Kennicutt R. C., Jr., 1998, ApJ, 498, 541

Khochfar S., Burkert A., 2005, MNRAS, 359, 1379

Kirkpatrick C. C. et al., 2009, ApJ, 697, 867

Koekemoer A. M. et al., 2007, ApJS, 172, 196

Koekemoer A. M., Fruchter A. S., Hook R. N., Hack W., 2002, in Arribas S., Koekemoer A., Whitmore B. (eds.), *The 2002 HST Calibration Workshop : Hubble after the Installation of the ACS and the NICMOS Cooling System*, pp. 337–+

Koekemoer A. M., O'Dea C. P., Sarazin C. L., McNamara B. R., Donahue M., Voit G. M., Baum S. A., Gallimore J. F., 1999, ApJ, 525, 621

Kormendy J., Richstone D., 1995, ARA&A, 33, 581

Lacy M. et al., 2004, ApJS, 154, 166

Laing R. A., Bridle A. H., Parma P., Feretti L., Giovannini G., Murgia M., Perley R. A., 2008, MNRAS, 386, 657

Laing R. A., Jenkins C. R., Wall J. V., Unger S. W., 1994, in G. V. Bicknell, M. A. Dopita, & P. J. Quinn (ed.), *The Physics of Active Galaxies*, vol. 54 of *Astronomical Society of the Pacific Conference Series*, pp. 201–+

Lauer T. R. et al., 2005, AJ, 129, 2138

Lea S. M., Silk J., Kellogg E., Murray S., 1973, ApJ, 184, L105+

Ledlow M. J., Owen F. N., 1996, AJ, 112, 9

Leitherer C. et al., 1999, ApJS, 123, 3

Lilly S. J., Longair M. S., 1982, MNRAS, 199, 1053

Lloyd-Davies E. J., Ponman T. J., Cannon D. B., 2000, MNRAS, 315, 689

Loubser S. I., Sánchez-Blázquez P., Sansom A. E., Soechting I. K., 2009, MNRAS, 398, 133

Lynden-Bell D., 1967, MNRAS, 136, 101

Lynds R., 1970, ApJ, 159, L151

Machalski J., Kozieł-Wierzbowska D., Jamrozy M., Saikia D. J., 2008, ApJ, 679, 149

Mack K.-H., Klein U., O'Dea C. P., Willis A. G., 1997, A&AS, 123, 423

Madrid J. P. et al., 2006, ApJS, 164, 307

Magorrian J. et al., 1998, AJ, 115, 2285

Malyshkin L., Kulsrud R., 2001, ApJ, 549, 402

Markevitch M., 1998, ApJ, 504, 27

Markevitch M., Govoni F., Brunetti G., Jerius D., 2005, ApJ, 627, 733

Martel A. R. et al., 1999, ApJS, 122, 81

Matthews T. A., Morgan W. W., Schmidt M., 1964, ApJ, 140, 35

McCarthy I. G., Balogh M. L., Babul A., Poole G. B., Horner D. J., 2004, ApJ, 613, 811

McCarthy P. J., 1993, ARA&A, 31, 639

McCarthy P. J., Miley G. K., de Koff S., Baum S. A., Sparks W. B., Golombek D., Biretta J., Macchetto F., 1997, ApJS, 112, 415

McDonald M., Veilleux S., Mushotzky R., 2011, ApJ, 731, 33

McDonald M., Veilleux S., Rupke D. S. N., Mushotzky R., 2010, ApJ, 721, 1262

McNamara B. R., 1997, in N. Soker (ed.), *Galactic Cluster Cooling Flows*, vol. 115 of *Astronomical Society of the Pacific Conference Series*, pp. 109–+

McNamara B. R., 2004, in T. Reiprich, J. Kempner, & N. Soker (ed.), *The Riddle of Cooling Flows in Galaxies and Clusters of galaxies*, pp. 177–+

McNamara B. R., Jannuzi B. T., Sarazin C. L., Elston R., Wise M., 1999, ApJ, 518, 167

McNamara B. R., Nulsen P. E. J., 2007, ARA&A, 45, 117
McNamara B. R., O'Connell R. W., 1989, AJ, 98, 2018
McNamara B. R., O'Connell R. W., 1993, AJ, 105, 417
McNamara B. R. et al., 2000, ApJ, 534, L135
McNamara B. R., Wise M. W., Murray S. S., 2004, ApJ, 601, 173
McNamara B. R. et al., 2001, ApJ, 562, L149
Meier D. L., 1999, ApJ, 522, 753
Mewe R., 1999, in J. van Paradijs & J. A. M. Bleeker (ed.), *X-Ray Spectroscopy in Astrophysics*, vol. 520 of *Lecture Notes in Physics, Berlin Springer Verlag*, pp. 109–+
Micelotta E. R., Jones A. P., Tielens A. G. G. M., 2010, A&A, 510, A37+
Miley G., De Breuck C., 2008, A&A Rev., 15, 67
Minkowski R., 1957, in H. C. van de Hulst (ed.), *Radio astronomy*, vol. 4 of *IAU Symposium*, pp. 107–+
Mitchell R. J., Culhane J. L., Davison P. J. N., Ives J. C., 1976, MNRAS, 175, 29P
Mittal R., Hudson D. S., Reiprich T. H., Clarke T., 2009, A&A, 501, 835
Mittaz J. P. D. et al., 2001, A&A, 365, L93
Mobasher B. et al., 2007, ApJS, 172, 117
Morris R. G., Fabian A. C., 2005, MNRAS, 358, 585
Murgia M., Govoni F., Markevitch M., Feretti L., Giovannini G., Taylor G. B., Carretti E., 2009, A&A, 499, 679
Mushotzky R. F., 2004, Clusters of Galaxies: Probes of Cosmological Structure and Galaxy Evolution, pp. 123–+
Narayan R., Medvedev M. V., 2001, ApJ, 562, L129
Nulsen P. E. J., 1986, MNRAS, 221, 377
Nulsen P. E. J., McNamara B. R., Wise M. W., David L. P., 2005, ApJ, 628, 629
O'Dea C. P., Baum S. A., 1987a, AJ, 94, 1476
O'Dea C. P., Baum S. A., 1987b, AJ, 94, 1476
O'Dea C. P., Baum S. A., 1997, in N. Soker (ed.), *Galactic Cluster Cooling Flows*, vol. 115 of *Astronomical Society of the Pacific Conference Series*, pp. 147–+
O'Dea C. P., Baum S. A., Gallimore J. F., 1994a, ApJ, 436, 669
O'Dea C. P., Baum S. A., Mack J., Koekemoer A. M., Laor A., 2004, ApJ, 612, 131
O'Dea C. P., Baum S. A., Maloney P. R., Tacconi L. J., Sparks W. B., 1994b, ApJ, 422, 467
O'Dea C. P. et al., 2008, ApJ, 681, 1035
O'Dea C. P., Baum S. A., Stanghellini C., 1991, ApJ, 380, 66

O'Dea C. P., Koekemoer A. M., Baum S. A., Sparks W. B., Martel A. R., Allen M. G., Macchetto F. D., Miley G. K., 2001, AJ, 121, 1915

O'Dea C. P., Owen F. N., 1987, ApJ, 316, 95

O'Dea C. P., Payne H. E., Kocevski D., 1998, AJ, 116, 623

O'Dea K. P. et al., 2010, ApJ, 719, 1619

Oegerle W. R., Cowie L., Davidsen A., Hu E., Hutchings J., Murphy E., Sembach K., Woodgate B., 2001, ApJ, 560, 187

Ogle P. M., Cohen M. H., Miller J. S., Tran H. D., Fosbury R. A. E., Goodrich R. W., 1997, ApJ, 482, L37+

Oonk J. B. R., Hatch N. A., Jaffe W., Bremer M. N., van weeren R. J., 2011, ArXiv e-prints

Oonk J. B. R., Jaffe W., Bremer M. N., van Weeren R. J., 2010, MNRAS, 405, 898

Osterbrock D. E., 1989, *Astrophysics of gaseous nebulae and active galactic nuclei*

Owen F. N., Ledlow M. J., 1994, in G. V. Bicknell, M. A. Dopita, & P. J. Quinn (ed.), *The Physics of Active Galaxies*, vol. 54 of *Astronomical Society of the Pacific Conference Series*, pp. 319–+

Owen F. N., Ledlow M. J., Keel W. C., 1996, AJ, 111, 53

Owen F. N., White R. A., Burns J. O., 1992, ApJS, 80, 501

Parma P., Murgia M., Morganti R., Capetti A., de Ruiter H. R., Fanti R., 1999, A&A, 344, 7

Pentericci L., McCarthy P. J., Röttgering H. J. A., Miley G. K., van Breugel W. J. M., Fosbury R., 2001, ApJS, 135, 63

Peres C. B., Fabian A. C., Edge A. C., Allen S. W., Johnstone R. M., White D. A., 1998, MNRAS, 298, 416

Pérez-González P. G. et al., 2008, ApJ, 675, 234

Perley R. A., Bridle A. H., Willis A. G., 1984, ApJS, 54, 291

Peterson B. M., 1978, ApJ, 223, 740

Peterson J. R., Fabian A. C., 2006, Phys. Rep., 427, 1

Peterson J. R., Kahn S. M., Paerels F. B. S., Kaastra J. S., Tamura T., Bleeker J. A. M., Ferrigno C., Jernigan J. G., 2003, ApJ, 590, 207

Peterson J. R. et al., 2001, A&A, 365, L104

Piffaretti R., Jetzer P., Kaastra J. S., Tamura T., 2005, A&A, 433, 101

Pipino A., Kaviraj S., Bildfell C., Babul A., Hoekstra H., Silk J., 2009, MNRAS, 395, 462

Pollack L. K., Taylor G. B., Allen S. W., 2005, MNRAS, 359, 1229

Pratt G. W., Arnaud M., Pointecouteau E., 2006, A&A, 446, 429

Privon G. C., O'Dea C. P., Baum S. A., Axon D. J., Kharb P., Buchanan C. L., Sparks W., Chiaberge M., 2008, ApJS, 175, 423

Punsly B., Coroniti F. V., 1990, ApJ, 354, 583
Quillen A. C., Bland-Hawthorn J., 2008, MNRAS, 386, 2227
Quillen A. C. et al., 2008, ApJS, 176, 39
Rafferty D. A., McNamara B. R., Nulsen P. E. J., 2008, ApJ, 687, 899
Rafferty D. A., McNamara B. R., Nulsen P. E. J., Wise M. W., 2006, ApJ, 652, 216
Rector T. A., Stocke J. T., 2001, AJ, 122, 565
Rees M. J., 1989, MNRAS, 239, 1P
Rees M. J., Ostriker J. P., 1977, MNRAS, 179, 541
Reynolds C. S., Heinz S., Begelman M. C., 2002, MNRAS, 332, 271
Robinson A., Binette L., Fosbury R. A. E., Tadhunter C. N., 1987, MNRAS, 227, 97
Robinson K. et al., 2004, ApJ, 601, 621
Robinson R. D., Cram L. E., Giampapa M. S., 1990, ApJS, 74, 891
Romanishin W., 1987, ApJ, 323, L113
Rosati P., Borgani S., Norman C., 2002, ARA&A, 40, 539
Rosner R., Tucker W. H., 1989, ApJ, 338, 761
Russell H. R., Fabian A. C., Sanders J. S., Johnstone R. M., Blundell K. M., Brandt W. N., Crawford C. S., 2010, MNRAS, 402, 1561
Russell H. R., Sanders J. S., Fabian A. C., 2008, MNRAS, 390, 1207
Ruszkowski M., Begelman M. C., 2002, ApJ, 581, 223
Sabra B. M., Shields J. C., Filippenko A. V., 2000, ApJ, 545, 157
Sadler E. M. et al., 2007, MNRAS, 381, 211
Sakelliou I. et al., 2002, A&A, 391, 903
Salomé P., Combes F., 2003, A&A, 412, 657
Salomé P. et al., 2006, A&A, 454, 437
Salpeter E. E., 1955, ApJ, 121, 161
Sanders D. B. et al., 2007, ApJS, 172, 86
Sanders J. S., 2006, MNRAS, 371, 829
Sanders J. S., Fabian A. C., Allen S. W., Morris R. G., Graham J., Johnstone R. M., 2008, MNRAS, 385, 1186
Sanderson A. J. R., Edge A. C., Smith G. P., 2009, MNRAS, 398, 1698
Sanderson A. J. R., Ponman T. J., O'Sullivan E., 2006, MNRAS, 372, 1496
Sarazin C. L., 1986, Reviews of Modern Physics, 58, 1
Sarazin C. L., 1988, *X-ray emission from clusters of galaxies*
Sarazin C. L., Burns J. O., Roettiger K., McNamara B. R., 1995, ApJ, 447, 559

Sarazin C. L., McNamara B. R., 1997, ApJ, 480, 203
Scannapieco E., Silk J., Bouwens R., 2005, ApJ, 635, L13
Scarpa R., Urry C. M., 2001, ApJ, 556, 749
Schawinski K. et al., 2006, Nature, 442, 888
Schilizzi R. T. et al., 2001, A&A, 368, 398
Schinnerer E. et al., 2007, ApJS, 172, 46
Schmidt M., Schneider D. P., Gunn J. E., 1991, in Crampton D. (ed.), *The Space Distribution of Quasars*, vol. 21 of *Astronomical Society of the Pacific Conference Series*, pp. 109–114
Schmidt R. W., Allen S. W., Fabian A. C., 2001, MNRAS, 327, 1057
Schoenmakers A. P., de Bruyn A. G., Röttgering H. J. A., van der Laan H., 2000a, MNRAS, 315, 395
Schoenmakers A. P., de Bruyn A. G., Röttgering H. J. A., van der Laan H., Kaiser C. R., 2000b, MNRAS, 315, 371
Scoville N. et al., 2007, ApJS, 172, 1
Serlemitsos P. J., Smith B. W., Boldt E. A., Holt S. S., Swank J. H., 1977, ApJ, 211, L63
Shostak G. S., Gilra D. P., Noordam J. E., Nieuwenhuijzen H., Vermue J., de Graauw T., 1980, A&A, 81, 223
Sijacki D., Springel V., 2006, MNRAS, 366, 397
Sijacki D., Springel V., Di Matteo T., Hernquist L., 2007, MNRAS, 380, 877
Silk J., 1968, Nature, 218, 453
Silk J., 1977, ApJ, 211, 638
Silk J., Rees M. J., 1998, A&A, 331, L1
Silverman J. D. et al., 2008, ApJ, 675, 1025
Smith E. P., Bohlin R. C., Bothun G. D., O'Connell R. W., Roberts M. S., Neff S. G., Smith A. M., Stecher T. P., 1997, ApJ, 478, 516
Smith E. P., Heckman T. M., 1989, ApJ, 341, 658
Smith E. P., Heckman T. M., Illingworth G. D., 1990, ApJ, 356, 399
Snellen I. A. G., Best P. N., 2001a, MNRAS, 328, 897
Snellen I. A. G., Best P. N., 2001b, MNRAS, 328, 897
Sodroski T. J. et al., 1994, ApJ, 428, 638
Soker N., 2003, MNRAS, 342, 463
Soker N., Blanton E. L., Sarazin C. L., 2002, ApJ, 573, 533
Soker N., Sarazin C. L., 1990, ApJ, 348, 73
Soker N., White R. E., III, David L. P., McNamara B. R., 2001, ApJ, 549, 832

Sparks W. B., 1992, ApJ, 399, 66
Sparks W. B., Macchetto F., Golombek D., 1989, ApJ, 345, 153
Sparks W. B., Pringle J. E., Donahue M., Carswell R., Voit M., Cracraft M., Martin R. G., 2009, ApJ, 704, L20
Spinrad H., Marr J., Aguilar L., Djorgovski S., 1985, PASP, 97, 932
Spitzer L., 1962, *Physics of Fully Ionized Gases*
Springel V., Di Matteo T., Hernquist L., 2005, MNRAS, 361, 776
Statler T. S., McNamara B. R., 2002, ApJ, 581, 1032
Steffen A. T., Barger A. J., Cowie L. L., Mushotzky R. F., Yang Y., 2003, ApJ, 596, L23
Sun M., 2009, ApJ, 704, 1586
Sunyaev R. A., Zeldovich Y. B., 1970, Ap&SS, 7, 3
Sunyaev R. A., Zeldovich Y. B., 1972, Comments on Astrophysics and Space Physics, 4, 173
Sutherland R. S., Dopita M. A., 1993, ApJS, 88, 253
Tamura T. et al., 2001, A&A, 365, L87
Taniguchi Y. et al., 2007, ApJS, 172, 9
Taylor G. B., O'Dea C. P., Peck A. B., Koekemoer A. M., 1999, ApJ, 512, L27
Tohline J. E., Simonson G. F., Caldwell N., 1982, ApJ, 252, 92
Tran H. D., Tsvetanov Z., Ford H. C., Davies J., Jaffe W., van den Bosch F. C., Rest A., 2001, AJ, 121, 2928
Tremblay G. R., Chiaberge M., Donzelli C. J., Quillen A. C., Capetti A., Sparks W. B., Macchetto F. D., 2007, ApJ, 666, 109
Tremblay G. R. et al., 2009, ApJS, 183, 278
Tremblay G. R., O'Dea C. P., Baum S. A., Koekemoer A. M., Sparks W. B., de Bruyn G., Schoenmakers A. P., 2010, ApJ, 715, 172
Tremblay G. R. et al., 2006, ApJ, 643, 101
Tribble P. C., 1989, MNRAS, 238, 1247
Tubbs A. D., 1980, ApJ, 241, 969
Ueda Y., Akiyama M., Ohta K., Miyaji T., 2003, ApJ, 598, 886
Urry C. M., Padovani P., 1995, PASP, 107, 803
van Breugel W., Fragile C., Anninos P., Murray S., 2004, in P.-A. Duc, J. Braine, & E. Brinks (ed.), *Recycling Intergalactic and Interstellar Matter*, vol. 217 of *IAU Symposium*, pp. 472–+
van Breugel W., Heckman T., Miley G., 1984, ApJ, 276, 79
van Breugel W., Jagers W., 1982, A&AS, 49, 529
Vázquez G. A., Leitherer C., 2005, ApJ, 621, 695

Voit G. M., 2005, Reviews of Modern Physics, 77, 207
Voit G. M., Bryan G. L., Balogh M. L., Bower R. G., 2002, ApJ, 576, 601
Voit G. M., Cavagnolo K. W., Donahue M., Rafferty D. A., McNamara B. R., Nulsen P. E. J., 2008, ApJ, 681, L5
Voit G. M., Donahue M., 1990, ApJ, 360, L15
Voit G. M., Donahue M., 1997, ApJ, 486, 242
Voit G. M., Donahue M., 2005, ApJ, 634, 955
von der Linden A., Best P. N., Kauffmann G., White S. D. M., 2007, MNRAS, 379, 867
Whysong D., Antonucci R., 2004, ApJ, 602, 116
Wilkinson P. N., Booth R. S., Cornwell T. J., Clark R. R., 1984, Nature, 308, 619
Willott C. J., Rawlings S., Blundell K. M., Lacy M., 2000, MNRAS, 316, 449
Willott C. J., Rawlings S., Jarvis M. J., Blundell K. M., 2003, MNRAS, 339, 173
Wilman R. J., Edge A. C., Swinbank A. M., 2006, MNRAS, 371, 93
Wilman R. J., Edge A. C., Swinbank A. M., 2009, MNRAS, 395, 1355
Wise M. W., McNamara B. R., Nulsen P. E. J., Houck J. C., David L. P., 2007, ApJ, 659, 1153
Wright A., Otrupcek R., 1990, in *PKS Catalog (1990)*, pp. 0–+
Wuyts S. et al., 2009, ApJ, 700, 799
Xu H. et al., 2002, ApJ, 579, 600
York D. G. et al., 2000, AJ, 120, 1579
Zakamska N. L. et al., 2005, AJ, 129, 1212
Zamfir S., Sulentic J. W., Marziani P., 2008, MNRAS, 387, 856
Zanstra H., 1929, Publications of the Dominion Astrophysical Observatory Victoria, 4, 209
Zirbel E. L., 1996, ApJ, 473, 713
Zirbel E. L., 1997, ApJ, 476, 489
Zirbel E. L., Baum S. A., 1995, ApJ, 448, 521
Zirm A. W. et al., 2005, ApJ, 630, 68

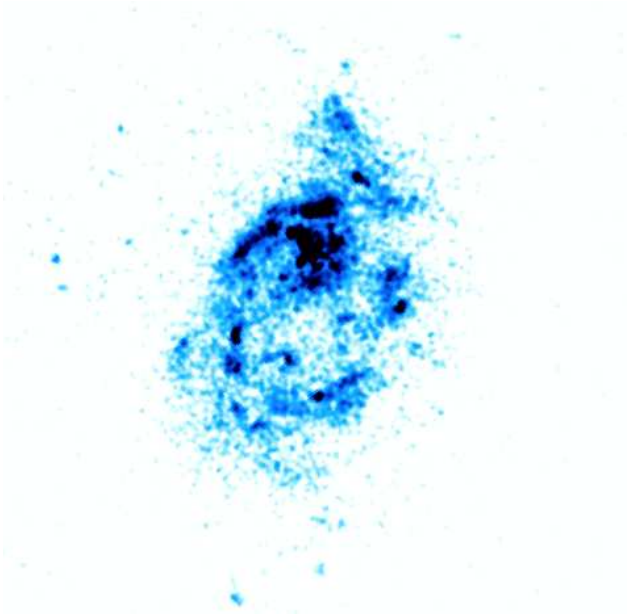

GRANT RUSSELL TREMBLAY
ROCHESTER INSTITUTE OF TECHNOLOGY